

ATHEROSCLEROTIC PLAQUE CHARACTERIZATION IN HUMANS WITH ACOUSTIC
RADIATION FORCE IMPULSE (ARFI) IMAGING

Tomasz J. Czernuszewicz

A dissertation submitted to the faculty at the University of North Carolina at Chapel Hill in partial fulfillment of the requirements for the degree of Doctor of Philosophy in the Department of Biomedical Engineering in the School of Medicine.

Chapel Hill
2015

Approved by:

Caterina M. Gallippi

Paul A. Dayton

Xiaoning Jiang

Timothy C. Nichols

Jonathon W. Homeister

© 2015
Tomasz J. Czernuszewicz
ALL RIGHTS RESERVED

ABSTRACT

Tomasz J. Czernuszewicz: Atherosclerotic Plaque Characterization in Humans with Acoustic Radiation Force Impulse (ARFI) Imaging.
(Under the direction of Caterina M. Gallippi)

Cardio- and cerebrovascular diseases (CVD) are among the leading causes of death and disability in the United States. It is estimated that every 43 seconds someone experiences a heart attack, and every four minutes someone dies of a stroke, resulting in an annual cost of \$312.6 billion in health care expenditures and lost productivity. A vast majority of heart attacks and strokes are linked to atherosclerosis; a condition characterized by inflammation and plaque accumulation in the arterial wall that can rupture and propagate an acute thrombotic event. Identification of plaques that are vulnerable to rupture is paramount to the prevention of heart attacks and strokes, but a noninvasive plaque characterization imaging technology that is cost-effective, safe, and accurate has remained elusive.

The goal of this dissertation is to evaluate whether acoustic radiation force impulse (ARFI) imaging, an ultrasound-based elastography technique, can noninvasively characterize plaque components and identify features that have been shown to correlate with plaque vulnerability. Data are presented from preclinical studies, done in a porcine model of atherosclerosis, and clinical studies, performed in patients undergoing carotid endarterectomy (CEA), to demonstrate the sensitivity and specificity of ARFI for various plaque components. Additionally, the ability of ARFI to measure fibrous cap thickness is assessed with finite element method (FEM) modelling, and the limits of ARFI fibrous cap resolution are analyzed. Lastly, advanced ARFI-based plaque imaging methods are explored, including intravascular ARFI for coronary plaque characterization. Overall, these studies demonstrate that ARFI can delineate features consistent with vulnerable plaque in a clinical imaging context and suggest that ARFI has the potential to improve the current state of the art in atherosclerosis diagnostics.

To my parents,
Roman and Grazyna,
And to my (soon to be) wife,
Cassidy,

Without your love and endless support, none of this would have been possible.

Thank you for always pushing me to be better.

ACKNOWLEDGEMENTS

First and foremost, I would like to acknowledge my advisor, Dr. Caterina Gallippi. You have been a never-ending source of encouragement, inspiration, optimism, knowledge and patience, and I could not have asked for a better mentor. You opened the door to the world of ultrasound for me, and for that, I sincerely thank you. To my committee, Drs. Paul Dayton, Xiaoning Jiang, Timothy Nichols, and Jonathon Homeister, it has been a pleasure working with you and I would like to thank you for your guidance and support. The fact that I have co-authored manuscripts with each of you speaks volumes to your willingness to collaborate, and you have enriched my experience as a graduate student greatly.

There are a number of other individuals that I would like to recognize who were instrumental in this project's success. First, I would sincerely like to thank Melrose Fisher and Dr. Melissa Caughey, who served as clinical nurse coordinator and research sonographer, respectively. You were there with me for every patient and you made those early morning calls that much brighter. Thank you to the surgeons, residents, and staff of UNC Vascular Surgery, your input in the study design and expertise in extracting carotid specimens were critical to the success of this project. Thank you Kirk McNaughton and Ashley Ezzell of the UNC Research Histology Core for spending countless hours sectioning and staining tricky carotid specimens. Thank you Jon Frank, Joseph Merrill, Xiaopeng Zong, and others at the UNC Biomedical Research Imaging Center for helping with *ex vivo* sample imaging. Thank you to Drs. Ben Huang, Carlos Zamora, and Ellie Lee of UNC Radiology and my other blinded readers for your help painstakingly annotating ARFI images. Thank you Elizabeth Merricks, Robin Raymer, Kent Passingham, and others at the Francis Owen Blood Research Laboratory who aided with the preclinical studies. Thanks to Mike Waldron and the staff of UNC Research Computing, for enabling and supporting my use of the Killdevil supercomputer cluster for simulation studies. Thank you also to Drs. Kathy Nightingale, Gregg

Trahey, Brett Byram, Jeremy Dahl, and Mark Palmeri from Duke University. I spent almost as much time in your classes at Duke as I did at UNC, and an enormous part of my success can be attributed to you.

I would also like to thank past and present Gallippi lab members, you made coming to lab every day a joy, and the countless insights, discussions, and multi-hour lab meetings we had were invaluable to my success. Special thanks to former graduates, Drs. Russ Behler and Mallory Selzo, who trained me in ARFI and countless other techniques that helped me through my graduate career. I would also like to thank Jiang lab members, Zhuochen Wang and Dr. Jianguo Ma, for their transducer fabrication expertise, and former Dayton lab members Drs. Jason Streeter, Paul Sheeran, and Ryan Gessner for collaborations, discussions, and general shenanigans. Lastly, I would like to acknowledge my funding sources including the Integrative Vascular Biology Fellowship, the Glaxo Fellowship in Biomedical Imaging, and the NIH.

Finally, I would like to thank my parents for giving me every opportunity imaginable to succeed and never asking for anything in return other than I keep learning. And, of course, thank you Cassidy. Words cannot express how happy I am that we found each other. You have been the light of my life, constantly supporting me through this journey, and I cannot wait to see where we end up next.

TABLE OF CONTENTS

ABSTRACT.....	iii
ACKNOWLEDGEMENTS.....	v
TABLE OF CONTENTS.....	vii
LIST OF TABLES.....	xiv
LIST OF FIGURES.....	xvi
LIST OF ABBREVIATIONS.....	xxi
1 Introduction.....	1
1.1 Purpose.....	1
1.2 Hypothesis.....	2
1.3 Overview.....	2
2 Clinical Background.....	4
2.1 Pathogenesis of Atherosclerosis.....	4
2.2 Atherosclerosis Classification System.....	8
2.3 The “Vulnerable” Plaque.....	9
2.3.1 Thin Fibrous Cap.....	11
2.3.2 Enlarged Necrotic Core.....	11
2.3.3 Positive Arterial Remodeling Index.....	12
2.3.4 Neovascularization and Intraplaque Hemorrhage.....	13
2.3.5 Comparing Vulnerable Plaque in Different Arterial Locations.....	14
2.4 Treatment.....	15

2.4.1	Pharmaceutical	15
2.4.2	Surgical.....	17
2.5	Animal Models.....	19
2.5.1	Murine (mouse).....	19
2.5.2	Porcine (pig).....	20
2.6	Summary	20
3	Atherosclerosis Imaging Techniques.....	22
3.1	X-ray Techniques	22
3.1.1	Fluoroscopy.....	23
3.1.2	Computed Tomography (CT).....	25
3.1.3	Advantages and Disadvantages	27
3.2	Magnetic Resonance Imaging (MRI)	28
3.2.1	Advantages and Disadvantages	30
3.3	Ultrasound (US) Imaging	31
3.3.1	Plaque Echogenicity.....	33
3.3.2	Virtual Histology (VH)	33
3.3.3	Advantages and Disadvantages	35
3.4	Optical Techniques.....	37
3.4.1	Optical Coherence Tomography (OCT).....	37
3.4.2	Optical Spectroscopy Methods.....	38
3.4.3	Intravascular Photoacoustic (IVPA) Imaging	38
3.5	Elasticity Imaging.....	39
3.5.1	Intrinsic Motion Sources	40
3.5.2	Extrinsic Motion Sources	41

3.6	Summary	42
4	Radiation Force Elasticity Imaging.....	43
4.1	Soft-Tissue Biomechanics.....	44
4.2	Acoustic Radiation Force Theory.....	47
4.3	Vascular ARF-Based Imaging Methods.....	49
4.3.1	Vibroacoustography (VA).....	50
4.3.2	Shear Wave Elasticity Imaging (SWEI) and Supersonic Imaging (SSI).....	50
4.3.3	Shear/Lamb Wave Dispersion Vibrometry and Spectroscopy.....	52
4.3.4	Acoustic Radiation Force Impulse (ARFI) Imaging	53
4.4	Challenges/Future Developments.....	55
4.4.1	Bioeffects	55
4.4.2	Physiologic Motion	58
4.4.3	Jitter.....	58
4.4.4	Displacement Underestimation	60
4.4.5	Clutter.....	62
4.4.6	Depth-of-Field.....	63
4.4.7	Real-Time ARFI.....	65
4.5	Summary	66
5	Acoustic Radiation Force Beam Sequence Performance for Detection and Material Characterization of Atherosclerotic Plaques: Preclinical, <i>Ex Vivo</i> Results.....	67
5.1	Introduction	67
5.2	Methods.....	69
5.2.1	Animal Model	69
5.2.2	Ultrasonic Imaging, Data Collection, and Data Processing	69
5.2.3	Histology	74

5.2.4	Reader Training.....	75
5.2.5	Reader Evaluation Study.....	77
5.2.6	ROC Analysis.....	79
5.3	Results.....	80
5.3.1	Plaque Detection.....	80
5.3.2	Plaque Characterization.....	81
5.3.3	Image Exclusions.....	85
5.4	Discussion.....	86
5.5	Conclusion.....	91
5.6	Addendum.....	92
5.6.1	ROC Calculation.....	92
5.6.2	ROC Example.....	94
6	ARFI-Derived Carotid Plaque Stiffness Measurements Compared with Histology I: Preliminary Results.....	97
6.1	Introduction.....	97
6.2	Methods.....	99
6.2.1	Patients.....	99
6.2.2	Ultrasonic Imaging and Data processing.....	100
6.2.3	Histology.....	103
6.3	Results.....	105
6.4	Discussion.....	111
6.5	Conclusion.....	116
7	On the Feasibility of Quantifying Fibrous Cap Thickness with Acoustic Radiation Force Impulse Ultrasound: A Simulation Study.....	117
7.1	Introduction.....	117

7.2	Methods.....	119
7.2.1	Finite Element Method Simulations.....	119
7.2.2	Ultrasound Simulations.....	122
7.2.3	Processing of Tracked Data.....	122
7.2.4	Fibrous Cap Thickness Measurement.....	123
7.2.5	Additional Performance Metrics.....	125
7.2.6	Comparison with <i>In Vivo</i> Data.....	125
7.3	Results.....	126
7.4	Discussion.....	139
7.5	Conclusion.....	143
8	ARFI-Derived Carotid Plaque Stiffness Measurements Compared with Histology II: In Vivo Assessment of Fibrous Cap Thickness and Rupture.....	144
8.1	Introduction.....	144
8.2	Methods.....	145
8.2.1	Patients.....	145
8.2.2	Ultrasonic Imaging.....	145
8.2.3	<i>Ex Vivo</i> Specimen Imaging.....	146
8.2.4	Histology.....	147
8.3	Results.....	148
8.4	Discussion.....	156
8.5	Conclusion.....	157
9	Blinded-Reader Performance of ARFI Plaque Characterization.....	159
9.1	Introduction.....	159
9.2	Methods.....	159
9.2.1	Reader Evaluation Study.....	160

9.2.2	Histology	162
9.2.3	Statistical Analysis	163
9.2.4	Image Inclusion Criteria.....	164
9.3	Results	165
9.4	Discussion	173
9.5	Conclusion.....	178
10	Towards Intravascular ARFI (IV-ARFI) Imaging.....	179
10.1	Introduction	179
10.2	Methods.....	180
10.2.1	Transducer Design (1 st Generation).....	180
10.2.2	Optical Phantom Construction	181
10.2.3	Optical Tracking of ARF Displacement.....	182
10.2.4	Acoustic Backscatter Test	184
10.2.5	Transducer Design (2 nd Generation).....	185
10.2.6	Transducer Characterization.....	187
10.2.7	ARFI Testing.....	188
10.3	Results/Discussion.....	189
10.3.1	First-Generation Transducer.....	189
10.3.2	Second-Generation Transducer	192
10.4	Conclusion.....	195
11	Conclusions and Future Directions.....	196
11.1	Conclusions	196
11.2	Future Directions.....	197
A	Experimental Validation of Displacement Underestimation in ARFI Ultrasound.....	200

A.1	Introduction	200
A.2	Methods.....	203
A.2.1	Optical Phantom Construction	203
A.2.2	Experimental Setup	206
A.2.3	Data Collection.....	208
A.2.4	Data Processing	210
A.2.5	Speed of Sound and Attenuation Measurements.....	211
A.3	Results	214
A.4	Discussion	218
A.5	Conclusion.....	223
B	Optimal ARFI Frequency Derivation.....	224
B.1	Theory	224
B.2	Methods.....	225
B.3	Results/Discussion.....	225
	REFERENCES.....	228

LIST OF TABLES

Table 2.1:	American Heart Association plaque rating scale.	8
Table 3.1:	Noninvasive imaging signal characteristics of plaque components	25
Table 3.2:	Diagnostic performance, strengths, limitations, and pitfalls of CTA in the evaluation of stenosis, plaque morphology, and composition.....	27
Table 3.3:	Diagnostic performance, strengths, limitations, and pitfalls of MRA and CE-MRA in the evaluation of stenosis, plaque morphology, and composition.	30
Table 3.4:	Diagnostic performance, strengths, limitations, and pitfalls of DUS in the evaluation of stenosis, plaque morphology, and composition.....	35
Table 5.1:	Classification system for atherosclerotic plaques established by the AHA Committee on Vascular Lesions.....	75
Table 5.2:	Rating system used by the pathologist.	76
Table 5.3:	Number of plaque types and features as determined by the pathologist collapsed according to the dichotomization thresholds.....	77
Table 5.4:	Expected ARF-induced responses of different plaque features in parametric images, presented to the reader as part of the training regimen	78
Table 5.5:	Rating system used by the readers.	79
Table 5.6:	Comparison of ARF beam sequence sensitivity and specificity for plaque detection and characterization versus published sensitivity and specificity for MRI and CT.....	85
Table 5.7:	Reader response for lipid pools versus pathologist response.....	95
Table 5.8:	Reader response for lipid pools versus dichotomized pathologist response.	95
Table 6.1:	UNC stenosis grading scale.....	100
Table 6.2:	Patient characteristics.....	101
Table 6.3:	Histological stain guide.....	105
Table 7.1:	Material model constants.	121
Table 7.2:	Simulation parameters.....	123
Table 8.1:	Patient characteristics.....	148

Table 9.1:	Sensitivity and specificity for combined plaque categories.	169
Table 10.1:	Parameters of 2 nd -generation IV-ARFI design	185
Table A.1:	Phantom recipes and material parameters	204
Table A.2:	Empirically determined power settings for the Antares for each phantom and pushing pulse focal configuration (F/#) to yield equivalent displacement.....	209
Table A.3:	Time points at which mean acoustic and optical displacements become non-significantly different.....	217
Table A.4:	Mean peak displacement, time to 67% recovery, and time to peak measured optically across 10 beads.....	220
Table B.1:	Predicted optimal pushing frequency for various targets.....	227

LIST OF FIGURES

Figure 2.1:	Stages in the development of atherosclerosis.....	5
Figure 2.2:	Histological examples of coronary plaques representing the spectrum of atherosclerotic lesions.....	10
Figure 3.1:	Examples of three angiography techniques.....	24
Figure 3.2:	MR images of a carotid artery plaque with a large lipid-rich necrotic-core with an intact fibrous cap.	29
Figure 3.3:	Longitudinal duplex ultrasound images of a predominantly echolucent, concentric, carotid artery plaque with >60% stenosis.....	32
Figure 3.4:	Classification of various coronary plaques with virtual histology intravascular ultrasound	34
Figure 4.1:	Motion filtering of ARFI displacement profiles.....	59
Figure 4.2:	B-mode and qualitative ARFI imaging of a phantom with a soft spherical inclusion (8 kPa) embedded in a stiffer background (25 kPa).	65
Figure 5.1:	Pressurization apparatus for ex vivo imaging	70
Figure 5.2:	Diagrams of the five different ARFI beam sequences that were investigated in ex vivo reader study	73
Figure 5.3:	Boxplots of AUC and SCC vs. beam sequence for plaque detection and individual plaque features	82
Figure 5.4:	Three examples of ARFI images with matched histology.	84
Figure 5.5:	Image exclusion results.	86
Figure 5.6:	Example of ROC curve calculation.....	96
Figure 6.1:	Example of a sample preparation for histology.....	104
Figure 6.2:	Type Va plaque from the CCA of a 57 year-old, symptomatic male (patient A).	106
Figure 6.3:	Type Va plaque from the ICA of a 53 year-old, symptomatic female (patient B).	108
Figure 6.4:	Type Vb plaque from the ICA of a 72 year-old, asymptomatic male (patient C).	110
Figure 6.5:	Type Vb plaque from the ICA of a 65 year-old, asymptomatic male (patient D).	112

Figure 7.1:	Schematic of the layered model used to approximate an atherosclerotic plaque.....	120
Figure 7.2:	Block diagram describing semi-automated FC thickness measurement.	124
Figure 7.3:	Example of k-means clustering algorithm and FC thickness measurement.....	126
Figure 7.4:	Comparison of FEM simulated data to an in vivo example.	127
Figure 7.5:	FEM-measured peak displacement results with and without saturation.	128
Figure 7.6:	FEM thickness bias as a function of image saturation level.	129
Figure 7.7:	Examples of simulated 2D ARFI peak displacement images for the ten fibrous cap thicknesses taken with tracking pulses centered at 6 MHz and using a 1λ kernel (0.257 mm).	130
Figure 7.8:	Examples of simulated 2D ARFI peak displacement images for the ten fibrous cap thicknesses taken with tracking pulses centered at 12 MHz and using a 2λ (0.257 mm) kernel.	130
Figure 7.9:	Simulated ARFI-measured fibrous cap thickness compared to true thickness grouped by relative kernel size (given as a fraction of wavelength, λ).	131
Figure 7.10:	Simulated ARFI-measured fibrous cap thickness compared to true thickness grouped by absolute kernel length.....	132
Figure 7.11:	Simulated ARFI-measured thickness bias a function of absolute kernel size.....	133
Figure 7.12:	ARFI-measured contrast between the simulated fibrous cap and necrotic core layers as a function of fibrous cap thickness for three different saturation levels ($\beta = 0.0$, $\beta = 0.5$, and $\beta = 0.75$).	134
Figure 7.13:	ARFI-measured contrast between the simulated fibrous cap and necrotic core layers as a function of absolute kernel size for three different fibrous cap thicknesses (0.2 mm, 0.5 mm, and 1.0 mm).....	134
Figure 7.14:	ARFI-measured CNR between the simulated fibrous cap and necrotic core layers as a function of fibrous cap thickness for three different saturation levels ($\beta = 0.0$, $\beta = 0.5$, and $\beta = 0.75$).	136
Figure 7.15:	ARFI-measured CNR between the simulated fibrous cap and necrotic core layers as a function of absolute kernel size for three different fibrous cap thicknesses (0.2 mm, 0.5 mm, and 1.0 mm).....	136
Figure 7.16:	FC thicknesses measured from ARFI images taken in vivo and compared against histology.....	137
Figure 7.17:	The impact of kernel size and dynamic range (DR) color scaling on mean ARFI-measured fibrous cap thickness for two in vivo examples.....	138

Figure 7.18:	ARFI-measured contrast and CNR between the necrotic core and fibrous cap for two in vivo examples	139
Figure 8.1:	Comparison of gross CEA specimen and μ CT 3D rendering	149
Figure 8.2:	Example of plaque alignment using ex vivo μ CT imaging.....	150
Figure 8.3:	Carotid ARFI image with matched histology and ex vivo μ CT imaging from a symptomatic 71 year-old male.....	151
Figure 8.4:	Carotid ARFI image with matched histology and ex vivo μ CT imaging from a 45 year-old symptomatic female.....	152
Figure 8.5:	Series of ARFI peak displacement images taken from six CEA patients.	153
Figure 8.6:	Linear regression and Bland-Altman analysis on ARFI-measured fibrous cap thickness versus histology-measured fibrous cap thickness for an unblinded reader.....	155
Figure 9.1:	GUI used by readers to grade and segment ARFI images.....	161
Figure 9.2:	GUI used by pathologist to grade and segment histology.....	163
Figure 9.3:	Flowchart for specimen inclusion in blinded reader study.....	166
Figure 9.4:	Histograms showing counts of excluded and included subsections broken down by AHA plaque types.	167
Figure 9.5:	Boxplots of reader AUC for various plaque composition elements.....	168
Figure 9.6:	ROC curves for radiologists for detecting combined stiff features (collagen and calcium) and combined soft features (necrotic core and intraplaque hemorrhage).	169
Figure 9.7:	Barplots showing the difference in median AUC when readers were given the plaque outline versus when they were not.....	170
Figure 9.8:	Spearman correlation coefficient between reader-assigned qualitative stiffness score and plaque components.....	171
Figure 9.9:	Cohen's kappa for AHA plaque type ratings.	172
Figure 9.10:	ARFI-measured fibrous cap thickness measurements by blinded readers compared against histological thickness.	173
Figure 9.11:	Regression and Bland-Altman analysis of ARFI-measured fibrous cap thickness versus histology from three blinded radiologists.....	174

Figure 9.12: Comparison of B-mode and ARFI contrast between fibrous cap and necrotic core.....	175
Figure 10.1: Photograph of the front face of the first-generation dual-frequency IVUS probe mounted on the end of a 20-gauge needle tip.....	181
Figure 10.2: Illustration of IV-ARFI optical tracking setup.....	183
Figure 10.3: Structure of the second-generation IV-ARFI transducer.....	184
Figure 10.4: Fabrication process of a dual-frequency IVUS transducer.....	186
Figure 10.5: Experimental setup for ARFI test in the phantom.....	189
Figure 10.6: Displacements measured optically from first generation IV-ARFI transducer.....	190
Figure 10.7: A-line acquired by the high-frequency element of first generation IV-ARFI transducer in a graphite phantom to illustrate the capability for pulse/echo imaging.....	191
Figure 10.8: Two A-lines taken with the high-frequency element, one prior to movement, and the other after ~0.1 mm of bulk motion with a manual motion stage.....	191
Figure 10.9: Electrical impedance and phase spectrum of 2nd-generation transducer.....	192
Figure 10.10: Pulse/echo and hydrophone characterization of 2nd-generation transducer.....	193
Figure 10.11: Acoustically-tracked displacements with 2nd-generation transducer.....	194
Figure 10.12: Acoustically-measured peak displacement vs. time for three different ARF-burst durations.....	195
Figure A.1: Schematics of phantom design and confocal alignment of optical and acoustic foci showing the axial/elevational view and the axial/lateral view.....	205
Figure A.2: Schematic and photograph of optical experimental setup.....	207
Figure A.4: Example of displacement profiles tracked optically and acoustically.....	215
Figure A.5: Displacement through time measured both acoustically and optically for the 6.6, 19.8, and 30.2 kPa phantoms with F/1.5 and F/3 excitation pulse focal configurations.....	216
Figure A.6: Percentage of optical displacement tracked acoustically in phantoms of 6.6 kPa, 19.8 kPa, and 30.2 kPa with two different excitation pulse focal configurations (F/1.5 and F/3).....	218

Figure A.7: Mean optically traced displacements with F/1.5 and F/3 ARF pulse focal configurations plotted on top of each other to show the effect of pushing F/# on phantom recovery time.....	219
Figure B.1: ARF magnitude as a function of frequency and focal depth for three attenuation coefficients.	226
Figure B.2: Frequency of maximum ARF as a function of focal depth.	227

LIST OF ABBREVIATIONS

μ CT	Micro Computed Tomography
1D	One Dimensional
2D	Two Dimensional
3D	Three Dimensional
A/D	Analog to Digital
ACE	Angiotensin Converting Enzyme
ACS	Acute Coronary Syndrome
AHA	American Heart Association
AIUM	American Institute of Ultrasound in Medicine
A-line	Amplitude line
apo	Apolipoprotein
ARF	Acoustic Radiation Force
ARFI	Acoustic Radiation Force Impulse
AUC	Area Under the Curve
BA	Bland-Altman
B-mode	Brightness mode
CABG	Coronary Artery Bypass Graft
CAC	Coronary Artery Calcification
CCA	Common Carotid Artery
CDF	Cumulative Distribution Function
CEA	Carotid Endarterectomy
CE-MRA	Contrast-Enhanced Magnetic Resonance Angiography
CME	Combined Masson's Elastin
CNR	Contrast to Noise Ratio

CRLB	Cramér-Rao Lower Bound
CT	Computed Tomography
CTA	Computed Tomography Angiography
CUDA	Compute Unified Device Architecture
CVD	Cardiovascular Disease
CW	Continuous Wave
DDG	Depth-Dependent Gain
DH	Dietary Hypercholesterolemia
DNA	Deoxyribonucleic Acid
DSA	Digital Subtraction Angiography
DUS	Duplex Ultrasound
ECA	External Carotid Artery
ECG	Electrocardiogram
EEL	External Elastic Lamina
F/#	F-Number (Focal Ratio)
FC	Fibrous Cap
FD	Frequency-Domain
FDA	Food and Drug Administration
FEM	Finite Element Method
FH	Familial Hypercholesterolemia
FN	False Negative
FOV	Field of View
FP	False Positive
FPR	False Positive Rate
FWHM	Full Width Half Max

GPU	Graphical Processing Unit
GSM	Gray-Scale Median
GUI	Graphical User Interface
H&E	Hematoxylin and Eosin
HDL	High Density Lipoprotein
HMG-CoA	3-Hydroxy-3-Methylglutaryl-Coenzyme A
HR	Hazard Ratio
HU	Hounsfield Unit
IACUC	Institutional Animal Care and Use Committee
ICA	Internal Carotid Artery
ICAM	Intracellular Adhesion Molecule
IEL	Internal Elastic Lamina
IL	Interleukin
IMT	Intima-Media Thickness
IPH	Intraplaque Hemorrhage
IQR	Inter-Quartile Range
IRB	Institutional Review Board
IVPA	Intravascular Photoacoustic
IVUS	Intravascular Ultrasound
LAD	Left Anterior Descending
LDL	Low Density Lipoprotein
LDLR	Low Density Lipoprotein Receptor
LDUV	Lamb Wave Dispersion Ultrasound Vibrometry
LMT	Lillie's Modified Masson's Trichrome
LSME	Lagrangian Speckle Model Estimator

MAD	Median Absolute Deviation
MESA	Multi-Ethnic Study of Atherosclerosis
MHz	Megahertz
MI	Mechanical Index
MLE	Maximum Likelihood Estimation
M-mode	Motion mode
MMP	Matrix Metalloproteinase
MRA	Magnetic Resonance Angiography
MRE	Magnetic Resonance Elastography
MRI	Magnetic Resonance Imaging
NC	Necrotic Core
NCC	Normalized Cross Correlation
NF	Nuclear Factor
NIR	Near Infrared
NIVE	Non-Invasive Vascular Elastography
NNT	Number Needed to Treat
OCT	Optical Coherence Tomography
oxLDL	Oxidized Low Density Lipoprotein
P/E	Pulse/Echo
PA	Photoacoustic
ParRx	Parallel Receive
PCA	Principal Component Analysis
PCI	Percutaneous Coronary Intervention
PD	Peak Displacement
PI	Polyimide

PMN-PT	Lead Magnesium Niobate-Lead Titanate
PPAR	Peroxisome Proliferator-Activated Receptor
PRF	Pulse Repetition Frequency
PSF	Point Spread Function
PVL	Peripheral Vascular Laboratory
PWI	Pulse Wave Imaging
QUS	Quantitative Ultrasound
RF	Radiofrequency
ROC	Receiver Operating Characteristic
ROE	Region of Excitation
ROI	Region of Interest
RT	Recovery Time
SCC	Spearman Correlation Coefficient
SCD	Sudden Cardiac Death
SDUV	Shear Wave Dispersion Ultrasound Vibrometry
SMC	Smooth Muscle Cell
SNR	Signal to Noise Ratio
SOS	Speed of Sound
SRx	Single Receive
SSI	Supersonic Shear Imaging
SWEI	Shear Wave Elasticity Imaging
SWV	Shear Wave Velocity
T1	Longitudinal Relaxation Time
T2	Transverse Relaxation Time
TD	Time Domain

TDE	Time Delay Estimator
TF	Tissue Factor
TGC	Time-Gain Compensation
THI	Tissue Harmonic Imaging
TI	Thermal Index
TIA	Transient Ischemic Attack
TN	True Negative
TNF	Tumor Necrosis Factor
TOF	Time of Flight
TP	True Positive
TPR	True Positive Rate
TTP	Time to Peak
URI	Ultrasound Research Interface
US	Ultrasound
VA	Vibroacoustography
VCAM	Vascular Cell Adhesion Molecule
VH	Virtual Histology
VisR	Viscoelastic Response
VK	Von Kossa
VLDL	Very Low Density Lipoprotein
VTI	Virtual Touch Imaging
VVG	Verhoeff-Van Geison

CHAPTER 1

Introduction

1.1 Purpose

Cardiovascular disease (CVD) is the leading cause of death in the United States and globally [1]. Heart attacks and strokes represent the majority of CVD-related deaths and are predominantly caused by ischemia secondary to atherosclerotic disease of major arteries. Unsurprisingly, considerable research effort has gone into understanding the etiology of atherosclerosis and developing diagnostic tools that can identify the early onset of the disease prior to ischemic event.

Atherosclerosis has often been dubbed the “silent killer” because it generally develops asymptotically for decades before presenting as a heart attack or stroke. While atherosclerosis itself can narrow arteries over time and eventually cause ischemia, an acute-onset event such as a heart attack often occurs when a plaque is disrupted or ruptured. In the 1990s and early 2000s, numerous histopathology studies determined that certain morphological features made plaques more prone to rupture, leading to the development of the “vulnerable plaque” hypothesis. Namely, plaques that were composed of large lipid-rich necrotic cores and active inflammation covered with thin fibrous caps were highly associated with rupture and thrombosis [2]. Importantly, these and other studies revealed that ruptured plaques were not necessarily those with the highest degree of stenosis, suggesting that plaque composition may be a superior biomarker to stratify plaque risk.

Ultrasound is currently the most widely applied diagnostic imaging modality for atherosclerosis due to its sensitivity to detect stenosis, widespread availability, and relatively low cost. Unfortunately, conventional ultrasound, which relies on the acoustic *backscatter* properties of tissue, has been shown to be unreliable for plaque characterization [3]. The purpose of this dissertation therefore, is to investigate

the application of a novel ultrasound modality – acoustic radiation force impulse (ARFI) imaging – for plaque characterization. Unlike conventional ultrasound, ARFI interrogates the *mechanical* properties of tissue, in a method akin to palpation. Therefore, the work presented herein proposes a new vulnerable plaque-imaging paradigm that has the potential to substantially improve the accuracy of ultrasonic plaque characterization and facilitate its use in the clinic.

1.2 Hypothesis

The underlying hypothesis driving this research is that **by interrogating mechanical properties, ARFI imaging can noninvasively describe the composition and structure of atherosclerotic plaques.** To test this hypothesis, a clinical study was designed in which ARFI images were taken in patients undergoing carotid endarterectomy. The ARFI images were then compared to histology from the corresponding endarterectomy samples in order to validate whether ARFI is capable of identifying vulnerable plaque features such as necrotic core, fibrous cap, and intraplaque hemorrhage. This dataset proved to be very rich and instigated further hypothesis-driven research, for example, testing the limits of ARFI resolution for measuring fibrous cap thickness. Throughout this dissertation, data from this clinical study will be referred to and analyzed.

1.3 Overview

As mentioned above, this dissertation primarily focuses on the clinical validation of ARFI imaging for plaque characterization compared against a histological gold standard. The organization of this work is the following.

Chapter 2 begins by describing the natural history of atherosclerosis and introduces the concept of the vulnerable plaque. Chapter 3 reviews the current state-of-the-art atherosclerosis imaging techniques that are implemented either clinically or in development in research laboratories, and introduces elasticity imaging as a novel modality for plaque characterization. In Chapter 4, elasticity-imaging techniques that specifically utilize acoustic radiation force are described in detail, including ARFI imaging, which is the focus of this dissertation. A detailed description of the physics underlying acoustic radiation force

generation is also provided in this chapter. Chapter 5 presents a pre-clinical reader study done in *ex vivo* porcine arteries that demonstrates the sensitivity and specificity of ARFI for delineating various plaque compositional elements compared with matched histology. The methods of this pre-clinical study serve as a basis for the following chapters, which implement ARFI clinically in a human patient population. Chapter 6 presents preliminary results from four carotid plaques imaged *in vivo* in patients undergoing endarterectomy. In Chapter 7, the feasibility of ARFI for quantifying fibrous cap thickness is assessed with FEM modeling. Chapter 8 continues analysis of *in vivo* ARFI images from a greater number of endarterectomy patients and proposes improved methods for spatially aligning histology. Chapter 9 concludes the evaluation of transcutaneous ARFI for *in vivo* carotid plaque characterization by reporting on the performance of ARFI for delineating plaque features as measured by a statistical reader study. Chapter 10 presents a novel intravascular ultrasound (IVUS) transducer that has potential for performing ARFI imaging in the coronary arteries. Finally, Chapter 11 presents the overall conclusions of this dissertation and discusses the future of ARFI plaque characterization.

CHAPTER 2

Clinical Background

Atherosclerosis, originating from the Greek words *athere* meaning “gruel” and *skleros* meaning “hard”, is a chronic disease of the arterial vasculature. It is characterized by the development of atheromatous plaque in the walls of either elastic or muscular arteries that feed critical organs, such as the heart and brain, and without warning can result in a fatal heart attack or stroke.

While the etiology of atherosclerosis is still not completely known, our understanding of the key mechanisms has grown substantially over the past few decades. This chapter will begin by discussing the basic anatomy of an artery and review the pathological changes that occur during atherosclerosis. Next, the concept of the “vulnerable plaque” will be introduced, which is a term used to describe plaques that are at highest risk for causing acute ischemic events. Finally, to conclude the chapter, various clinical therapies for treating atherosclerosis, as well as the animal models that drive atherosclerosis research, will be presented.

2.1 Pathogenesis of Atherosclerosis

The normal muscular artery in humans consists of three layers, each with its own unique structural characteristics and functions (Figure 2.1a). The inner layer, the tunica intima, consists of a single layer of endothelial cells supported by a small amount of sub-endothelial connective tissue. The tunica intima is in constant contact with luminal blood and it is in this layer that atherosclerosis first develops. The middle layer, which is typically the thickest of the three layers, is known as the tunica media and is comprised of smooth muscle cells (SMCs) embedded in a complex matrix of elastic lamellae. The SMCs in this layer give the artery the ability to vasoconstrict or vasodilate, while the elastic fibers help mitigate variations in pressure from pulsation. Finally, the outer layer, the tunica adventitia, is

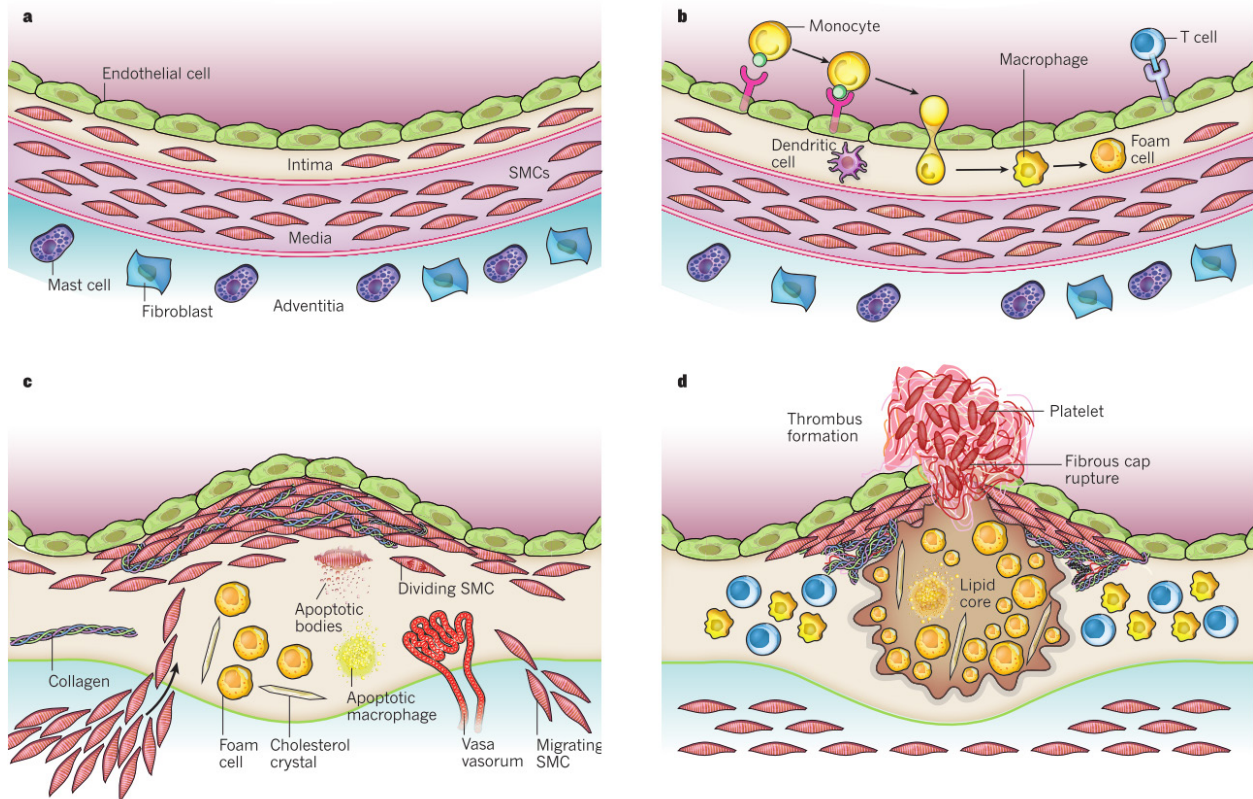


Figure 2.1: Stages in the development of atherosclerosis. (a) Normal arterial wall depicting the three arterial layers: intima, media, and adventitia. (b) Initial stage of atherosclerosis, characterized by monocyte trafficking into the subintimal space, differentiation of monocytes into macrophages, and macrophage uptake of lipid yielding foam cells. (c) Lesion progression into a “fibroatheroma”, characterized by smooth muscle cell infiltration, heightened synthesis of collagen, apoptosis of foam cells that lead to formation of a necrotic core and calcification, and neovascularization of the vasa vasorum. (d) Thrombosis due to fibrous cap rupture, the ultimate complication of atherosclerosis. Reprinted with permission from [6] (Copyright © 2011 Macmillan Publishers Ltd.).

mostly comprised of connective tissue (including collagen and free elastin fibers) and adipose tissue that serves to support the artery and it houses nutrient vessels, known as *vasa vasorum*, and nerves, known as *nervi vasorum*. The three layers are separated by two dense elastic membranes called the internal elastic lamina (IEL) and external elastic lamina (EEL), at the intima/media and media/adventitia borders, respectively.

The first step in atherogenesis involves the sub-endothelial deposition and retention of apolipoprotein (apo) B-containing lipoproteins, more commonly known as very-low and low density lipoproteins (VLDL and LDL, respectively) [4]. Once inside the arterial wall, LDL can undergo oxidative

stress and be modified to oxidized-LDL (oxLDL), a process exacerbated by hypertension, diabetes, and smoking. The retained LDL and oxLDL particles ultimately trigger an inflammatory response in the arterial wall and initiate the cycle of atherosclerosis (Figure 2.1b). The presence of oxLDL in the intima, through activation of transcription factors such as NF- κ B, leads to the expression of leukocyte adhesion molecules (e.g. VCAM and ICAM) on the surface of the endothelium and initiates monocyte recruitment into the intimal space. Monocytes go on to differentiate into macrophages and attempt to scavenge oxLDL, however they are incapable of clearing the cholesterol-laden proteins and become trapped in the intima (these lipid-filled macrophages are typically referred to as “foam cells”). While the foam cells remained trapped, they continue to produce inflammatory cytokines, such as IL-1 β , IL-12, and TNF- α , that, not only amplify the inflammatory response, but also cause more lipoprotein movement into the intima by increasing transcription of LDL-receptor gene [5]. Thus the vicious cycle is propagated, including altered lipoprotein trafficking and oxidation, and chronic inflammation, which is maintained in the artery for decades and leads to the development of an “atheroma”.

In addition to lipid accumulation and inflammation, atheroma formation also typically involves the activation and migration of vascular SMCs from the medial layer (Figure 2.1c). In response to inflammation, quiescent SMCs down-regulate expression of differentiation marker genes, including those for smooth muscle α -actin and smooth muscle myosin heavy chain, and switch to a remodeling phenotype that is characterized by SMC migration, proliferation, and an increase in the production of extracellular matrix [4]. This increase in extracellular matrix, which includes the production of collagen and elastin fibers, is one the major factors leading to the general stiffening of arteries for which atherosclerosis derives its name, and is responsible for the formation of a fibrous cap which covers the growing atheroma. While the SMCs are laying down collagen to try to isolate and protect the growing plaque, foam cells trapped within the atheroma can die from apoptosis, releasing lipids and cellular debris into the extracellular space. Over time, a substantial number of foam cells die forming a localized region of extracellular lipids and debris known as a lipid-rich pool or necrotic core [6].

An interesting phenomenon that occurs in the late stages of atherosclerosis development is the potential for intimal calcification. Calcification tends to occur in one of two forms, either as diffuse microcalcifications, or as large, focal punctate fragments or sheets. Diffuse microcalcifications tend to localize in areas of fibrosis, including the fibrous cap, whereas the larger fragments are typically found in the necrotic core where microcalcifications are able to coalesce. The general consensus is that calcifications originate from the cellular debris of apoptotic SMCs or macrophages [7]. Precipitation of calcium occurs when the local ionic concentration increases over the salt solubility product in the local microenvironment of the plaque. This is known as the “passive” hypothesis for atherosclerotic calcification [8]. Apoptotic macrophages in particular have been shown to release high concentrations of mitochondrial phosphate and phosphatidylserine-containing molecules that may tip the ionic balance and lead to precipitation [8]. Recent studies though, have shown that calcification may also be driven as an “active” process, whereby arterial cells in the atheroma can differentiate into osteoblast-like phenotypes and express potent osteogenic factors such as BMP-2 [8]. This suggests that calcification may occur in a manner similar to conventional bone formation.

Finally, the most significant complication that can occur during late atherosclerosis is the development of a blood clot, a term referred to as thrombosis or hemorrhage (Figure 2.1d). Thrombosis arises when plaque material is exposed to the flowing blood within the vessel lumen. This scenario occurs most frequently when the fibrous cap ruptures or fissures develop, uncovering the thrombogenic lipid/necrotic core; an event known as plaque rupture [9]. In other cases, the endothelial layer that lines the plaque can deteriorate causing a clot to form on the surface, which is known as plaque erosion [10]. Arterial thrombosis and atherosclerosis have traditionally been considered separate entities with distinct pathogenic mechanisms, but new evidence has suggested that the two are more closely linked, with thrombosis being a significant promoter of the rapid progression of the underlying atherosclerotic lesion [11]. In many cases, plaque rupture and thrombosis can be a clinically silent event and the body is able to heal the site of rupture [12]. Indeed, plaques may undergo a number of rupture and healing cycles prior to the event that causes sudden death, and recent studies have shown that a unique constellation of

Table 2.1: American Heart Association plaque rating scale.

Plaque Type	Morphological Description
0	Normal artery; no intimal thickening
I	Initial lesion; not grossly apparent plaque; foam cells.
II	Fatty streak; lesion grossly apparent; foam cells and smooth muscle cells (SMC) contain lipid droplets.
III	Preatheroma; raised fatty streak in gross morphology, multiple but small extracellular lipidic cores, foam cells contain lipid droplets, increasing number of SMCs.
IV	Atheroma; single and massive extracellular lipid pool (lipid core), grossly visible, well delimited, covered by a proteoglycan-rich layer infiltrated with foam cells and smooth muscle cells with and without lipid droplet inclusion.
Va	Fibroatheroma; type IV with a cap rich in fibrosis (collagen), possible small calcification.
Vb	Calcified plaque; lesion with a lipid core or fibrotic tissue, with large calcifications.
Vc	Fibrotic plaque; fibrous connective tissue, no lipid core.
VI	Intraplaque hemorrhage, thrombosis, ulceration.

prothrombotic processes (e.g. systemic suppression of fibrinolytic pathways, or increase inflammatory activity) may be necessary to facilitate the final catastrophic occlusion event [13].

2.2 Atherosclerosis Classification System

In the mid-1990's the American Heart Association (AHA) developed a numerical classification system for atherosclerotic plaques based on the natural history of the disease that has since been widely adopted in the field [14]–[16]. In this system, plaque progression was broken into six broad categories (Type I – VI) starting from the initial formation of foam cells all the way through plaque rupture and thrombosis. The details of each plaque category are presented in Table 2.1 and will be briefly summarized in this section.

Type I plaques represent the earliest stage of atherosclerosis, where enough atherogenic lipoprotein has been deposited in the intima to elicit an accumulation of macrophages and scattered foam

cells. Type II plaques consist primarily of layers of foam cells that are grossly visible as “fatty streaks” and include the infiltration of SMCs that initiate adaptive intimal thickening. Type III plaques are an intermediate stage of plaque, where the fatty streaks of a Type II plaque begin to coalesce in scattered collections of extracellular lipid droplets which are the precursor to the large, confluent, and more disruptive core of extracellular lipid that characterizes Type IV lesion (known as an atheroma). Over time, Type IV lesions can develop thick layers of fibrous connective tissue (i.e. fibrous caps), that marks the transition to a Type Va lesion (known as the fibroatheroma). Alternatively, Type IV lesions can progress into Type Vb or Vc lesions, which represent highly calcified or highly fibrotic lesions, respectively. Finally, Type VI lesions are Type V lesions that have experienced a thrombogenic event (such as a plaque rupture or erosion). In this system, Type VI lesions can further be subdivided into Type VIa, VIb, and VIc plaques, which indicate plaques with ulcerations, hemorrhage/hematoma, and surface thrombus, respectively.

In the year 2000, the classification system was updated to better reflect the dynamic nature of atherosclerotic plaques, and allow for non-linear progression and regression through the various plaque types [17]. In the updated classification, Type Vb and Vc plaques were renamed to Type VII and VIII, and various pathways were added to allow for plaque type switching. The updated scale was developed in direct response to pathological studies done by Virmani et al. who suggested that the original classification system was inadequate [18].

2.3 The “Vulnerable” Plaque

As described previously, one of the most devastating features of atherosclerotic plaque is the ability to quickly transition from a silent, non-obstructive lesion to one that becomes obstructive and symptomatic. Lesions that are at the highest risk for this have classically been termed “vulnerable” plaques [19]. The transformation is most commonly precipitated by atherothrombosis, a process characterized either by the rupture of the fibrous cap or erosion of the endothelial layer followed by an acute clotting event that can occlude the vessel or embolize and obstruct downstream vessels.

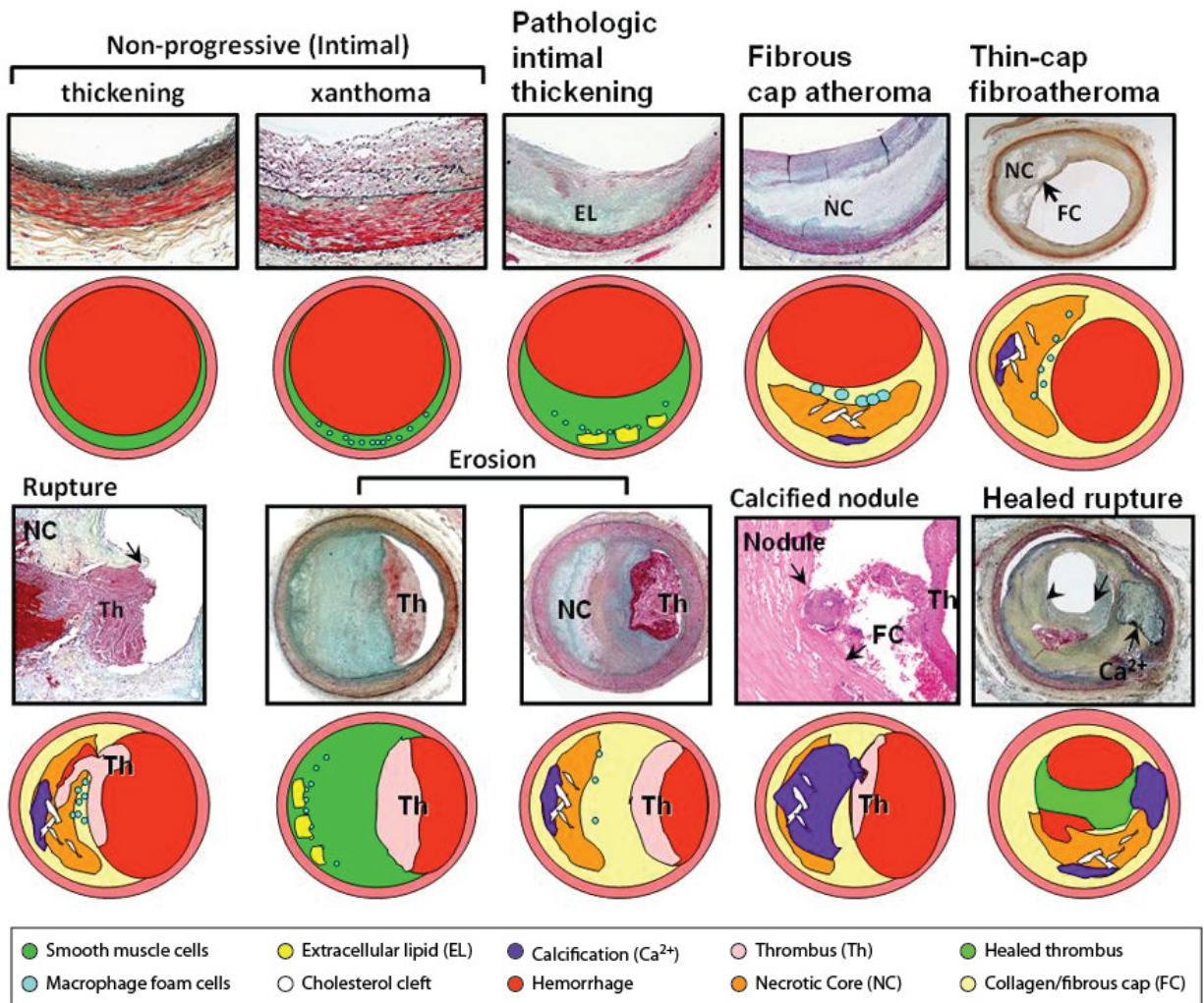


Figure 2.2: Histological examples of coronary plaques representing the spectrum of atherosclerotic lesions. Initial lesions, intimal thickening and intimal xanthoma, represent non-progressive lesions characterized by macrophage infiltration and fatty streak deposition (AHA type I and II). Pathologic intimal thickening (AHA type III) represents an intermediate lesion where extracellular lipids begin to coalesce into large lipid pools that can progress into a fibroatheroma (Type IV or Va). Thin-cap fibroatheroma, which is not explicitly captured in the AHA scale, is considered to be the precursor to plaque rupture. Finally, complicated plaques (AHA type VI), either via rupture or erosion, can occur with various amounts of hemorrhage and thrombosis. Reprinted with permission from [18] (Copyright © 2000 Wolters Kluwer Health, Inc.).

The concept of the vulnerable plaque, by and large, was derived from post-mortem histopathological studies done on ruptured coronary plaques (Figure 2.2) [2], [18]. While erosion-prone plaques also fall under the definition of “vulnerable”, researchers have yet to identify features in precursor lesions that reliably predict erosion, representing a major limitation of the vulnerable plaque paradigm (it

is thought that 30-35% of SCD is caused by erosion, compared to 55-60% by rupture) [2]. Therefore, the following discussion on vulnerable plaque characteristics will be limited to the hallmarks of rupture-prone plaques, which include: (1) thin fibrous cap, (2) large necrotic core with increased free/esterified cholesterol ratio, (3) increased plaque inflammation, (4) positive vascular remodeling, (5) increased vasa vasorum neovascularization, and (6) intraplaque hemorrhage.

2.3.1 Thin Fibrous Cap

Fibrous cap thickness was one of the first plaque features to be associated with rupture potential. The fibrous cap is a layer of stiff collagenous tissue that protects the soft underlying necrotic core. In the coronary arteries, autopsy studies in men who died suddenly from SCD showed that 95% of plaques with ruptured caps (and consequently, atherothrombosis) had a thickness of $<65 \mu\text{m}$ [20]. In the carotid arteries, the critical value is substantially higher, and has been reported as $<200 \mu\text{m}$ (minimum thickness) and $<500 \mu\text{m}$ (average thickness) [21]. Numerous finite element method (FEM) studies have shown that as the fibrous cap thickness decreases, the circumferential stress experienced by the plaque increases exponentially, which can lead to rupture if the ultimate stress (i.e. maximum stress at failure) is exceeded [22], [23].

In addition to thickness, there are a number of additional factors that can weaken the fibrous cap and make it susceptible to rupture. First, in caps with substantial inflammation, macrophage apoptosis can result in the continuous release of MMPs that can degrade collagen in the cap [24], [25]. Second, loss of SMCs, which produce collagen, can lead to the thinning of the fibrous cap. Finally, high resolution μCT and 3D FEM studies have demonstrated that microcalcifications in the fibrous cap can act as local stress concentrators and cause rupture either through cavitation or interfacial debonding [26].

2.3.2 Enlarged Necrotic Core

The necrotic core is one of the main destabilizing features of the atherosclerotic plaque. It is characterized by a lack of supporting collagen and cells, as well as the accumulation of free/esterified cholesterol. Following plaque rupture, the necrotic core is the most thrombogenic component of an

atherosclerotic plaque, estimated to be six-fold greater than collagen due to the high concentration of tissue factor (TF) [27]. Initial pathology studies identified a wide range of necrotic core areas that were associated with vulnerability; on the low end, necrotic core areas of 24% and 34% were considered vulnerable [28], while on the high end the values were above 50% [19]. Subsequent FEM modelling studies demonstrated that necrotic core *thickness* is a better indicator of plaque vulnerability compared to necrotic core *area*, and that no single value can reliably confer vulnerability without considering the thickness of the fibrous cap as well [29].

2.3.3 Increased Plaque Inflammation

Plaques with active inflammation, characterized by an abundance of macrophages and T-cells, have been shown to be more vulnerable to rupture than plaques in more quiescent states [19]. Macrophages increase the vulnerability of the plaque by producing proteolytic enzymes (e.g. plasminogen activators and MMPs) that are capable of degrading extracellular matrix and weakening/thinning the fibrous cap. Additionally, activated T-cells have been shown to secrete interferon- γ , which can impair the ability of SMCs to express interstitial collagen genes, further weakening the protective layers of fibrosis that stabilize the plaque from rupturing [2]. Clinical studies have demonstrated that macrophage content is increased in plaques from patients experiencing ACS when compared with plaques from patients with stable angina [19].

2.3.4 Positive Arterial Remodeling Index

As the atherosclerotic process begins to degrade the elastic lamellae and impact the medial layer, positive arterial remodeling can occur [30]. This phenomenon was demonstrated in human coronary arteries by Glagov et al. [31], and is characterized by a compensatory enlargement of the artery to maintain luminal diameter. Glagov estimated that luminal diameter in human coronary arteries could remain constant up until the percent stenosis exceeded 40%, meaning that lesions can incur a significant plaque burden without any restriction of flow. Positive remodeling has been shown to increase the

circumferential stress on eccentric plaques in FEM studies [29], and in clinical studies is found more frequently in patients experiencing ACS and less frequently in patients experiencing stable angina [32].

2.3.5 Neovascularization and Intraplaque Hemorrhage

When the plaque continues to grow, oxygen diffusion to the cells within the plaque is impaired, instigating growth of the vasa vasorum, or neovascularization. The predominant form of neovascularization is angiogenesis, which is characterized by the sprouting of endothelial cells from existing vasa vasorum in the adventitia [33]. It has been demonstrated that neovascularization tends to occur when the tunica intima thickens to 500 μm , however there is evidence suggesting that it may occur earlier and can be mediated by hypoxia-independent pathways linked to inflammation [34]. A number of studies have suggested that neovascularization may serve as a substantial pathway for additional lipoprotein deposition and leukocyte recruitment in the plaque. In neovessels, leukocyte adhesion molecules, such as VCAM, ICAM, and E-selectin, are expressed 2- to 3-times higher than on the luminal endothelium, suggesting that plaques with increased neovascularization will also have increased inflammation.

Exacerbating the situation further is the fact that neovessels tend to be leaky and extravasate erythrocytes into the plaque, a phenomenon commonly referred to as intraplaque hemorrhage. The release of red blood cells into the sub-intimal space triggers the recruitment of additional macrophages for the purpose of erythrophagocytosis. This can activate pathways leading to macrophage production of matrix metalloproteinases (MMPs) that can not only degrade the IEL but also disrupt protective fibrosis through collagenolysis [33]. Furthermore, hemoglobin, which is released from lysing red blood cells, can act as a potent inflammatory agent [35].

Intraplaque hemorrhage from leaky neovessels should not be confused with hemorrhage/hematoma secondary to plaque rupture and thrombosis, which was described in the previous sections. In addition to greater spatial extent, hemorrhage/hematoma is typically characterized on histology by the presence of fibrin and fibrin degeneration products [36]. Previous studies have shown

that the age of a hemorrhage secondary to rupture (acute, recent, or old) can be predicted by examining the color of the hemorrhage on trichrome staining as well as the level of inflammatory response around it [37].

2.3.6 Comparing Vulnerable Plaque in Different Arterial Locations

While the features of vulnerability described in the previous sections are mostly generalizable to all atherosclerotic plaques, substantial differences in plaque morphology have been noted in various arterial beds. This section will briefly summarize some of the key similarities and differences in plaque morphology and vulnerable characteristics across the coronary, carotid, and femoral vasculature.

Vulnerable plaque in the coronary and carotid systems is typically considered to be very similar. In both cases, plaque rupture tends to be the dominant etiology of ischemic event, and vulnerable characteristics include thin fibrous cap, large necrotic core, intraplaque hemorrhage and dense macrophage infiltrate [38]. The first key difference in vulnerable characteristics is that critical fibrous cap thickness tends to be higher in carotid plaques (<200 μm minimum thickness, and <500 μm average thickness) as compared to coronary plaques (<65 μm minimum thickness), which is attributed to the larger gauge and increased hemodynamic forces of the carotid arteries [39]. Second, the level of stenosis at plaque rupture may be higher in carotid arteries [21] compared to coronary arteries [40]. Finally, there is some evidence that macrophages may play more of a role in coronary plaque rupture as compared to carotid plaque [39].

While the description of coronary and carotid vulnerable plaque may be similar, studies have shown the femoral plaques tend to be phenotypically different. In an interesting study by Dalager et al. [41], histological sections were compared between femoral, carotid, and coronary arteries from 100 autopsies. Patients included in the study spanned the ages of 20-70+, allowing the authors to analyze the time course of plaque development as well. It was shown that plaques in the femoral arteries occurred later in life and were more prone to fibrotic phenotypes, rather than the foam cell/lipid core phenotypes of the carotid and coronary arteries. This data supported an earlier study [42] that also reported a heavily

fibrotic phenotype and relatively small amount of lipid in femoral plaques. In another immunohistochemistry study [43], it was shown that femoral plaques had reduced expression of MMP-9, a protein responsible for degrading collagen, compared to carotid plaques. Finally, in a study analyzing arterial remodeling across different vascular beds, it was shown that lower extremity arteries experienced significantly less remodeling compared to the carotid and coronary arteries [44]. Therefore, while plaque rupture is the dominant cause of thrombotic events in the coronary/carotid arteries, it is likely that femoral artery plaques are much more prone to experience plaque erosion and surface thrombus.

2.4 Treatment

To date, there is no cure for atherosclerosis. Treatment typically includes a combination of pharmaceutical therapies and lifestyle changes that are intended to reduce risk factors and slow the buildup of plaque. Numerous surgical techniques exist as well including procedures to widen/bypass occluded arteries, or procedures to remove plaque that may precipitate a fatal ischemic event. In the following section, these techniques and their efficacy will be described briefly.

2.4.1 Pharmaceutical

Current pharmaceutical therapies for atherosclerosis are largely restricted to controlling major risk factors such as hyperlipidemia and hypertension, and/or controlling hemostasis to prevent thrombosis.

Lipid-Lowering Therapy (Hyperlipidemia)

Lipid lowering has mainly been achieved by a class of drugs known as statins (e.g. atorvastatin or rosuvastatin). Statins work by inhibiting an intermediate protein, 3-hydroxy-3-methylglutaryl-coenzyme A (HMG-CoA) reductase, that produces cholesterol in the liver, ultimately lowering both the total and LDL cholesterol circulating in the blood stream [45]. Statins not only have been shown to reduce plaque lipids and cause plaque regression [46], but also have been demonstrated to reduce major cardiovascular event rates in patients with ACS [47]. More recently, the FDA approved the use of a statin in combination

with ezetimibe, a drug that inhibits cholesterol absorption in the small intestine. The combination of simvastatin and ezetimibe has been shown to lower total and LDL cholesterol levels more than just a statin alone [48], and shows modest improvement of preventing vascular events compared to a statin alone [49]. Statins have also been used in combination with fibrates (e.g. fenofibrate or bezafibrate); broad-spectrum lipid lowering drugs that, in addition to lowering LDL, lower triglycerides and raise HDL. Fibrates are a peroxisome proliferator-activated receptor (PPAR)- α agonist, and have been demonstrated to both reduce plaque burden and reduce the number of cardiovascular events [50], [51].

Anti-Hypertensives

Hypertension, or high blood pressure, is typically controlled using either β -adrenergic blockers (beta-blockers) or angiotensin-converting enzyme (ACE) inhibitors, both of which have been shown to have atheroprotective effects beyond simply reducing blood pressure [52]. Beta-blockers have been used to effectively reduce recurrent myocardial infarction and SCD since the 1980s, and primarily work by blocking the action of epinephrine and norepinephrine. ACE inhibitors, on the other hand, interfere with the renin-angiotensin system by blocking the conversion of angiotensin I to angiotensin II and lowering arteriolar resistance. In serial monitoring studies, patients on beta blockers showed a statistically significant decrease in atheroma volume, compared to patients who were not on beta blockade [53]. Likewise, ACE inhibitors have been shown to improve endothelial function and lower the rate of coronary events [54].

Anti-Platelet Therapy (Hemostasis)

Finally, antithrombotic therapies have long been a staple of atherosclerosis management, with the most common being aspirin. Aspirin primarily interferes with platelet aggregation, and prevents the acute formation of an occlusive thrombi at the site of plaque rupture or erosion [55]. Other antithrombotic drugs such as clopidogrel, prasugrel, or ticagrelor have also been shown to be efficacious for secondary prevention in patients with ACS [56].

Despite the significant improvement in patient outcomes when employing the modern atherosclerosis drug cocktail, some patients still experience cardiovascular events. As shown in the PROVEIT trial, patients on a combination of ACE inhibitors, beta blockers, aspirin, and high doses of atorvastatin showed a 22% recurrent event rate within 2 years [57]. These data suggest that, while we have come far, there is still a need for improved atherosclerosis therapies, particularly in high-risk patients.

2.4.2 Surgical

Percutaneous Coronary Intervention (PCI)

Percutaneous coronary intervention (PCI) is an umbrella term for minimally invasive procedures that use a catheter to access and treat the coronary arteries. The most common PCI procedure to treat atherosclerosis is balloon angioplasty and stent deployment. The PCI catheter is typically inserted either in the femoral artery (located near the groin) or the radial artery (located near the wrist), and guided to the coronary arteries using contrast-enhanced X-ray angiography. Once the catheter is placed in the stenosed region of the artery, a balloon is expanded to widen the artery and a stent is placed to maintain the vascularized luminal diameter. Stents can come in many different forms including simple bare-metal stents, or drug-eluting stents that are doped with chemicals intended to prevent neointimal hyperplasia and restenosis. While drug-eluting stents have been shown to be less susceptible to restenosis, there is evidence that they may be more susceptible to thrombosis, suggesting that there is still work to be done in designing the ideal stent [58]. PCI is typically indicated by cardiovascular symptoms including: myocardial infarction, stable/unstable angina, anginal equivalent (dyspnea, arrhythmia, or dizziness), or high-risk stress-test findings.

Coronary Artery Bypass Grafting (CABG)

Coronary artery bypass grafting (CABG) surgery is one of the most common open-heart surgeries, and is an alternative to PCI. In CABG, a healthy artery or vein is connected to the blocked

coronary artery forming a bypass for blood to flow around the obstruction. There are several vessels that are commonly used as grafts: internal mammary arteries, saphenous veins, and the radial artery. CABG is typically utilized as an option when PCI is not possible or fails to revascularize the artery. Primary indications for CABG include: >50% stenosis of left main coronary artery, >70% stenosis of proximal left anterior descending (LAD) artery and circumflex, 3-vessel disease in asymptomatic patients or those with mild or stable angina, 3-vessel disease with proximal LAD stenosis in patients with poor left ventricular function, 1- or 2-vessel disease and a large area of viable myocardium in high-risk area in patients with stable angina, >70% proximal LAD stenosis with either ejection fraction <50% or demonstrable ischemia on noninvasive testing [59].

Carotid Endarterectomy (CEA)

Carotid endarterectomy (CEA) is a surgical procedure used to remove atherosclerotic plaque from the carotid arteries in order to prevent stroke. In the procedure, the surgeon makes an incision along the front of the neck to expose the carotid artery, clamps the carotid on either side of the stenosis (typically located at the carotid bifurcation), and removes the inner lining of the artery through a single arteriotomy made on the top surface of the carotid. The plaque is typically removed *en bloc*, and most of the medial layer is stripped away during the procedure. To complete the surgery, a bovine patch is sutured to the damaged portion of the artery to avoid restenosis, and the arteriotomy is closed. As with the cardiac procedures mentioned previously, the primary indications for CEA are symptoms of ischemic event, including transient ischemic attack (TIA), stroke, contralateral weakness of the face, arm, and/or leg, paresthesia, facial droop, and amaurosis fugax. Severe carotid stenosis (>70%), in combination with neurological symptoms, has been shown to be a strong indicator of CEA efficacy for future stroke prevention with the number needed to treat (NNT) at 6 procedures to prevent one stroke at 5 years[60]. When stenosis is reduced to 50-69% in symptomatic patients, NNT increases to 15 procedures at 5 years.

Interestingly, in patients with asymptomatic carotid stenosis, CEA only provides a modest improvement in future stroke risk. In patients with 60-90% asymptomatic stenosis, the NNT is 25, and at

50-69% NNT increases so much that CEA is currently not indicated for these patients [61]. While CEA is still utilized in patients with high-grade asymptomatic stenosis, there has been a trend away from surgical management to medical management alone. The groups supporting this movement have cited the reduction in smoking rates and the great improvements in medical management of atherosclerosis (statins, etc.) that were not available during the time of the CEA randomized controlled trials [62], [63]. Current estimates suggest that only 5% of patients with asymptomatic carotid stenosis will benefit from prophylactic CEA [62]. Therefore, there is a great need for an improved method of predicting which patients are at high risk for stroke to enhance the benefit and cost-efficacy of CEA (as well as other interventions).

2.5 Animal Models

Animal models have proven crucial to our understanding of the pathogenesis of atherosclerosis as well as in the development of therapies to treat the disease. Two of the most commonly used models for atherosclerosis are the mouse and the pig.

2.5.1 Murine

The mouse is the most widely used animal for atherosclerosis research; the genetics are well understood, they grow and breed relatively quickly, and are inexpensive to maintain. Atherosclerotic mouse models are typically developed by generating non-HDL based hypercholesterolemia [64]. The two most common approaches to achieving this is through knockout of either apolipoprotein-E (ApoE) or LDL receptor (LDLR) genes, the latter of which occurs in humans that have familial hypercholesterolemia. One advantage of the ApoE mouse is that it develops complex atherosclerotic lesions when fed a regular diet, and the lesions can be exacerbated by feeding a high-fat diet. The LDLR mice, on the other hand, need to be fed an atherogenic diet and the progression of atherosclerosis is notably slower, most likely due to the specific role of LDL receptor in the lipoprotein uptake and clearance chain. In mice, atherosclerosis mainly develops in the aorta (aortic root, innominate artery, and other branches), as well as in the pulmonary and carotid arteries. One of the major limitations of the

mouse models is the notable lack of atherosclerosis in the coronary arteries. The lesions typically follow a similar pathogenesis as in humans, with foam cells appearing first, followed by SMC infiltration, and lastly the development of a necrotic core covered by a fibrous cap. However, these lesions do not undergo plaque rupture and atherothrombosis. Various authors have reported that more complicated genetic modifications can precipitate coronary atherosclerosis and myocardial infarction in mice, for example in a double-knockout of ApoE and LDLR [64]. Overall, the mouse has been incredibly useful to understanding the biology of atherosclerosis and, despite its limitations, will continue to be used heavily in future research.

2.5.2 Porcine

Unlike mice, pigs can spontaneously develop atherosclerosis in a manner more closely resembling the human condition [65], [66]. This process can be accelerated either by feeding a high-fat diet to induce dietary hypercholesterolemia (DH), or by genetic modification to induce familial hypercholesterolemia (FH). FH pigs spontaneously exhibit hypercholesterolemia in the range of 350-500 mg/dl when eating low fat pig feed due to a missense mutation in the LDL receptor [67], [68]. DH and FH pigs grow large (weighing between 200 and 700 lbs.) and have arterial geometries and gauges similar to an equivalently sized human. Additionally, pigs exhibit a human-like lipoprotein profile (including LDL-driven hypercholesterolemia), atherosclerosis development in the coronary arteries, and complex lesions that include thick fibrous caps, necrotic cores, calcification, and hemorrhage. While the main drawback of the porcine model is the expense to maintain the animal colony, the pig is an invaluable asset to translating medical device technologies that target atherosclerosis to humans.

2.6 Summary

Atherosclerosis is a complex, systemic, inflammatory disease that is influenced by many factors, including genetics, diet, and lifestyle. Left undiagnosed and untreated, atherosclerosis can have severe consequences including physical disability, pain, and death. We have made great strides in last few decades in understanding atherosclerosis, and developing strategies to fight it; however, it remains the

number one health epidemic facing the world. Continued improvements in early detection and diagnostic technologies, in addition to novel therapeutic strategies, will be crucial to combating atherosclerosis and reducing its impact on healthcare. Advancements in medical imaging technologies specifically are needed not only to diagnose the presence of atherosclerosis before it becomes symptomatic, but also to help clinicians determine if intervention strategies are being effective. In the next chapter, the state of the art of atherosclerosis imaging techniques will be comprehensively reviewed detailing how atherosclerosis is diagnosed in the clinic and highlighting areas where it needs to be improved.

CHAPTER 3

Atherosclerosis Imaging Techniques

Diagnostic atherosclerosis imaging has classically been implemented with techniques that interrogate luminal diameter, a field of imaging termed “angiography”. These techniques work by imaging blood flow, typically with the use of a contrast agent, and infer the presence of atherosclerosis by identifying regions where the lumen narrows and becomes stenotic. While angiography has been largely successful in the clinic, as described in the previous chapter, stenosis only occurs in very late stages of atherosclerosis and is not the best indicator of plaque vulnerability due to vascular remodeling. This has driven researchers to develop techniques that can look past the lumen, and identify not only the percentage of stenosis, but also the composition and morphology of the plaque itself.

In this chapter, the various techniques for imaging atherosclerosis will be described, including methods for stenosis visualization (i.e. angiography) and methods of vulnerable plaque characterization. The following sections are organized by imaging modality, with specific attention given to ultrasound imaging, which is the focus of this dissertation. Note that not all diagnostic medical imaging modalities will be described, only those pertaining to atherosclerosis imaging.

3.1 X-ray Techniques

X-ray imaging, also known as radiography, was pioneered by German physicist Wilhelm Roentgen in the late 1800’s and was the first technique used to visualize the inside of the human body. Roentgen discovered that X-rays, which are a form of electromagnetic radiation with wavelengths between 0.001 and 10 nm, are able to pass through soft tissue but are attenuated by dense material such as bone. By placing X-ray sensitive film on the other side of an imaging target, these subtle variations of X-

ray attenuation could be captured and turned into a two-dimensional (2D) image, a process known as projection radiography.

With the advent of digital electronics and computer technology, there was an explosion of novel X-ray modalities that went beyond static 2D projection images – namely, fluoroscopy and computed tomography (CT) – that have become clinical standards for atherosclerosis imaging. Fluoroscopy is a form of real-time X-ray imaging that continuously updates a 2D projection and is used to visualize moving targets such as a catheter or contrast agent travelling through the body. CT, on the other hand, is a form of X-ray imaging where multiple projection images are taken from various angles and reconstructed to form cross-sectional 3D volumes of the body. While noninvasive CT imaging is largely replacing fluoroscopy for diagnostic atherosclerosis imaging, both techniques continue to be important tools in the clinic and will be described in the following sections.

3.1.1 Fluoroscopy

The most common form of fluoroscopy that is used for atherosclerosis imaging is known as digital subtraction angiography (DSA) (Figure 3.1a) [69]. DSA is a real-time contrast-enhanced X-ray imaging technique that is used in conjunction with a catheter to produce images of blood vessels. The catheter is inserted into the femoral artery and guided with fluoroscopy to a site of atherosclerosis (e.g. the coronary arteries). Once positioned, a small amount of radio-opaque contrast is injected through the catheter, and two X-ray images, one pre-injection and the other post-injection, are captured. The pre-injection image serves as a mask and is subtracted from the post-injection images to remove overlying tissue, resulting in a very clear image of the luminal pathway of blood vessels [70]. The presence of atherosclerosis can be inferred from DSA by the reduction or blockage of flow, which appears as an absence of contrast in the image.



Figure 3.1: Examples of three angiography techniques. (a) Digital subtraction angiography of the carotid bifurcation showing a 50-69% stenosis. (b) Contrast-enhanced magnetic resonance angiography. (c) Computed tomography angiography. Reprinted with permission from [69] (Copyright © 2003 American Society of Neuroradiology).

DSA is strictly a luminal imaging technique, and consequently, is most efficacious in diagnosing percentage stenosis. However, DSA has been shown to be capable of identifying plaque ulceration, defined as a crater from the lumen into a stenotic plaque, which can be used to infer plaque rupture and vulnerability [71]. DSA is unable though, to detect plaque composition and non-occlusive atherosclerosis in vessels that have undergone positive remodeling, which has led some to conclude that it has little value in preventing future coronary events [70], [72]. Due to these limitations, DSA is quickly being supplanted by safer noninvasive imaging technologies that can determine both percent stenosis and plaque composition, but will continue to be an important modality for coronary interventions such as balloon angioplasty and stenting where real-time catheter imaging is required.

Table 3.1: Noninvasive imaging signal characteristics of plaque components. Table adapted from [3].

Histology	Ultrasound	CT	MRI T1-weighted	MRI T2-weighted	MRI PD-weighted
Ulceration	Irregular border	Irregular border	Irregular border	Irregular border	Irregular border
Lipid Core	Echolucent Homogenic	Hypodense	Very hyperintense	Hypointense	Hyperintense
Intraplaque hemorrhage	Echolucent Heterogenic	Hypodense	Age dependent	Age dependent	Age dependent
Fibrous plaque	Echogenic Homogenic	Isodense	Hyperintense	Hyperintense	Hyperintense
Calcifications	Echogenic Heterogenic	Hyperdense	Hypointense	Very hypointense	Very hypointense
Thrombus	Echolucent	Hypodense	Very hyperintense	Isointense	Hyperintense
Inflammation	Echolucent		SPIO signal loss	SPIO signal loss	SPIO signal loss
Vasa vasorum	Contrast enhancement		MRI signal increase		

Abbreviations: *CT*, computed tomography; *MRI*, magnetic resonance imaging; *PD*, proton density; *SPIO*, super paramagnetic iron oxide.

3.1.2 Computed Tomography

In computed tomography (CT) imaging, an X-ray source and detector unit is synchronously rotated around the patient's body capturing hundreds of projection images that are then fed into a tomographic reconstruction algorithm to produce cross-sectional X-ray images and 3D volumes. Modern CT scanners can acquire volumetric scans in seconds or fractions of a second, with isotropic spatial resolution of approximately 400 to 600 μm [73]. Like DSA, CT imaging can be paired with an injectable contrast agent (iodine-based) to interrogate stenotic vessels, in a technique known as CT angiography (CTA) (Figure 3.1c). CTA has been shown to have high correlation with DSA (0.892 to 0.922) [74], and good sensitivity and specificity (0.77 and 0.95) for detecting $>70\%$ stenosis [75].

Identification of plaque composition with CT is mainly based on radiodensity measurements (Table 3.1), expressed in terms of Hounsfield units (HU), which are normalized to the density of water (0

HU). In general, dense plaque components, e.g. calcifications, appear as hyperintense regions in CT images, while loose plaque components, e.g. lipid/necrotic core or thrombus, appear as hypointense. Due to the substantial difference in density of calcium compared to other features, CT is highly accurate for detecting calcified plaque, with sensitivities of 100% and specificities of 93%-100% [3], [76], [77]. However, because of substantial overlap in radiodensity values, accuracy for loose components (i.e. necrotic core) and fibrous plaque is only moderate with sensitivities ranging from 62% - 94% and specificities ranging from 74% - 100% [3], [76], [77].

The ability of CT to distinguish calcification has led to the development of the coronary artery calcification (CAC) scoring system, which is currently one of the only noninvasive coronary plaque characterization techniques routinely implemented in the clinic today [78], [79]. In this semi-automated system, the area of each calcified “speck” is weighted by the HU intensity, and summed together to derive a single CAC score (also known as an Agatston score). The severity of calcification is then determined using a five-point scale, which reflects the patient’s atherosclerotic burden and, consequently, risk of future ischemic event. A CAC of 0 indicates no evidence of atherosclerosis, 1 – 10 indicates “minimal”, 11 – 100 indicates “mild”, 101 – 400 indicates “moderate”, and >400 indicates “severe”. In the Multi-Ethnic Study of Atherosclerosis (MESA), it was demonstrated that high CAC score was statistically-significantly associated with future coronary events, yielding hazard ratios ranging from 2.6 to 9.5 in patients without diabetes or metabolic syndrome [79]. In patients with diabetes or metabolic syndrome, the hazard ratios ranged from 2.9 to 6.2, and 3.9 to 11.9 [79], respectively, and doubling CAC score was associated with a 29% increased risk of cardiovascular event in patients with diabetes [80].

While CAC has been shown to be effective at predicting patient risk, as described in the previous chapter, calcification represents a more advanced stage of atherosclerosis and may occur as a stabilizing force in the setting of high-risk atherosclerotic plaque [81]. Therefore, it remains to be seen whether high CAC will have different prognostic implications as compared to total plaque volume or the identification of thin-cap fibroatheroma.

Table 3.2: Diagnostic performance, strengths, limitations, and pitfalls of CTA in the evaluation of stenosis, plaque morphology, and composition. Table adapted from [103].

CTA	Stenosis (>70%)	Plaque Morphology	Plaque Composition
Diagnostic performance	Sensitivity 77% Specificity 95%	Sensitivity 100% Specificity 100%	Moderate correlation with histopathology
Strength points	Higher spatial resolution as compared to MRA	Higher spatial resolution as compared to MRA	Direct visualization of calcium
Limitations	May be hampered by wall calcifications, needing longer post-processing	May be hampered by wall calcifications, needing longer post-processing	Reduced accuracy in differentiation of “soft” components
Pitfalls	Beam-hardening artifacts induced by heavily calcified plaques	Beam-hardening artifacts induced by heavily calcified plaques	Impossibility to detect hemorrhage

Abbreviations: *CTA*, computed tomography angiography; *MRA*, magnetic resonance angiography

3.1.3 Advantages and Disadvantages

One of the greatest advantages of CT compared to other noninvasive imaging modalities is the ability to noninvasively image atherosclerosis of the coronary arteries. The coronary arteries are a particularly challenging imaging target due to their small size (which necessitates high resolution) and the substantial motion of the heart during the cardiac cycle (which necessitates high frame rate). Currently, CT is the only modality with adequate resolution and speed of acquisition that can reliably image coronary atherosclerosis noninvasively. Another advantage of CT is that it provides isotropic 3D volumes through the entire depth of the human body. This not only allows for a wide field of view and entire organ imaging, but also enables implementation of automated segmentation techniques.

However, the main disadvantage to CT and other X-ray based imaging modalities is the ionizing nature of X-ray radiation. The term ionizing radiation refers to any kind of radiation that carries enough energy to free electrons from atoms, thereby forming ions. This process of ionization is generally harmful to living organisms; specifically, it can damage DNA and lead to the formation of cancer. Although it is difficult to predict what amount of radiation is necessary to cause cancer, modelling studies suggest that the lifetime risk after CTA is 1 in 284 for a 40-year-old woman and 1 in 1,007 for a 40-year-old man [82].

In addition to ionizing radiation, CT scanners are typically expensive, and require significant amount of hardware, which make them immobile. Given these limitations, CT imaging may be precluded from being used a screening modality.

3.2 Magnetic Resonance Imaging

Magnetic resonance imaging (MRI) is an advanced noninvasive imaging technique that uses the magnetic resonance properties of hydrogen atoms in order to make images of the human body. When the hydrogen atoms in the body are subjected to a strong magnetic field, they align with the field in either high or low energy states (known as antiparallel and parallel states, respectively) and create a net body magnetization. The net magnetization is then flipped by introducing an RF pulse that is matched to the Larmor frequency of hydrogen atoms. As the hydrogen atoms gradually return to the original magnetization direction, they release energy in the form of an RF signal that can be detected. Hydrogen molecules bound in different tissues (fat, muscle, etc.) will exhibit different relaxation times, which results in contrast in the MRI image. The signal intensity in an MRI image is determined by four basic parameters that are directly related to tissue composition: 1) proton density, 2) longitudinal relaxation time (T1), 3) transverse relaxation time (T2), and 4) flow. Each parameter can be imaged independently by designing specialized RF pulse sequences, in a process known as “multicontrast-weighted” MRI (Figure 3.2), and is used in conjunction with the other parameters to determine tissue composition (Table 3.3).

As with CT, MRI can be used with a contrast agent (gadolinium-based) for improved visualization of the lumen in a technique known as contrast-enhanced magnetic resonance angiography (CE-MRA) (Figure 3.1b). Alternatively, because the movement of protons in blood can alter the MR signal, pulse sequences can be designed for non-contrast MRA as well, these are known as Time-of-Flight (TOF) or phase-contrast (PC-MRA) sequences. CE-MRA has been shown to have slightly better sensitivity and specificity (94% and 93%) for detecting >70% stenosis compared to non-contrast MRA (88% and 84%) with DSA as a gold standard [75].

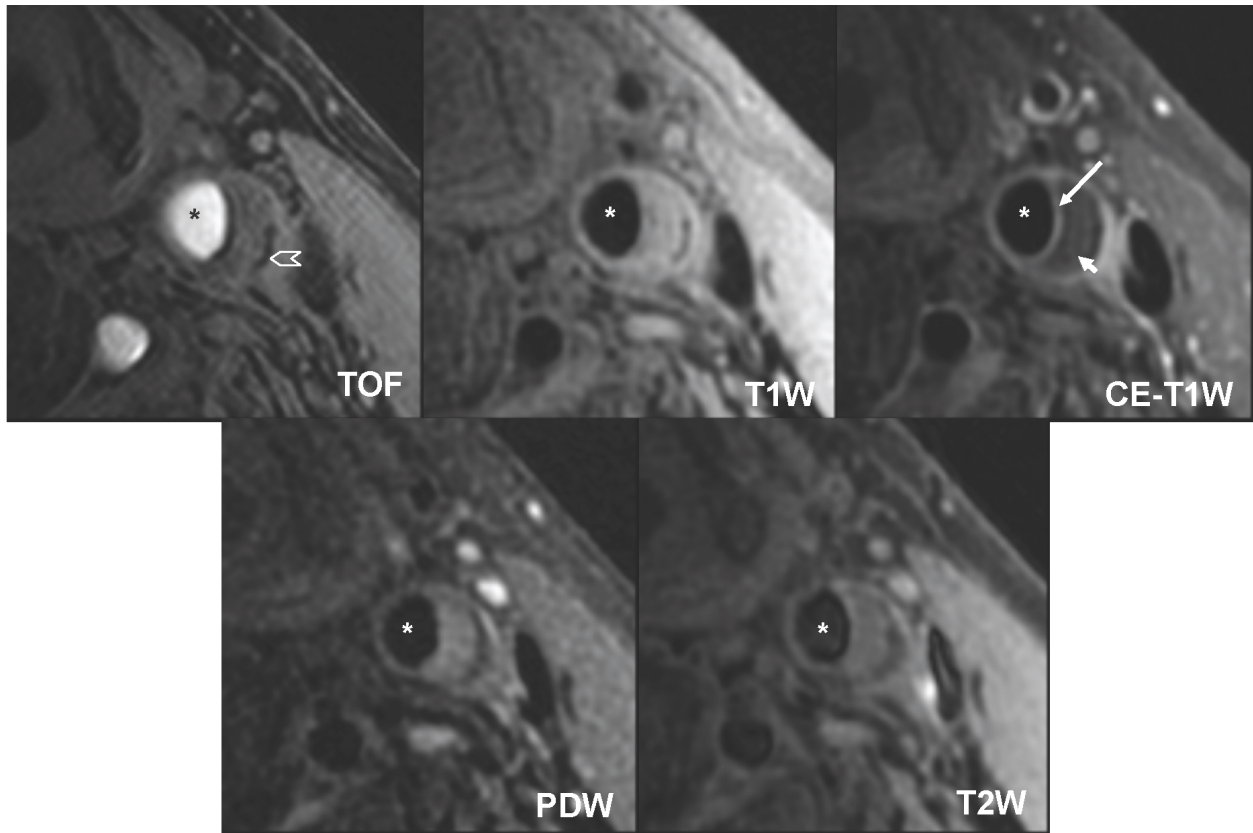


Figure 3.2: MR images of a carotid artery plaque with a large lipid-rich necrotic-core (small arrow) with an intact fibrous cap (long arrow). Calcification is also visible at the base of the plaque (chevron). Asterisks represent the lumen. Abbreviations: *TOF*, time of flight; *T1W*, T1-weighted; *CE-T1W*, contrast-enhanced T1-weighted; *PDW*, proton density weighted; *T2W*, T2-weighted. Reprinted under open access license from [98] (Copyright © 2009 BioMed Central Ltd.).

In the context of plaque characterization, multicontrast-weighted MRI has been shown to be very sensitive to the “soft” plaque components such as lipid/necrotic core, fibrosis, and hemorrhage [83]–[98]. An example of a plaque with large lipid/necrotic core and thin intact fibrous cap is shown in Figure 3.2 [98]. Using a standardized imaging protocol and classification criteria shown in Table 3.1, Watanabe et al. [96] reported a sensitivity of 96% and specificity of 93% to “soft” components when using both T1- and T2-weighted images; a substantial improvement compared to using T1 images alone (sensitivity 79%, specificity 84%) [97]. Cai et al. [89] reported similar results suggesting high sensitivity (range 80% - 84%) and specificity (range 90% - 98%) for the detection of AHA plaque classes III-VII, however the

Table 3.3: Diagnostic performance, strengths, limitations, and pitfalls of MRA and CE-MRA in the evaluation of stenosis, plaque morphology, and composition. Table adapted from [103].

MRA	Stenosis (>70%)	Plaque Morphology	Plaque Composition
Diagnostic performance (MRA and CE-MRA)	Sensitivity 88-94% Specificity 84-93%	Sensitivity 96% Specificity 97%	Significant correlation with histopathology
Strength points	Not hampered by wall calcification, luminographic view	Not hampered by wall calcification, luminographic view	Differentiation between various “soft” plaque components
Limitations	Lower spatial and temporal resolution as compared to CTA.	Lower spatial and temporal resolution as compared to CTA.	Long acquisition, dedicated hardware
Pitfalls	Loss of signal at the site of extremely tight stenoses	Susceptibility artifacts induced by heavily calcified plaques	Partial signal overlap between fibrous core and hemorrhage

Abbreviations: *CTA*, computed tomography angiography; *MRA*, magnetic resonance angiography;

ability of MRI to detect calcifications by other groups have been shown to be more modest, with mean sensitivity of 77% and specificity of 88% [3].

Prospective studies have demonstrated that MRI-derived plaque characteristics are associated with future ischemic events. In the PRIMARI study [99], it was shown that the presence of lipid-rich necrotic-core (HR: 4.4), intraplaque hemorrhage (HR: 5.2), or thin/ruptured fibrous cap (HR: 17.0) were all associated with future ischemic events. Results from MESA [100], a larger clinical trial, have shown similar trends, indicating that positive remodeling and the presence of lipid-rich necrotic-core on MRI are independent predictors of cardiovascular events.

3.2.1 Advantages and Disadvantages

In addition to high soft-tissue contrast, one of the greatest advantages of MRI for plaque characterization is the benefit of non-ionizing radiation. To date, there is no evidence of long-term adverse effects from the magnetic fields used in MRI, and short-term effects appear to be limited to mechanical risk associated with ferromagnetic devices or implants in the presence of a high powered magnet [101]. Therefore, from a patient safety standpoint, MRI is currently superior to CT. Other

benefits include the ability to measure flow without the need of contrast, the ability to produce 3D tomographic data for whole-organ imaging, and the relative insensitivity to heavy calcification that can be detrimental to both ultrasound and CT imaging.

There are, however, a number of disadvantages to the modality (Table 3.3). First, MRI is one of the most expensive imaging systems on the market, which makes it difficult to implement broadly and precludes it from being used for general screening. Second, compared to CT, the spatial resolution is poor which prevents MRI from reliably imaging atherosclerosis in smaller arteries such as the coronary arteries. In current practice, MRI plaque characterization is limited to peripheral vessels, such as the carotid arteries, and requires specialized phase-array surface coils to achieve adequate spatial resolution [102]. Finally, the long acquisition time necessary to acquire MR images makes it susceptible to motion artifacts.

3.3 Ultrasound Imaging

Ultrasound (US) imaging (also known as sonography) is a technique that uses high-frequency acoustic waves (typically 3 MHz - 15 MHz) to make tomographic images of tissue structures. As ultrasound waves travel through the body, they encounter interfaces between tissues and are partially reflected back toward the ultrasound probe. The proportion of the wave that is reflected versus transmitted across the interface is related to the tissues' acoustic impedance, Z , which is given by the product of the tissue density, ρ , and speed of sound, c .

Images are made by recording the ultrasonic echoes and assigning grayscale values to their intensities. This mode of imaging is known as pulse/echo (P/E) ultrasound, and results in a one-dimensional tomographic data set (amplitude vs. depth) referred to as a radiofrequency line (RF-line). RF data is then envelope-detected and log compressed to form an amplitude line (A-line), which encodes the intensity of the echo at a given depth position. To create two-dimensional images, successive A-lines are taken at various positions across the tissue of interest and stitched together to create a brightness mode (B-mode) image. A-lines can also be fired sequentially in the same location in a technique known as

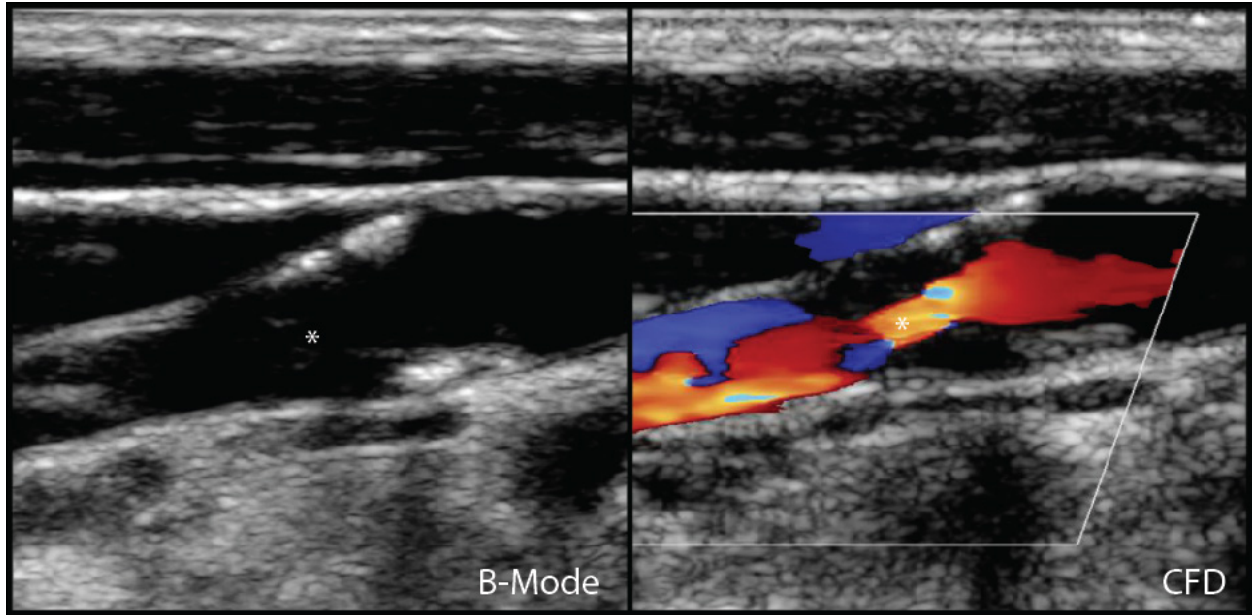


Figure 3.3: Longitudinal duplex ultrasound images of a predominantly echolucent, concentric, carotid artery plaque with $>60\%$ stenosis. Asterisks represent point of maximal stenosis. Abbreviations: *CFD*, color-flow Doppler.

motion mode (M-mode), which as the name suggests, is used to track motion such as blood flow.

Variations on M-mode sequencing underlie the flow-mapping techniques of pulsed, color, and power Doppler that are utilized to perform non-contrast angiography-style imaging with ultrasound.

Ultrasound imaging, specifically duplex ultrasonography (DUS), is globally accepted as the first-line diagnosis of stenosis in peripheral vessels [103]. In DUS, a combined-imaging mode, conventional B-mode ultrasound is used to visualize the anatomy of the vessel and Doppler imaging is used to measure both systolic and diastolic flow velocities in the artery (Figure 3.3). Velocity values are then used to derive stenosis percentages, with higher velocities indicating more severe stenosis [104]. Another common ultrasound metric used to diagnose atherosclerosis is carotid intima-media thickness (IMT) [105], which are typically done in the common carotid artery, and have been used for many years as a biomarker to indicate overall patient plaque burden and cardiovascular risk [106]–[108].

3.3.1 Plaque Echogenicity

Vulnerable plaque characterization with ultrasound has classically been implemented by measuring plaque echogenicity (Table 3.1). In the late 1980s, studies revealed that vulnerable plaque features such as lipid/necrotic core and intraplaque hemorrhage tended to correlate with plaque echolucency on grayscale ultrasound whereas fibrosis and calcification were echogenic [109]. From this work, a qualitative plaque echolucency ranking system was proposed, named the Gray-Weale scale (after the author that developed it), which included four categories ranging from “uniformly echolucent” to “uniformly echogenic”. In the following years, the scale was modified/improved [110] and implemented in a number of clinical studies that showed association of plaque echolucency with plaque vulnerability [111]–[113]. Additionally, B-mode ultrasound was shown to be capable of directly visualizing fibrous cap thickness (down to ~500 μm) [114]. To help standardize grayscale measurements, a quantitative metric of plaque echogenicity scoring, termed grayscale median (GSM), was subsequently developed and is currently the subject of ongoing clinical trials [115]. In this method, a histogram of pixel intensity values is computed for a given plaque, and the median grayscale value is calculated and thresholded to determine plaque vulnerability [116]–[118].

In a recent review of noninvasive plaque characterization techniques [3], the authors reported a wide range of sensitivities (ranging from 39% to 94%) and specificities (ranging from 57% to 80%) of echolucency-derived composition compared to histology. It has been proposed that the accuracy of grayscale ultrasound to characterize plaque is hampered by a number of factors: 1) the considerable overlap in echogenicity of many “soft” plaque features, 2) differences in ultrasonic beamforming methods between manufacturers, and 3) inter-operator variability.

3.3.2 Virtual Histology

One interesting ultrasonic technique that has been used extensively in the characterization of coronary plaques is known as Virtual Histology (VH) [119]. VH is a quantitative ultrasound (QUS) method that is implemented on an intravascular ultrasound (IVUS) array. VH not only interrogates the

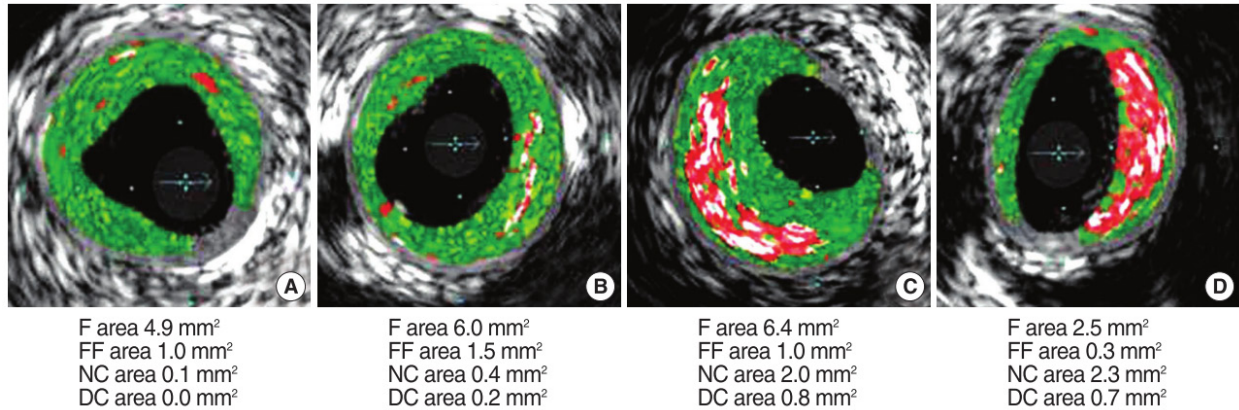


Figure 3.4: Classification of various coronary plaques with virtual histology intravascular ultrasound. (a) Pathological intimal thickening with significant fibrous and fibro-fatty disposition (green color). (b) Early fibroatheroma. (c) Thick-cap fibroatheroma with necrotic core (red color) and calcifications (white color). (d) Thin-cap fibroatheroma. Abbreviations: *F*, fibrous; *FF*, fibro-fatty; *NC*, necrotic core; *DC* dense calcium. Reprinted under open access license from [120] (Copyright © 2009 The Korean Academy of Medical Sciences)

backscatter amplitude but also the spectral characteristics of the raw ultrasonic radiofrequency (RF) data. After computing the frequency spectrum for a given region of interest in the RF data, spectral parameters such as maximum power, mid-band fit, slope, and *y*-intercept are calculated, which are fed into a statistical classification algorithm. Four tissue types are identified [120]: 1) fibrous, 2) fibro-fatty, 3) necrotic core, and 4) dense calcium, and fibrous cap thickness can be measured as the region of fibrous tissue separating necrotic core from lumen (Figure 3.4).

Since being developed in the early 2000s, IVUS-VH has been implemented in a large number of clinical trials including vulnerable plaque identification studies (PROSPECT trial [121]–[123]), longitudinal response-to-therapy studies [124], and stent deployment studies [125]. Early results from clinical trials have simultaneously demonstrated the efficacy of identifying vulnerable plaque features and confounded the vulnerable plaque hypothesis by elucidating the highly dynamic nature of coronary atherosclerosis [126].

Table 3.4: Diagnostic performance, strengths, limitations, and pitfalls of DUS in the evaluation of stenosis, plaque morphology, and composition. Table adapted from [103].

DUS	Stenosis (>70%)	Plaque Morphology	Plaque Composition
Diagnostic performance	Sensitivity 89% Specificity 84%	Sensitivity 85% Specificity 84%	Moderate correlation with histopathology
Strength points	Fast and cost-effective	Detailed view of the plaque with high-resolution probes	Faster as compared to CTA and MRA; use of power Doppler
Limitations	Operator dependent	Calcium induced acoustic shadowing	Heavily calcified plaques may hamper detection of other components
Pitfalls	Poorly reproducible	Calcium can obscure subtle surface alterations	Amorphous calcifications and hemorrhage are similar

Abbreviations: *DUS*, duplex ultrasound; *CTA*, computed tomography angiography; *MRA*, magnetic resonance angiography;

3.3.3 Advantages and Disadvantages

There are a number of advantages of ultrasound imaging. First, the acoustic waves used in ultrasound are non-ionizing and do not increase patient risk of cancer. Second, the acquisition time is very fast due to the high speed of sound in tissue (~1540 m/s) allowing ultrasound images to be generated in real-time. Conventional raster-scanned B-modes can be generated up to 100 times per second, while novel plane-wave ultrasound techniques can exceed 1000 frames per second (these techniques will be discussed in the subsequent chapter). This makes ultrasound particularly suited to capturing high-speed motion (such as blood flow or cardiac dynamics), which is unparalleled in other modalities. Finally, ultrasound requires minimal hardware, which not only makes the systems inexpensive but also allows them to be very portable. Therefore, ultrasound is widely accessible and has potential to be used as an atherosclerosis screening modality in the general population.

While the mobility and speed of ultrasound are some of its greatest strengths, these features are also responsible for one of its greatest weaknesses – inter-operator variability. As opposed to MR or CT systems, where a patient lies in an immobile bore, the majority of clinical ultrasound images are produced

dynamically by a hand-held transducer that is manipulated into position by a skilled technician. Even after years of training, error in probe placement, or incorrect angle measurement for Doppler studies can result in statistically-variable performance of the technique [127]. Indeed the U.S. Preventative Services Task Force currently does not recommend DUS for screening the general population for asymptomatic carotid stenosis of 60-99% because the specificity (which they estimate to be 92%) results in too many false positives [128]. As mentioned previously, inter-operator variability has also plagued echogenicity measurements and resulted in highly disparate accuracies for plaque characterization [3].

Another limitation with ultrasound imaging is that only peripheral vessels can be reliably imaged. While ultrasound has the temporal resolution necessary to image the fast-moving heart, the frequencies and aperture sizes in transcutaneous cardiac imaging severely limit the spatial resolution. The major problem is the ribs; ultrasound is highly absorbed/reflected by bone, and, therefore, the ribs must be avoided, either by designing small-aperture phased-array probes to look between the ribs (which reduces the lateral resolution), or using a low-frequency array to image from below the ribs (which reduces the axial resolution). This difficulty with bone penetration also limits the use of ultrasound in cerebral arteries, which are covered by the skull, and imaging through heavy calcifications in plaque.

The last challenge with ultrasound image is the presence of speckle and clutter. Speckle is phenomenon related to coherent imaging systems that appears as a granular “noise” or local intensity fluctuations in the image that is the result of constructive and destructive wave interference from subwavelength scatterers. Clutter is a term used to describe spurious echoes that originate from spatial locations other than the interrogated tissue volume (e.g. reverberation, side-lobes, grating-lobes, etc.). Both speckle and clutter can have substantial impact on the local grayscale intensity in a given region of an ultrasound image, which can confound plaque characterization. Multiple techniques have been developed to reduce both speckle (spatial compounding [129]), and clutter (harmonic imaging [130], coherence imaging [131]), however their impact on grayscale plaque imaging is not well characterized.

3.4 Optical Techniques

Optical imaging refers to the use of electromagnetic radiation in the visible to near-infrared spectrum (wavelengths between 400 and 1500 nm) to interrogate atherosclerotic plaques. While there is a plethora of optical methods that vary considerably in their mode of operation, almost all of them are implemented on catheters for intravascular deployment due to the poor penetration depth of light in tissue. In this section, a summary of the more popular techniques will be given, with brief descriptions of the underlying physics that make them work.

3.4.1 Optical Coherence Tomography

Optical coherence tomography (OCT) is a high-resolution optical imaging technique ($\sim 10 \mu\text{m}$) that uses low-coherence interferometry to produce two-dimensional images of optical scattering from tissue microstructure in a manner similar to ultrasound pulse-echo imaging [132]. OCT utilizes near-infrared (NIR) light, with wavelengths from 1250 to 1350 nm, and measures an interference signal of the light backscattered from the tissue and the light backscattered from a reference mirror [133]. The frequency of the interference signal corresponds to the depth in the tissue. The two approaches to analyze the interference signal include a time-domain (TD) analysis and a frequency-domain (FD) analysis, with the latter being the faster of the two. In the TD approach, a reference arm is mechanically translated in the longitudinal direction interrogating one wavelength of NIR light at a time. In the FD approach, a broadband interference is acquired with no moving parts, and each individual wavelength is demodulated in software through the Fourier transform. The FD approach has largely supplanted the TD approach in clinical OCT systems due to its substantial increase in frame rate.

OCT has been implemented successfully in a number of coronary plaque imaging products, and has been shown to be very sensitive to lipid/necrotic core, thin fibrous cap ($< 65 \mu\text{m}$), calcification, thrombus, macrophage infiltrate, and IEL and EEL [133]. There are two significant limitations to OCT: first, the penetration depth is limited to $\sim 2 \text{ mm}$, which means that the full extent of plaque burden cannot always be accurately identified, and second, arterial blood needs to be flushed away prior to imaging,

which may not always be tolerated well by the patient. To account for these limitations, newer hybrid OCT/IVUS systems are being developed to leverage the strengths of both imaging modalities.

3.4.2 Optical Spectroscopy Methods

Spectroscopy is a general term that refers to the measurement of radiation intensity as a function of wavelength or frequency. Spectroscopy takes advantage of the phenomenon that different substances absorb and scatter radiation to different degrees at various wavelengths, which can be used as a unique identifier or fingerprint of the material in question. Spectroscopic methods for characterizing plaque include diffuse reflectance near-infrared (NIR) spectroscopy [134], [135], Raman spectroscopy [136], and fluorescence spectroscopy [137], [138], which mainly differ by their optical excitation method. The end-result of any of these methods is a spectra or “chemogram” that encodes the absorbance characteristics of the tissue, and then multivariate mathematical techniques such as principal component analysis (PCA) are used to classify the spectra uniquely to a known tissue type. The benefit of these techniques is that they give quantitative biochemical characterization of the underlying tissue composition, which may serve as a powerful predictor for plaque vulnerability. The drawback, however, is that the techniques do not provide anatomical/structural information about the plaque, meaning that these modalities typically need to be combined with either IVUS or OCT.

3.4.3 Intravascular Photoacoustic Imaging

Photoacoustic (PA) imaging is a powerful new technology that combines both light and sound to produce diagnostic medical images [139]. In PA imaging, short-duration (ns) laser pulses are used to irradiate the tissue. The absorption of the light by the tissue causes heating and thermal expansion, which generates a high frequency, broadband ultrasonic wave that can be detected with conventional transducers. The advantage of PA imaging is that the ultrasound image is weighted by an optical contrast mechanism that can be tuned specifically to various tissue types; in this way, the chemical specificity of optical imaging is retained while largely maintaining the depth of penetration of ultrasound.

In intravascular photoacoustic (IVPA) imaging, both a light source and an IVUS transducer are mounted on the tip of a catheter, which allows PA imaging to be used to classify atherosclerotic plaque. The laser source can then be tuned to accentuate various features, such as lipids (wavelength of 1210 nm), to improved IVUS visualization of plaque components [139]. With the development of tunable lasers, it is quickly becoming possible to capture PA scans with multiple wavelengths, which will only improve the specificity of the technique.

3.5 Elasticity Imaging

Elasticity imaging is a relatively new field of medical imaging that creates maps of the mechanical properties (i.e. elasticity and/or viscosity) of soft tissue. The hypothesis underlying these techniques is that certain pathologies, such as fibrosis or necrosis, will have predictable impacts on the mechanical properties of tissue, which can be used to infer disease states and progression. To measure elastic properties, a mechanical excitation source (either intrinsic or extrinsic) is used to apply a stress to the tissue and induce a deformation or strain, which is then measured with a medical imaging technique. The predominant imaging method has been ultrasound due to its unique ability to measure motion very precisely; however, novel elastographic techniques utilizing MRI and OCT have recently been developed as well.

In the case of atherosclerosis plaque characterization, fibrosis and calcification are expected to stiffen arteries, while lipid deposition and necrosis are expected to soften arteries. In Lee et al. [140], radial Young's modulus values for the different plaque components were measured to be 354 kPa for calcium, 81 kPa for fibrous, and 41 kPa for non-fibrous, while other groups have estimated the lipid/necrotic core to be 1 kPa [29], [141]. The following sections break down the various elastographic plaque imaging techniques by their respective excitation sources and indicate their strengths and weaknesses.

3.5.1 Intrinsic Motion Sources

Intrinsic-motion elastographic imaging techniques do not introduce any additional mechanical stress into the body; they simply monitor deformations in the arterial wall induced by cardiac pulsation. This methodology has been implemented both noninvasively and invasively utilizing ultrasonic imaging to measure tissue deformation.

In the noninvasive approaches, a transcutaneous linear array is used to image the artery in cross-section and a speckle-tracking approach is used to capture tissue motion to predict the radial and/or circumferential strains on the artery. Technologies that utilize cross-correlation algorithms for speckle tracking are usually referred to as “strain imaging” [142]–[145], while technologies that utilize the Lagrangian speckle model estimator (LSME) have been dubbed noninvasive vascular elastography (NIVE) [146]–[149]. In a recent clinical study [149], Naim et al. compared NIVE strain measurements to MRI plaque characterization in 31 subjects with 50% or greater carotid stenosis. They demonstrated that strains were statistically lower in plaque containing lipid core, and reported sensitivities ranging from 77-100% and specificity ranging from 57-79% for detecting lipid-rich plaque.

Not only can strain imaging be used to directly image local plaque stiffness, but it can also be used to measure pulse wave velocity in a technique known as pulse wave imaging (PWI) [150]. As blood travels through the vasculature, it generates a pressure wave that travels down the length of the artery. The velocity of this wave is influenced by arterial stiffness, i.e. stiffer arteries lead to higher velocities, and can be related to Young’s modulus by the modified Moens-Korteweg equation [151]. PWI has been demonstrated most thoroughly in the aorta [152]–[155], and has recently been implemented in the carotid arteries for focal plaque characterization [156], [157].

The invasive techniques use a very similar approach, however, instead of a transcutaneous probe, an IVUS probe is used, and the method is referred to as IVUS elastography or IVUS palpography [158]–[161]. As in the noninvasive approaches, various speckle-tracking algorithms are utilized to measure the compression of the artery from pulsation and estimate a 2D strain field. Due to the concentric geometry of the IVUS probe and position of the probe within the artery, radial displacements are much easier to

measure in IVUS palpography as compared to NIVE. IVUS palpography initially demonstrated high sensitivities (88%) and specificities (89%) in postmortem studies for detecting vulnerable plaque [161], however the modality has seen limited clinical use in the past decade.

While intrinsic motion elastography techniques are elegant in that they do not require any additional hardware, using intrinsic motion presents a number of challenges. First, the frame rate of these techniques is inherently tied to the patient's heart rate, which typically beats once or twice a second, meaning that imaging refresh rates can never be truly real-time (~30 times per second). Second, lateral motion tracking with ultrasound is substantially worse than axial motion tracking, which usually limits the estimation of the strain tensor to axial strain and shear components [162]. Third, complex geometries of atherosclerotic plaques can alter intraplaque strain fields and inhibit direct translation to plaque mechanical properties [163]. Finally, unwanted sources of motion, such as operator hand vibrations, can corrupt displacement measurements and need to be compensated for.

3.5.2 Extrinsic Motion Sources

Extrinsic-motion elastographic techniques utilize outside sources of mechanical stress to create deformations in tissue. These techniques are typically classified by the duration of the excitation, which can be applied 1) quasi-statically, 2) transiently, or 3) harmonically. Quasi-static excitation achieves a steady-state response of the tissue similar to manual palpation, while transient and harmonic excitations give dynamic responses utilizing impulses and frequency-oscillations, respectively.

An example of quasi-static elastography is ultrasonic compression elastography [164]. In this technique, a handheld ultrasound probe is used to compress tissue while performing real-time imaging to measure the deformation. Displacements are monitored with speckle-tracking algorithms by comparing pre-compression and post-compression images, and are used to determine the strain field. Compression elastography has been studied extensively for the diagnosis of breast, liver, thyroid, and prostate pathologies [165], however, due to the relative success of intrinsic-motion techniques discussed in the previous section, has largely been unused for arterial imaging.

The techniques for dynamic elastography are much more diverse, and include vibrating the tissue with a mechanical shaker, as in magnetic resonance elastography (MRE), or exciting the tissue with acoustic radiation force (ARF). In MRE, an external vibrator is used to introduce low-frequency mechanical waves (called shear waves) into the tissue of interest, which are visualized using phase-contrast MRI [166]. MRE is capable of capturing tissue motion in three dimensions and providing full reconstruction of the tissue modulus. The main clinical application of MRE has been in staging liver fibrosis [167], however a number of groups have been investigating MRE for measuring abdominal aorta stiffness [168]–[172]. In ARF-based techniques, a high-intensity acoustic pulse is used to generate displacements and shear waves in tissue. As ARF-based imaging is the focus of this dissertation, a thorough description of these techniques is given in the next chapter.

3.6 Summary

A number of vascular imaging techniques were presented, and their efficacy for imaging atherosclerosis was assessed. In the clinic today, angiographic-type modalities such as DUS and CTA continue to be the gold standard; however, early data from clinical trials utilizing MRI- or IVUS-based plaque characterization techniques have demonstrated that information beyond stenosis can be extremely useful in predicting patient risk. The improvements in atherosclerosis imaging have also led to a dramatic increase in our understanding of atherosclerosis pathology, which is beginning to shape the next generation of hypotheses about how to treat and manage cardiovascular disease. Unfortunately, many of the plaque characterization modalities have significant drawbacks in terms of cost (for MRI) and patient safety (for IVUS and CT), which may preclude them for being applied as screening tools for the general population. Advances to transcutaneous ultrasound, as will be described in the next chapter, have the potential to bring the diagnostic power of plaque characterization to a significantly wider range of patients and possibly lead to significant advances in the diagnosis and treatment of CVD.

CHAPTER 4

Radiation Force Elasticity Imaging

Radiation force is a phenomenon in wave motion where part of the energy of the travelling wave is converted into momentum after experiencing absorption, scattering, or reflection. The first description of radiation force can be traced back to Johannes Kepler in the 17th century who suggested that energy from solar rays was responsible for deflecting comet tails [173]. Almost two centuries later, radiation force was found to be associated with acoustic waves as well, and emerged as a unique field of study in 1902 after the extensive work of Lord Rayleigh [173], [174]. However, it wasn't until 1990, when ultrasound was already an established field, that acoustic radiation force (ARF) was proposed to be utilized as an extrinsic excitation source for elasticity-based medical imaging techniques [175]. Over the last few decades, a multitude of ARF elasticity imaging methods have been developed and commercialized for clinical adoption.

In this chapter, a brief background on the physics underlying soft-tissue biomechanics and ARF are given first, followed by a review of the different ARF imaging methods that are currently used for arterial imaging. Specific attention will be given to acoustic radiation force impulse (ARFI) imaging, a qualitative technique, which is the focus of this dissertation. Finally, the bioeffects that govern patient safety of all ARF-based imaging as well as some of the challenges in implementing the techniques are discussed briefly to conclude.

The derivations in this chapter are adapted from Palmeri et al. [176] and Doherty et al. [177].

4.1 Soft-Tissue Biomechanics

To understand the physics behind ARF elasticity imaging, the biomechanics and wave propagation in soft tissue will be explored in detail first. The elastodynamic equation of motion in solids is primarily based on three fundamental properties: 1) the constitutive equation that relates stress to strain, 2) the balance of linear momentum, which utilizes Newton's second law, and 3) the infinitesimal strain tensor that relates strain to displacement.

Soft tissues are often approximated as linear, isotropic, perfectly elastic solids with the following balance of linear momentum equation,

$$\nabla \cdot \boldsymbol{\sigma} + \mathbf{f} = \rho \mathbf{a} \quad (4.1)$$

and constitutive stress-strain equation,

$$\boldsymbol{\sigma} = \lambda \psi + 2\mu \boldsymbol{\varepsilon} \quad (4.2)$$

$$\psi = \text{tr}(\boldsymbol{\varepsilon}) \mathbf{I} = \nabla \cdot \mathbf{u} \quad (4.3)$$

where $\nabla \cdot$ is the divergence operator, $\boldsymbol{\sigma}$ is the Cauchy stress tensor, \mathbf{f} represents an external, steady-state force (e.g. gravity), ρ is material density, \mathbf{a} represents an externally applied acceleration (e.g. radiation force), λ is the Lamé modulus, ψ is the material dilatation, μ is the shear modulus that describes the material resistance to shear, $\boldsymbol{\varepsilon}$ is the infinitesimal strain tensor, $\text{tr}(\cdot)$ is the trace operator, \mathbf{I} is the identity matrix, and \mathbf{u} is the particle displacement vector.

Using the infinitesimal strain approximation, the strain ($\boldsymbol{\varepsilon}$) can be defined as the symmetric gradient of displacement (\mathbf{u}) represented by the following equation,

$$\boldsymbol{\varepsilon} = \frac{1}{2} (\nabla \mathbf{u} + (\nabla \mathbf{u})^T) \quad (4.4)$$

where $(\cdot)^T$ is the transpose operator. Substituting equation (4.4) into (4.2), and differentiating yields an expression for the divergence of stress as a function of particle displacement,

$$\nabla \cdot \boldsymbol{\sigma} = \lambda \nabla \psi + \mu (\nabla^2 \mathbf{u} + \nabla(\nabla \cdot \mathbf{u})) \quad (4.5)$$

where ∇ is the gradient operator, and ∇^2 is the Laplacian operator. Substituting equation (4.5) into equation (4.1), and assuming no external body forces, $\mathbf{f} = 0$, as well as substituting the second derivative

of displacement for the applied acceleration, $\mathbf{a} = \frac{\partial^2 \mathbf{u}}{\partial t^2}$, an expression for particle displacement as a function of time (t) and space can be derived,

$$(\lambda + \mu)\nabla\psi + \mu\nabla^2\mathbf{u} = \rho \frac{\partial^2 \mathbf{u}}{\partial t^2} \quad (4.6)$$

or,

$$(\lambda + \mu)\nabla(\nabla \cdot \mathbf{u}) + \mu\nabla^2\mathbf{u} = \rho \frac{\partial^2 \mathbf{u}}{\partial t^2} . \quad (4.7)$$

From equation (4.7), two different types of wave equations can be derived to describe elastic wave propagation. These two waves are known as dilatational waves (P-waves) and shear waves (S-waves), and can be analyzed separately by performing a Helmholtz decomposition, which resolves a 3D vector field into the sum of the rotation-free component (dilatation wave) and divergence-free component (shear wave).

In dilatational waves, the particle motion is in the same direction as the wave propagation, and there is no particle rotation. This is described mathematically by taking the divergence of the equation of motion,

$$\nabla \cdot \left\{ (\lambda + \mu)\nabla(\nabla \cdot \mathbf{u}) + \mu\nabla^2\mathbf{u} = \rho \frac{\partial^2 \mathbf{u}}{\partial t^2} \right\} \quad (4.8)$$

$$(\lambda + \mu)\nabla^2 \underbrace{(\nabla \cdot \mathbf{u})}_{\psi} + \mu\nabla^2 \underbrace{(\nabla \cdot \mathbf{u})}_{\psi} = \rho \frac{\partial^2}{\partial t^2} \underbrace{(\nabla \cdot \mathbf{u})}_{\psi} \quad (4.9)$$

where $\nabla \cdot \nabla^2\mathbf{u} = \nabla^2(\nabla \cdot \mathbf{u})$ and $\nabla \cdot \nabla\mathbf{u} = \nabla^2\mathbf{u}$. After combining terms, equation (4.9) becomes

$$(\lambda + 2\mu)\nabla^2\psi = \rho \frac{\partial^2 \psi}{\partial t^2} . \quad (4.10)$$

This equation can be rewritten in the familiar “wave equation” format to represent the propagation of dilatation (ψ),

$$\nabla^2\psi = \frac{1}{c_L^2} \frac{\partial^2 \psi}{\partial t^2} \quad (4.11)$$

where the dilatational or longitudinal wave speed (c_L) is,

$$c_L = \sqrt{\frac{(\lambda + 2\mu)}{\rho}} = \sqrt{\frac{K + \frac{4}{3}\mu}{\rho}}. \quad (4.12)$$

The shear (μ) and Lamé (λ) moduli are related to the material Young's modulus (E), which describes resistance to uniaxial compression, and material bulk modulus (K), which describes resistance to uniform compression, via the Poisson's ratio (ν), which describes the deformation that occurs orthogonal to the applied force.

$$E = \frac{\mu(3\lambda + 2\lambda)}{\lambda + \mu} \quad (4.13)$$

$$\nu = \frac{\lambda}{2(\lambda + \mu)} \quad (4.14)$$

$$\mu = \frac{E}{2(1 + \nu)} \quad (4.15)$$

$$K = \frac{E}{3(1 - 2\nu)} \quad (4.16)$$

Most soft tissues are assumed to be incompressible ($\nu = 0.5$), which simplifies the relationship of shear and Young's modulus ($\mu = E/3$).

The second type of wave that can be derived from equation (4.7) is a shear wave, which is a transverse wave where the particle motion is orthogonal and the deformation does not cause a volume change. Mathematically, this can be represented by taking the curl ($\nabla \times$) of the equation of motion,

$$\nabla \times \left\{ (\lambda + \mu)\nabla(\nabla \cdot \vec{u}) + \mu\nabla^2\vec{u} = \rho \frac{\partial^2\vec{u}}{\partial t^2} \right\} \quad (4.17)$$

$$(\lambda + \mu)\nabla \times (\nabla(\nabla \cdot \vec{u})) + \mu\nabla \times (\nabla^2\vec{u}) = \rho \frac{\partial^2}{\partial t^2} \underbrace{(\nabla \times \vec{u})}_{\boldsymbol{\theta}}. \quad (4.18)$$

By definition, $\nabla \times (\nabla(\nabla \cdot \vec{u})) = 0$, and using the identity $\nabla \times (\nabla^2\vec{u}) = \nabla^2(\nabla \times \vec{u})$, equation (4.18) can be simplified to,

$$\mu\nabla^2\boldsymbol{\theta} = \rho \frac{\partial^2\boldsymbol{\theta}}{\partial t^2} \quad (4.19)$$

and rewritten as a “wave equation” to represent the propagation of the transverse component ($\boldsymbol{\theta}$),

$$\nabla^2 \boldsymbol{\theta} = \frac{1}{c_T^2} \frac{\partial^2 \boldsymbol{\theta}}{\partial t^2} \quad (4.20)$$

where the transverse wave speed (c_T) is,

$$c_T = \sqrt{\frac{\mu}{\rho}}. \quad (4.21)$$

The derivation thus far has modelled soft tissue as being perfectly elastic; however, it is well known that biological tissues are viscoelastic. Viscosity is a measure of a material's resistance to deformation or flow, and adds a time-dependency to the mechanical response of tissue. This can be represented by allowing the Lamé constants to take on complex values, λ^* and μ^* , which modifies equation (4.12) to the following in viscoelastic solids [176],

$$c_L^* = \sqrt{\frac{(\lambda^* + 2\mu^*)}{\rho}}. \quad (4.22)$$

A common 1D solution to the longitudinal wave equation (4.11) for particle displacement (u) as a function of position (x) and time (t) using the complex wave speed in (4.22) is the following,

$$u(x, t) = A_0 e^{-\alpha x + j(\omega t - kx)} \quad (4.23)$$

where A is the original wave amplitude, k represents the wave number (ω/c_L^*), ω is the angular frequency, and α is the frequency-dependent attenuation coefficient of the material. Finally, taking the temporal derivative of equation (4.23) yields a solution for the particle velocity (v),

$$v(x, t) = j\omega A_0 e^{-\alpha x + j(\omega t - kx)}. \quad (4.24)$$

4.2 Acoustic Radiation Force Theory

Acoustic radiation force (ARF) is a unidirectional body force (i.e. a force per unit volume) generated from the transfer of momentum from an acoustic wave to the propagating medium [176]. The transfer of momentum occurs with energy-loss mechanisms such as absorption, scattering, and/or reflection, therefore the derivation of acoustic radiation force cannot be directly obtained from the purely elastic stress-strain relationships developed in the previous section. Classically, the derivation of ARF has

been approached by modelling the tissue as a linearly viscous fluid, where the balance of linear momentum equation is given by the Navier-Stokes equation [178]. Using a perturbative expansion of equation (4.1) with respect to density (ρ), pressure (p), and particle velocity (\mathbf{v}), the radiation force can be related to the change in momentum from second-order terms as [176],

$$\mathbf{F} = \nabla p_2 - \mu_f \nabla^2 \mathbf{v}_2 \quad (4.25)$$

$$\mathbf{F} = \rho \langle \mathbf{v}_1 \nabla \cdot \mathbf{v}_1 + \mathbf{v}_1 \nabla \mathbf{v}_1 \rangle \quad (4.26)$$

where $\langle \rangle$ represents the time-average quantity, \mathbf{v}_1 and \mathbf{v}_2 are the first and second-order terms in the expansion of particle velocity, p_2 is the second-order pressure term. For a plane wave, equation (4.26) can be reduced to,

$$\mathbf{F} = 2\rho \langle \mathbf{v} \nabla \mathbf{v} \rangle . \quad (4.27)$$

Substituting the solution to the attenuating wave equation (4.24) into (4.27), the magnitude of acoustic radiation force can be expressed as,

$$|\mathbf{F}| = A_0^2 e^{-2\alpha x} \rho \alpha . \quad (4.28)$$

Therefore, at any spatial location the magnitude of ARF can be simplified to,

$$|\mathbf{F}| = \frac{2\alpha I}{c_L} \quad (4.29)$$

where α [Np/cm] is the absorption coefficient of the tissue, and I [W/cm²] is the temporal average intensity of the acoustic beam at a given point in the tissue. The units of F are given as force per unit volume [kg/(s²cm²)], or [dynes/(1000cm³)], and the units of c_L are [m/s].

While (4.29) is an extremely useful approximation, it must be noted that it generally underestimates the true radiation force magnitude experienced in tissue due to the underlying second-order approximation. In tissue, an acoustic wave with high amplitude and short duration experiences significant nonlinear distortion, which results in the formation of harmonics and consequently, an increase in absorption [179]. In 2012, Dontsov and Guzina proposed a revised formulation of the classic ARF equation that included higher-order nonlinear terms [180]:

$$|\mathbf{F}| = \left(\frac{C}{K} - 1\right) \left[\frac{2\alpha I}{c_L} + \frac{1}{c_L^2} \frac{\partial I}{\partial t} \right]. \quad (4.30)$$

In this formulation, two additional terms are added: 1) a non-linear multiplier $(C/K - 1)$ and 2) a modulation-driven term $c_L^{-2} \partial I / \partial t$. In a Newtonian fluid, $C/K = 2$, however in biological tissue the C/K factor ranges from 8 to 25 [181], which can explain discrepancies in force magnitude which arise when using (4.29).

4.3 Vascular ARF-Based Imaging Methods

As mentioned previously, ARF can be utilized as an extrinsic motion source for diagnostic elasticity imaging of tissue. The primary benefit of ARF, in contrast to other extrinsic motion sources such as a mechanical vibrator or cardiac pulsation, is that ARF is highly controllable and can achieve a level of spatial precision that is simply not possible with the other techniques. From equation (4.29), it can be seen that ARF will be generated wherever acoustic energy is deposited, and will be particularly strong in areas of high acoustic intensity. Diagnostic ultrasound pulses are typically too low-energy to generate a measurable deformation, and therefore to utilize ARF for imaging purposes, acoustic intensity is increased either by increasing the driving voltage of the transducer or by increasing the duration of the output sound pulse.

ARF-based imaging techniques are typically categorized by their excitation duration (impulsive or harmonic) and by the location of the tracking beams that are utilized to monitor the deformation (on-axis or off-axis). On-axis tracking methods measure deformation directly in-line with the acoustic radiation force beam, while off-axis methods monitor shear wave propagation that is induced by the radiation force. The primary radiation force-based imaging techniques that have been developed for vascular imaging include vibroacoustography, shear wave elasticity imaging, shear/lamb wave dispersion vibrometry, and acoustic radiation force impulse imaging.

4.3.1 Vibroacoustography

Vibroacoustography (VA) is an on-axis technique that uses harmonic radiation force to elicit an acoustic response (acoustic emission) in the tissue [182], [183]. The acoustic emission is produced by focusing two continuous-wave (CW) ultrasound beams of slightly different frequency at the same spatial location in the tissue. The ARF exerted on the tissue by the two beams generates a vibration with frequency equal to the difference in frequency between the excitation beams (typically on the order of kHz). This acoustic emission is then captured with a low frequency receiver (hydrophone). VA images, unlike conventional ultrasound images, have the unique property of being speckle-free, which can improve image quality significantly.

In the context of atherosclerotic arteries, VA imaging has been shown to be particularly sensitive to arterial calcifications as shown by *ex vivo* studies done on breast tissue [184] and *ex vivo* and *in vivo* in porcine arteries [185]. Pislaru et al. [185] artificially induced arterial calcification in 11 farm pigs and found VA to have high sensitivity (100%), specificity (86%), positive predictive value (77%) and negative predictive value (100%) to calcium. However, because of the model used in these studies, the sensitivity of VA to lipid/necrotic core or hemorrhage could not be evaluated, and therefore the capability of VA to detect vulnerable plaque characteristics remains to be determined.

4.3.2 Shear Wave Elasticity Imaging and Supersonic Shear Imaging

Shear wave elasticity imaging (SWEI) [186] and its successor, supersonic shear imaging (SSI) [187], are techniques that use off-axis tracking of shear waves to make images of tissue elasticity. These two methods are largely considered “quantitative” because the shear wave velocity can be directly related to tissue modulus following equation (4.21). Pulse sequences for SWEI require three types of pulses: reference, pushing, and tracking. However, instead of tracking displacements in the region of excitation, displacements are tracked at a number of positions lateral to the region of excitation. A minimum of two tracking positions spaced some distance apart laterally are necessary to make a single shear wave

measurement, however 2D images are produced by tracking many lateral locations after many sequential ARF bursts.

In contrast, SSI is a massively parallelized version of SWEI that utilizes plane-wave beamforming and coherent compounding to achieve very high 2D framerates (3-5 kHz). In SSI, only one ARF excitation is necessary to generate a full 2D image, whereas in SWEI, each lateral tracking line requires an ARF excitation. Additionally, SSI utilizes multiple ARF bursts focused at different axial depths to create a constructively interfering planar shear wave (propagating in a Mach-cone) in the tissue. In this way, the entire imaging depth of field is traversed by a shear wave. SWEI and SSI datasets are motion tracked using correlation or phase-based estimators, and the displacement matrices are then used to calculate shear wave velocity. Classically, the method for estimating shear wave velocity was via inversion of the Helmholtz equation [187], [188], however, due to the challenge of noisy ultrasound data and computation time, time-of-flight methods have become preferred in modern implementations [189]–[192]. Because time-of-flight techniques follow the wave packet in the time domain, these methods yield a measurement of “group” shear wave velocity, which is not to be confused with the “phase” velocity, which represents the velocity of single frequency component of the shear wave. SWEI technology has been implemented commercially by a number of ultrasound developers including Siemens (Virtual Touch™ Quantification), Philips (ElastPQ), and GE (Shear Wave elastography). SSI is currently implemented on the Supersonic Imagine Aixplorer® (ShearWave™ Elastography).

While shear wave imaging techniques can be utilized to give quantitative shear modulus values by following (4.21), this simple relationship is only applicable in tissues that are homogeneous, linearly elastic materials. Arteries, however, are nonlinear, anisotropic, and highly heterogeneous [193]. Mechanical wave propagation in an artery is more properly modelled as a guided Lamb wave, which is similar to a shear wave in that the particle motion is perpendicular to wave propagation, but, unlike a shear wave, is dispersive even in the absence of viscosity due to the unique geometry of the propagating medium. Dispersion is a property whereby different frequencies of the wave packet travel at different

speeds, and if not taken into account, can significantly confound the relationship between shear wave velocities and shear modulus.

A number of groups have investigated ARF-induced wave propagation in normal arteries [194]–[196] and atherosclerosis phantoms [197] using the guided-wave model, while others have reported shear wave-derived Young’s modulus values *in vivo* in atherosclerotic carotid arteries for the purpose of identifying vulnerable plaques [198], [199]. Ramnarine et al. [198] recruited 81 patients with carotid stenosis that underwent SSI and it was demonstrated that patients with focal neurological symptoms had significantly lower mean Young’s modulus values than plaques in asymptomatic patients. The authors followed up this work by comparing SSI-derived Young’s modulus values to carotid endarterectomy (CEA) specimens in 25 patients [199], and found that the mean Young’s modulus was significantly lower in plaques that had “unstable” plaque characteristics (large necrotic core, and hemorrhage) as compared to “stable” plaques. While these clinical studies corroborate the hypothesis that vulnerable/symptomatic plaques are composed of mechanically softer components, the quantitative values of modulus that are reported in the studies are unreliable because they are derived from the simple shear wave equation (4.21). In a phantom study, Widman et al. [197] demonstrated substantial underestimation of true modulus, particularly in the stiffer phantom components, when using equation (4.21) as compared to the Lamb wave model. While SWEI/SSI may be able to discriminate vulnerable plaque features *in vivo* qualitatively, it remains to be seen whether quantitative assessment is feasible.

4.3.3 Shear/Lamb Wave Dispersion Vibrometry and Spectroscopy

Shear wave dispersion ultrasound vibrometry (SDUV) [200] and lamb wave dispersion ultrasound vibrometry (LDUV) [201] are complimentary off-axis techniques that measure mechanical wave propagation in a manner similar to SWEI. As opposed to SWEI, which typically implements an impulsive (i.e. broadband) ARF excitation to measure “group” shear wave velocity, SDUV utilizes harmonic (i.e. narrow-band) shear waves and measures “phase” velocity for a range of frequencies. In the initial description of the technique, harmonic shear waves were generated with AM-modulation of CW

ultrasound [200], however newer implementations have utilized pulsed ARF bursts at the desired frequency [202], or even single broadband pulses with frequency decomposition techniques to gather similar data (in a method known as shear wave spectroscopy, SWS) [203]. Once phase velocity is measured for a given range of frequencies, the data can be fit to either a simple two-parameter Voigt model (for SDUV), or more complex models such as the Lamb-wave model (for LDUV) as necessary. The main benefit of the SDUV/LDUV techniques over conventional SWEI is that viscosity can be measured in addition to elasticity (whereas SWEI only measures elasticity).

LDUV has been applied to arterial mimicking phantoms (polyurethane tubes) and non-diseased *ex vivo* porcine arteries to try to quantitatively estimate tissue modulus [204]. Using this technique, Bernal et al. [204] measured shear moduli of 24 - 46 kPa for 10 - 100 mmHg static pressures in *ex vivo* arteries, which slightly underestimated *in vivo* stiffnesses of 130 kPa in systole and 80 kPa in diastole measured by SSI and a similar model by Couade et al. [195]. While LDUV techniques have shown promising results in early experiments, they have yet to be demonstrated in larger *in vivo* clinical studies or in atherosclerotic plaque.

4.3.4 Acoustic Radiation Force Impulse Imaging

In acoustic radiation force impulse (ARFI) imaging, which is the focus of this dissertation, a single ultrasound transducer is used to both induce and monitor on-axis deformation in order to generate qualitative images of tissue stiffness [205]. At a single lateral location, an ARFI pulse sequence consists of three pulse types: 1) reference pulses that precede the ARF burst and are used as a baseline for tissue position, 2) pushing (ARF) pulse that consist of a high-intensity impulse to displace the tissue, and 3) tracking pulses that monitor the tissue dynamics following the ARF burst. Tissue displacement is measured using correlation or phase-shift estimation techniques on raw RF data from the reference and tracking pulses [206]. The pulse sequence and motion estimation is repeated at a number of lateral positions across the imaging field of view (FOV) to build up a 3D data set consisting of tissue displacement as a function of axial position, lateral position, and time. From this data, 2D parametric

images can be rendered by extracting various features from displacement vs. time curves at a given spatial location, such as peak displacement (PD) and time to 67% recovery from the peak (RT).

Displacements induced in ARFI are typically small (1-10 μm) and the tissue fully recovers to its baseline position quickly (4-6 ms). Areas of higher displacement are indicative of mechanically softer regions in the tissue, while smaller displacements indicate stiffer regions. Calculating quantitative tissue modulus from ARFI-measured displacements is currently not feasible due to uncertainties in the exact magnitude of force delivered to the tissue, which is materially-dependent as shown in equation (4.29). However, novel methods that fit ARFI-derived displacement profiles to biomechanical models, as done in viscoelastic response (VisR) imaging [207], may be capable of determining quantitative parameters in the future. ARFI has been commercialized on the Siemens ACUSON S2000 and S3000 scanners under the brand name Virtual TouchTM Imaging (VTI).

Using ARFI to characterize atherosclerotic plaque was first proposed by Trahey et al. [208]. The initial studies were performed *ex vivo* in femoral and popliteal arteries acquired from amputated human legs, and showed that regions of higher displacement (i.e. qualitatively soft) correlated with areas of lipid/necrotic core from matched histological sections, while regions of lower displacement (i.e. qualitatively stiff) correlated with areas of fibrosis and calcification. Subsequent studies done both *ex vivo* and *in vivo* in a porcine model of spontaneous atherosclerosis corroborated these initial findings with matched histology in a small number of animals [209], [210], and were followed up by *in vivo* human studies in the carotid and popliteal arteries [211]–[213]. While these preliminary results utilizing ARFI imaging have been encouraging, all the studies cited thus far were performed either with very small sample sizes or were done without histological validation, making it difficult to quantify accuracy of ARFI for various plaque features. The subsequent chapters in this dissertation will thoroughly detail experiments undertaken to quantify ARFI performance for plaque characterization.

4.4 Challenges/Future Developments

Thus far, the theory and implementation of ARF have been discussed thoroughly; however, the safety and challenges of various techniques have not been given much consideration. In this section, the bioeffects of ARF-based imaging is explored first, followed by a number of phenomena that can negatively affect atherosclerosis imaging. Novel developments and technical improvements in ARFI used to mitigate or overcome these challenges are presented where applicable.

4.4.1 Bioeffects

Clinical ultrasound imaging, as with any medical device, is regulated in the United States by the Food and Drug Administration (FDA). When it comes to ultrasound safety, the two major bioeffects that the FDA is concerned about are thermal effects (tissue heating) and mechanical effects (cavitation), both of which can be exacerbated with the high-intensity acoustic pulses necessary for ARF pushing pulses. A third concern, which is unique to vulnerable plaque imaging, is the possibility of instigating rupture of a thin fibrous cap with ARF. So far, the FDA has cleared ARF-based imaging technology for abdominal, breast, thyroid, small parts, and musculoskeletal exams, but has not yet cleared the technology for vascular application.

Thermal Effects

Thermal effects of ultrasound relate to the heating of tissue as acoustic energy is introduced into the body. Heating is primarily the result of frictional mechanisms and is directly related to the intensity of the acoustic pulse. If the tissue is exposed to elevated temperatures for long periods, cell death can occur. Historically, the FDA has limited ultrasound output intensity (spatial-peak, temporal-average, or I_{SPTA}) to $\leq 720 \text{ mW/cm}^2$ for general imaging. However with the advent of novel pulsing schemes, an additional metric was introduced, termed the thermal index (TI), which is determined by the following formula [214],

$$TI = \frac{W_p}{W_{deg}} \quad (4.31)$$

where W_p is the relevant (attenuated) acoustic power at the depth of interest, and W_{deg} is the estimated power necessary to raise the tissue equilibrium temperature by 1 °C according to a chosen specific tissue model. On modern systems, the TI is displayed on the ultrasound screen to give the sonographer an indication of how much heating will occur with a given imaging mode. Temperature increases below 6 °C are usually accepted as an upper limit on TI and additional tissue heating above 6 °C needs to be justified. Although equation (4.31) is useful in most cases, it does not take into account the temporal duration of the pulse train, which may include significant “off” time, and therefore is limited [214].

The American Institute of Ultrasound in Medicine (AIUM) proposed revised recommendations for tissue heating which allow going above 6 °C, if the exposure is for a short time [215]. For example, no adverse biological effects have been observed for temperature increases of 12.6 °C for 5 s, 14.9 °C for 1 s, and 18.6 °C for 0.1, suggesting that substantial heating can occur and still be within a safe regime if the pulse is short. Heating from general ARF imaging though, has been shown to not exceed 1 °C of temperature rise with FEM and thermocouple measurements [216], [217], suggesting that much higher acoustic intensities could be utilized safely.

Mechanical Effects

Mechanical bioeffects in ultrasound imaging primarily refer to cavitation – a phenomenon characterized by the formation and/or destruction of bubbles in tissue. When a gas bubble experiences an ultrasonic field it expands and contracts with the rarefaction and compression of the ultrasound wave. If the rarefaction component (i.e. negative pressure) of the ultrasound pulse is too high, the bubble can expand so much that a vacuum is generated and the bubble instantaneously collapses in on itself. This event causes rapid temperature increase that can be damaging to cells [218]. Cavitation potential is captured by a metric termed the “mechanical index” (MI) which is given as,

$$MI = \frac{p^-}{\sqrt{f_0}} \quad (4.32)$$

where p^- is the derated peak rarefactional pressure in units of MPa, and f_0 is the ultrasound center frequency in units of MHz. MI is limited by the FDA to a value of 1.9 for diagnostic imaging. In general the risk of cavitation is much higher in organs containing stabilized gas bodies, such as the intestine or the lung, or when exogenous microbubble contrast agents are used for imaging [218]. In organs not known to contain well-defined gas bodies (e.g. spinal cord), the risk is thought to be much lower with no adverse bioeffects up to a MI of 4 [218].

In ARF imaging, many superficial organs (e.g. carotid arteries) can be evaluated with pulse sequences that fall below the FDA limit of 1.9, however when deeper penetration is necessary (e.g. in obese patients, or in deeper organs such as the liver) MI limits may need to be exceeded in order to generate a measureable ARF deformation. A recent study by Church et al. [219] revisited the derivation of equation (4.32) with an improved biomechanical model and long ARF pulse durations, and found that the exponent of 0.5 on frequency may be too conservative (it should be closer to 0.75). These results suggest that higher acoustic outputs can be utilized (particularly for generating ARF with higher frequencies), however additional studies are necessary to confirm this assertion.

Plaque Disruption

The last bioeffect that should be considered when implementing ARF-based elasticity for atherosclerosis imaging is the potential for plaque disruption. To date, no studies have reported adverse events when implementing ARF on plaques in either animals or humans; however, the concept that an ARF pulse may impart enough stress on the fibrous cap to cause a rupture is not an unreasonable concern. To date, only one study has been published that has specifically evaluated the stress imparted by ARF on a fibrous cap using FEM simulations [220]. In this study, the authors segmented a number of plaque geometries taken from the MRI literature and implemented them in the ARFI FEM framework developed by Palmeri et al. [176] to determine the stress imparted on the fibrous cap by ARFI. The results

demonstrated that the maximum von Mises stress of an ARFI excitation was ≤ 1.2 kPa, which, compared to the circumferential stress from blood pulsation, was considerably small [220]. In the biomechanics literature, a value of 300 kPa is typically cited as the critical stress necessary to cause plaque rupture [26]. While this study is encouraging, it does suggest that ARFI can impart an additional stress on the fibrous cap that may be non-negligible if combined with blood pressure. Therefore, it is advisable that ARF-based imaging be gated to diastole to ensure that circumferential stress is at a minimum prior to imaging.

4.4.2 Physiologic Motion

One of the main advantages for using ultrasound to measure ARF-induced deformation is that that it is particularly sensitive to motion. The drawback however is that it is sensitive to non-ARF motion as well, such as sonographer hand trembling or physiologic motion (breathing, pulsation, etc.), which can introduce unwanted artifacts into ARF elastograms. In vascular ARF imaging, arterial pulsation is perhaps the greatest source of unwanted motion, and must be filtered out prior to making an image. This is commonly done by implementing interpolation-based motion filters that assume the underlying non-ARF motion is either linear or quadratic, and that the unwanted motion is primarily in the axial direction [205], [221], [222]. An example of a linear motion filter applied to an ARFI displacement curve is given in Figure 4.1.

4.4.3 Jitter

Jitter is a term used to describe the error, or variance, associated with an ultrasonic displacement estimate. Jitter errors are the result of signal decorrelation, noise, and finite window length that causes a slight shift in the correlation peak between two successive A-lines [223]. Jitter represents a fundamental lower limit of unbiased displacement estimator performance in ultrasound tracking, and the standard deviation of jitter ($\hat{\sigma}$) can be predicted using the Cramér-Rao lower bound (CRLB) as,

$$\hat{\sigma} \geq \sqrt{\frac{3}{2f_0^3 \pi^2 T (B^3 + 12B)} \left(\frac{1}{\rho^2} \left(1 + \frac{1}{SNR^2} \right)^2 - 1 \right)} \quad (4.33)$$

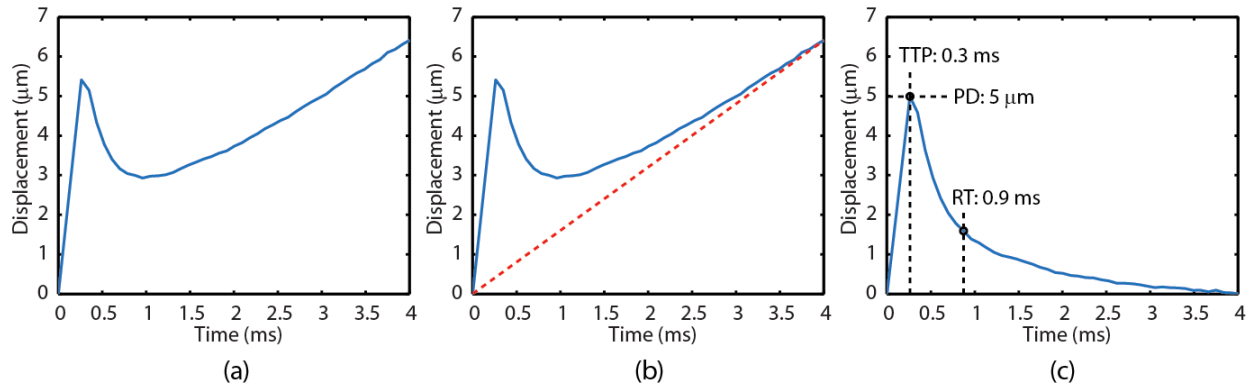


Figure 4.1: Motion filtering of ARFI displacement profiles. (a) ARFI displacement curve corrupted by a constant velocity, non-ARFI motion. (b) An idealized fit to the non-ARFI motion estimated from the first and last data points (i.e. time points where ARFI-induced motion is assumed to be zero). (c) Motion-filtered ARFI displacement curve with linear motion profile subtracted from raw ARFI data. Common parameters measured from ARFI displacement curves to produce 2D images include peak displacement (PD), time-to-peak (TTP), and recovery time (RT) to two-thirds of peak displacement.

where f_0 is the ultrasound center frequency, T is the tracking kernel length, B is the bandwidth, ρ is the correlation coefficient, and SNR is the signal-to-noise ratio of the received RF data. In ARF-based imaging, correlation coefficients between successive A-lines is typically high (0.999) because of the small displacements (1-10 μm) induced by ARF and under these conditions the CRLB can reach as low as 0.5 μm . However, if ARF-induced displacement falls below this level, it is usually undetectable using conventional motion tracking algorithms. Simulation studies have demonstrated that normalized cross-correlation (NCC) algorithms produce the lowest jitter magnitudes, followed by the Loupas [224] and Kasai [225] autocorrelation methods [206]. The CRLB can be exceeded by using biased estimation techniques, such as a Bayesian estimator [226], [227], however these methods are currently very computationally expensive and require substantial optimization before they can be implemented on commercial systems.

4.4.4 Displacement Underestimation

A significant source of bias in ARFI imaging occurs due to differential motion decorrelation, or tissue shearing, under the imaging point spread function (PSF). In on-axis techniques, such as ARFI, the same transducer is typically used to both induce and track displacements. This creates a situation where scatterers on the edge of the tracking resolution cell tend to displace less than scatterers in the middle of the tracking resolution cell due to the non-uniformity of applied radiation force (which follows a sinc^2 pattern in the lateral and elevation directions). The consequences of this phenomenon are two-fold. First, peak displacement measured in the ROE will tend to underestimate true tissue peak displacement due to averaging of scatterer motion under the resolution cell. This can lead to a reduction in contrast in peak displacement images because soft features may appear stiffer than they truly are due to underestimated displacement. Second, due to the non-uniform displacement of scatterers, the correlation between the reference pulse and tracking pulses immediately following the ARF excitation will decrease. This reduction in correlation will ultimately lead to an increase in jitter and, therefore, noisier images.

Differential motion decorrelation was first explored analytically by McAleavey et al. [228] under simplifying assumptions that modeled the displacement field and tracking beam pattern as Gaussians and ignored the effects of non-axial motion. In this work, expressions were derived for echo correlation, jitter, and mean ARF displacement as functions of lateral and elevational beam widths for pushing and tracking pulses. A significant conclusion was that displacement underestimation can be mitigated by adjusting the ratio of pushing and tracking beam widths; specifically, when the pushing beam width is much wider than the tracking beam width, the peak displacement estimate matches the true tissue displacement much more closely than when the pushing and tracking beam widths are identical. In a common imaging scenario (1D linear array) where control over $F/\#$ can only be exerted in the lateral dimension, measured peak displacement could be only $1/\sqrt{2}$ of the true tissue peak displacement.

The expressions derived by McAleavey et al. were later improved by Dhanaliwala et al. [229] by adding additional terms to account for the effect of mechanical coupling of tissue in three dimensions. In

the original derivation, McAleavey et al. assumed that the dimensionality of the tissue region displaced by ARF was equal to the width of the two-way response of the pushing beam. Dhanaliwala et al., using 3D finite element simulations, demonstrated that the displaced tissue region is actually wider than the pushing beam width due to mechanical coupling and adjusted McAleavey's expression accordingly. Using the Dhanaliwala modification, the expression for the jitter lower bound ($\hat{\sigma}$) in ARFI imaging can be rewritten as the following [229]:

$$\hat{\sigma} \geq \sqrt{\frac{3}{2f_0^3 \pi^2 T (B^3 + 12B)} \left(\frac{1}{\left(1 - \frac{1}{c_L^2} 4A^2 f_0^2 \pi^2 L_x L_y \left(\frac{1}{\sqrt{(1+L_x^2)(1+L_y^2)}} - \frac{4L_x L_y}{(1+2L_x^2)(1+2L_y^2)} \right) \right)^2 \left(1 + \frac{1}{SNR_E^2} \right)^2 - 1} \right)} \quad (4.34)$$

$$L_x = \frac{D_x}{T_x}, \quad L_y = \frac{D_y}{T_y} \quad (4.35)$$

Where A is the maximum scatterer displacement, c is the speed of sound, and D_x, T_x, D_y, T_y , are displacement and tracking beam widths in the lateral and elevational dimensions, respectively. Likewise, the expression for mean ARFI-derived displacement ($\hat{\mu}$) can be written as the following:

$$\hat{\mu} = \frac{2AL_x L_y}{\sqrt{(2L_x^2 + 1)(2L_y^2 + 1)}} \quad (4.36)$$

Finally, using equations (4.34) and (4.36) and scaling by $c_L/2$ to maintain consistent units, an expression for the upper bound of SNR_{ARFI} can be written as the following:

$$\overline{SNR}_{ARFI} \leq \frac{\hat{\mu}}{\hat{\sigma} \frac{c_L}{2}} \quad (4.37)$$

Using equation (4.37) it can be shown that increasing ARF-induced displacement has diminishing returns in terms of improving SNR_{ARFI} due to displacement underestimation and differential motion decorrelation [229].

Interestingly, underestimation bias in on-axis displacement measurements is not constant with time. Palmeri et al. [230], [231], using 3D FEM simulations, demonstrated that underestimation is worst in the early times points following the ARF excitation, but resolves over time at a rate corresponding to the shear wave speed of the material. Therefore, stiffer materials with faster shear wave speeds are less susceptible to underestimation bias compared to softer materials with slower shear wave speeds. These results were experimentally validated in optically translucent tissue mimicking phantoms as part of this dissertation and are presented in Appendix A.

To mitigate differential motion decorrelation in post-processing, Mauldin et al. proposed using principal component analysis (PCA) as either a filter prior to conventional time-delay estimation [232], or as a unique time-delay estimator itself [233]. In PCA, a linear transformation is used to convert a set of possibly correlated variables (e.g. scatterer displacements encoded as phase shifts in RF data) into a set of uncorrelated variables or basis vectors, with the stipulation that the basis vectors are orthogonally distributed. While PCA-based approaches are not necessarily able to resolve underestimation bias completely, results suggest that they are more robust to decorrelation, and provide estimates with lower jitter compared to conventional estimation techniques such as the Loupas autocorrelation method [224].

4.4.5 Clutter

Clutter is a noise artifact found in ultrasound imaging that is characterized as diffuse echoes overlaying the signal of interest. Clutter echo sources include sound reverberation between tissue layers (coherent ring down), scattering from off-axis tissue structures, ultrasound beam distortion (phase aberration), returning echoes from previously transmitted pulses, and random acoustic/electronic noise [234]. Clutter is particularly a problem in ultrasonic blood flow estimation where the stationary echoes from sound reverberation can be 20-40 dB stronger than the echoes from blood [235]. Motion estimators will preferentially track the strongest echoes, and will therefore output a value of zero for blood velocity in the presence of stationary clutter. Similarly in ARF-based techniques, if a strong off-axis clutter signal is present, the measured displacement will be biased by the motion of the clutter [206].

One of the most successful clutter rejection techniques in ultrasound imaging has been the use of tissue harmonic imaging (THI) [130]. In THI, sound is transmitted into the tissue at a given center frequency but instead of listening for echoes at the fundamental frequency, echoes at the second harmonic are received (either through bandpass filtering, or pulse inversion techniques). The main mechanism through which THI improves clutter has been demonstrated through nonlinear acoustic simulation and is through a reduction of reverberation artifact [236].

Doherty et al. [237] and Song et al. [238] were the first to propose the use of harmonic sequences to track ARFI- and SWEI-induced displacements, respectively, to improve clutter suppression. For ARFI, Doherty et al. [237] implemented two conventional THI methods –bandpass filtering and pulse inversion. In the bandpass approach, conventional ARFI ensembles are acquired with a broadband transducer, and a bandpass filter is used to isolate the harmonic component in each tracking line prior to motion estimation. In the pulse inversion approach, tracking pulses of opposite polarity are transmitted serially, and the echoes are summed to cancel out the fundamental signal. One of the disadvantages of the pulse inversion approach is that the PRF of the ARFI ensemble is effectively cut in half. To mitigate this, the authors developed a fully sampled pulse inversion sequence to maintain PRF, which utilized a sliding window when summing pulses of opposite polarity.

The results of this work demonstrated a marked improvement in both B-mode and ARFI image quality of the carotid when using THI tracking pulses (particularly with the fully sampled pulse inversion sequence). In the pulse inversion images, the lumen/plaque border is much clearer and a region of increased displacement becomes visible that was otherwise obfuscated in the fundamental image. As was the case in conventional B-mode imaging, harmonic ARFI is likely to replace fundamental ARFI in the future for a majority of clinical applications due to improvements in contrast and image quality.

4.4.6 Depth-of-Field

One of the major challenges with conventional ARFI imaging is the limitation in depth of field. ARFI pulses are typically tightly focused in order to increase acoustic intensity and deposit more

radiation force. Consequently, tissues outside of the focal zone do not displace very far, resulting in non-uniform contrast through depth. Two methods have been proposed to overcome this limitation: 1) acquire multiple, separate ARFI images with the push beam focused at different depths and blend the data in post processing [239], or 2) implement multiple pushes in rapid succession [240] as is done in SSI imaging (see section 4.3.2). While the first method is feasible, a significant drawback is the length of the acquisition, where physiological motion and mis-registration can introduce artifacts. However, using the second method, ARFI acquisition time is unchanged because all pushes happen in succession in the ensemble. Rosenzweig et al. [240] demonstrated that using rapid multi-focal-zone ARFI acquisitions substantially improves ARFI depth-of-field, increases CNR by up to 40% compared to conventional single-focal-zone ARFI, and incurs less than 20% loss in contrast compared to sequential multi-focal-zone ARFI.

The main drawback to using rapid multi-focal-zone ARFI is the acoustic energy that is delivered to the patient. Unlike SSI, where only three ARF excitations are required to generate a 2D image, multi-focal-zone ARFI image may require upwards of 100 ARF excitations to capture a 2D image. Therefore, the benefits in image quality have to be weighed against the potential bioeffects when using rapid multi-focal-zone ARFI.

Improving ARFI contrast through depth can also be achieved by applying depth-dependent gain (DDG) normalization in a manner similar to time-gain compensation (TGC) that is done in conventional B-mode (Figure 4.2). During ARFI excitation, non-uniform force is deposited through depth in the tissue due to focusing and tissue-dependent attenuation, which can lead to spatial gradients in otherwise homogeneous tissue. To account for this, the ARFI displacement response can be normalized by the applied force field [241], which can either be measured experimentally in a phantom or predicted with FEM simulation. While this technique works well in tissue with largely homogeneous attenuation coefficients, it can be challenging in heterogeneous tissues in which the applied force field is not so easily predicted.

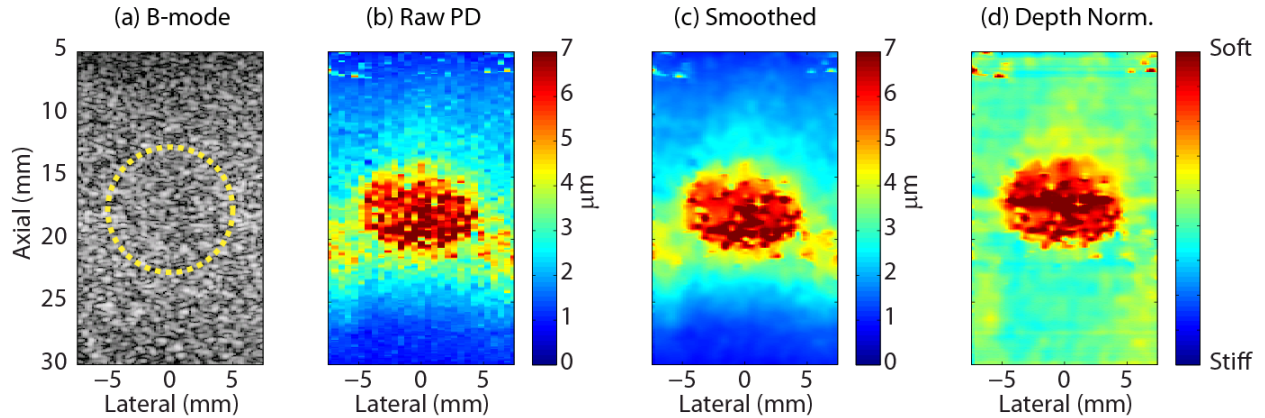


Figure 4.2: B-mode and qualitative ARFI imaging of a phantom with a soft spherical inclusion (8 kPa) embedded in a stiffer background (25 kPa). The spherical inclusion (outlined in yellow) is nearly invisible on B-mode imaging (a), but is obvious as an area of increased peak displacement (PD) in the ARFI image (b). The quality of an ARFI imaging can be improved by applying lateral interpolation and a smoothing filter, such as a two-dimensional (1 mm^2) Wiener filter (c). Finally, depth-dependent gain (DDG) normalization can be applied, in a manner similar to time-gain compensation, to improve the uniformity of the ARFI image through depth.

4.4.7 Real-Time ARFI

Real-time implementation of ARFI imaging (i.e. 20-30 frames per second) is challenging due to a number of factors: thermal safety, frame acquisition time, and data transfer/processing rates. While no commercial implementations of real-time ARFI exist at this time, a substantial amount of research has gone into developing solutions that may enable real-time ARFI in the future. Thermal safety and frame acquisition time can be addressed by utilizing parallel-receive beamforming techniques [242] and clever beam sequencing approaches [243]. This section will focus on the third area challenging real-time implementation, namely, computation time.

To address the computation time requirements for ARFI processing, ultrasound researchers have turned to using graphical processing units (GPU). GPUs are specialized computer circuits that include hundreds of processing cores for highly parallelized computation. Rosenzweig et al. [244] demonstrated that a GPU-based implementation of the ARFI processing chain can substantially improve computation performance (by approximately $40\times$) and enable ARFI frame-rates of less than a second. To achieve this,

the authors developed custom implementations of cubic spline interpolation and Loupas' autocorrelation estimator [224] written in Compute Unified Device Architecture (CUDA), a programming interface developed by NVIDIA to facilitate using GPUs for general purpose processing. Using the GPU processing chain, the authors showed that displacement estimate computation was no longer the rate-limiting step; instead, displaying the image to the monitor took the most time due to an additional RAM copy.

The greatest challenge with implementing ARFI on the GPU is the significant development time that is needed to efficiently port algorithms into a parallelized environment. Cubic spline interpolation, for example, is not well suited for parallel execution because the solution is dependent upon all data points. Nevertheless, once a parallel version of a given algorithm is developed, the GPU can serve as a powerful tool to speed up lengthy computations and make real-time implementations feasible.

4.5 Summary

In conclusion, ARF-based elasticity imaging techniques have opened a new frontier for elasticity imaging, and have shown great promise for characterizing atherosclerotic plaques based on mechanical stiffness. The main advantage of ARF imaging is that it can be readily implemented into the current clinical workflow without additional overhead, allowing physicians to probe an entirely new biomarker for plaque vulnerability. The rest of this dissertation will be focused on validating ARFI imaging specifically for plaque characterization against histology to quantitatively demonstrate its efficacy for detecting various vulnerable plaque features such as necrotic core, which to date has only been done in small sample animal studies. In the next chapter, results from a preliminary blinded reader study done in *ex vivo* porcine femoral plaques will be presented. These methods will then be utilized and improved upon in subsequent chapters that detail further studies done in human carotid plaques.

CHAPTER 5

Acoustic Radiation Force Beam Sequence Performance for Detection and Material Characterization of Atherosclerotic Plaques: Preclinical, *Ex Vivo* Results.

The following chapter presents preclinical data demonstrating performance of acoustic radiation force (ARF)-based elasticity imaging with five different beam sequences for atherosclerotic plaque detection and material characterization. Twelve trained, blinded readers evaluated parametric images taken *ex vivo* under simulated *in vivo* conditions of 22 porcine femoral arterial segments. Receiver operating characteristic (ROC) curve analysis was carried out to quantify reader performance using spatially matched histology for validation. The beam sequences employed had high sensitivity and specificity for detecting Type III+ plaques (Sens: 85%, Spec: 79%), lipid pools (Sens: 80%, Spec: 86%), fibrous caps (Sens: 86%, spec: 82%), calcium (Sens: 96%, Spec: 85%), collagen (Sens: 78%, Spec: 77%), and disrupted internal elastic lamina (Sens: 92%, Spec: 75%). 1:1 single-receive tracking yielded the highest median areas under the ROC curve (AUC), but was not statistically significantly higher than 4:1 parallel-receive tracking. Excitation focal configuration did not result in statistically different AUCs.

5.1 Introduction

One aspect of ARFI-based plaque characterization that has not yet been extensively investigated is the difference in performance between various beam sequence configurations. As described in the previous chapter, an ARFI-based beam sequence consists of two types of ultrasonic pulses: long-duration

© 2013 IEEE. Portions reprinted, with permission, from R. H. Behler, T. J. Czernuszewicz, C. Wu, T. C. Nichols, H. Zhu, J. W. Homeister, E. P. Merricks, and C. M. Gallippi, "Acoustic radiation force beam sequence performance for detection and material characterization of atherosclerotic plaques: preclinical, ex vivo results.," IEEE Trans. Ultrason. Ferroelectr. Freq. Control, vol. 60, no. 12, pp. 2471–87, Dec. 2013

ARF excitation pulses, which deform the tissue, and standard B-mode pulses, which track the deformation. Previous studies have shown that the beamforming of these pulses can significantly impact a number of factors, including displacement tracking accuracy, contrast-to-noise ratio (CNR), tissue heating, and frame rate [228], [230], [231], [241], [242]. For example, it has been modeled that the focal configuration, or $F/\#$ (which is given by the ratio of focal depth, z , to aperture width, d), of the excitation pulse can mitigate displacement underestimation due to shearing artifact [228], [230]. Shearing artifact is a phenomenon that occurs when the distribution of scatterer motion within the point spread function (PSF) of the tracking beam is non-uniform and leads to averaging, and consequently underestimation, of ultrasonic displacement tracking. A large $F/\#$ excitation pulse (relative to the tracking pulse) deposits energy over a wide lateral region of tissue within the tracking resolution cell to create a relatively uniform displacement field and less shearing. A large $F/\#$ excitation also changes the ARF distribution in the axial dimension; the axial range over which displacement is constant is increased while the force magnitude in a given position decreases [241].

In addition to $F/\#$, receive beamforming methods such as parallel receive tracking, where multiple A-lines are beamformed from a single transmit event, can be used to reduce the number of ARF excitations necessary to interrogate a given lateral range, thereby decreasing tissue heating and increasing frame rate [242]. Depending on the parallel beam spacing and excitation pulse beamwidth, the displacements observed in the A-lines furthest from the region of excitation (ROE) could be due entirely to shear wave propagation, which may not be uniform in a heterogeneous medium such as an atheroma.

In this chapter, the performance of ARF-based techniques for atherosclerosis imaging is quantitatively assessed with a reader validation study. Atherosclerotic arteries were harvested from a dietary hypercholesterolemic porcine model and imaged *ex vivo* under simulated *in vivo* conditions. Twelve blinded readers were recruited and trained to read images created with ARF-based techniques. Plaque detection and characterization performance for each reader was assessed using receiver operating characteristic (ROC) curve analysis and a pathologists reading of spatially matched histology. ARF-based imaging performance results assessed under simulated *in vivo* conditions are compared to published *in*

in vivo MRI and CT results to demonstrate the potential relevance of ARF-based ultrasound methods to detecting and characterizing atherosclerotic plaques.

5.2 Methods

5.2.1 Animal Model

Diet-induced hypercholesterolemic (DH) pigs were used as the model for atherosclerosis. DH pigs are genetically normocholesterolemic (NC) swine that are fed a high-fat diet (20% beef tallow, 1% cholesterol or ~10 g cholesterol daily, 0.75% cholate) to induce hypercholesterolemia and cause the animals to develop atherosclerotic lesions spontaneously that closely mimic histopathology seen in humans. Detailed descriptions of the lipid and hemostatic profiles of DH swine, as well as a summary of the atherogenic diet, are available in a previous manuscript [67]. For this study, nineteen phenotypically normal pigs were selected from the closed colony at the Francis Owen Blood Research Laboratory at the University of North Carolina, Chapel Hill, and thirteen of those pigs were put on an atherogenic diet for 12 months prior to imaging. The remaining six were continued to be fed a regular low-fat diet (3.58% crude fat including 60 to 65 mg cholesterol total daily), the same diet that the DH pigs were on prior to this study. All animal procedures were approved by the University of North Carolina Institutional Animal Care and Use Committee (IACUC).

5.2.2 Ultrasonic Imaging, Data Collection, and Data Processing

Left and right iliac arteries were harvested from all pigs (13 DH and 6 NC), yielding 38 arteries, each ~20 to 25 cm in length. The mean (\pm standard deviation) age of DH animals at necropsy was 3.8 (\pm 0.8) years, while the mean age of NC animals was 4.6 (\pm 2.2) years. These arteries were stripped of excessive adventitial connective tissue, mounted, and pressurized statically to 80 mmHg in a saline water bath kept at room temperature (22 °C), as illustrated in Figure 5.1. To assist in mounting, a scaffold was erected across the top of the water tank with two clamps that extended into the water. The arteries were

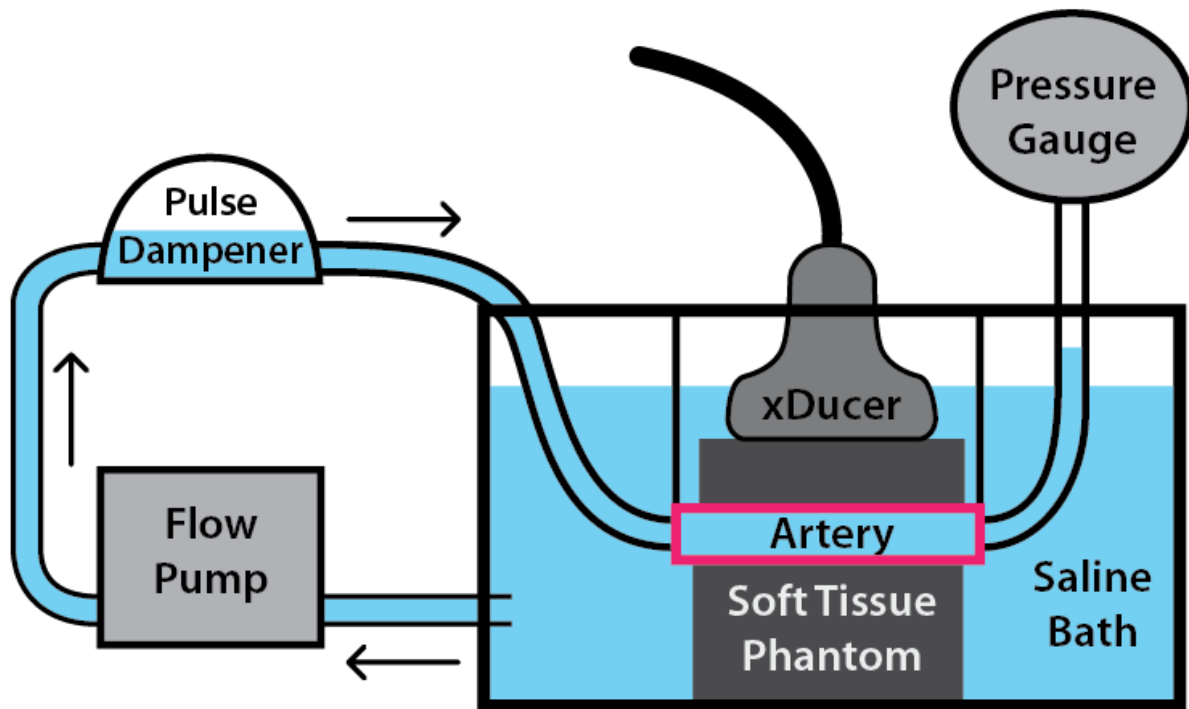


Figure 5.1: Pressurization apparatus for ex vivo imaging. Excised arteries were mounted in a saline water bath between ~ 20 kPa tissue mimicking gelatin phantoms and statically pressurized to 80 mmHg to simulate *in vivo* imaging conditions during diastole. The saline bath was kept at room temperature (22 °C).

fitted with barbed plastic tubing connectors inserted into either end of the vessel, and each end was placed in a clamp to hold the artery in place. Using the clamps, arteries were stretched to approximately 1.5 times their recoil length to estimate *in vivo* lengths [245]. One end of the vessel was attached, via the barbed connector, to a hose coming from a Masterflex LS 7550-30 computerized pump drive (Cole-Parmer Instrument Co. Chicago, IL, USA), while the other end was connected to a hose that lead to a GE Druck DPI 104 digital pressure gauge (Druck Ltd. Leicester, UK). To convert the output of the flow pump from pulsatile to laminar flow, a Windkessel-type pulse damper (EW-07596-20, Cole-Parmer Instrument Co. Chicago, IL, USA) was placed in series with the water pump and the artery. In some cases, branch points in the arteries that were cut during tissue harvesting were sutured closed to maintain

pressure in the artery. Branch points that had sutures in the imaging field of view (FOV) were not included as candidate imaging locations.

To simulate *in vivo* imaging conditions, two homogeneous soft tissue mimicking phantoms with a Young's modulus of ~20 kPa were created and placed above (~15-18 mm thickness) and below (~30-40 mm thickness) the vessel during imaging. The phantom recipe consisted of the following ingredients (with percent composition by mass in parentheses): type-A gelatin (13%; Acros Organics, Geel, Belgium), Photo-Flo (2%; Eastman Kodak Co., Rochester, NY, USA), *n*-propanol (1%), powdered graphite (1%), and de-ionized water (83%). The acoustic attenuation of the phantom was determined to be $0.2 (\pm 0.02)$ dB/cm/MHz, based on 5 repeated measurements. A modulus of ~20 kPa was selected to mimic the modulus of soft tissue (e.g. muscle) surrounding peripheral vessels *in vivo* [246]. Phantom modulus values were determined by measuring shear wave velocities in the phantom materials (in separate, homogeneous, 64 cm^3 blocks) using a time-to-peak algorithm [189]. The arterial mimicking phantoms were poured from the same phantom mixtures as those measured. The SWV and Young's modulus measurement methods were validated in a model 049A Computerized Imaging Reference Systems phantom (CIRS, Norfolk, VA, USA) with 25 kPa background material; the measured SWV was 2.81 ± 0.08 m/s, which matches the expected SWV of 2.89 m/s for a 25 kPa material. The arteries were not completely embedded in the tissue mimicking material to preserve the tissue for histological processing after imaging. The phantom above the artery was held in place by the transducer, while the phantom below the artery was held in place by weights. Pressure was applied, via the transducer face, to the upper pad such that it would not float away or move during acquisition.

Imaging was performed with a Siemens SONOLINE Antares™ imaging system (Siemens Medical Solutions USA, Inc., Ultrasound Division), equipped for modifiable beam sequencing for research purposes and a VF7-3 transducer. The transducer was secured in a holder connected to a digital three-axis motion controller mounted on an optical air table (Newport Corp., Irvine, CA, USA). The transducer was positioned to image the arteries longitudinally and was translated down the length of each artery to generate up to four non-overlapping FOVs.

ARF ensembles consisted of two reference lines, one ARF excitation impulse, and 60 tracking lines with an 11.5 kHz pulse repetition frequency (PRF). ARF excitations were 300 cycles at 4.21 MHz, and both tracking and reference lines were two cycles at 6.15 MHz. Two types of ARF excitations were combined with three types of tracking to generate five total beam sequences (Figure 5.2). The two types of excitations included: 1) single excitation with an F/1.5 focal configuration (SP1.5), and 2) single excitation with an F/3 focal configuration (SP3). The three types of tracking included: 1) single-receive (SRx) in the ROE, 2) 4:1 parallel-receive (ParRx) in the ROE [242], and 3) 4:1 parallel-receive lateral to the ROE (LatRx), the last being a method comparable to shear wave elasticity imaging (SWEI) [186]. On transmit, SRx tracking pulses had either an F/1.5 or F/3 focal configuration, matching the corresponding excitation F/#. On receive, all sequences used dynamic focusing and aperture growth (F/0.75). Figure 5.2 depicts the different beam sequences and associated labeling scheme used in this study. For SRx tracking, 40 ROEs and tracking locations laterally spaced 0.53 mm apart were used for an overall lateral FOV of 2.1 cm. ParRx tracking used 15 ROEs laterally spaced 1.4 mm apart and 60 tracking locations spaced 0.35 mm apart for a 2.1 cm lateral FOV. LatRx tracking was performed using a single ROE centered laterally, with 60 tracking locations laterally spaced 0.35 mm apart spanning a 2.1 cm lateral FOV. ARF ensembles were acquired using wiperblading, a scanning mode that acquired lines in a non-serial order across the lateral FOV to minimize heating and reduce interference between consecutive ARF excitations. A single ensemble was captured from the far left of the FOV, then the center, then one position to the right of the far left, then one position right of center, etc., such that no two ensembles were captured in two consecutive lateral locations.

One-dimensional normalized cross correlation using an interpolation factor of 4, a search window length of 80 μm , and a kernel length of 376 μm (i.e. 1.5λ , where λ is the wavelength of the tracking pulse assuming a speed of sound of 1540 m/s) was applied to the raw, radio frequency (RF) data ensembles to measure axial motion induced by ARF [206]. ARF displacement profiles were then processed to reject luminal and reverberation signals using a previously described algorithm [247]. The algorithm was also implemented to automatically segment arterial wall tissue. Finally, parametric images were adaptively

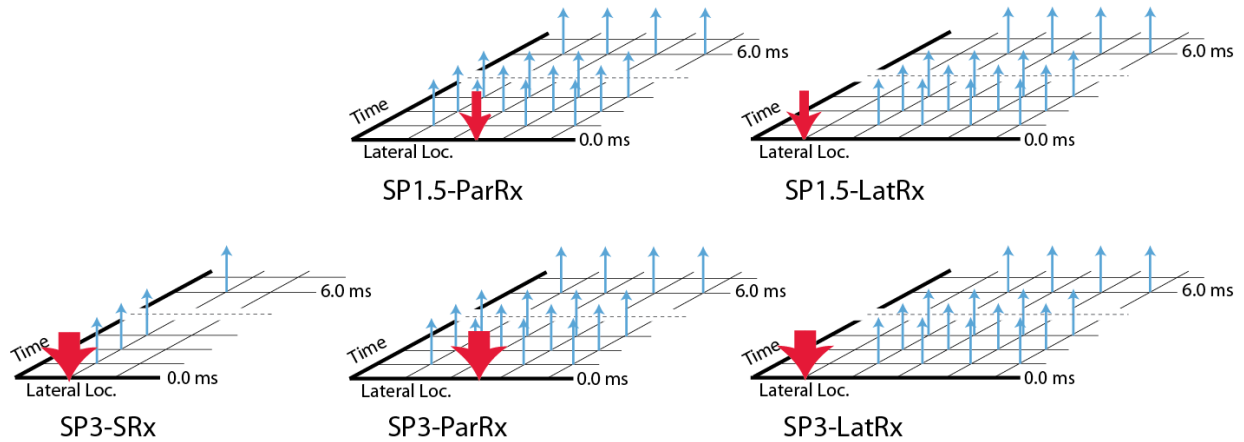


Figure 5.2: Diagrams of the five different ARFI beam sequences that were investigated in ex vivo reader study. Downward arrows represent excitation beams, while upward arrows represent tracking beams. The width of the downward arrows signifies the focal configuration (F/#), with the narrow arrows representing F/1.5 and the wide arrows representing F/3. Figures are not drawn to scale.

rendered by automatically adjusting color scale limits according to the median parameter value measured in the segmented arterial wall (which ranged from zero to median + $[3 \times \text{parameter standard deviation}]$). Rendered parametric images included peak displacement (PD) and recovery time (RT) for non-LatRx sequences and shear wave velocity (SWV) for all LatRx sequences. SWV was calculated using lateral time-to-peak (TTP) methods [189] with least-squares linear regression for regions measuring 0.5 mm axially and 3 mm laterally. Due to this windowing approach and the positioning of the ROE, the effective FOV in the LatRx images was reduced by ~ 6 mm (3 mm lost on the edges from windowing, and 3 mm lost due to the ROE). Matched B-modes were acquired and used for histological registration but were not presented to the readers during the course of the reader evaluation study.

A total of 22 arterial locations were imaged, each using the five different beam sequences with four matched acquisitions per sequence to ensure successful data acquisition. Twelve imaging locations focused on distal and ten on proximal arterial walls (where “proximal” and “distal” are relative to the transducer). The number of imaging locations was determined by the number of areas where plaques developed in the arteries. Due to the spontaneous nature of plaque generation in these animals, it was not

guaranteed that disease would be present in every DH pig; only 6 of the 26 DH arteries yielded plaques that could be imaged, and from these 6 arteries, 10 non-overlapping imaging FOVs, each containing plaques, were acquired. Similarly, 12 non-overlapping “control” data sets were taken from 5 NC arteries. Therefore, data from 11 harvested arteries were included in this study.

Following *ex vivo* imaging, the upper tissue-mimicking phantom was removed, and a biologically inert carbon particle solution (undiluted Carbon Black Dispersate No. 8; Eberhard Faber, Bedminster, NJ, USA) was deposited from a 28-gauge syringe onto the exterior of the proximal arterial wall following the entire length of the transducer. While the carbon was being deposited, the needle was visualized with B-mode to ensure that the particles were co-located with the imaging plane. Approximately 10 deposits were made along the imaging FOV. The nature of the carbon particles was such that they diffused into the outermost adventitial layers of the vessel, making a semi-permanent dark stain that remained even after formalin fixation. This stain served as the marker for the imaging plane, and all sectioning was performed using it as a reference. The carbon particles were both macroscopically visible during sectioning and microscopically visible after histological processing.

5.2.3 Histology

After imaging, arteries were removed from the pressurization apparatus and fixed in 10% buffered formalin. Using the macroscopically visible carbon markings, portions of the arteries corresponding to the imaging plane were cut out with a scalpel and embedded in paraffin for spatially matched histological analysis. The arteries were sectioned and stained with hematoxylin and eosin (H&E), Von Kossa (VK) for calcium, Lillie’s modified Masson’s Trichrome (LMT) for collagen and fibrin, and Verhoeff-Van Gieson (VVG) for elastin. Slides containing the stained sections were digitized using an Aperio Scanscope (Aperio Technologies Inc., Vista, CA, USA) at 20× magnification.

The microscopy images were then divided into four laterally adjacent, equally sized subsections spatially corresponding to four laterally adjacent, equally sized quarters in the ARFI images. A pathologist with experience in atherosclerosis then graded each subsection using the criteria established

Table 5.1: Classification system for atherosclerotic plaques established by the AHA Committee on Vascular Lesions.

Type	Plaque Composition
I	Isolated macrophage foam cells
II	Multiple foam cell layers formed, fatty streak
III	Pre-atheroma with isolated extracellular lipid pools
IV	Atheroma with confluent extracellular lipid core
Va	Fibroatheroma surrounded by fibromuscular tissue layers with lipid or necrotic core (sometimes classified as simply type V)
Vb	Calcification predominates (sometimes classified as Type VII)
Vc	Fibrous tissue changes predominate, absent/minimal lipid core (sometimes classified as Type VIII)
VI	Fissured, ulcerated, hemorrhagic, thrombotic lesion

by the American Heart Association (AHA) Committee on Vascular Lesions (Table 5.1). First, the pathologist graded plaque absence or presence on a 7-point scale, indicating the grade of the plaque when applicable (Table 5.2). If a plaque was present in a given subsection, the pathologist also graded the compositional and structural features of the plaque (including collagen deposition, calcium deposition, degradation of the IEL, the presence of lipid pools, and fibrous caps) on 3- or 5-level scales (Table 5.2). The pathologist’s analysis was facilitated using a custom graphical user interface (GUI) developed in Matlab (Mathworks Inc., Natick, MA, USA). Table 5.3 lists the pathologist’s analysis for the entire data set, which shows the sample sizes in the gold standard used to assess performance.

5.2.4 Reader Training

All 110 parametric image sets (5 beam sequences \times 22 non-overlapping arterial FOVs) were evaluated by 12 trained, blinded readers with varying backgrounds in biomedical imaging and levels of prior experience analyzing ARFI/SWEI images (ranging from less than one year ($n = 7$) to greater than ten ($n = 1$) years). Prior to beginning the study, each reader underwent a training regimen. The readers were given a handout that included a number of items: instructions on the reader graphical user interface

Table 5.2: Rating system used by the pathologist.

Rating Category	Pathologist's Rating Levels						
	Plaque Not Present	Type I	Type II	Type III	Type IV	Type V	Type VI
Collagen	Severe Decrease (>50%)	Mild Decrease (<50%)	No Change	Mild Increase (<50%)	Severe Increase (>50%)	-	-
IEL	Intact	Somewhat Disrupted	Heavily Disrupted	-	-	-	-
Calcium	None	Low	High	-	-	-	-
Lipid Pool	None	Small	Large	-	-	-	-
Fibrous Cap	None	Small	Large	-	-	-	-
Ordinal Value	1	2	3	4	5	6	7

*Ratings were done in a qualitative fashion, i.e. the ratings of “High” and “Low”, or “Large” and “Small”, were subjectively determined by the pathologist rather than being determined by a quantitative measurement. Ratings for collagen were made in regards to the “average” atherosclerotic plaque, e.g. a collagen rating of 2 indicates a mild decrease in the collagen levels relative to an average plaque as judged by the experience of the pathologist. Dashed vertical bars indicate where each rating system was dichotomized to perform ROC analysis (see ‘ROC Analysis’). Ordinal values that are used for statistical analysis are given at the bottom of the table.

(GUI), a brief tutorial on the manifestation of atherosclerosis, examples of images from previous studies with matched histology, and a table of expected responses of ARFI/SWEI parameters for each class of a plaque feature (Table 5.4).

As part of the atherosclerosis tutorial, the readers were told that 1) plaques are generally fibrotic, 2) calcium depositions tend to be focal, and 3) fibrous caps may develop on top of large lipid pools or necrotic regions. Furthermore, the readers were instructed to 1) make no assumptions of the number of plaques in an image, 2) assess each subsection independently of other subsections in an image set, and 3) make no assumptions about mutual exclusion of plaque features (e.g. if calcium is observed, this does not exclude the possibility of a lipid pool or any other feature). Table 5.4 was modeled after a cardiovascular MRI study [98] and modified to reflect ARF-based imaging characteristics. Response predictions for each category were assigned based on published vascular data with matched histology when possible

Table 5.3: Number of plaque types and features as determined by the pathologist collapsed according to the dichotomization thresholds. Each entry represents the number of image subsections under each rating, with each row totaling 88 (22 arterial FOVs × 4 subsections/FOV), the total number of subsections rated by the pathologist.

Rating Category	True Negatives	True Positives
Plaque Detection	<u>None, Type I - II</u> 71	<u>Type III – V(a/b/c)*</u> 17
Collagen	<u>No Plaque Present or Decreased Compared to Average Plaque</u> 65	<u>Comparable or Increased Compared to Average Plaque</u> 23
IEL	<u>Intact</u> 64	<u>Degraded</u> 24
Calcium	<u>Not Present</u> 82	<u>Present</u> 6
Lipid Pool	<u>Not Present</u> 73	<u>Present</u> 15
Fibrous Cap	<u>Not Present</u> 73	<u>Present</u> 15

*The pathologist could rate up to Type VI plaques, but no arteries in this study developed plaques of this type

[208]–[210]. In the cases where no published literature existed, grades were predicted from unpublished preliminary data collected by the authors. Readers were allowed to reference all training materials during the image evaluation without restriction.

5.2.5 Reader Evaluation Study

A custom GUI was developed to show the image sets in a random order to the reader and to save responses to the reader’s hard drive. Upon starting, the GUI loaded the first of 110 image sets displaying the full 2.1 cm FOV captured in each parametric image. The reader was then prompted to assign an overall image quality rating of 1 (“very bad”) to 5 (“very good”) to the set. This perceptual image quality value was later used as an exclusion criterion for reader responses (described further in the section titled

Table 5.4: Expected ARF-induced responses of different plaque features in parametric images, presented to the reader as part of the training regimen.

Tissue Classification	PD	RT	SWV
Collagen Deposition	-	-/0	+
Disrupted IEL	0	+	-/0
Calcium Deposition	-	0	+
Lipid Pool/Necrosis	+++	0	-
Fibrous Cap	-	-/0	+

A ‘-’ indicates that the metric should be low relative to adjacent arterial tissue (i.e. peak displacement of calcium should be relatively low). A ‘+’ indicates that the metric should be high relative to adjacent arterial tissue (i.e. recovery time of a disrupted IEL should be relatively high). A ‘0’ indicates that the metric should remain unchanged. A ‘/’ is used to indicate a situation where two results may occur (i.e. recovery time with collagen deposition may be decreased, or may be unchanged). Multiple symbols, e.g. ‘+++’, indicate that the metric is expected to change substantially.

“ROC Analysis”). Next, a black box outline was overlaid on the parametric images representing the first of four equally spaced subregions (-1.0 cm to -0.5 cm in the lateral dimension). The reader was then asked to assign a rating for plaque presence for the boxed subregion using a five-point scale: 1 (plaque definitely absent), 2 (plaque probably absent), 3 (unsure if plaque absent or present), 4 (plaque probably present), 5 (plaque definitely present). If the reader believed that a plaque was present in a given subregion, she/he was also asked to judge the compositional and structural elements of the plaque (including collagen deposition, calcium deposition, degradation of the IEL, the presence of lipid pools, and fibrous caps). After the reader finished rating the first subsection, the GUI moved the black box to the second of the four subregions (-0.5 cm to 0 cm in the lateral dimension), and the reader was again asked for a rating. This process continued until all four subregions of the image set were rated. Table 5.5 lists the rating system used by the readers and the ordinal numbers associated with each response. As mentioned previously, multiple matched acquisitions were taken. Two of the four acquisitions were selected for each image set and randomized across reader such that six readers read acquisition 1 and six readers read acquisition 2.

Table 5.5: Rating system used by the readers.

Rating Category	Reader's Rating Levels					
Plaque Detection	Plaque Definitely Not Present	Plaque Probably Not Present	Unclear	Plaque Probably Present	Plaque Definitely Present	-
Collagen	Definitely Not Present	Probably Not Present	Unclear	Probably Present	Definitely Present	-
Calcium	Definitely Not Present	Probably Not Present	Unclear	Probably Present	Definitely Present	-
Lipid Pool	Definitely Not Present	Probably Not Present	Unclear	Probably Present	Definitely Present	-
IEL	Definitely Intact	Probably Intact	Unclear	Probably Disrupted	Definitely Present	-
Fibrous Cap	Not Present	Definitely Intact	Probably Intact	Unclear	Probably Disrupted	Definitely Disrupted
Ordinal Value	1	2	3	4	5	6

5.2.6 ROC Analysis

The performance of different beam sequences to detect and materially characterize atherosclerotic plaques was evaluated using receiver operating characteristic (ROC) curve analysis, with area under the curve (AUC) used as a metric of performance. A detailed description of ROC calculation from ordinal reader responses is given in Section 5.6 along with an example from the data set. Briefly, the ROC analysis was performed by first dichotomizing the pathologist's response into "case" (feature is present) and "control" (feature is absent) groups for each plaque feature. Next, frequencies of ordinal reader responses were organized along pathologist ratings of "case" or "control". The "case" and "control" rows in this frequency table were then assumed to be discrete random variables latently distributed as normal distributions, and the parameters of these distributions were estimated with maximum likelihood estimation (MLE) and AUC values were calculated. Following the multi-reader methods of [39],

summary ROC curves were created for sequences with the highest AUC values, and “optimal” operating points were chosen from the median summary curves to report sensitivity and specificity. The operating point was selected by maximizing the sum of sensitivity and specificity. Image sets that were rated by readers as having an image quality of “Very Bad” or “Bad” were excluded from the ROC analysis. ROC computation was performed using the R programming language and development environment (R Foundation for Statistical Computing, Vienna, Austria).

To test for performance differences between beam sequences, pairwise Wilcoxon rank sum tests were performed on the resulting distributions of AUCs. To assess inter-reader variability for a given beam sequence and feature, pairwise Spearman’s rank correlation coefficients (SCC) were computed for every reader combination. Finally, to highlight the impact of reader experience, the AUC of Reader 1 (the most experienced reader in the study) was compared to the median AUC for a given beam sequence by subtracting the median from Reader 1’s AUC.

5.3 Results

The results for plaque detection are presented first, followed by the results for the five plaque components investigated for plaque characterization (calcium, lipid pools, fibrous caps, degraded IEL, and collagen). The responses of one reader were excluded from the results because she/he did not fully complete the evaluation. Finally, due to the large number of beam sequences and plaque features, ROC curves are not shown for brevity.

5.3.1 Plaque Detection

Figure 5.3(a) shows boxplots of AUC and SCC for plaque detection across all five beam sequences. SP3-SRx yielded the highest median AUC (0.899) for plaque detection, followed by SP1.5-ParRx (0.854). Summary ROC curve analysis for this sequence showed an optimal operating point corresponding to a sensitivity of 0.847 and a specificity of 0.791. The two LatRx sequences (SP3-LatRx and SP1.5-LatRx) had the two lowest median AUCs (0.771 and 0.758, respectively), but had large IQRs and were not statistically different from SP3-SRx, the highest median AUC sequence. Mean shear wave

group velocity was 6.6 ± 1.1 m/s (range: 4.4 – 8.1 m/s) in control arteries, and 6.7 ± 2.6 m/s (range: 4.0 – 13.2 m/s) in disease arteries. SP3-SRx also had the highest SCC between readers with a median value of 0.583.

It is important to note that the dichotomization threshold used for the plaque detection ROC analysis was Type III plaques (i.e. plaques rated as Type I or Type II were counted as true negatives). Therefore, the AUCs reported in Figure 5.3(a) are only valid for plaques of Type III (pre-atheroma) and above. Performance was compromised when the threshold was set to include Type I (isolated macrophage foam cells) and Type II (fatty streaks) plaques, with the highest median AUC dropping to 0.612. This suggests that beam sequences used in this study do not perform well at detecting the earliest stages of plaque formation.

5.3.2 Plaque Characterization

The median beam sequence AUCs for calcium detection ranged from 0.914 to 0.779 (Figure 5.3(b)). SP1.5-LatRx had the highest median AUC of 0.914, but was also seen to have a high IQR, and was not statistically different from any of the other sequences. SP3-SRx had the second highest median AUC of 0.892, but had a much smaller IQR and was statistically different from SP3-ParRx ($p < 0.009$). The summary ROC curve for SP3-SRx showed generally high performance for calcium detection, with an optimal operating point for the “average” reader at 0.964 sensitivity and 0.852 specificity. The median (25th and 75th percentiles) SCC across all sequences was 0.56 (0.36 - 0.66). The AUCs for Reader 1 were, on average, substantially lower than the medians for each beam sequence (by 19.6 percentage points). Reader 1’s AUC with SP3-SRx (52.0 percentage points lower than the median), was a considerable outlier despite the sequence having the highest median AUC for calcium detection across all the readers. Examples of plaques with calcium are shown in Figure 5.4(a) and (b).

The median beam sequence AUCs for lipid pool detection ranged from 0.888 to 0.726 (Figure 5.3(c)). SP3-SRx had the highest median AUC of 0.888 and was statistically different from SP1.5-LatRx ($p < 0.04$). The summary ROC curve for SP3-SRx lipid pool/necrotic core detection showed an optimal

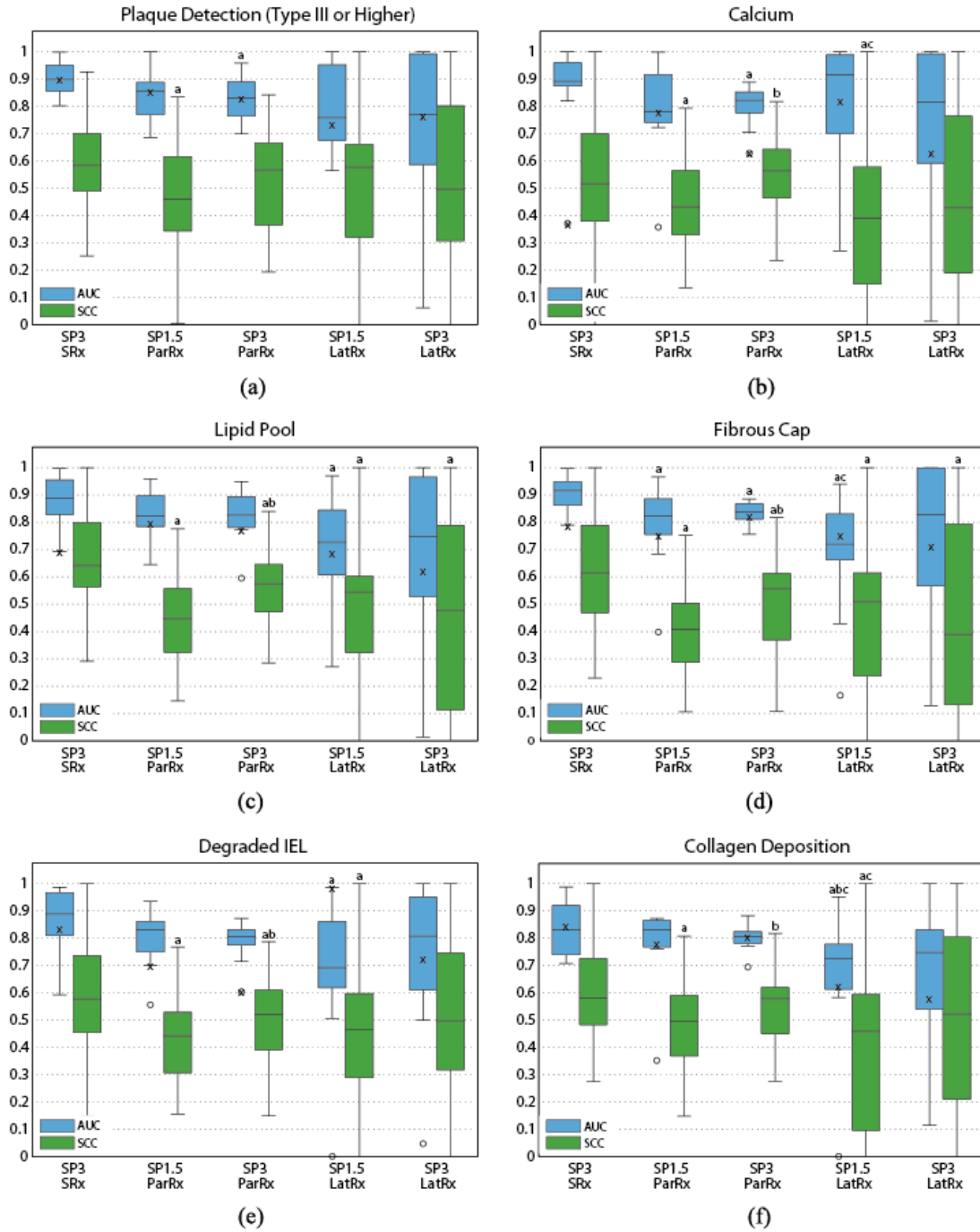


Figure 5.3: Boxplots of AUC and SCC vs. beam sequence for plaque detection and individual plaque features: calcium, lipid pool, fibrous cap, degraded IEL, and collagen deposition. Whiskers represent the highest and lowest data points still within 1.5 IQR, and outliers are depicted with circles. AUC value of the most experienced reader is indicated with an 'x'. Letters 'a' through 'g' are used to indicate statistical differences ($\alpha = 0.05$), where each letter identifies the sequence for comparison (a = SP3-SRx, b = SP1.5-ParRx, c = SP3-ParRx, d = SP1.5-LatRx, e = SP3-LatRx). Sequences marked with multiple letters were statistically different from multiple sequences.

operating point for the “average” reader at 0.797 sensitivity and 0.857 specificity. The median (25th and 75th percentiles) SCC across all sequences was 0.56 (0.39 - 0.67). The AUCs for Reader 1 were, on average, slightly lower than the medians for each beam sequence (8.8 percentage points). Examples of plaques with lipid pools are shown in Figure 5.4(a) and (b).

The median beam sequence AUCs for fibrous cap detection ranged from 0.916 to 0.721 (Figure 5.3(d)). SP3-SRx had the highest median AUC of 0.916, followed by SP1.5-ParRx with a median AUC of 0.825. The SP3-SRx sequence was statistically different from every other sequence ($p < 0.03$) except SP3-LatRx. The summary ROC curve for SP3-SRx showed an optimal operating point for the “average” reader at 0.855 sensitivity and 0.819 specificity. The median (25th and 75th percentiles) SCC across all sequences was 0.50 (0.32 - 0.64). The AUCs for Reader 1, as with lipid pools, were, on average, slightly lower than the medians for each beam sequence (by 5.9 percentage points).

The median beam sequence AUCs for degraded IEL detection ranged from 0.889 to 0.692, with SP3-SRx having the highest median AUC (Figure 5.3(e)) and being statistically different from SP1.5-LatRx. The corresponding summary ROC curve for the “average” reader using a SP3-SRx sequence revealed a sensitivity of 0.916 and specificity of 0.754 for detecting degraded IEL. The median (25th and 75th percentiles) SCC across all sequences was 0.49 (0.34 - 0.63). The AUCs for Reader 1 varied considerably around the corresponding median AUC value for each beam sequence. For SP1.5-LatRx, Reader 1’s AUC was very high, 0.986 (29.3 percentage points higher than the median), but low for SP3-SRx, 0.603 (20.2 percentage points lower than the median). An example of a plaque with a degraded IEL and heavy collagen deposition is shown in Figure 5.4(c).

The median beam sequence AUCs for collagen deposition detection ranged from 0.832 to 0.726 (Figure 5.3(f)). SP1.5-ParRx had the highest median AUC but was followed closely by SP3-SRx, and SP3-ParRx, all of which were statistically different from the lowest median AUC sequence (SP1.5-LatRx). The summary ROC curve for SP1.5-ParRx showed an optimal operating point for the “average” reader at 0.784 sensitivity and 0.765 specificity. The median (25th and 75th percentiles) SCC across all sequences was 0.54 (0.38 - 0.65). The AUCs for Reader 1 were, on average, slightly lower than the

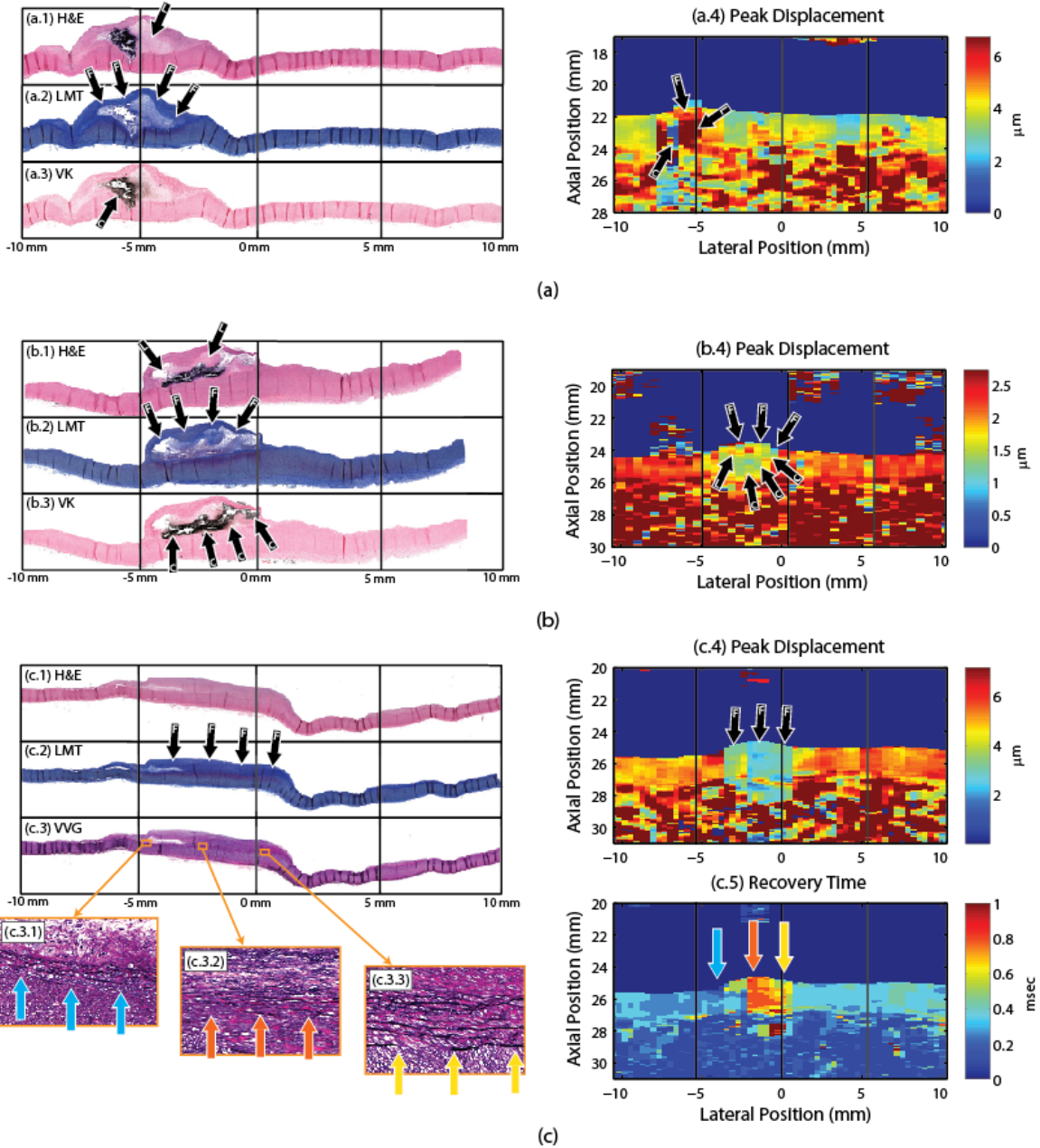


Figure 5.4: Three examples of ARFI images with matched histology. Stains include hematoxylin and eosin (H&E) (shown in (a.1), (b.1), and (c.1)); Lillie's modified Masson's trichrome (LMT) staining collagen blue (shown in (a.2), (b.2), and (c.2)); Von Kossa (VK) staining calcium black (shown in (a.3) and (b.3)); and Verhoeff-Van Gieson (VVG) staining elastin black (shown in (c.3)). Black arrows are used to indicate plaque features (C = calcium, L = lipid, F = fibrous cap or fibrosis). In (a), an advanced Type Vb atheroma is seen with a large calcium deposit located to the left part of a lipid pool. In (b), an advanced type Vb atheroma is seen with a large calcium deposit underneath a small lipid pool and fibrous cap. In (c), a type IV plaque is shown with significant collagen deposition and degradation/duplication of the IEL.

Table 5.6: Comparison of ARF beam sequence sensitivity and specificity for plaque detection and characterization (measured *ex vivo* in porcine femoral arteries under simulated *in vivo* conditions) versus published sensitivity and specificity for MRI and CT (measured *in vivo* in human carotids) [3], [248].

	ARF-Based Ultrasound		CT		MRI	
	<i>(Ex vivo, porcine femoral)</i>		<i>(In vivo, human carotid)</i>			
	Sensitivity	Specificity	Sensitivity	Specificity	Sensitivity	Specificity
Detection						
Type III-Va,b,c	85%	79%	-	-	80-84%	90-98%
Type unreported	-	-	88-95%	90-96%	-	-
Characterization						
Calcium	96%*	85%*	100%	100%	76-80%	86-94%
Lipid/necrotic	80%*	86%*	76%	74%	91-98%	65-100%
Fibrous cap	86%*	82%*	-	-	81%	90%
Degraded IEL	92%*	75%*	-	-	-	-
Collagen	78%†	77%†	86%	94%	-	-

Values marked with ‘*’ are reported from SP3-SRx sequence results. Values marked with ‘†’ are reported from SP1.5-ParRx sequence results.

medians for each beam sequence (6.1 percentage points). Reader 1’s AUCs for SP1.5-LatRx and SP3-LatRx were the furthest from the median, at 10.1 and 16.9 percentage points lower, respectively.

To give the results of this study context to the field of atherosclerosis imaging, ARFI performance numbers (*ex vivo* in porcine femoral arteries) are loosely compared in Table 5.6 to published numbers for two other non-invasive atherosclerosis imaging modalities where the data was taken *in vivo* in human carotid arteries: MRI, and X-ray CT [3], [248].

5.3.3 Image Exclusions

Out of 1210 image set readings (22 arteries × 5 beam sequences × 11 readers), 432 were excluded by reader assessment of perceptual image quality, resulting in an overall exclusion fraction of 0.357.

Figure 5.5(a) shows the image exclusion fraction by artery. The median exclusion fractions for control

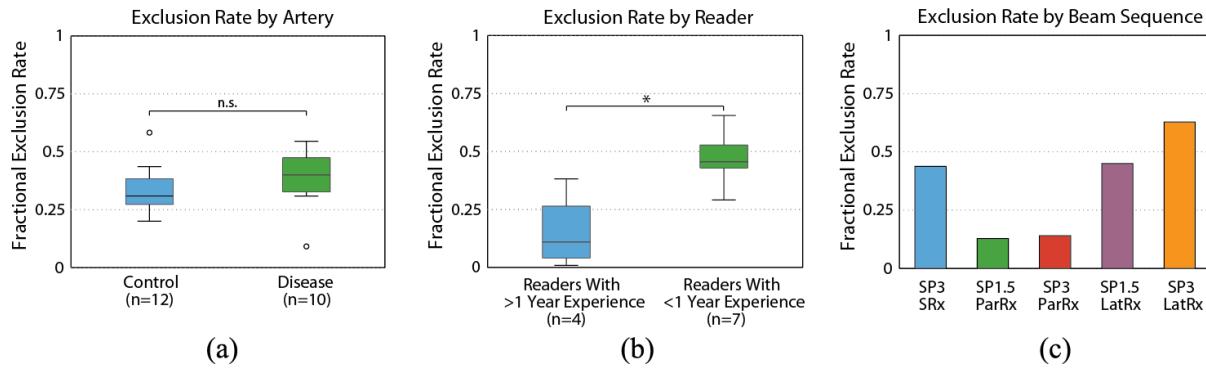


Figure 5.5: Image exclusion results. (a) Fractional image exclusion rate versus artery. The exclusion rate for control arteries was not statistically different ($p > 0.11$) from the exclusion rate for disease arteries. (b) Fractional image exclusion rate versus readers. The exclusion rate for readers with less than 2 years of experience was statistically higher from the exclusion rate for readers with greater than 2 years of experience ($p < 0.02$). Note that Reader 1 was the most experienced reader and had the lowest fractional exclusion rate, 0.007. (c) Fractional image exclusion rate versus beam sequence.

and diseased arteries were similar, at 0.309 and 0.400 respectively, and these groups were not statistically significantly different ($p > 0.11$). Figure 5.5(b) shows the image exclusion rate by reader. The median exclusion fractions for readers with greater than one year of experience and less than one year of experience were substantially different, 0.109 and 0.455 respectively, and these groups were statistically significantly different ($p < 0.02$). Figure 5.5(c) shows the image exclusion rate by beam sequence. SP3-LatRx had the highest exclusion fraction (0.628), while the SP1.5-ParRx had the lowest exclusion fraction (0.128).

5.4 Discussion

Comparing the distributions of AUC values achieved by the readers (Figure 5.3), a number of observations can be made about the performance of different beam sequences for detecting and materially characterizing atherosclerotic plaques. Overall, the F/# of the excitation pulse did not have much of an impact on readers' AUCs for plaque detection or characterization. A large F/# excitation when tracking within the ROE could be beneficial for two reasons: first, the shearing in the tracking resolution cell would be reduced, improving displacement underestimation [230]; and second, the axial range over which

the displacement is constant would be increased [241]. In this study though, there was no statistically significant differences in AUC performance for plaque detection or component characterization between the F/1.5 and F/3 parallel-receive tracking sequences (SP1.5-ParRx and SP3-ParRx). In combination with displacement tracking lateral to the region of excitation to observe shear wave propagation, F/1.5 and F/3 also did not have statistically different AUCs. Similar to the within-ROE tracking case, a larger F/# with lateral tracking could be advantageous because it would increase the axial range over which the shear wave is travelling parallel to the arterial wall. The lateral time-to-peak algorithm used to measure shear wave group velocity in this study assumed that the shear waves propagate parallel to the lateral dimension, an assumption more quickly violated with a more focused excitation [189]. In this study though, axial range likely was not a factor because none of the plaques exceeded ~2 mm in thickness, which could explain the lack of statistical differences in AUCs between F/1.5 and F/3.

The investigation of different tracking methods centered on two main questions: 1) what is the impact on performance of single versus parallel-receive tracking and 2) what is the performance of shear wave tracking lateral to the region of excitation? Parallel-receive tracking (ParRx), in which four tracking lines are simultaneously beamformed in positions centered around the region of excitation (ROE), results in slightly poorer lateral resolution and CNR relative to single-receive tracking (SRx) [242], [249]. This loss of resolution is attributable to both the widening of the tracking point spread function (PSF) and the increased beam spacing with fewer ARF excitations that, ultimately, could negatively affect the detection of small, focal features, such as small calcifications. Despite these drawbacks, the readers achieved comparable AUCs with parallel-receive sequences as compared to the single-receive sequences; for lipid pools, degraded IEL, and collagen neither SP1.5-ParRx nor SP3-ParRx was statistically different from SP3-SRx, the highest median AUC sequence, and for calcium and overall plaque detection, only one of the two parallel-receive sequences was statistically lower. Only in the case of fibrous caps were both parallel-receive sequences statistically significantly lower than SP3-SRx. Given that single-receive tracking did not appear to have a large impact on reader AUC, parallel-receive tracking may be favored

due to the factor of four reduction in incident acoustic energy and up to a factor of four increase in frame rate.

For lateral receive tracking, the results of this study showed that in the case of calcium, a stiff material, AUCs were not statistically significantly different from the sequence with the highest sensitivity and specificity. However, in the case of lipid pools, a soft material, the LatRx sequences exhibited relatively low AUC performance. Lipid pools are generally comprised of water, phospholipids, cholesterol monohydrate (present as plate-like crystals), and cholesterol esters (present as oils) [250], [251], and exist in either liquid or liquid-crystalline form, which may not support shear wave propagation. Therefore, poor LatRx performance in lipid regions may be related to inhibited shear wave propagation through the lipid region. Further studies are needed to understand the shear wave dynamics in such media.

While the AUC results presented in this study may indicate that SWV images yielded lower sensitivity and specificity, the sequence implementation must be taken into careful consideration. In both LatRx sequences, the FOV was significantly reduced compared to the within-ROE sequences due to two design choices. First, to measure SWV with more accuracy, a sliding window of ~ 3 mm (laterally) was used, meaning that 1.5 mm was lost from the left and right edges of the image from windowing. Second, the ROE, which was located in the center of the FOV in this case, was not moved during the sequence and, consequently, no SWVs were measured within it, reducing the FOV by an additional 2-3 mm. On top of the FOV reduction, the LatRx image sets were seen to have smaller magnitude displacements achieved away from the region of ARF excitation (due to high levels of shear wave attenuation), yielding noisy velocity measures near the edges of the image. As derived from the Cramér-Rao Lower Bound [223], the magnitude of jitter error for the imaging parameters used in this study was estimated to be ~ 0.75 μm (assuming 50% fractional bandwidth, 0.999 correlation coefficient, and 30 dB SNR). In the LatRx data, displacements at the edges of the image (8 mm laterally from the ROE) were measured to be ~ 1 μm , suggesting that the SWV values plotted on the edge of the FOV were calculated from displacement just above the absolute lower bound of the displacement tracking algorithm. Finally, it should be noted that shear wave reflections and the irregular boundary conditions created by the lesions may have impacted

the time-to-peak estimates (and consequently the SWV measurements) drastically [252]. More sophisticated shear wave excitation techniques such as supersonic shear imaging (SSI) or signal processing techniques such as directional filtering could have improved the LatRx images and subsequently the AUCs achieved by the readers with these sequences [187], [195], [253].

It is interesting that, while the mean shear wave group velocity between control and diseased arteries was not statistically different, the standard deviation and range of group velocities was larger for diseased arteries. Direct artery-to-artery comparisons of SWVs can be confounded by variables such as pre-tension [254] and wall thickness [195], therefore an in-depth analysis of SWV as it pertains to plaque detection and material and structural characterization was outside the scope of this manuscript.

Table 5.6 shows a comparison of the sensitivities and specificities of the highest median AUC sequence to two other non-invasive atherosclerosis-imaging modalities, MRI and CT. While the ARF-based approaches described here interrogate the mechanical properties of arteries to delineate plaque, MRI evaluates the nuclear magnetic resonance properties, and CT exploits x-ray attenuation properties [255]. Another important difference between the ARFI, MRI and CT data presented in Table 5.6 is that the CT and MRI performance numbers are reported for *in vivo* human carotid arteries, while the ARFI numbers are reported for *ex vivo* porcine femoral arteries under simulated *in vivo* imaging conditions. Therefore, the comparison in Table 5.6 is shown simply to give the results in this study context to the field of non-invasive atherosclerosis imaging and highlight the current state of the art. CT performs well for hard features (calcium, collagen), but does not do as well for soft features (lipid pools), while MRI has the reverse trend, leading experts [3] to conclude that MRI may be more promising to stratify the vulnerability of a plaque to rupture. Comparing the performance numbers for ARFI, it appears that ARFI is most sensitive to calcium deposits, but is also generally sensitive to soft components such as lipid pools. ARFI also had high sensitivity for detecting degraded IEL, which was particularly interesting because this feature is not currently detectable by other imaging modalities. As noted previously [210], degradation of the IEL appears to change the elastic properties of the arterial wall substantially. Therefore, although the actual feature is far below the resolution of the imaging system, the IEL's impact

on mechanical properties is detectable and could prove to be an important advantage of using ARF-based elastography techniques.

On average, the inter-reader agreement across all beam sequences and plaque features in this study was moderate. The median SCCs ranged from 0.641 (SP3-SRx, lipid pools) down to 0.390 (SP3-LatRx, fibrous caps), with generally large IQRs across all sequences. As expected from the high AUC values, SP3-SRx had the best inter-reader agreement, with SCCs being statistically higher than most other sequences for any given feature (in the case of lipid pools and fibrous caps, SCCs for SP3-SRx were statistically higher than all other sequences). The variability of the SCCs was most likely a consequence of the range of experience levels between the readers, with seven out of the eleven readers having never seen an ARFI image before the training regimen. For these readers, the training regimen was largely responsible for their performance, and readers had to rely heavily on the guidance table (Table 5.4) when interpreting images. Since ARF-based atherosclerosis imaging is a relatively new field, the training set was limited to one or two examples of each compositional element with one or two beam sequences. Providing training that is more comprehensive for the readers would likely improve the readers' ability to accurately characterize atherosclerotic plaques and reduce inter-reader variability.

Another interesting observation regarding reader experience was that the most experienced reader, Reader 1, had an equal or lower AUC than the median for most beam sequence and plaque feature combinations (Figure 5.3). One explanation for this phenomenon is that Reader 1 rated more of the “poor quality” images than the inexperienced readers, and therefore had a more challenging task. As seen in Figure 5.5(b), the experienced readers had a significantly lower exclusion rate compared to the inexperienced readers; in fact, out of the experienced readers, Reader 1 had the lowest exclusion rate, excluding only 1 out of 110 images. This suggests that as a reader gains experience, she/he is able to make relatively accurate assessments on images that an inexperienced reader would not be able to read.

It would be expected that *in vivo* sensitivity numbers may initially be poorer than those reported in this study due to a number of physiological challenges (motion artifact, intraluminal pressure variation, oblique imaging perspectives, increased imaging depths in obese patients, etc.), but with the development

of real time ARFI imaging solutions [244], clever beam sequencing [243], [256], and improvements to motion filtering [221], [222] equal or better sensitivities may be achievable.

Finally, due to the extreme complexity and heterogeneity of the atherosclerotic disease process, a larger study than this would provide the possibility of performing a more robust statistical analysis of detection of all compositional elements. The arteries included in this analysis provided a broad spectrum of atherosclerotic manifestations, but a wide range of possibilities was not represented. For example, this analysis did not include arteries with intra-plaque hemorrhage or ruptured plaques, preventing any assessment of beam sequence performance for detecting thrombus formation. A recent review concluded that thrombi forming at the sites of plaque rupture have an important role in promoting the rapid progression of the underlying lesion which can lead to future ischemic events [11]. Therefore, performance for detecting thrombus and plaque hemorrhage should be assessed. This study also did not quantify the effect of lesion size on reader performance. It has previously been shown that the resolution limit of transcutaneous ARFI ultrasound is generally between 0.5 to 1.0 mm, depending on the imaging parameters used and the underlying mechanical properties of tissue [257]. These numbers though, were derived from experiments done in phantoms and porcine liver, so their pertinence to heterogeneous tissue such as atherosclerotic plaque is unclear. Quantifying the resolution limits of ARFI on features and structures in plaques is further explored in Chapter 7.

5.5 Conclusion

Based on the sensitivity and specificity numbers calculated in this *ex vivo* study, ARF-based ultrasound has been demonstrated to be relevant for detecting type III and higher plaques in peripheral vasculature, and for characterizing plaque features such as calcium and collagen deposits as well as lipid pools and fibrous caps (the latter two features being linked to plaque vulnerability). This study also showed that ARFI is relevant for detecting degraded IEL, while no other imaging method has been demonstrated in this regard. As such, degraded IEL detection may prove to be a significant advantage of ARF-based imaging. Furthermore, this study demonstrated that 1:1 single-receive tracking yielded the

highest median AUC values for plaque detection and for delineating all of the compositional elements evaluated. In many cases though, AUCs from the 4:1 parallel-receive sequences were comparably high and not statistically significantly different from the single-receive tracking sequence, suggesting these sequences may be preferred for *in vivo* application due to their improved frame rate and lower energy requirements. ARF-based imaging modalities are relatively facile, as even relatively unskilled readers achieved high performance marks, but more extensive reader training may improve AUC values further. Overall, these results add to the growing body of evidence that suggests ARF-based imaging is relevant to detecting plaques and describing their composition and structure with potential application to diagnosis, monitoring, and assessment of lipid lowering treatment efficacy.

5.6 Addendum

5.6.1 ROC Calculation

The general setting and notation of the ROC calculation can be described as follows. There are I blinded readers involved, indexed by $i = 1, 2, \dots, I$; J images involved, indexed by $j = 1, 2, \dots, J$; and K subsections involved, indexed by $k = 1, 2, \dots, K$, that represent the number of sections into which each image is broken. The value $X_{i,j,k}$ will represent the evaluation of the i^{th} reader on the k^{th} subsection of the j^{th} image. On the histological side, a similar labeling scheme is used; $Y_{j,k}$ denotes the histological evaluation on the k^{th} section of j^{th} image, which represents the gold standard. For this study, one pathologist was recruited to read the gold standard histology slides so the i^{th} indexing is omitted for simplicity for Y .

Recall from the section titled “Reader Evaluation Study”, each reader rated features on a graded scale that has a naturally increasing order (e.g. “Definitely Not Present”, “Probably Not Present”, “Unclear”, “Probably Present”, “Definitely Present”). To represent these rating levels numerically, each is assigned a monotonically increasing integer; the possible values of $X_{i,j,k}$ are $1, 2, \dots, n$, where a value of 1 is equivalent to a “Definitely Not Present” response, a value of 2 is equivalent to a “Probably Not Present” response, etc. Similarly, the pathologist’s ratings, $Y_{j,k}$, are represented numerically as $1, 2, \dots, m$.

It is important to note that values of m and n (i.e. the maximum possible value for $Y_{j,k}$ and $X_{i,j,k}$, respectively) are not necessarily the same, and depend on the feature that is being rated (e.g. for calcium, $m = 3$ and $n = 5$).

To begin the ROC calculation, all pairs of $(X_{i,j,k}, Y_{j,k})$ are organized into an m -by- n frequency table, which represents the histogram of reader responses given the corresponding histological responses. Next a threshold, t , is chosen on $Y_{j,k}$ to dichotomize the m levels of the gold standard into “control” and “case” classes. In other words, a $Y_{j,k}$ value less than or equal to t means the k^{th} section of the j^{th} image does not have the feature in question; whereas a $Y_{j,k}$ value greater than t means the k^{th} section of the j^{th} image does have the feature present. After dichotomization, the m -by- n table becomes a 2-by- n table.

Following Ch. 4.2.2 of [258] the two rows of the frequency table are considered as two discrete random variables latently distributed as normal distributions (referred to as Z_1 and Z_2 for “control” and “case” respectively), whose parameters can be determined with maximum likelihood estimation (MLE). The correspondence between the discrete $X_{i,j,k}$ distribution and the continuous normal distributions is described by $n-1$ parameters, or cuts, (referred to as c_1, c_2, \dots, c_{n-1}) which can take on any value between $-\infty$ to ∞ . Without loss of generality, Z_1 can be assumed to have zero mean ($\mu_1 = 0$) and standard deviation of 1 ($\sigma_1 = 1$) by rescaling the $n-1$ cuts appropriately. This assumption does not change the discrete probability mass distribution of $X_{i,j,k}$, and consequently, Z_2 can be described as a function of $\mu_2, \sigma_2, c_1, c_2, \dots, c_{n-1}$, and solved for by maximizing the log-likelihood function:

$$\begin{aligned} \log(L(\mu_2, \sigma_2, c_1, \dots, c_{n-1})) = & \\ E11 * \log(\Phi(c_1; \mu = 0, \sigma = 1)) + E12 * \log(\Phi(c_2; \mu = 0, \sigma = 1) - \Phi(c_1; \mu = 0, \sigma = 1)) + \dots + E1n * \log(1 - \Phi(c_{n-1}; \mu = 0, \sigma = 1)) + & \quad (A.1) \\ E21 * \log(\Phi(c_1; \mu = \mu_2, \sigma = \sigma_2)) + E22 * \log(\Phi(c_2; \mu = \mu_2, \sigma = \sigma_2) - \Phi(c_1; \mu = \mu_2, \sigma = \sigma_2)) + \dots + E2n * \log(1 - \Phi(c_{n-1}; \mu = \mu_2, \sigma = \sigma_2)) & \end{aligned}$$

where $\Phi(x; \mu, \sigma)$ is the cumulative distribution function (CDF) of the normal distribution, and the $E_{m,n}$ variables represent the frequency counts of reader responses. The resultant parameter estimates are denoted as $(\hat{\mu}_2, \hat{\sigma}_2, \hat{c}_1, \dots, \hat{c}_{n-1})$ and from these parameters a continuous ROC curve can be drawn based on $\hat{\mu}_2$ and $\hat{\sigma}_2$.

Note that this statistical analysis assumes all subsections as independent, but, due to the study design, not all subsections are truly independent from each other. Although readers were asked to rate each subsection independently of any other subsection, readers viewed each arterial segment in its entirety while rating each of the four individual subsections. This means that there is an inherent correlation structure in the reader response data, as readers most likely rated plaques based on information from adjacent subsection. Therefore, the rationale for assuming independence needs to be justified as this assumption was made in this study.

Mathematically, the correlation structure between subsections in an MLE operation would be represented as follows (in a simple example where MLE is being used to estimate the mean, μ , from some number of observations, $\{Y_i\}_{i=1}^n$):

$$\frac{d}{d\mu} \log(L(\mu)) = -\frac{1}{\sigma^2} \left\{ \frac{d}{d\mu} [Y_1 - \mu \quad \cdots \quad Y_n - \mu] \right\} \begin{bmatrix} 1 & 0 & \cdots & 0 \\ & 1 & \cdots & 0 \\ & & \ddots & \vdots \\ & & & 1 \end{bmatrix}^{-1} \begin{bmatrix} Y_1 - \mu \\ \vdots \\ Y_n - \mu \end{bmatrix} = 0 \quad (\text{A.2})$$

The center matrix represents the “correlation structure” between 4 subsections viewed simultaneously. Unfortunately, quantifying the true correlation structure in a study where human observers are looking at images is difficult because each reader combines information in a unique and subjective way. In the ROC analysis presented in this manuscript, the correlation structure matrix is set to the identity matrix to indicate observations are independent from each other. Statistical theory indicates that using the identity matrix (i.e. assuming independence) can still achieve a *consistent* estimate of μ_2 and σ_2 (if the true correlation structure was known, the estimate of μ_2 and σ_2 would be *consistent* and *efficient*), as the correlation structure mostly affects more subtle statistics like the variance of $\hat{\mu}_2$ and $\hat{\sigma}_2$ [259].

5.6.2 ROC Example

To demonstrate these methods, the AUC will be calculated for Reader 5 using beam sequence SP3-ParRx to identify lipid pools. The m -by- n frequency table depicting reader response vs. pathologist response is as follows (Note: Reader 5 rated one image set as having “Bad” image quality, so responses

Table 5.7: Reader response for lipid pools versus pathologist response.

Pathologist Response	Reader 5 response				
	Def. Not Pres. ($X=1$)	Prob. Not Pres. ($X=2$)	Unclear ($X=3$)	Prob. Pres. ($X=4$)	Def. Pres. ($X=5$)
None ($Y=1$)	42	15	0	12	0
Small ($Y=2$)	1	0	0	8	1
Large ($Y=3$)	0	0	0	5	0

for only 84 subsections are given, out of a maximum of 88): see Table 5.7. The next step is to dichotomize the pathologist’s responses. In the case of lipid pools, the pathologist used a 3-point scale (1 – no lipid pool, 2 – small lipid pool, and 3 – large lipid pool), and the threshold was chosen such that $t > 1$, indicating that both small and large lipid pools would be counted as “positives”, as shown in Table 5.8.

Finally the distributions Z_1 and Z_2 are estimated; μ_1 and σ_1 are assumed to be 0 and 1 respectively, and $\hat{\mu}_2$ and $\hat{\sigma}_2$ are calculated to be 4.52 and 2.57, respectively, from MLE. These distributions are depicted graphically in Figure 5.6(a). Note that the area under the ROC curve (AUC) can be computed at this point without actually plotting the ROC curve itself as the AUC is defined as the $P(Z_2 > Z_1)$. Once the distributions are known, a continuous ROC curve can be plotted by sliding the decision threshold (indicated by a vertical line in Figure 5.6(a)), and computing the false positive rate (FPR, the x-axis of the ROC curve) and the true positive rate (TPR, the y-axis of the ROC curve). The FPR is given as the probability that Z_1 is greater than the decision threshold, while the TPR is given as the probability that Z_2 is greater than the decision threshold. The continuous ROC curve is depicted in Figure 5.6(b), with an AUC value of 0.95.

Table 5.8: Reader response for lipid pools versus dichotomized pathologist response.

Pathologist Response	Reader 5 response				
	Def. Not Pres. ($X=1$)	Prob. Not Pres. ($X=2$)	Unclear ($X=3$)	Prob. Pres. ($X=4$)	Def. Pres. ($X=5$)
None ($Y=1$)	42	15	0	12	0
Small or large ($Y=2,3$)	1	0	0	13	1

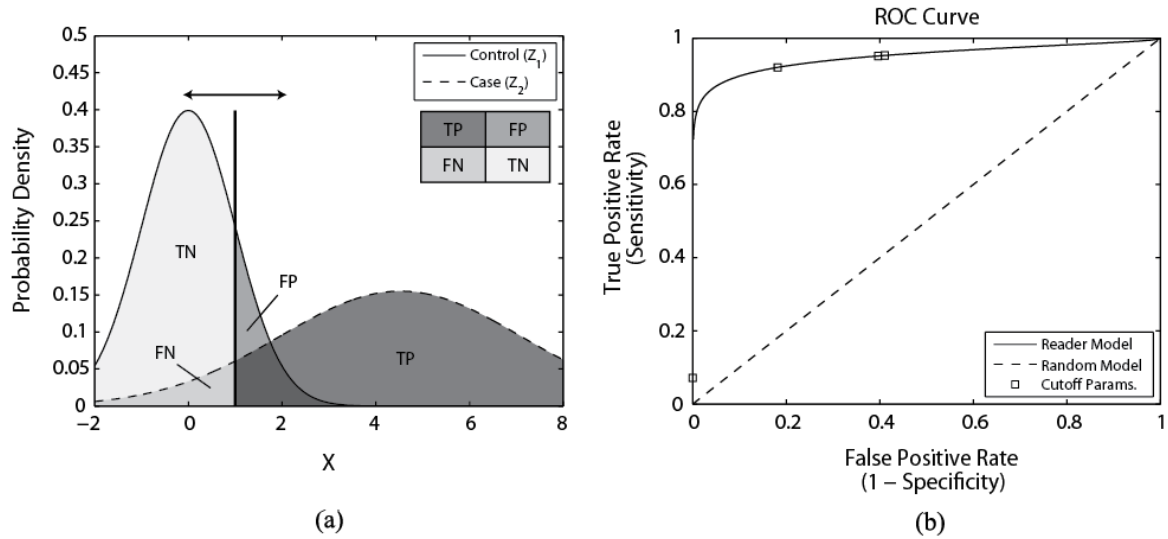


Figure 5.6: Example of ROC curve calculation. (a) Estimated normal distributions representing the variables “control” (Z_1) and “case” (Z_2) which depict Reader 5’s responses for lipid pools using SP3-ParRx. For the Z_1 distribution, the mean (μ_1) and standard deviation (σ_1) were assumed to be 0 and 1 respectively. For the Z_2 distribution the mean and standard deviation were estimated by maximum likelihood estimation (MLE) as follows; $\hat{\mu}_2 = 4.52$ and $\hat{\sigma}_2 = 2.57$. The vertical line represents one possible decision threshold and the corresponding regions of the two distributions are labeled accordingly (TN – true negative, FN – false negative, FP – false positive, TP – true positive). An ROC curve is computed by sliding the decision threshold along the X-axis to compute both false positive rate (FPR) and true positive rate (TPR). (b) Corresponding ROC curve depicting Reader 5’s performance using beam sequence SP3-ParRx to identify lipid pools. The result for the reader is depicted as a solid line, while the result for a random classifier is depicted as a dashed line. The discrete operating points (estimated with MLE) are depicted as square boxes plotted on top of the reader curve. In this case, the area under the curve is 0.95.

CHAPTER 6

ARFI-Derived Carotid Plaque Stiffness Measurements Compared with Histology I: Preliminary Results

The following chapter presents *in vivo* ARFI images taken from four patients undergoing clinically indicated carotid endarterectomy and compared to histology in case-study format. In two type Va plaques, characterized by lipid/necrotic cores covered by fibrous caps, mean ARFI displacements in focal regions were high relative to the surrounding plaque material, suggesting soft features covered by stiffer layers within the plaques. In two type Vb plaques, characterized by heavy calcification, mean ARFI peak displacements were low relative to the surrounding plaque and arterial wall, suggesting stiff tissue. These initial results demonstrate the feasibility and challenges of transcutaneous ARFI for characterizing the material and structural composition of carotid atherosclerotic plaques via mechanical properties, in humans, *in vivo*.

6.1 Introduction

As described previously, stroke is one of the leading causes of death and long-term disability in the United States. It is estimated that 87% of all strokes are related to ischemia secondary to atherosclerotic disease with 15-20% attributable to plaques located in the carotid arteries [260]. Degree of carotid stenosis is a standard metric in the evaluation of cerebrovascular risk and, as of today, is one of the most valued parameters used to guide the course of medical treatment in the clinic [261]. In

© 2015 Elsevier. Portions reprinted, with permission, from T. J. Czernuszewicz, J. W. Homeister, M. C. Caughey, M. A. Farber, J. J. Fulton, P. F. Ford, W. A. Marston, R. Vallabhaneni, T. C. Nichols, and C. M. Gallippi, "Non-invasive *in Vivo* Characterization of Human Carotid Plaques with Acoustic Radiation Force Impulse Ultrasound: Comparison with Histology after Endarterectomy," *Ultrasound Med. Biol.*, vol. 41, no. 3, pp. 685–697, 2015.

asymptomatic patients with high grade stenosis, it has been shown that prophylactic carotid endarterectomy (CEA) can reduce the absolute risk of stroke by ~5% as compared to medical management [61]. Based on these numbers though, 20 patients must undergo CEA to prevent one stroke, and potential non-stroke complications in CEA patients such as myocardial infarction or cranial nerve injury could reduce quality of life. Some have even questioned the applicability of these data to today's patients given the significant improvements in pharmaceutical therapies, e.g. statins, anti-hypertensives, etc., and reduction in smoking rates [62], [63]. Current estimates suggest that only 5% of patients with asymptomatic carotid stenosis will benefit from prophylactic CEA [62]. Therefore, there is a great need for an improved method of predicting which patients are at high risk for stroke to enhance the benefit and cost-efficacy of CEA (as well as other interventions).

Many have argued that plaque vulnerability based on plaque structure and composition is a more appropriate biomarker, compared to luminal stenosis, for predicting future thromboembolic events [19]. Vulnerable plaque has been studied extensively in the coronary arteries [2]. For carotid arteries, the literature is somewhat sparser, but it has been shown that the same general compositional elements correlate with plaque instability, i.e. thin fibrous cap, large lipid/necrotic core, and dense macrophage infiltrate [38]. Although the mechanisms are not completely understood and may include destabilizing effects of matrix metalloproteinases [262] and endothelial cell apoptosis [263], it is thought that at least one of the reasons these compositional elements confer a higher risk for rupture is that the softer plaque components (e.g. lipids, inflammation, etc.) significantly increase the local circumferential stress experienced by the fibrous cap [26]. When local stresses exceed the ultimate stress (i.e. maximum stress at failure), plaque rupture occurs, and an ischemic event is likely to follow. The "critical" fibrous-cap thickness in carotid plaques, based on CEA specimens, has been reported as a minimum thickness of <200 μm and a representative/average thickness of <500 μm , which is higher than the <65 μm critical thickness reported in coronary arteries [21].

A relatively new approach to characterizing material properties of arteries with ultrasound has been the use of elasticity imaging. Unlike conventional B-mode ultrasound, which generates images of

the *acoustic* properties of tissue, elasticity imaging generates images of the *mechanical* properties of tissue. Typically, these methods work by measuring a strain that is the result of either an intrinsic (e.g. cardiac pulsation) or extrinsic (e.g. ARFI) stress. In ARFI imaging, which is the focus of this current work, radiation-force impulses are generated by a commercially available ultrasound scanner to focally displace tissue (on the order of 1-10 μm). The resulting displacements in the region of excitation (ROE) are monitored with correlation-based motion tracking methods and used to qualitatively infer tissue stiffness, which indicates plaque composition. Although the numbers vary widely in the literature, studies on the mechanical properties of atherosclerotic plaques have shown significant differences in the radial Young's modulus of various plaque components suggesting applicability of elasticity imaging; in Lee et al. [140] calcified tissue was shown to be significantly stiffer (~ 354 kPa) than non-fibrous (~ 41 kPa) or fibrous tissue (~ 81 kPa), whereas lipid/necrotic tissue has been estimated to be the softest component (~ 1 kPa) by other groups [29], [141].

Although ARFI has begun to be translated to *in vivo* settings in humans, these preliminary experiments were not performed with histological validation. The goal of this study is to compare ARFI images of human carotid plaques taken *in vivo* to CEA specimens characterized histologically and test the hypothesis that ARFI can be used to characterize human carotid plaque, *in vivo*. In this chapter, data is presented from a select few patients and analyzed qualitatively in a case-study format. In subsequent chapters, ARFI performance for identifying features is assessed quantitatively across a larger patient pool.

6.2 Methods

6.2.1 Patients

Data sets were obtained from eight patients scheduled for CEA in an on-going clinical study (ClinicalTrials.gov number, NCT01581385) at the University of North Carolina (UNC) at Chapel Hill. Selected subjects either had symptomatic carotid artery disease with a stenosis or lesion in the carotid artery thought to be the source of emboli, or asymptomatic carotid artery disease with a $>60\%$ internal carotid artery (ICA) stenosis. Carotid duplex ultrasounds were performed by the IAC-accredited UNC

Table 6.1: UNC stenosis grading scale

Class	Vel. Systolic (cm/sec)	Vel. Diastolic (cm/sec)	Category
1	< 160	< 80	0-39%
2	> 160	< 80	40-59%
3	> 160	80-109	Possibly > 60%
4	> 160	> 110	60-99%
5	0	0	Occluded
6*	See comment	See comment	See comment

*This grade is only given in special circumstances where further comments by the sonographer are necessary.

Peripheral Vascular Lab (PVL) as part of the patients' standard medical care. The degree of stenosis was determined with an internally validated velocity profile criteria (Table 6.1). Subjects were considered symptomatic if they had a history of amaurosis fugax, transient ischemic attack (TIA), or minor (non-disabling) stroke referable to the carotid artery distribution. Institutional review board (IRB) approval was obtained for both the patient consent forms and the study protocol, and informed consent was obtained from each study participant. A comprehensive list of patient characteristics is given in Table 6.2.

6.2.2 Ultrasonic Imaging and Data processing

Investigative B-mode and ARFI imaging were performed with a Siemens Acuson Antares imaging system (Siemens Medical Solutions USA, Ultrasound Division), equipped with the Axis Direct Ultrasound Research Interface (URI) that allowed customizable beam sequencing and access to the raw radiofrequency (RF) data, and a VF7-3 linear array transducer. ARFI ensembles consisted of 2 reference pulses, one acoustic radiation force (ARF) excitation pulse, and 60 tracking lines with an 11.5 kHz pulse repetition frequency (PRF). ARFI excitations were 300 cycles ($\sim 71 \mu\text{sec}$) at 4.21 MHz with a scanner output power of 55%, and both tracking and reference lines were two cycles at 6.15 MHz. The focal configuration, or f-number ($F/\#$, defined as the ratio of focal depth, z , to aperture width, d), of the excitation pulse was set to 1.5. The reference/tracking pulses used an $F/1.5$ configuration on transmit and

Table 6.2: Patient characteristics

Patient ID	A	B	C	D
Gender (M/F)	M	F	M	M
Age (years)	57	53	72	65
Stenosis grade	Class 6*	Class 4	Class 4	Class 4
Doppler-indicated systolic velocity (cm/s)	402	295	458	455
Doppler-indicated diastolic velocity (cm/s)	54	115	138	143
Arterial location of Doppler measurement	LCCA-Mid	RICA-Prox.	RICA-Prox.	LICA-Prox.
Symptomatic	Y	Y	N	N
Amaurosis fugax	N	Y	-	-
TIA	Y	Y	-	-
Completed stroke	N	N	-	-
ARFI focal depth (cm)	3.0	2.6	2.3	2.0
Peripheral vascular disease	N	Y	N	N
Diabetes mellitus	Y	Y	N	N
Hyperlipidemia	Y	Y	Y	Y
Hypertension	Y	Y	Y	Y
Smoking history	Y	Y	Y	Y

*Due to stenosis in CCA, sonographer noted that velocities in ICA might underestimate grade of ICA stenosis.

dynamic focusing and aperture growth on receive ($F/0.75$). The focus in elevation, set by a cylindrical lens, was 3.8 cm. The ARFI beam sequence acquired 40 ensembles spaced 0.35 mm apart, generating an effective lateral field of view (FOV) of 1.4 cm. ARF ensembles were acquired using wiperblading, a scanning mode that acquired lines in a non-serial order across the lateral FOV to minimize heating and reduce interference between consecutive ARF excitations. A single ensemble was captured from the far left of the FOV, then the center, then one position to the right of the far left, then one position right of center, etc., such that no two consecutive ensembles were captured in two adjacent lateral locations. One spatially matched B-mode frame (220 A-lines, 0.18 mm spacing) preceded each two-dimensional (2D)

ARFI acquisition for anatomical reference. The MI_3 of the ARFI sequences employed in this study was 1.81, measured at a focal depth of 2 cm that was representative of the imaging depths investigated in this study. The $I_{SPTA,3}$ was measured to be 1.67 W/cm^2 . Acoustic intensity measurements were made using an Onda HGL-0200 hydrophone (Onda Corp., Sunnyvale, CA) in a water tank (21 °C) and the phantom-substitution technique described in Palmeri et al. [176]. Heating associated with ARFI sequences was estimated (neglecting perfusion and other cooling effects) to be below 1°C in tissue [176], [216].

Images were acquired the day of surgery prior to patient sedation by a registered sonographer trained in ARFI and peripheral vascular imaging. The carotid bifurcation and ICA were imaged longitudinally, using electrocardiogram (ECG) gating to capture sequences during diastole. The ARFI imaging focal depth was chosen based on the location of the plaque, which in all cases in this study was the distal (relative to the transducer) arterial wall. Two repeated acquisitions were acquired in case of scanner failure or unexpected patient motion. The number of repeated acquisitions was limited to two in order to reduce the time of patient imaging and prevent delays to the surgical procedure. Raw RF data was saved to the hard drive of the scanner and transferred to a computer for offline post-processing using custom software implemented in MATLAB (Mathworks Inc., Natick, MA). Of the repeated acquisitions, the one included for analysis was chosen subjectively for best image quality based on the authors' experience evaluating arterial ARFI images.

Axial displacements induced by ARF were measured using one-dimensional normalized cross correlation applied to the RF data ensembles as described by Pinton et al. [206]. Specific parameters of the motion tracking algorithm included; $4\times$ spline-based upsampling of RF data (natively sampled at 40 MHz), 376- μm kernel length (i.e. 1.5λ , where λ is the wavelength of the tracking pulse assuming a speed of sound of 1540 m/s), and an 80- μm search region. Motion tracking error for this imaging configuration based on the Cramér-Rao Lower Bound was estimated to be 0.7 μm , assuming 53% fractional bandwidth, 0.999 correlation coefficient, and 40 dB SNR [223]. Linear motion filtering was applied to the displacement profiles to reduce artifacts introduced by physiological motion [205], [221]. From the acquired ARFI data, 2D parametric images of peak ARFI-induced displacement (PD) were generated. For

analysis, ARFI images were overlaid on top of spatially matched B-mode images with transparency in order to better visualize anatomical structure. B-mode images were generated from raw RF data, and were calculated as the log compressed, absolute value of the Hilbert-transformed RF data. Interpretation of ARFI images was performed by a single reader not blinded to the histological images.

6.2.3 Histology

After CEA specimens were extracted *en bloc*, the vascular surgeon placed a colored suture to indicate specimen orientation (proximal vs. distal relative to the heart), and specimens were photographed and immediately transferred to 10% neutral-buffered formalin for a minimum of 48 hours. Once fixed, the specimens were cut with a scalpel into two halves following the surgeon's anterior/longitudinal arteriotomy (Figure 6.1). The arteriotomy was assumed to approximately follow the ultrasound-imaging plane as both ultrasound and the surgical approach followed an anterior trajectory to avoid the sternocleidomastoid muscle. In all samples obtained in this study, the surgical arteriotomy extended through the length of the sample and was easily identifiable without extra marking. To preserve sample orientation in histological slides, sutures were removed and replaced with tissue marking dyes (Polysciences Inc., Warrington, PA) that would remain on the exterior of the sample after histological staining. After mark-up, gross microscopic images were taken of the luminal face of each sample for reference with a Leica MZ9.5 dissecting microscope (Leica Microsystems GmbH, Wetzlar, Germany) at 6.3× magnification, and samples were embedded in paraffin.

The samples were sectioned (5- μ m slice thickness) and stained with hematoxylin and eosin (H&E), Von Kossa (VK) for calcium, and either Lillie's modified Masson's trichrome (LMT) or a combined Masson's elastin (CME) stain for collagen and elastin fibers. A detailed guide to histological stains is given in Table 6.3. De-calcification was not performed on any of the samples in order to preserve calcium for histological staining. For samples with heavy calcification, paraffin blocks were left to soak for 3 days in water to achieve usable sections. Approximately 1 mm of tissue was sectioned from each half of the specimen using a serial-interrupted protocol where 6 serial sections were taken (to allow

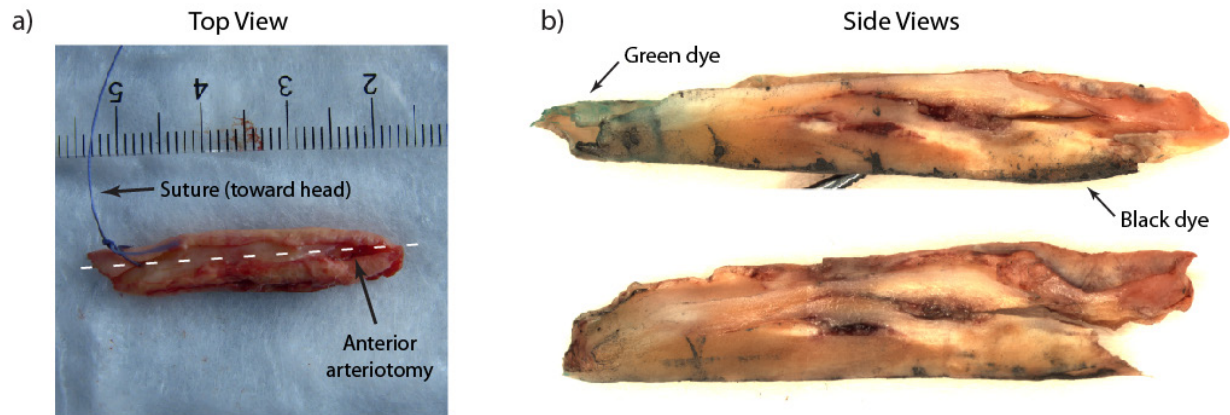


Figure 6.1: Example of a sample preparation for histology. Panel (a) shows a top-view photograph of the raw sample from the common carotid of Patient A. The suture placed by the surgeon indicates proximal vs. distal end of the sample (with respect to the heart). The anterior surgical arteriotomy is evident on the top surface of the sample. To prepare samples for histology, the suture is removed and replaced with tissue marking dye and the sample is cut into two halves following the arteriotomy that approximates the ultrasound plane. Side views of the cut sample are shown in panel (b). Note the green and black tissue marking dyes in panel (b); green indicates suture position and black indicates the opposite side of the arteriotomy (i.e. the distal wall in the ultrasound image).

multiple stains), followed by a 100 μm skip, and another 6 serial sections, etc. Slides containing the stained sections were digitized using a Scanscope digital-slide scanner (Aperio Technologies Inc., Vista, CA) at 20 \times magnification. The slides that qualitatively matched the plaque morphology from B-mode were chosen, and a blinded pathologist with experience in atherosclerosis examined and annotated the digitized slides using ImageScope (Aperio Technologies Inc., Vista, CA), a freely-available slide viewing/annotation software package. The following features, if present, were identified: fibrous cap/tissue, lipid/necrotic core, calcium, foam cells, vascularity, intra-plaque hemorrhage, and surface thrombus. As was done in Redgrave et al. [38], lipid/necrotic core was defined as amorphous material containing cholesterol crystals, intra-plaque hemorrhage was defined as an area of erythrocytes within the plaque causing disruption of the plaque architecture, and surface thrombus defined as an organized collection of fibrin and erythrocytes in the lumen. Plaques were then assigned a rating using the American Heart Association (AHA) classification scale (see Chapter 2). Alignment between ARFI images and

Table 6.3: Histological stain guide

Stain	Feature	Color
Hematoxylin and Eosin (H&E)	Nuclei	Dark blue
	Cytoplasm/extracellular matrix	Pink
	Erythrocytes	Red
Von Kossa (VK)	Calcium	Black
	Cytoplasm/extracellular matrix	Pink
Combined Masson's Elastin (CME)	Elastin fibers, nuclei	Black
	Collagen	Green
	Erythrocytes, thrombus, cytoplasm, muscle fibers, keratin	Red
Lillie's Modified Masson's Elastin	Nuclei	Black
	Collagen	Blue
	Erythrocytes, thrombus, muscle fibers, fibrin	Red

histological sections was achieved by manually identifying unique features in both ARFI and histology images (i.e. large calcium deposits or plaque morphological features such as the plaque shoulder).

6.3 Results

Carotid plaques were imaged without adverse event from five males and three females immediately prior to undergoing CEA. Data from four patients was excluded for various reasons; in two patients the extracted sample was damaged/lost during surgery, in a third patient, ARFI imaging was incorrectly focused on a portion of arterial wall rather than plaque, and in a fourth patient the ARFI image could not be successfully matched to histology due to lack of common morphology. Patient characteristics and labeling scheme for included patients are presented in Table 6.2. Matched B-mode and ARFI ultrasound images are presented with corresponding histological sections in Figure 6.2 through Figure 6.5. All images (both ultrasonic and histologic) are oriented such that the cephalad portion (i.e. towards the patient's head) of the artery is always on the left side of the image.

Figure 6.2 shows the imaging results from a symptomatic 57 year-old male (Patient "A") with a

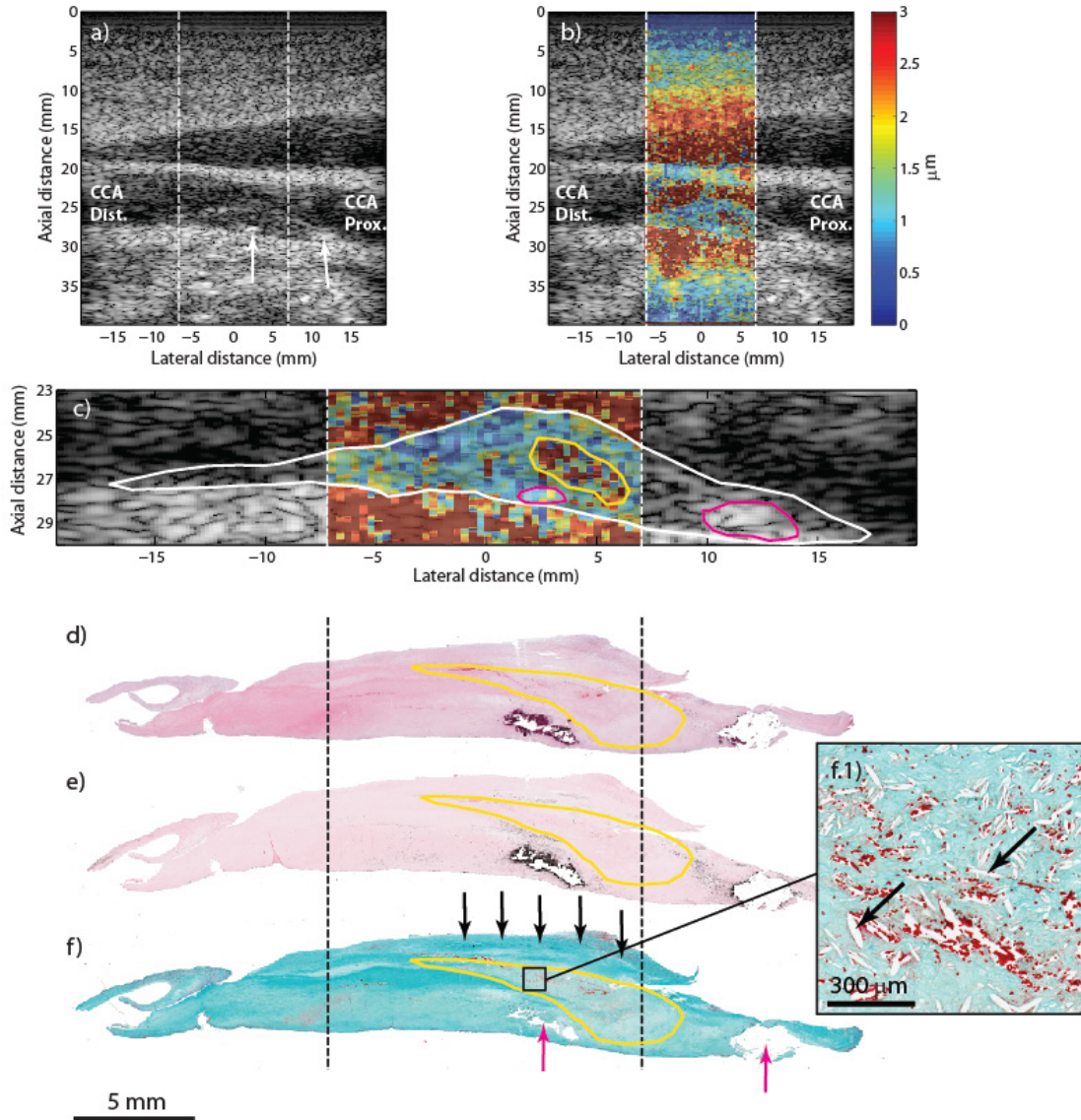


Figure 6.2: Type Va plaque from the CCA of a 57 year-old, symptomatic male (patient A). B-mode imaging (a) shows an echolucent plaque with two echogenic foci separated by approximately 10 mm (white arrows). ARFI imaging (b) shows that the plaque is generally low displacing except for a higher-displacing region located above the leftmost echogenic foci. ARFI magnification image is shown in (c); the solid white outline indicates extent of the plaque in the ultrasound image, the magenta outlines indicate the echogenic foci, and the yellow outline indicates the higher-displacing region. Histological staining with H&E (d), VK (e), and CME (f) shows a type Va plaque with a necrotic core and mild intra-plaque hemorrhage (yellow outline) and fibrous cap (f, black arrows). Two calcifications are seen at the bottom of the plaque (f, magenta arrows) separated by approximately 10 mm. Inset panel shows higher-magnification image of the necrotic/hemorrhagic region, which is denoted by cholesterol clefts (f.1, black arrows) and extravascular erythrocytes stained red (f.1). CCA, common carotid artery; CME, combined Masson's elastin; VK, Von Kossa.

past medical history of hypertension, hyperlipidemia, non-insulin dependent diabetes mellitus, and smoking (quit ~13 years). Indications for surgery included paresthesia (left face) and previous TIA. Duplex ultrasound revealed significant stenosis in the left CCA and ICA (it was noted that velocities may be underestimated in the ICA due to CCA occlusion). CEA was performed on both CCA and ICA, and results are shown for the CCA. B-mode imaging shows a generally echolucent plaque (Figure 6.2a), with two echogenic foci located at lateral positions 1.8 mm and 11.6 mm. ARFI imaging (Figure 6.2b) shows that the plaque exhibits generally low displacement throughout except for a focal, higher-displacing region located towards the right part of the plaque. A low-displacing region separating a high-displacing region from lumen has previously been shown to be indicative of fibrous cap ([210]). A magnification of the ARFI image is provided in Figure 6.2c, with the higher-displacing region outlined in yellow (mean PD: $3.11 \pm 3.6 \mu\text{m}$), the echogenic regions outlined in magenta (mean PD: $1.18 \pm 0.4 \mu\text{m}$), and the plaque outlined in white (mean PD excluding yellow and magenta regions: $1.25 \pm 0.7 \mu\text{m}$). Histological staining (Figure 6.2d, e, f) shows a type Va plaque with a necrotic core (Figure 6.2f, yellow outline) covered by a fibrous cap (Figure 6.2f, black arrows). Two calcium deposits are also apparent (Figure 6.2f, magenta arrows) on the bottom center and bottom right of the specimen separated by ~10 mm. A magnification of the necrotic core located above the left-most calcium deposit is displayed in the inset panel (Figure 6.2f.1) showing cholesterol clefts and extravascular erythrocytes, indicating mild intra-plaque hemorrhage.

Figure 6.3 shows the imaging results from a 53 year-old symptomatic female (Patient “B”) with a past medical history of hypertension, hyperlipidemia, diabetes mellitus, smoking, peripheral vascular disease, and claudication. Records note that the patient previously experienced right-sided facial droop, some right arm weakness, and symptoms consistent with amaurosis fugax (specifically, unable to see out of right eye for a few minutes). B-mode imaging shows a plaque in the distal wall with a number of small echogenic foci scattered throughout, suggesting small calcium deposits (Figure 6.3a, white arrows), and a focal stenosis extending ~4 mm into the lumen (Figure 6.3a, asterisk). ARFI imaging (Figure 6.3b), focused at a depth of 2.6 cm, shows that the plaque exhibits generally low displacement throughout except for a higher-displacing region located underneath the shoulder of the plaque, suggesting fibrous

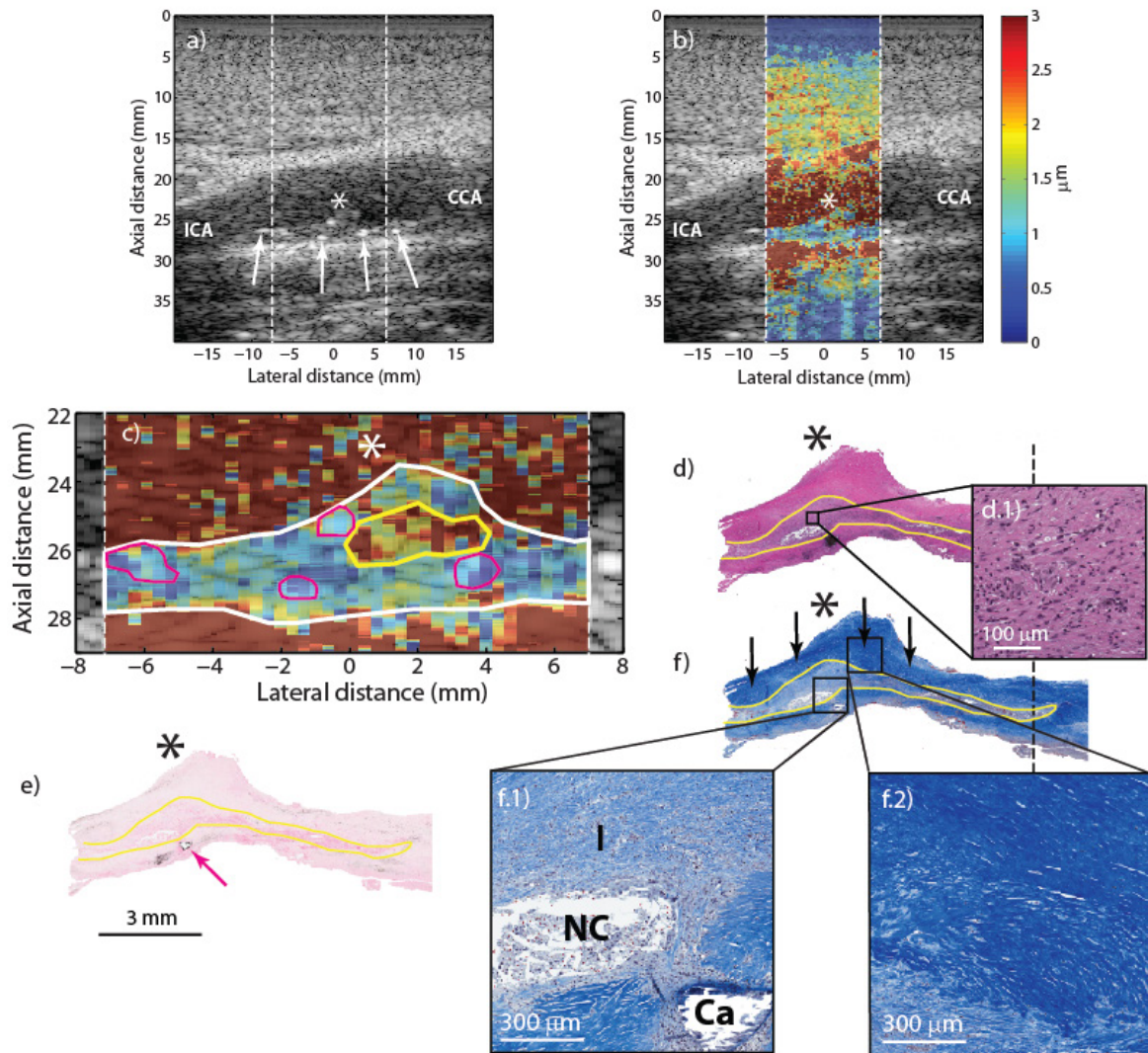


Figure 6.3: Type Va plaque from the ICA of a 53 year-old, symptomatic female (patient B). B-mode image (a) shows a plaque on the distal wall with a protruding shoulder region (a, asterisk) and a number of small echogenic foci scattered throughout (white arrows). ARFI imaging (b) shows that the area beneath the shoulder region displaces farther than the rest of the plaque. ARFI magnification image is shown in (c); the solid white outline indicates extent of the plaque in the ultrasound image, the yellow outline indicates the higher displacing region, and magenta outlines indicate echogenic foci. Histological staining with H&E (d) and VK for calcium (e) shows a type Va plaque with a protruding shoulder region (d, asterisk) and small, submillimeter calcifications (e, magenta arrow). LMT staining for collagen shows abundant fibrosis in the shoulder region, indicated by the deep blue color (f, black arrows), which covers a cellular area with inflammation and a small, developing necrotic core. Inset panels show higher-magnification images of the cellular area just above the necrotic core (d.1), the cellular area with the necrotic core (f.1) and the fibrous cap (f.2). The region of inflammation from histology is outlined in yellow. ICA, internal carotid artery; CCA, common carotid artery; LMT, Lillie's modified Masson's trichrome; VK, Von Kossa; I, inflammation; NC, necrotic core; CA, calcium.

cap. A magnified version of the ARFI image is depicted in Figure 6.3c, with the higher-displacing region outlined in yellow (mean PD: $2.77 \pm 1.7 \mu\text{m}$), the echogenic regions outlined in magenta (mean PD: $0.85 \pm 0.3 \mu\text{m}$), and the plaque outlined in white (mean PD excluding yellow and magenta regions: $1.35 \pm 0.8 \mu\text{m}$). Histological staining (Figure 6.3d, e, f) shows a type Va plaque with a cellular region with inflammation and early necrotic-core formation (Figure 6.3f, yellow outline) covered by a fibrous cap (Figure 6.3f, black arrows). Small, sub-millimeter calcifications are also apparent (Figure 6.3e, magenta arrow). Figure 6.3f.1 and Figure 6.3f.2 show magnified versions of the necrotic/inflamed region and fibrous-cap regions, respectively.

Figure 6.4 shows a highly occlusive plaque located in the bifurcation of an asymptomatic 72 year-old male (Patient “C”) with a history of hyperlipidemia, hypertension, and smoking. Duplex imaging studies measured a Class 4 stenosis with peak systolic and diastolic velocities of 458 cm/sec and 138 cm/sec, respectively, in the proximal portion of the right ICA. B-mode imaging shows a very complicated and obstructed lumen (Figure 6.4a) with large shadowing artifact (Figure 6.4a, white arrows) in the distal wall, suggesting heavy calcification. In this imaging plane, the proximal wall is not clearly defined and tissue appears to extend from the proximal wall to make contact with the calcification in the distal wall. In the ARFI image (Figure 6.4b), focused at a depth of 2.3 cm, there is a large displacement contrast between plaque in the distal wall (Figure 6.4b, asterisk) and the tissue that connects to the proximal wall (Figure 6.4b, dagger). Figure 6.4c shows a magnification of the ARFI image with the distal plaque outlined in solid white line (mean PD: $2.1 \pm 1.5 \mu\text{m}$). Mean PD of the tissue connecting to the proximal wall was measured to be $6.0 \pm 3.4 \mu\text{m}$. Histological staining shows a type Vb plaque with a large calcium deposit indicated by black stain outline (Figure 6.4d, asterisk), measuring approximately 7.9 mm laterally and 4.5 mm axially, located in the arterial wall distal to the transducer. The tissue extending from the calcification and connecting up to the proximal wall is comprised of collagen fibers (Figure 6.4d.1 and Figure 6.4e.1). As seen in the higher-magnification images, the collagen fibers appear loosely packed and disorganized and do not follow the longitudinal histology plane, suggesting that this tissue may be from the split in the bifurcation. Note that the disruptions in continuity of tissue surrounding the calcium

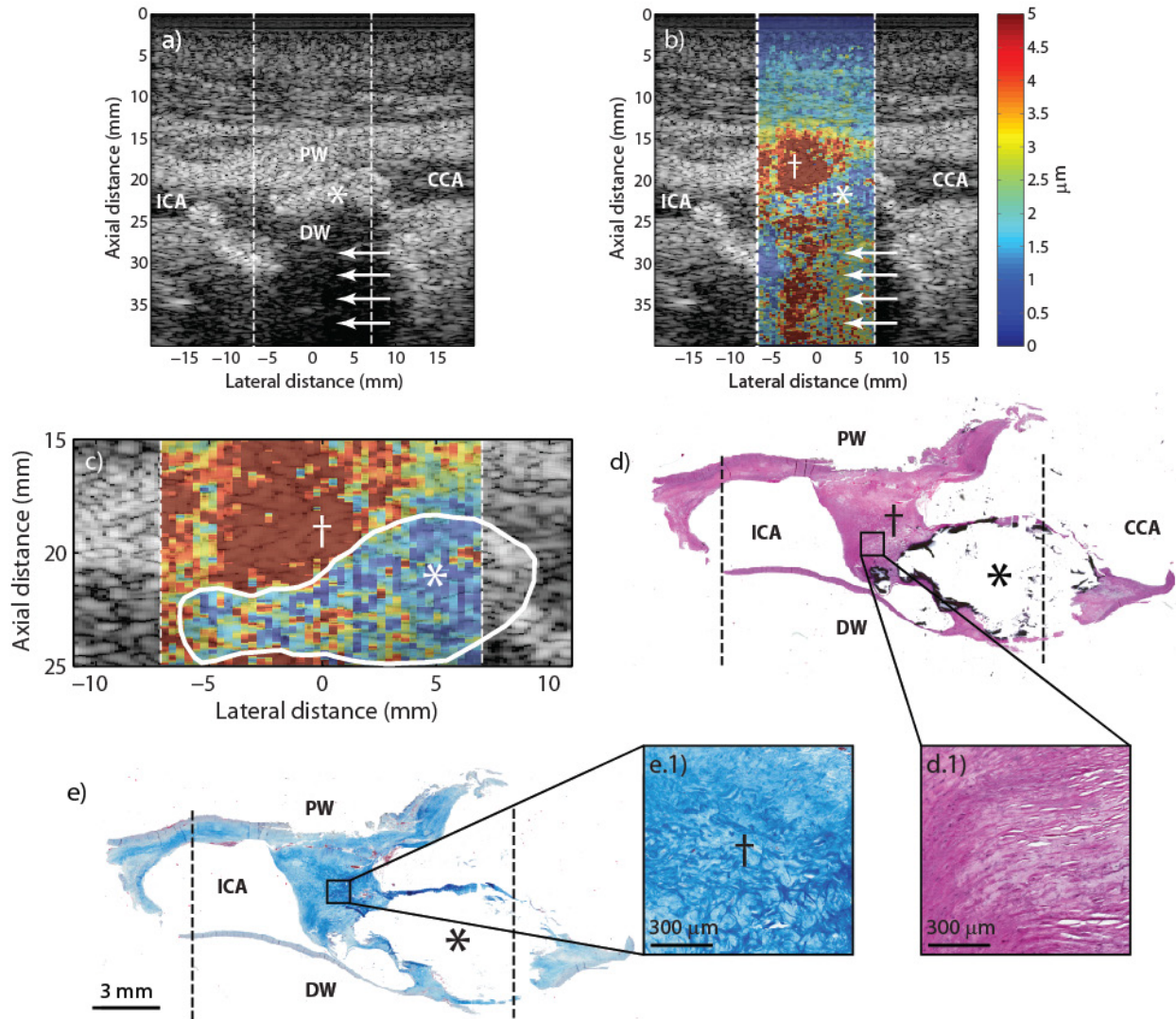


Figure 6.4: Type Vb plaque from the ICA of a 72 year-old, asymptomatic male (patient C). B-mode image (a) shows a complicated lumen with a large area of shadowing (a, white arrows) from plaque in the distal wall. ARFI imaging (b) shows lower displacement in the area of the calcium deposit (asterisk) and higher displacements in the adjacent tissue connecting to the proximal wall (dagger). ARFI magnification image is shown in (c) with a white outline indicating the plaque that is above the shadowed region. Histological staining with H&E (d) and LMT for collagen (e) shows a large calcification (asterisk) indicated by the black stain. The dotted black lines indicate the extent of the ARFI FOV. Magnification insets shows that the tissue connecting the calcification to the proximal wall is comprised of loosely packed (d.1) and disorganized (e.1) collagen fibers. ICA, internal carotid artery; CCA, common carotid artery; PW, proximal wall (with respect to transducer); DW, distal wall (with respect to transducer).

deposit are artifacts of histological processing and are not indicative of plaque rupture.

Figure 6.5 shows a calcified plaque from a 65 year-old male (Patient “D”) with a history of asymptomatic carotid artery stenosis. Previous cerebral angiogram of this patient demonstrated a 70% stenosis in the left ICA, and was corroborated by duplex scanning which measured peak systolic and diastolic velocities of 455 cm/sec and 143 cm/sec, respectively. B-mode imaging (Figure 6.5a) shows slight shadowing (Figure 6.5a, white arrows) below plaque located in the distal wall. In the ARFI image (Figure 6.5b), focused at a depth of 2.0 cm, the portion of the plaque encroaching into the lumen appears to consist primarily of low-displacing tissue except for a small high-displacing region located toward the bottom of the plaque, which could suggest a fibrous cap. Mean PDs in the plaque (excluding the high-displacing area) were measured to be $1.85 \pm 1.0 \mu\text{m}$ (Figure 6.5c, white outline) and $8.27 \pm 12.5 \mu\text{m}$ in the high displacing area (Figure 6.5c, yellow outline). Large amounts of calcium deposition in this sample can be observed in the gross microscopic image of this sample (Figure 6.5d, dashed black outline), and confirmed by dark staining on H&E and VK (Figure 6.5e, f) making this a type Vb plaque. In the CME stain (Figure 6.5g), there is evidence of degraded collagen surrounding parts of the calcification (Figure 6.5g.1, black arrow).

6.4 Discussion

This work represents a preliminary study of ARFI imaging for characterizing carotid plaque composition in patients undergoing CEA. From the patients that were imaged, a range of atherosclerotic lesions were observed during histological analysis including plaques with heavy calcium deposition, loose and dense fibrosis, necrotic cores containing crystallized cholesterol, and mild intra-plaque hemorrhage. Agreeing with previous animal and *ex vivo* studies [208]–[210], ARFI imaging showed regions of contrast that were consistent with underlying compositional elements determined from histology.

In this study, large lipid/necrotic core, dense inflammation, and/or intra-plaque hemorrhage was seen on histology in two of the four CEA specimens (patients A and B). ARFI images of plaques containing these features were characterized by an identifiable area of increased peak displacement ($\sim 3\times$

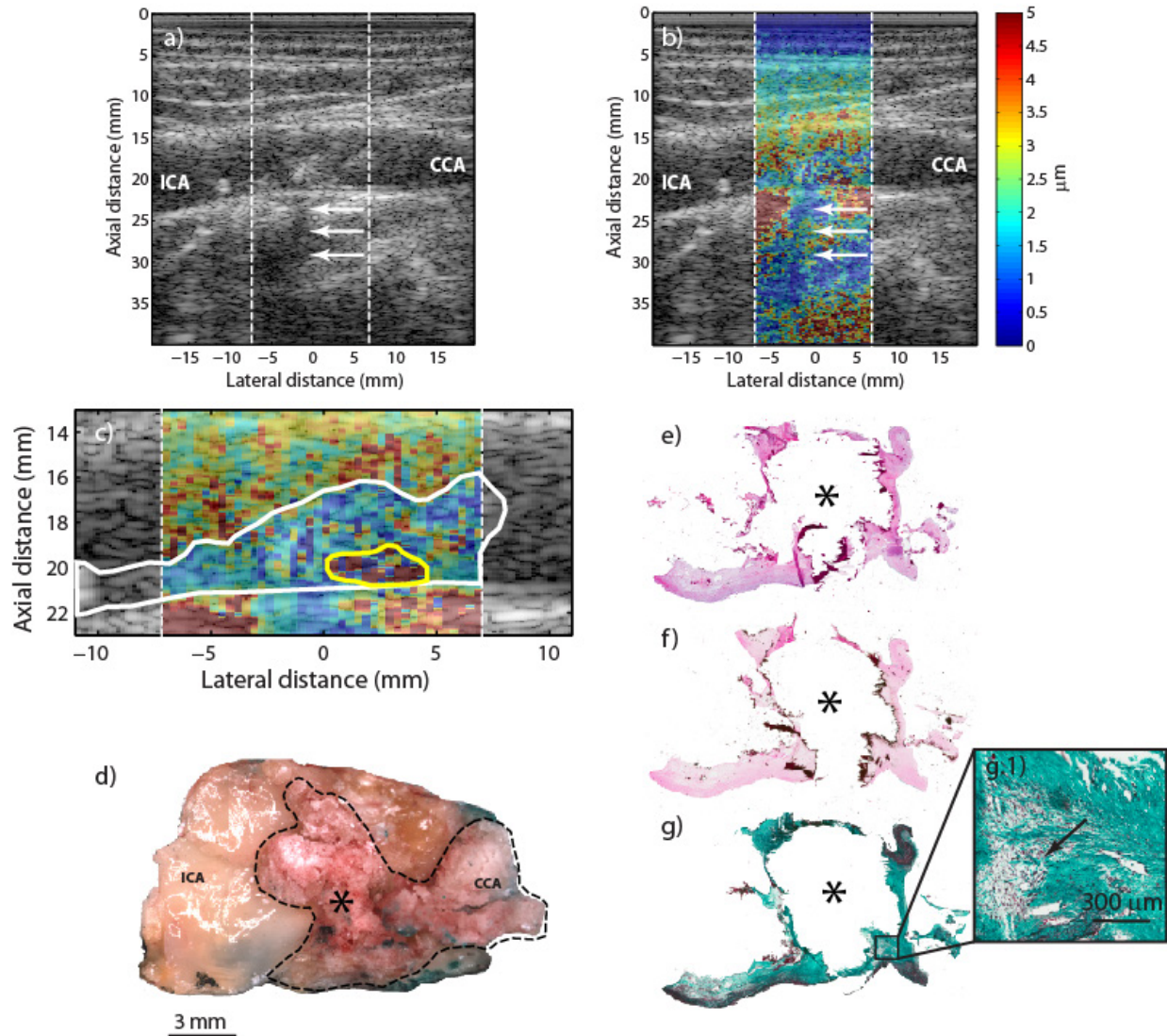


Figure 6.5: Type Vb plaque from the ICA of a 65 year-old, asymptomatic male (patient D). B-mode image (a) shows a plaque extending significantly into the lumen with faint shadowing (white arrows) in the distal wall. ARFI imaging (b) shows a plaque with low displacement, except for a focal area of higher displacements located near the bottom of the plaque. ARFI magnification image is shown in (c); the solid white outline indicates extent of the plaque in the ultrasound image, and the yellow outline indicates the higher-displacing region. Gross macroscopic *en face* image of plaque (d) show areas of mineralization protruding into the lumen (dashed black outline). H&E, VK, and CME stains are shown in (e), (f), and (g), respectively. VK staining shows extensive calcification (asterisk). CME staining shows degraded collagen in areas surrounding the calcification (g.1, black arrow). Note that the lateral extent of the calcification was not captured in histology due to poor adhesion to the slide. ICA, internal carotid artery; CCA, common carotid artery.

greater) below an area of lower displacement that has previously been shown to indicate a soft necrotic core covered by a stiff fibrous cap [210]. Indeed, in patient A, the plaque was composed of a large necrotic region (as seen by the cholesterol clefts left on histology) covered by a fibrous cap, and in patient B, the plaque had a cellular region of inflammation and early necrotic core surrounded by a large amount of fibrosis. By measuring the thickness of the low-displacing region separating the high-displacing region from the lumen, ARFI imaging may be able to estimate fibrous cap thickness, another potential indicator of plaque vulnerability [21], however this analysis was outside the scope of this manuscript.

The other two examples presented in this work included predominately calcified plaques. In general, ARFI displacements were low, which could be expected of a stiff calcification, but relatively higher ARFI displacements were also observed. In patient C, higher-displacing tissue was seen to extend up to the proximal wall from the calcification in the distal wall, and in patient D, a focal region of high displacement was noted in the bottom of the plaque (having a similar signature to patients A and B). In both of these cases, histology indicated that tissue surrounding the calcification was partially composed of loose/degraded collagen deposition, which could explain the higher displacements observed in these regions. The magnitude of displacements though, in these regions, was similar or greater to those seen in plaques with necrotic core, which would be expected to be mechanically softer than collagen. Likewise, the magnitude of displacements in the calcified regions of these plaques was similar to regions of dense collagen in the type Va examples, despite calcium being the stiffest plaque component [140]. One explanation for these confounding results may be that the applied force was not constant across the area of the plaque due to boundary conditions and/or variations in the absorption coefficient of plaque components. For example, calcium in particular has been shown to be highly absorbing [264], which could increase the magnitude of radiation force for a given acoustic intensity level. If the calcium deposit experiences more force, it may displace just as far as mechanically softer, less-absorbing tissue despite inherently having a higher Young's modulus value. Conversely, depending on the magnitude of attenuation, some parts of the plaque could experience less radiation force due to the exponential decay in

acoustic intensity of the ARF pulse through depth. An example of this can be seen in patient D (Figure 6.5b, white arrows); the soft tissue underneath the calcification appears to displace less than the surrounding, but this is most likely an artifact of unequal force distribution rather than a true contrast in tissue stiffness. These results suggest that ARFI measurements of displacement need to be interpreted with care and should be evaluated qualitatively taking boundary conditions and absorption into account.

There are a number of other factors that could influence the appearance of plaques in ARFI images. First, mechanical-wave propagation away from the ROE can affect both apparent lesion size and contrast [231], [241]. Typically, these effects are seen later in the ARFI imaging time-course and would not be expected to significantly alter a measurement of peak displacement, which is usually computed from the early time samples. To test this, we examined the median time-to-peak values for patients A and B, and found that a majority of the peak displacements occurred within 0.26 or 0.35 ms after the ARF excitation, suggesting minimal impact of mechanical-wave propagation on the PD images. Second, boundary artifacts of the cross-correlation method could affect the resolution of the ARFI images and impact low-displacing feature size measurements. The resolution of ARFI, like conventional compressive elastography, is comparable to the B-mode resolution and is dictated by both ultrasound parameters (frequency, bandwidth, etc.) and signal-processing parameters (kernel size and kernel step) [206], [265], [266]. Pinton et al. [206] examined the impact of kernel size on estimation of a step displacement and showed that as the kernel size increased, the slope of the measured step response decreased, effectively reducing the contrast of the 'edge'. For our ARFI images, a kernel size of 1.5λ was utilized suggesting features of $\sim 400\ \mu\text{m}$ axially could be detected given sufficient mechanical contrast. As has been hypothesized previously [267], it is possible that as the size of a plaque feature, such as fibrous cap, decreases, the feature will move in unison with underlying softer features, such as necrotic cores, making it difficult to resolve on an ARFI image even if the feature thickness exceeds axial resolution limits of the system. Despite this limitation, ARFI imaging may be able to infer the presence of a thin fibrous cap by virtue of the proximity of a high-displacing region to the lumen.

A significant challenge in this study was ensuring spatial alignment between the ultrasonic and histologic imaging planes. In order to accomplish this, the following general regions had to be identified on the specimen: cephalad vs. thoracic and distal vs. proximal (in relation to the transducer). Identifying distal vs. proximal wall was the more difficult task and relied on the assumption that the anterior arteriotomy made by the surgeon approximated the ultrasonic imaging plane. This assumption was based on the fact that the position of the patient during imaging and surgery was consistent (patient was in a supine position with head tilted away ~45 degrees from midline), and both imaging and surgery followed a trajectory just anterior to the sternocleidomastoid muscle. Although care was taken to ensure alignment, it was possible that the surgical cut did not exactly follow the ultrasonic imaging plane. Specifically, three degrees of freedom (translation in elevational dimension, rotation around lateral dimension, and rotation around axial dimension) could not be precisely controlled. Complicating alignment even further was the fact that histological specimens were both unpressurized and fixed, which could have caused significant changes in tissue size [41]. In order to overcome the limitations of alignment inherent in CEA histological validation, comparison between ARFI and other *in vivo* plaque characterization technologies, such as MRI, may be required, although aligning MRI and ARFI imaging planes could also pose significant challenges.

While these results are encouraging, there are a number of steps necessary to continue the development of ARFI for plaque characterization. First, given the small sample size of this pilot study, ARFI-derived plaque composition could not be statistically correlated with patients' symptoms. Much larger clinical end-point studies will need to be performed to confirm that ARFI-derived elastograms are relevant to predicting ischemic events. Second, atherosclerotic lesions imaged in this study were significantly advanced (all patients were Class 4 on the UNC Doppler-indicated stenosis scale) and may not be representative of earlier stage plaques. Prior non-validated studies in humans though [212], have shown that ARFI is capable of revealing areas of mechanical contrast similar to those seen in this study, suggesting that the technique may be relevant in plaques not indicated by Doppler for surgery. Third, ARFI beam sequences were designed conservatively; the number of ARFI interrogations was kept to a

maximum of 40, consequently limiting the imaging FOV to ~ 1.5 cm, and the output power of the scanner was kept relatively low (55% of total output). Under this regime, the full lateral extent of the plaque was not imaged in some cases, and the induced displacements sometimes challenged the limits of the displacement-tracking algorithm, which was estimated to be ~ 0.7 μm . In the future, more interrogation points along the lateral dimension could be acquired such that the full lateral extent of the plaque would be covered. Also, increasing the radiation force amplitude could improve the contrast and signal-to-noise ratio (SNR) of the images particularly for stiff plaque features where displacements were seen to fall below 1 μm .

6.5 Conclusion

In this chapter, ARFI imaging was applied successfully in a small number of patients undergoing clinically indicated CEA. With matched histology, it was shown that plaques composed of lipid/necrotic core, mild intra-plaque hemorrhage, inflammation, and loose/degraded collagen deposition had focal regions of relatively high peak displacements. On the contrary, plaques composed of dense collagen deposition and/or calcium were generally low displacing. Overall, these results represent the first comparison of histology and *in vivo* ARFI imaging of carotid plaque. Identification of plaque mechanical properties with ARFI could substantially improve plaque vulnerability assessment ultimately leading to better patient risk stratification not only in asymptomatic patients with high-grade stenosis, but also in patients with $<60\%$ occlusion where Doppler ultrasound may be less reliable [75], [95]. In the following chapter, this analysis will be extended to a larger patient pool and ARFI sensitivity and specificity for characterizing atherosclerotic features will be quantified with receiver operating characteristic (ROC) curve analysis.

CHAPTER 7

On the Feasibility of Quantifying Fibrous Cap Thickness with Acoustic Radiation Force Impulse Ultrasound: A Simulation Study

In this chapter, the feasibility of using transcutaneous acoustic radiation force impulse (ARFI) ultrasound to quantify fibrous cap thickness is assessed using finite element method (FEM) modeling. Fibrous caps with varying thickness (0.1 – 1.0 mm) were simulated using a simple layered geometry, and their mechanical response to an impulse of radiation force was solved using FEM modeling. Ultrasound tracking of FEM displacements was performed in Field II utilizing three center frequencies (6, 9, and 12 MHz) and eight motion tracking kernel lengths ($0.5\lambda - 4\lambda$). Additionally, fibrous cap thickness in two carotid plaques imaged *in vivo* was measured with ARFI and compared to matched histology. The results of this study demonstrate that 1) tracking pulse frequencies around 12 MHz are necessary to resolve caps around 0.2 mm, 2) large motion-tracking kernel sizes introduce bias into thickness measurements and overestimate the true cap thickness, and 3) color saturation settings on ARFI peak displacement images can impact thickness measurement accuracy substantially.

7.1 Introduction

As described previously, fibrous cap (FC) thickness is an important indicator of plaque vulnerability. The fibrous cap serves as a stiff protective layer covering the developing necrotic core. If the fibrous cap becomes thin and mechanically unstable, radial stress imparted by blood pulsation can exceed the maximum failure stress of the cap and result in rupture [26]. In the Oxford Plaque Study [38], one of the largest histological studies done on carotid plaque, the authors reported that a minimum FC thickness of <0.2 mm and a representative FC thickness of <0.5 mm were independently associated with

plaque rupture [21]. Therefore, an ideal noninvasive carotid plaque imaging system should be able to resolve FCs of 0.5 mm or less in order to detect plaques that may be vulnerable to rupture.

Among noninvasive imaging technologies, magnetic resonance imaging (MRI) was the first to report direct measurement of FC thickness *in vivo* with resolution down to 0.25 mm [86], [90], [93]. Subsequent prospective MRI studies demonstrated that the presence of a thin/ruptured FC carried the highest hazard ratio (HR: 17.0) for future cerebrovascular event compared to all other plaque features [99]. High-resolution computed tomography (CT) has also been shown to be sensitive to FC thickness in small sample patient studies [76]. However, wide-scale implementation of MRI and CT technology may be precluded due to the high monetary cost of both modalities, ionizing radiation in the case of CT, and specialized surface coils in the case of MRI that are necessary to achieve the appropriate resolution for FC thickness measurement.

Given the relevance of FC thickness to predicting future ischemic events [99], implementing a cost-effective, ultrasound-based imaging solution to noninvasively quantify FC thickness may be highly impactful and could revolutionize plaque risk stratification. Indeed, high-resolution B-mode assessment of FC thickness was proposed a decade ago [114], with the authors demonstrating that thicknesses of <0.65 mm were associated with cerebrovascular symptoms. However, despite these promising initial results, there has been a notable lack of publications on the topic, and measuring FC thickness has not seemed to translate into the clinic. One explanation could be that the inherent contrast in echogenicity between fibrous and necrotic components is highly variable, which leads to conflicting performance results when utilizing echogenicity outside of a highly-controlled research setting [3]. Ultrasound FC thickness measurement may be improved with ultrasound methods that do not strictly rely on echogenicity.

The objective of this chapter is to analyze the feasibility of ARFI imaging for transcutaneous measurement of FC thickness by using finite element method (FEM) and Field II-based simulations [176], [230] and by analysis of *in vivo* performance. A simple FEM mesh with multiple layers representing lumen, FC, and necrotic core (NC) is developed and ARFI is simulated for a range of FC

thicknesses. Various imaging and signal processing parameters are investigated to determine their impact on thickness measurement. Based on work previously done in compressive elastography [266] and time-delay estimation simulations [206], it is hypothesized that the resolution of ARFI for detecting FC thickness will be mainly dictated by the imaging pulse center frequency, and the length of the motion tracking kernel size. Additionally, we hypothesize that mechanical interaction between the FC and NC and ARFI displacement underestimation may influence FC measurement performance. These hypotheses are first tested *in silico* and then demonstrated clinically for two fibroatheromatous carotid plaques with validation by spatially-matched histology [268]. Overall, this study serves as a first evaluation of transcutaneous ARFI's ability to quantify FC thickness.

7.2 Methods

7.2.1 Finite Element Method Simulations

Soft tissue dynamics in response to an impulse of acoustic radiation force were simulated using previously developed finite element method (FEM) models [176] utilizing LS-DYNA (Livermore Software Technology Corporation, Livermore, CA), a commercially-available multi-physics solver. A fibrous cap covering a necrotic core was abstracted as a thin layer of stiff material covering a layer of soft material (Figure 7.1). Ten FEM models were generated with FC thicknesses of 0.1 mm to 1 mm, all covering a soft NC region with thickness of 1 mm. The models implemented a rectangular mesh with 131,712 elements with variable node spacing and quarter-symmetry boundary conditions about the transducer's axis of symmetry. The non-symmetry faces as well as the bottom face of the mesh were fully constrained, while the top face of the mesh (representing the lumen/FC border) was left unconstrained. From the axis of symmetry, the mesh extended 5.5 mm in the lateral dimension and 5.5 mm in the elevational dimension, and 20 mm in the axial dimension (with a 20 mm offset from the transducer face). Nodal spacing in the region of the FC and NC was set to 0.02 mm, while the rest of the mesh was 0.25 mm. The fine nodal spacing the region of the FC was necessary in order to have multiple elements in the thinnest simulated FC (0.1 mm).

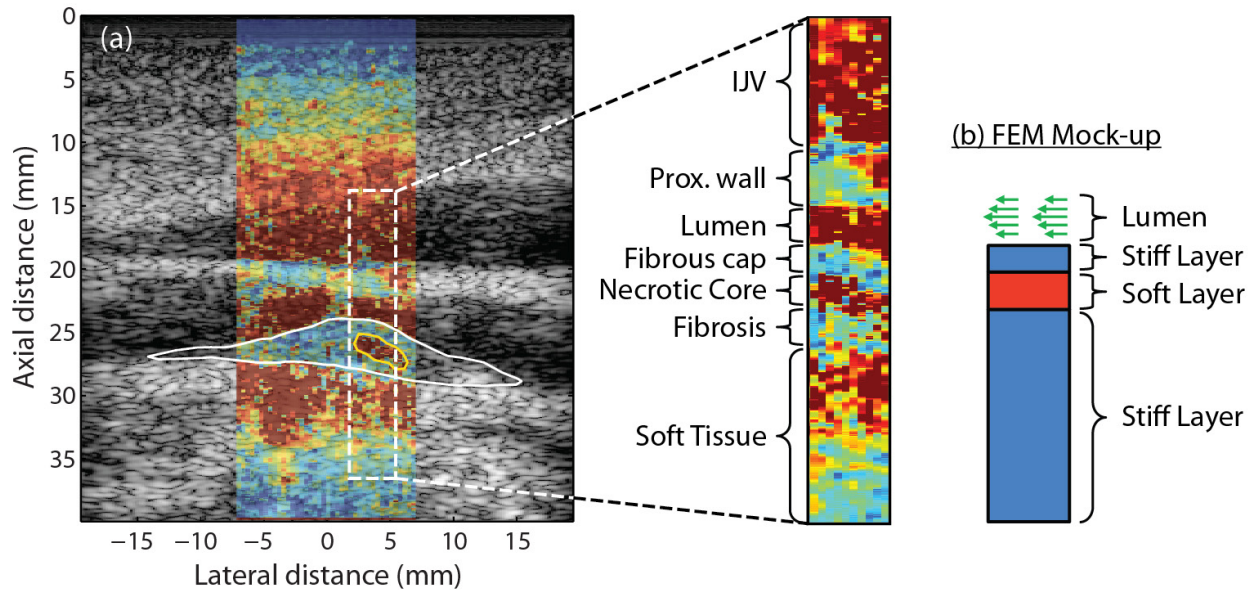


Figure 7.1: Schematic of the layered model used to approximate an atherosclerotic plaque. (a) ARFI peak displacement image of a carotid plaque (white outline) with histologically-validated fibrous cap and necrotic core (yellow outline) [268]. The various tissue layers that comprise the ARFI image are shown in the zoomed inset panel. The fibrous cap appears as a region of low displacement (blue pixels) above a region of high displacement (red pixels), which represents the necrotic core. (b) Simple layered geometry abstracted from the ARFI imaging including a stiff layer to represent the fibrous cap on top of a soft layer to represent the necrotic core. ARFI, acoustic radiation force impulse; IJV, internal jugular vein; FEM, finite element method.

Following the methods of Ohayon et al. [29], fibrosis was modeled as stiff transversely-isotropic material, while NC was modeled as soft isotropic material. For FC, LS-DYNA material model *MAT_002 was implemented with the same mechanical properties in the circumferential (θ) and longitudinal (z) directions and different ones in the radial (r) direction, while NC was implemented with *MAT_001, an isotropic elastic material model. The mesh was oriented such that the radial direction corresponded to the axial direction of the ultrasound transducer, while longitudinal and circumferential directions corresponded to lateral and elevational directions, respectively. Specific material parameters for both material models are given in Table 7.1. A perfect matching layer (PML), six elements wide, was defined around the mesh to simulate an infinite medium and remove spurious wave reflections from the

Table 7.1: Material model constants.

	<u>Young's Moduli</u> (kPa)			<u>Poisson Ratios</u>			<u>Shear Moduli (kPa)</u>		
	E_a	E_b	E_c	ν_{ba}	ν_{ca}	ν_{cb}	G_{ab}	G_{bc}	G_{ca}
Fibrous (MAT_002)	2312	2312	115.6	0.27	0.07	0.07	910.2	1175	1175
Necrotic (MAT_001)	Isotropic material with $E = 1$ kPa, and $\nu = 0.499$								

*The subscripts a , b , and c represent longitudinal, circumferential, and radial directions, respectively, and lateral, elevation, and axial, respectively, in the ultrasonic coordinate definition.

boundaries of the model. The PML was implemented using the built-in PML models *MAT_230 (isotropic elastic) and *MAT_245 (orthotropic elastic) and matched to the material parameters of the NC and FC, respectively.

Following Palmeri et al. [176], the ARF field was simulated by first computing the acoustic intensity at each nodal location using Field II, a linear acoustics modeling package [269], [270]. A transducer was simulated using *xdc_focused_array* with a transmitting frequency of 4.2 MHz and focal configuration of F/1.5. Field II-derived intensity values were converted to point-load forces (\vec{F}) using the expression [230]:

$$\vec{F} = \frac{2\alpha\vec{I}}{c} \quad (7.1)$$

where α is the absorption coefficient of the medium (assumed to be 0.5 dB/cm/MHz), \vec{I} is the temporal-average beam intensity, and c is the speed of the sound through the medium (assumed to be 1540 m/s). Point loads were then superimposed on the FEM mesh, and a load curve was defined to simulate a 70- μ s ARF burst starting at 0.2 msec. The simulation was allowed to run for 4 ms total, and data were sampled every 0.1 ms, approximating a conventional ARFI ensemble with 10 kHz pulse repetition frequency (PRF). Note that luminal blood was not simulated with the FEM model, but implemented within the ultrasound simulation described below.

7.2.2 Ultrasound Simulations

The method of simulating ultrasound imaging of ARF-induced dynamics and luminal blood flow was adapted from those described by Palmeri et al. [230]. First, a three-dimensional Field II scatterer phantom with fully developed speckle (11 scatterers per resolution cell) was defined to span a volume of $11 \text{ mm} \times 11 \text{ mm} \times 40 \text{ mm}$ (lateral \times elevation \times axial). Nodal displacements output by LS-DYNA were loaded into MATLAB (Mathworks Inc., Natick, MA) and used to linearly-interpolate scatterer positions for every time step in the ARFI ensemble. To simulate a lumen, a wall-less, 3-mm radius tube of scatterers running parallel to the transducer face (i.e. in the lateral direction) was defined above the FC (which was positioned at 20 mm in the Field phantom). The lumen scatterers were translated at 100 cm/s with a parabolic flow profile to simulate carotid blood flow, and were assigned amplitudes 10 times less (-20 dB) than scatterers in the FC and NC. A percentage of scatterers in the lumen (10%) were kept stationary with full backscatter amplitude to represent clutter that is typically present in vascular ultrasound imaging. Overall, 20 unique phantoms with independent speckle realizations were generated.

Three imaging transducers with varying center frequencies (6 MHz, 9 MHz, and 12 MHz) were defined in Field II using *xdc_focused_array* to investigate the impact of tracking frequency on FC thickness measurement. All other relevant transducer parameters are given in Table 7.2. Two-dimensional ARFI acquisitions were simulated by translating each scatterer phantom laterally from -2.1 mm to 2.1 mm in steps of 0.35 mm. At each lateral position, RF data from each time step in the ARFI ensemble was calculated with Field II.

7.2.3 Processing of Tracked Data

After generating all the RF data, white Gaussian noise was added to each RF line in the ensemble prior to motion tracking using the *awgn* function in MATLAB to simulate 40 dB electronic signal-to-noise ratio (SNR). Ensembles were motion tracked with one-dimensional normalized cross-correlation with parabolic interpolation using kernel lengths ranging from 0.5λ to 4λ [206]. Two-dimensional peak displacement (PD) images were then rendered by taking the maximum displacement at each axial

Table 7.2: Simulation parameters.

Parameter	Value
Transducer	Linear array with elevational lens
Bandwidth	60%
Lens focus	20 mm
Sampling frequency	200 MHz
Speed of sound	1540 m/s
ARF excitation center frequency	4.21 MHz
ARF F/#	1.5
ARF apodization	None
ARF focus	20 mm
Tracking center frequency	6, 9, 12 MHz
Tracking Tx/Rx apodization	Hamming
Tracking Tx F/#	1.5
Tracking Rx F/#*	1.5
Tracking Tx focus	20

*Aperture growth and dynamic Rx focusing enabled

position, resulting in 4,800 images for analysis (3 frequencies \times 8 kernel sizes \times 20 speckle realizations \times 10 FC thicknesses).

7.2.4 Fibrous Cap Thickness Measurement

Due to the large number of images in the data set, a semi-automatic FC thickness measurement algorithm was developed that utilized simple k-means clustering (Figure 7.2). First, a 2D ARFI PD image was loaded and cropped between axial depths 19 and 24 mm, which approximated the ARFI depth-of-field for the simulated ultrasonic parameters. Next, the image was saturated to an ideal color scaling based on the FEM simulated displacements. Because PD was variable with various thicknesses of FC, a different color scaling was chosen for each thickness, and was calculated as a percentage of the distance between the FEM-measured PD in the FC and NC using a simple formula,

$$PD_{max} = PD_n - (PD_n - PD_f)\beta \quad (7.2)$$

where PD_{max} is the upper-limit of the PD dynamic range, PD_n and PD_f are the FEM-measured peak displacements in the NC and FC respectively, and β represents a fractional multiplier ($0 \leq \beta < 1$). A β -value of 0 represents the case where the image is scaled based on the maximum displacement of the NC.

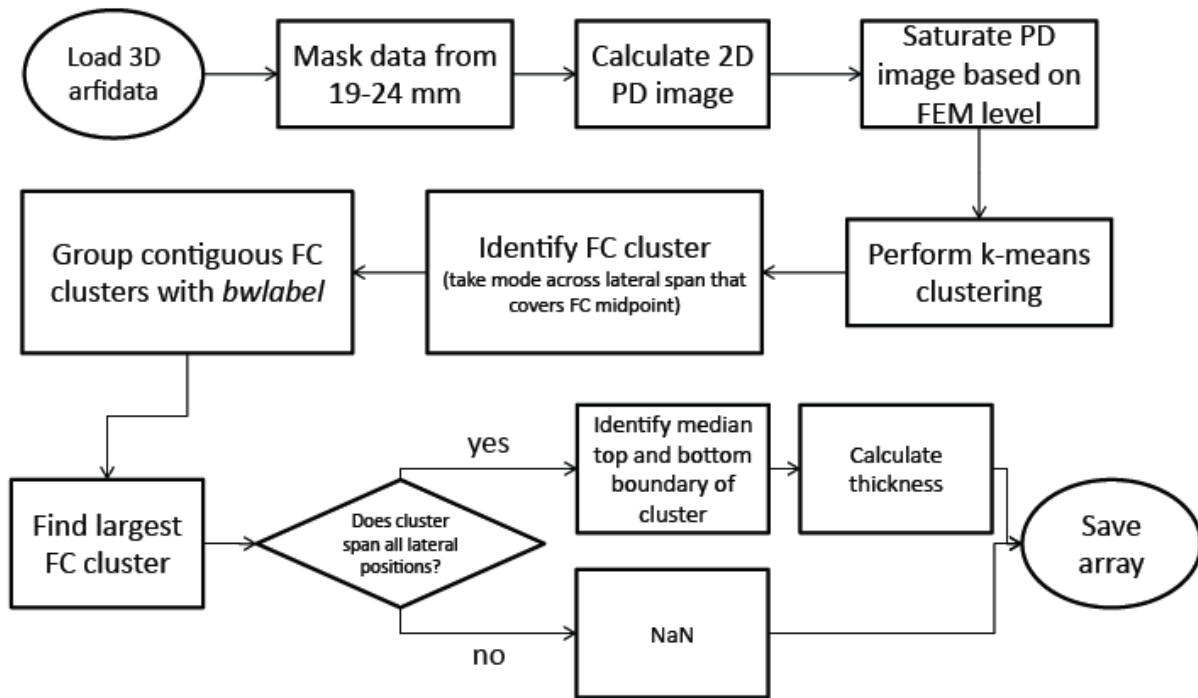


Figure 7.2: Block diagram describing the semi-automated FC thickness measurement procedure. FC, fibrous cap; PD, peak displacement; FEM, finite element method; NaN, not a number.

β -values greater than 0 represent increasing amounts of color saturation, which ultimately decreases the dynamic range of the PD image. The importance of color scaling is discussed in more detail in the following sections.

Next, the saturated image was passed into the *kmeans* function in MATLAB with the following parameters: cluster size of 4, uniform selection of initial cluster centroid positions, and 60 replicates. After clustering was complete, the cluster number corresponding to the FC had to be identified. This was done by taking the mode of the cluster map of all lateral locations at the axial position corresponding to the midpoint of the fibrous cap. With the FC cluster number identified, the largest contiguous cluster in this grouping was identified using *bwlabel*, and average thickness was measured by determining the top and bottom pixel of the cluster at each lateral location and calculating the median top/bottom across each image. If the largest contiguous cluster did not span the entire lateral extent of the ARFI image, this

indicated that the FC was not identified correctly or was otherwise not identifiable under the given imaging conditions and was assigned a value of NaN . This process was then repeated for every 2D ARFI image in the data set. An example of clustering and FC thickness measurement for a 0.5 mm FC thickness imaged at 9 MHz with a 1.5λ -tracking kernel is given in Figure 7.3.

Finally, a simple outlier rejection algorithm [271] was implemented to remove faulty clustering and spurious FC thickness measurements. For each simulated FC thickness, 20 measurements were taken representing one measurement from each speckle realization. Outliers were defined as any measurements that exceeded 3-times the median absolute deviation (MAD) of the given sample [271]. These data sets were rejected from the final analysis.

7.2.5 Additional Performance Metrics

In addition to measuring FC thickness, a number of metrics were computed across the simulations to characterize FC measurement performance. These metrics included contrast (C) and contrast-to-noise ratio (CNR) of the FC and NC, and were calculated using the following equations [131]:

$$C = 20 \log_{10} \left(\frac{\mu_n}{\mu_f} \right) \quad (7.3)$$

$$CNR = \frac{|\mu_n - \mu_f|}{\sqrt{\sigma_n^2 + \sigma_f^2}} \quad (7.4)$$

where μ_f and μ_n are the mean PD in the FC and NC, respectively, and σ_f and σ_n are the standard deviations of PD in the FC and NC, respectively.

7.2.6 Comparison with *In Vivo* Data

To validate simulation results, data were compared against two *in vivo* examples of carotid plaque with histologically verified fibrous caps from Chapter 6. As was done in the simulation study, *in vivo* data were motion tracked with eight kernel sizes whose length was determined with respect to the center frequency of the tracking pulses (6.15 MHz). To analyze the impact of color scaling, *in vivo* images were scaled using an adaptive algorithm that was previously described in Chapter 5. Plaque outlines were first

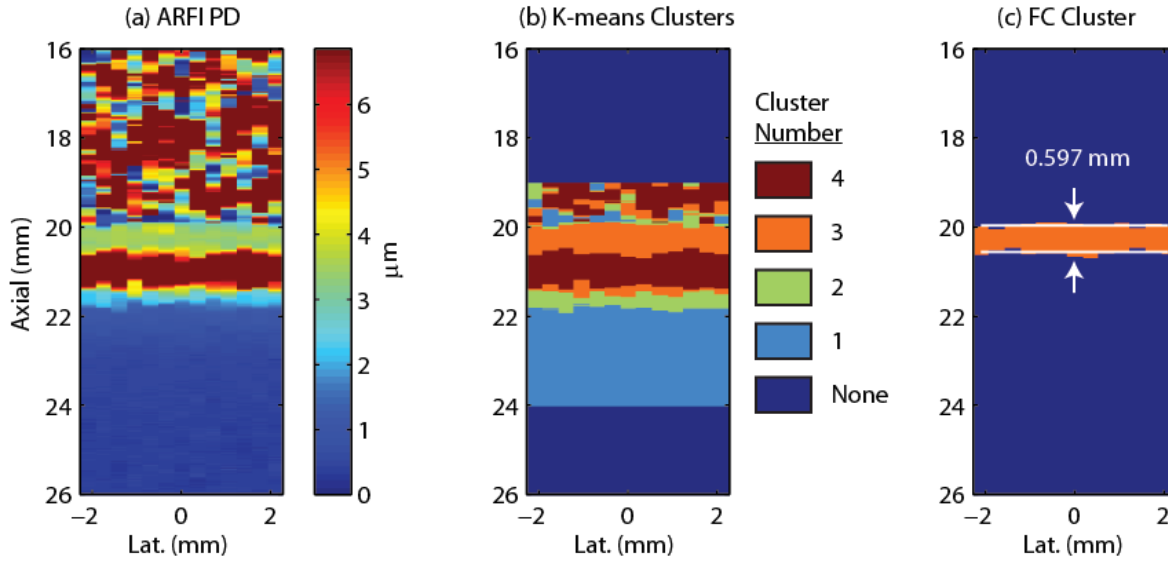


Figure 7.3: Example of k-means clustering algorithm and FC thickness measurement. Imaging parameters for the following data set were 9 MHz tracking pulse and 1.5λ kernel, and the simulated FC was 0.5 mm thick. (a) ARFI PD image. (b) Cluster image after performing k-means clustering. (c) Largest cluster corresponding to the location of the FC with semi-automatic thickness measurements (white lines) overlaid. The measured FC thickness in this example was 0.59 mm. FC, fibrous cap; PD, peak displacement; ARFI, acoustic radiation force impulse.

segmented by hand, and then the upper bound of the dynamic range of the ARFI image was set to the median + $2 \times \text{MAD}$ peak displacement calculated from the plaque outline. For additional test cases, images were scaled to median + $4 \times \text{MAD}$, and also scaled to the maximum PD within the necrotic core (representing an “unsaturated” image, similar to the $\beta = 0$ case described for the simulations). From these data sets, average fibrous cap thickness was measured from images by hand by drawing multiple lines using the *imdistline* tool in MATLAB. Finally, contrast and CNR were calculated between the FC and NC by drawing regions of interest around each respective feature and using the equations described above.

7.3 Results

To demonstrate the similarity between *in silico* and *in vivo* imaging scenarios, individual simulated ARFI lines were first compared against a clinical ARFI image of a carotid plaque. Figure 7.4(a)

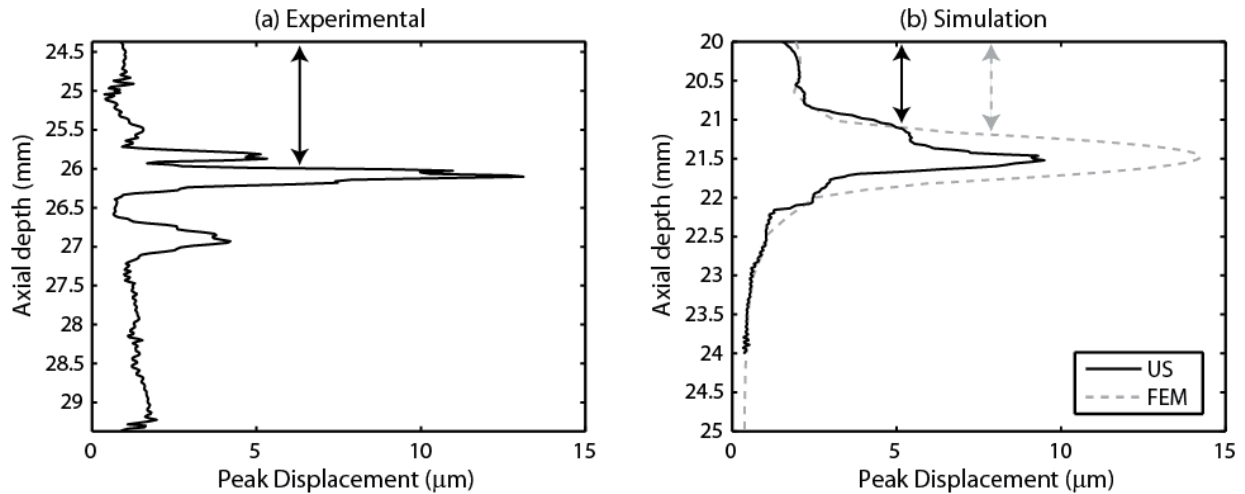


Figure 7.4: Comparison of FEM simulated data to an *in vivo* example. (a) ARFI peak displacement from *in vivo* example 1 (lateral position 3.63 mm). The fibrous cap appears as an area of low displacement from axial positions 24.5 mm to 26 mm while the necrotic core appears as an area of high displacement approximately spanning axial positions 25.5 mm to 27.5 mm. The full-width half-max of the fibrous cap is denoted by a black arrow. (b) Simulated data from FEM (gray, dashed line) and Field II (black, solid line) with fibrous cap thickness of 1 mm. The fibrous cap in the simulated data spans axial positions 20 mm to 21 mm, while the necrotic core spans positions 21 mm to 22 mm. Ultrasonic tracking of FEM displacements shows significant underestimation of displacement in the area of the necrotic core. The full-width half-max of the fibrous cap as measured by FEM and ultrasound are shown as gray and black arrows, respectively. US, ultrasound; ARFI, acoustic radiation force impulse; FEM, finite element method.

shows a plot of PD versus axial depth (oriented such that axial depth is on the Y-axis) taken from the 31st lateral location (3.63 mm) of the ARFI image shown in Figure 7.1. Figure 7.4(b) shows a corresponding simulation data set for an FC thickness of approximately the same size (~1 mm). Data in the *in vivo* image was tracked with 6.15 MHz and 1.5λ kernel, and is compared against a simulated data set at 6 MHz and 1.5λ kernel. In the *in vivo* example, PD in the FC (axial positions 24.5 mm to 25.5 mm) was approximately 1 μm while PD in the NC (axial positions 25.7 mm to 27.2 mm) reached as high as 13 μm . Similarly, the simulation predicted low displacement in the FC (axial positions 20 mm to 21 mm) of approximately 2 μm , and high displacement in the NC (axial positions 21 mm to 22 mm) of approximately 10 μm . Ultrasonic tracking of PD in the region of the NC underestimated the true PD by

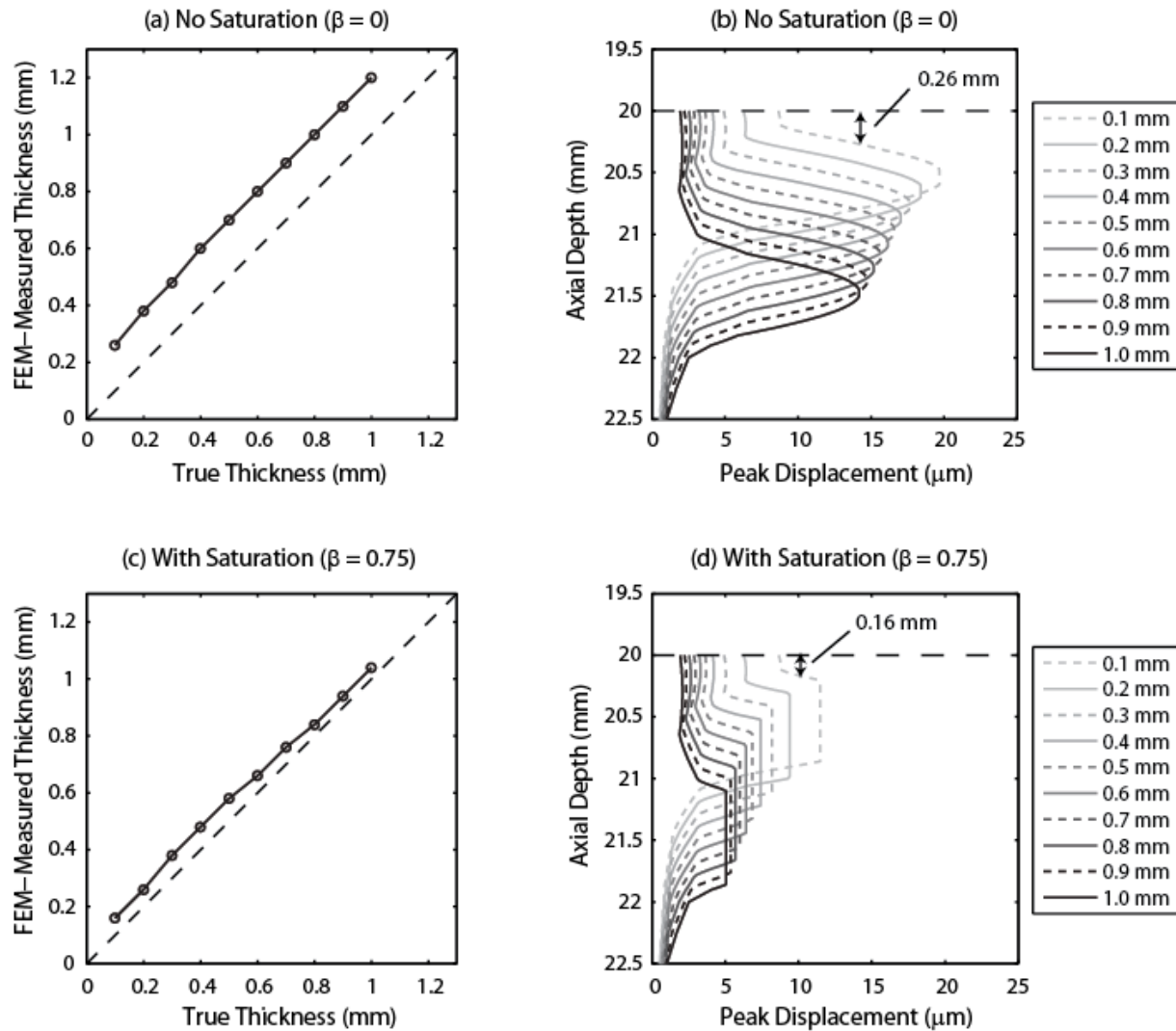


Figure 7.5: FEM-measured peak displacement results with and without saturation. (a) FEM-measured thickness versus true simulated thickness with no saturation. Dashed line indicates the line of equivalency. (b) FEM peak displacement profiles for all ten fibrous cap thicknesses with no saturation. Dashed line indicates border between lumen and fibrous cap. (c) FEM-measured thickness versus true simulated thickness with saturation. (d) FEM peak displacement profiles for all ten fibrous cap thicknesses with adaptive saturation. The cap thickness was measured as the full-width half-max between the fibrous cap and necrotic core layers, as shown by the black arrows in (b) and (d). Note that without saturation, FEM-measured thickness substantially overestimated the true simulated thickness due to mechanical coupling between the fibrous cap and necrotic core.

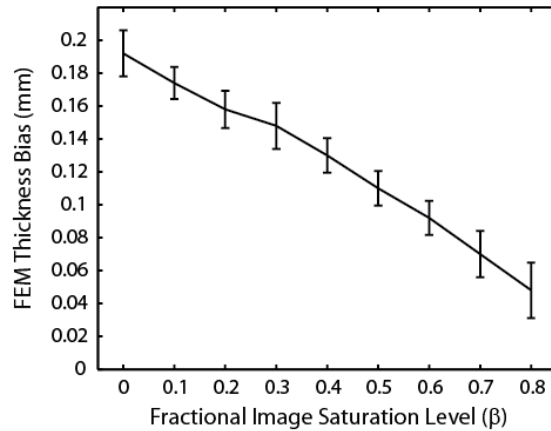


Figure 7.6: FEM thickness bias as a function of image saturation level. An image saturation level of 0 indicates the full dynamic range of peak displacement is used. Saturation levels greater than zero indicate reduction of dynamic range as depicted in Figure 7.5.

approximately 4 μm . This example suggests there was acceptable agreement between the FEM-simulations and data taken *in vivo* in a real carotid artery plaque.

Figure 7.5 shows the FEM-predicted PD profiles for all ten FC thicknesses simulated in this study, as well as a comparison of FEM-derived FC thickness measured as the full-width half-max (FWHM) between the FC and NC. The top row of images shows the results with no PD saturation ($\beta = 0$), while the bottom row of images shows the results with substantial PD saturation ($\beta = 0.75$). These simulations demonstrate that PD in the NC decreases as a function of FC thickness, suggesting that plaques with thin FCs may appear “softer” in ARFI images. Interestingly though, Figure 7.5(a) and (b) suggest that FC thickness measurements made with ARFI may experience a substantial positive bias (0.19 \pm 0.01 mm), particularly if the full dynamic range of PD is utilized. This bias arises not from ultrasonic imaging parameters, but rather from mechanical coupling between the stiff FC and soft NC. Coupling between these regions produces a gradient of PD at the interface between the layers, which changes the perceived location of the FC/NC edge. As demonstrated in Figure 7.5(c) and (d), the positive bias can be

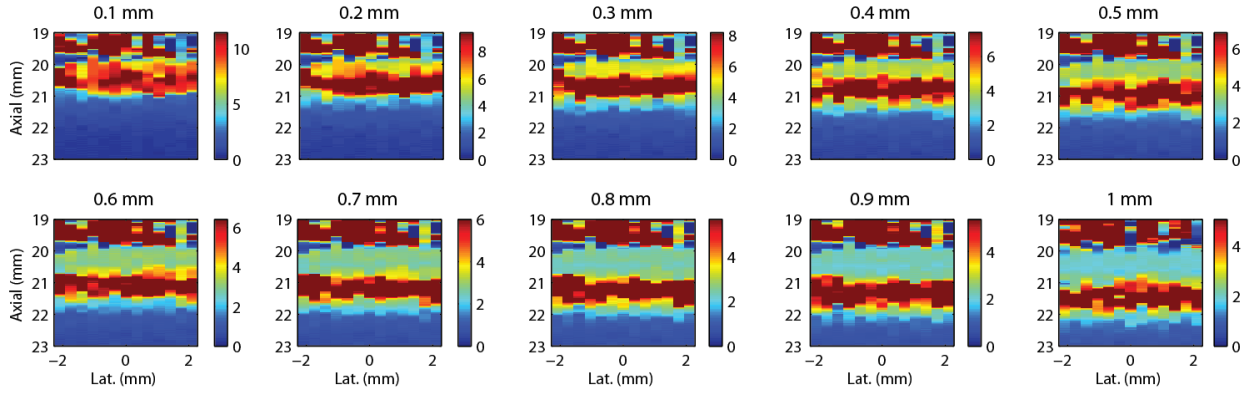


Figure 7.7: Examples of simulated 2D ARFI peak displacement images for the ten fibrous cap thicknesses taken with tracking pulses centered at 6 MHz and using a 1λ kernel (0.257 mm). The fibrous cap appears as a yellow-green band starting at axial position 20 mm. ARFI, acoustic radiation force impulse.

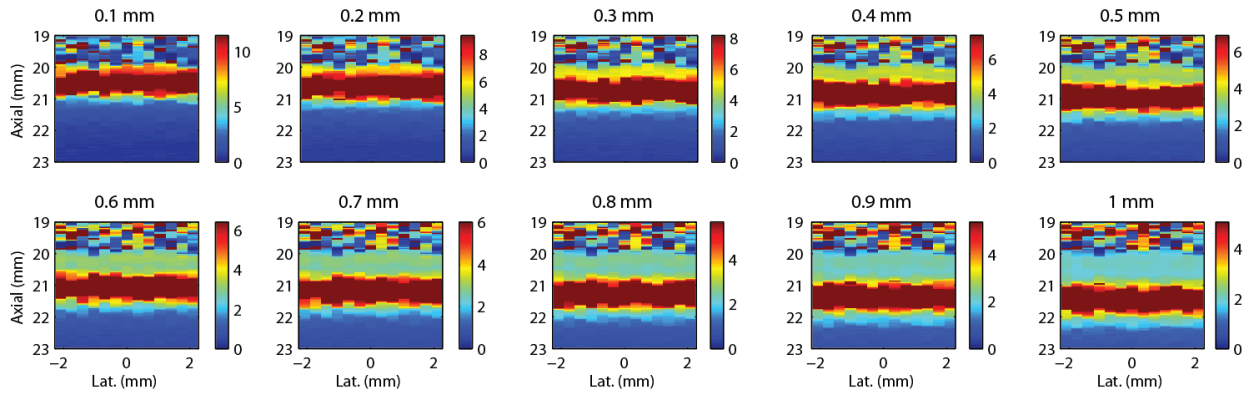


Figure 7.8: Examples of simulated 2D ARFI peak displacement images for the ten fibrous cap thicknesses taken with tracking pulses centered at 12 MHz and using a 2λ (0.257 mm) kernel. The fibrous cap appears as a yellow-green band starting at axial position 20 mm. Note that edge definition and contrast are qualitatively better compared to the lower tracking frequency shown in Figure 7.7. ARFI, acoustic radiation force impulse.

reduced substantially to $0.06 (\pm 0.016)$ mm if PD saturation is employed to reduce the dynamic range; however, no amount of saturation can remove it completely. This is depicted graphically in Figure 7.6, which shows the reduction of bias as a function of image saturation level.

Figure 7.7 and Figure 7.8 show examples of simulated ARFI images for all ten FC thicknesses taken at 6 MHz and 12 MHz, respectively, with adaptive color scaling. The absolute motion tracking kernel length was kept constant (0.257 mm) for both tracking frequencies, using a 1λ kernel at 6 MHz and

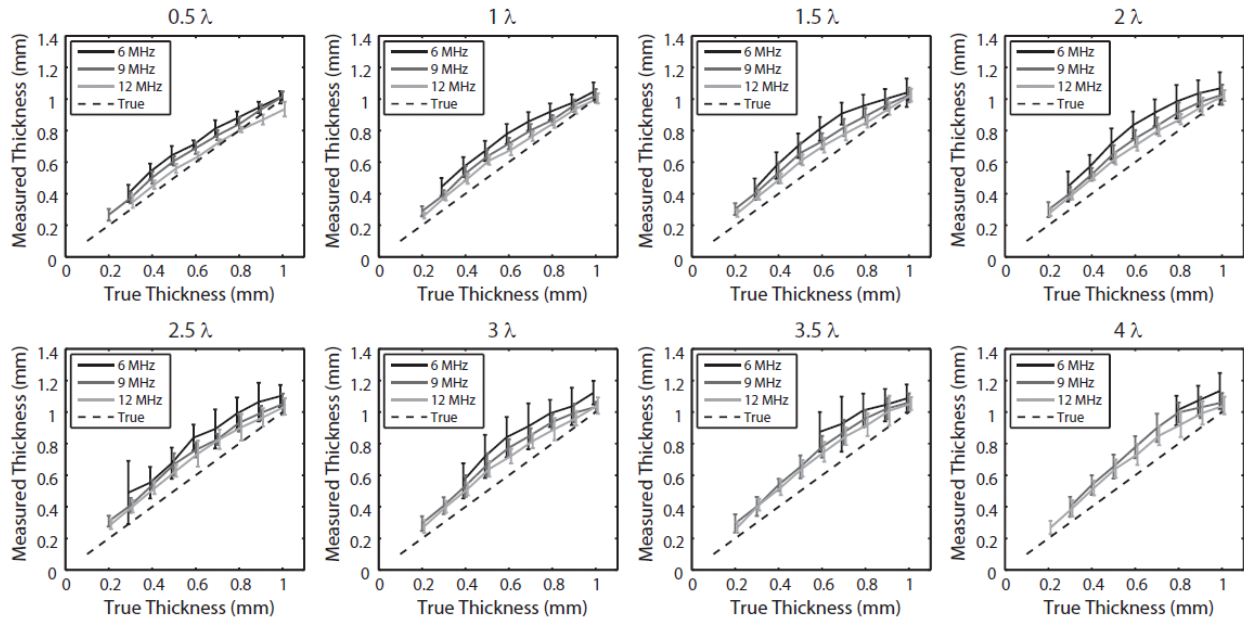


Figure 7.9: Simulated ARFI-measured fibrous cap thickness compared to true thickness grouped by relative kernel size (given as a fraction of wavelength, λ). Dashed line indicates the line of equivalency. ARFI, acoustic radiation force impulse.

2λ kernel at 12 MHz. In these images, the FC is denoted as a region of relatively low displacement (located between axial positions 20 mm and 21 mm), with the NC appearing as a region of high displacement directly below the FC regions. As expected based on the motion tracking kernel size, the stiff FC layer is difficult to resolve when it is 0.1 - 0.2 mm thick; however, at 0.3 mm it becomes readily identifiable, particularly at the 12 MHz frequency. Qualitatively, the images at 6 MHz appear notably worse (layer edges are less distinct, contrast is poorer, etc.) than at 12 MHz, despite having identical motion tracking kernel lengths, suggesting that higher frequency tracking is critical to FC thickness measurement performance.

These qualitative observations are confirmed in Figure 7.9 and Figure 7.10, which compare the ARFI-derived FC thickness to the true simulated thickness. Figure 7.9 depicts the results with respect to relative wavelength-based kernel sizes, while Figure 7.10 depicts the results with respect to absolute kernel sizes. In each of these graphs, the dotted line represents the line of equivalency. Cases where the algorithm failed to measure a FC thickness (i.e. values assigned as *NaN*) are not depicted and serve as a

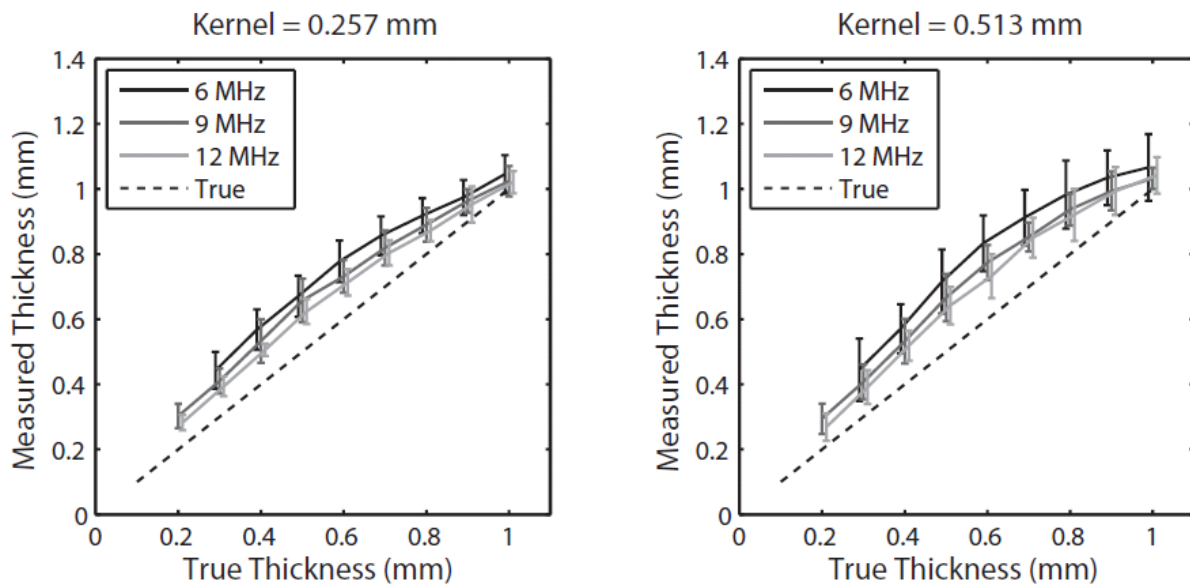


Figure 7.10: Simulated ARFI-measured fibrous cap thickness compared to true thickness grouped by absolute kernel length. The plot representing the 0.257 mm kernel sizes includes data for 1λ (6 MHz), 1.5λ (9 MHz), and 2λ (12 MHz). The plot representing the 0.513 mm kernel sizes includes data for 2λ (6 MHz), 3λ (9 MHz), and 4λ (12 MHz). Dashed line indicates the line of equivalency. ARFI, acoustic radiation force impulse.

lower limit for FC resolution for a given frequency and kernel size. A number of observations can be made from these results: 1) no combination of imaging parameters were able to resolve FC thicknesses of 0.1 mm, 2) the smallest resolvable FC with 6 MHz was 0.3 mm, while the smallest with 9 and 12 MHz was 0.2 mm, 3) positive bias and variance of FC measurement are inversely proportional to tracking frequency and directly proportional to kernel size. Interestingly, the positive bias decreased with increasing frequency even when kernel length was set to an absolute size (Figure 7.10). Finally, Figure 7.11 summarizes the results of FC detection accuracy by depicting bias as a function of kernel size and frequency. The lowest mean bias was achieved by a 0.064 mm (0.5λ) kernel at 12 MHz, however the variance on the estimates was higher compared to the next best performing kernel (0.128 mm, or 1λ , at 12 MHz).

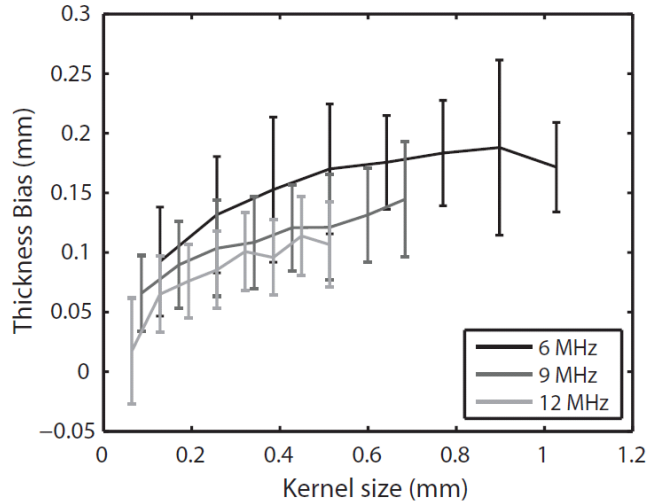


Figure 7.11: Simulated ARFI-measured thickness bias a function of absolute kernel size. ARFI, acoustic radiation force impulse.

Figure 7.12 shows the contrast between the FC and NC as a function of FC thickness using an absolute kernel length of 0.257 mm. Three levels of PD saturation are depicted ($\beta = 0.0$, $\beta = 0.5$, and $\beta = 0.75$). The dotted line indicates the inherent contrast calculated from FEM results directly. This figure demonstrates that PD contrast between the FC and NC increases nonlinearly with increasing FC thickness. Additionally, center frequency is demonstrated to be important in regards to contrast; higher center frequencies were able to capture more of the underlying contrast compared to the lower frequencies. The mean improvement in contrast between 6 MHz and 12 MHz was $1.8 (\pm 0.14)$ dB, however 12 MHz still underestimated the true tissue contrast by $2.1 (\pm 0.39)$ dB, which can be explained by displacement underestimation due to shearing [230], [272]. As PD saturation level increased, the inherent contrast in PD between the FC and NC was reduced proportionally, and the reduction in contrast due to displacement underestimation was mitigated. At significant levels of saturation ($\beta = 0.75$), the contrast achieved by 9 MHz and 12 MHz tracking was nearly identical. The effect of kernel size on contrast is depicted in Figure 7.13, which shows contrast as a function of kernel size for three FC thicknesses (0.2 mm, 0.5 mm, and 1 mm) and two dynamic ranges ($\beta = 0.0$ and $\beta = 0.75$). These figures

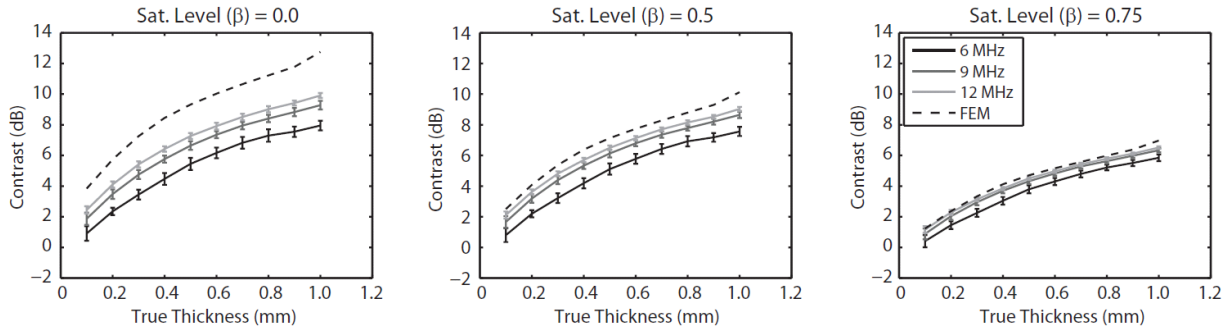


Figure 7.12: ARFI-measured contrast between the simulated fibrous cap and necrotic core layers as a function of fibrous cap thickness for three different saturation levels ($\beta = 0.0$, $\beta = 0.5$, and $\beta = 0.75$). Kernel size held constant at an absolute length of 0.257 mm. Dashed line indicates FEM-measured contrast. ARFI, acoustic radiation force impulse.

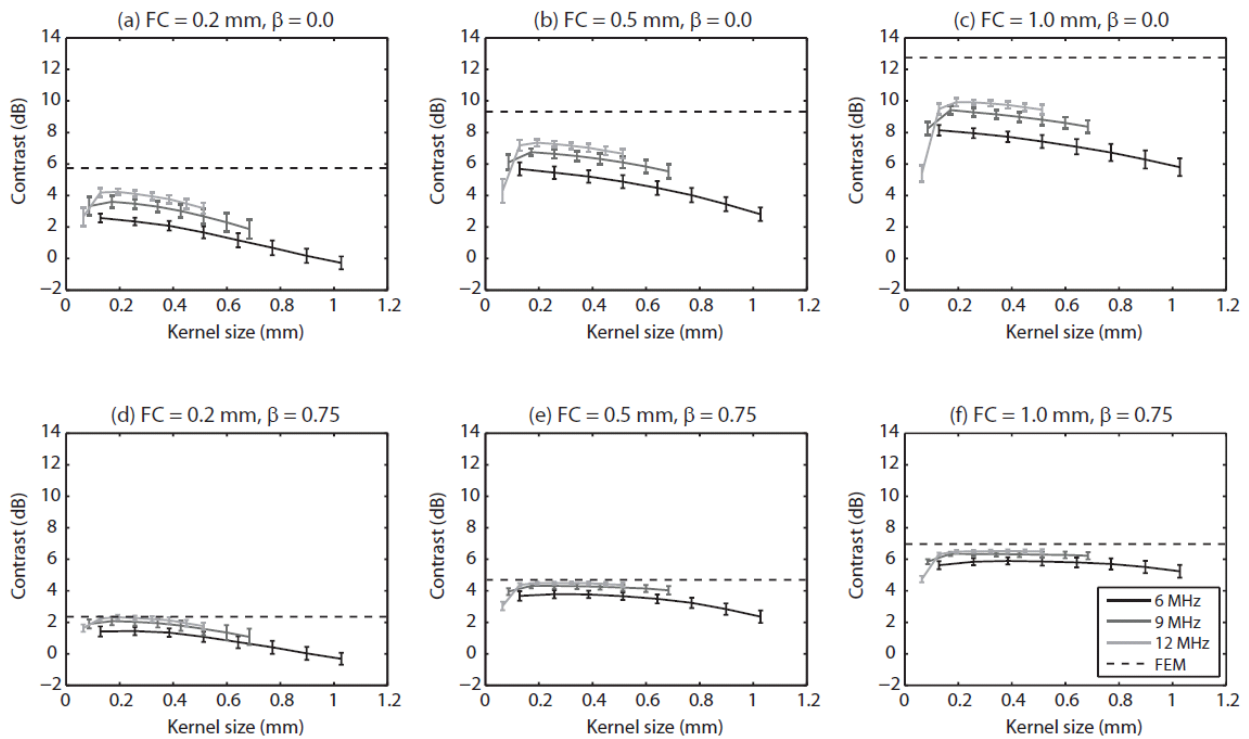


Figure 7.13: ARFI-measured contrast between the simulated fibrous cap and necrotic core layers as a function of absolute kernel size for three different fibrous cap thicknesses (0.2 mm, 0.5 mm, and 1.0 mm). The top row shows results for unsaturated images ($\beta = 0$), while the bottom row shows results for saturated images ($\beta = 0.75$). Note that saturation reduces contrast in some cases. Dashed line indicates FEM-measured contrast. ARFI, acoustic radiation force impulse; FC, fibrous cap.

show that both very small and very large kernel sizes tend to have poorer contrast, compared to intermediate kernel sizes. Specifically, in the 9 MHz and 12 MHz cases, there is a clear inflection point that occurs around the 1λ kernel size, where the contrast is maximized. Furthermore, image saturation effectively reduced contrast for all kernel sizes as shown in Figure 7.12. Interestingly, at high levels of image saturation, the difference in contrast between small and large kernels was not as pronounced as in Figure 7.13.

Figure 7.14 shows the CNR between the FC and NC as a function of FC thickness using an absolute kernel length of 0.257 mm. As was the case with contrast, this figure demonstrates that CNR also increases nonlinearly with increasing FC thickness. The mean improvement in CNR between 6 MHz and 12 MHz was $0.36 (\pm 0.05)$ with no color saturation, and increased to $0.66 (\pm 0.20)$ with the highest level of saturation ($\beta = 0.75$). The effect of kernel size on CNR is depicted in Figure 7.15 for two dynamic ranges ($\beta = 0.0$, and $\beta = 0.75$). Unlike contrast, which was typically maximized with small kernel sizes (i.e. 1λ) regardless of FC thickness, the kernel size that maximized CNR actually changed as a function of FC thickness. For thicker FCs, larger kernel sizes yielded higher mean CNR values, however higher variance of CNR was also observed. CNR versus kernel size plots for higher levels of saturation showed a similar trend, only with higher CNR values as was seen in Figure 7.14.

Figure 7.16, shows FC thicknesses measured from two carotid ARFI images taken *in vivo* (Chapter 6). Panels A and B (example 1) show the PD image and histology (combined Masson elastin stain; collagen in green) for a Type Va plaque in the common carotid of a symptomatic 57-year-old male. Panels C and D (example 2) show the PD image and histology (Lillie's-modified Masson's trichrome stain; collagen in blue) for a Type Va plaque in the internal carotid artery of a 53-year-old symptomatic female. In example 1, mean ARFI-derived FC thickness was $1.31 (\pm 0.07)$ mm and histology-derived mean thickness was $1.18 (\pm 0.30)$ mm, representing an 11.0% overestimation by ARFI. In example 2, mean ARFI-derived FC thickness was $0.92 (\pm 0.13)$ mm and histology-derived mean thickness was 0.88

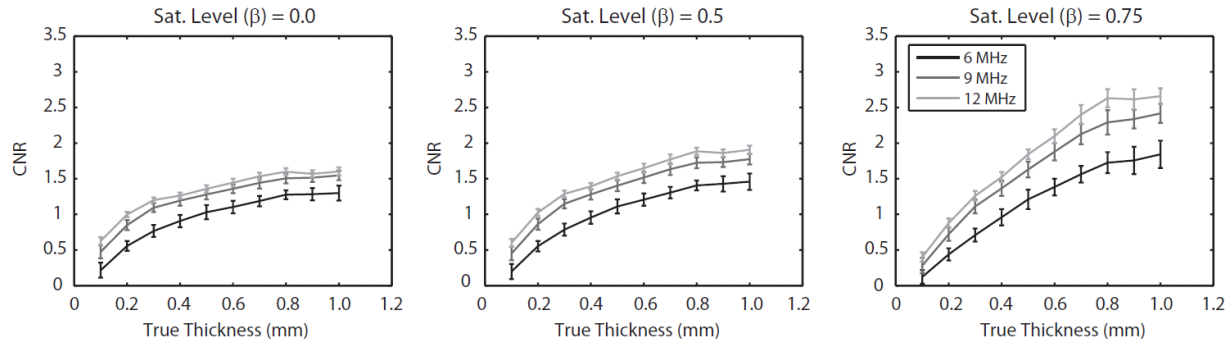


Figure 7.14: ARFI-measured CNR between the simulated fibrous cap and necrotic core layers as a function of fibrous cap thickness for three different saturation levels ($\beta = 0.0$, $\beta = 0.5$, and $\beta = 0.75$). Kernel size held constant at an absolute length of 0.257 mm. CNR, contrast to noise ratio; ARFI, acoustic radiation force impulse.

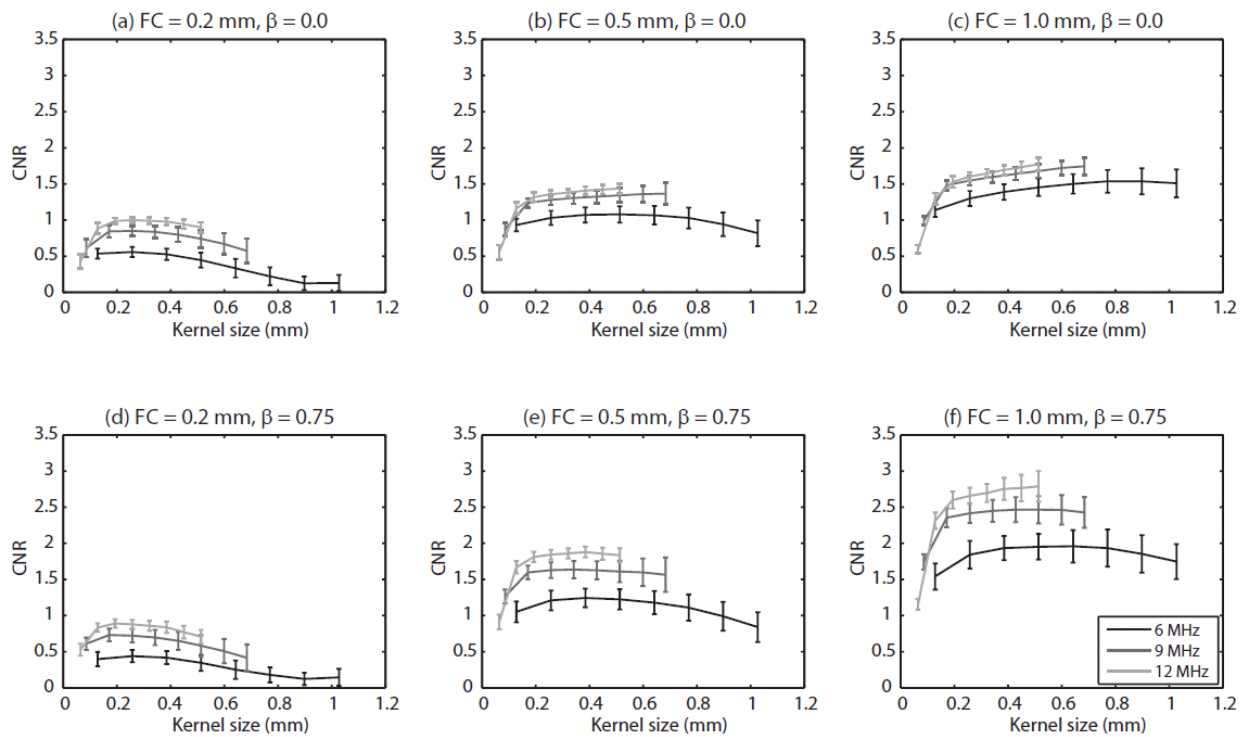


Figure 7.15: ARFI-measured CNR between the simulated fibrous cap and necrotic core layers as a function of absolute kernel size for three different fibrous cap thicknesses (0.2 mm, 0.5 mm, and 1.0 mm). The top row shows results for unsaturated images ($\beta = 0$), while the bottom row shows results for saturated images ($\beta = 0.75$). Note that saturation increases CNR in some cases. CNR, contrast to noise ratio; ARFI, acoustic radiation force impulse; FC, fibrous cap.

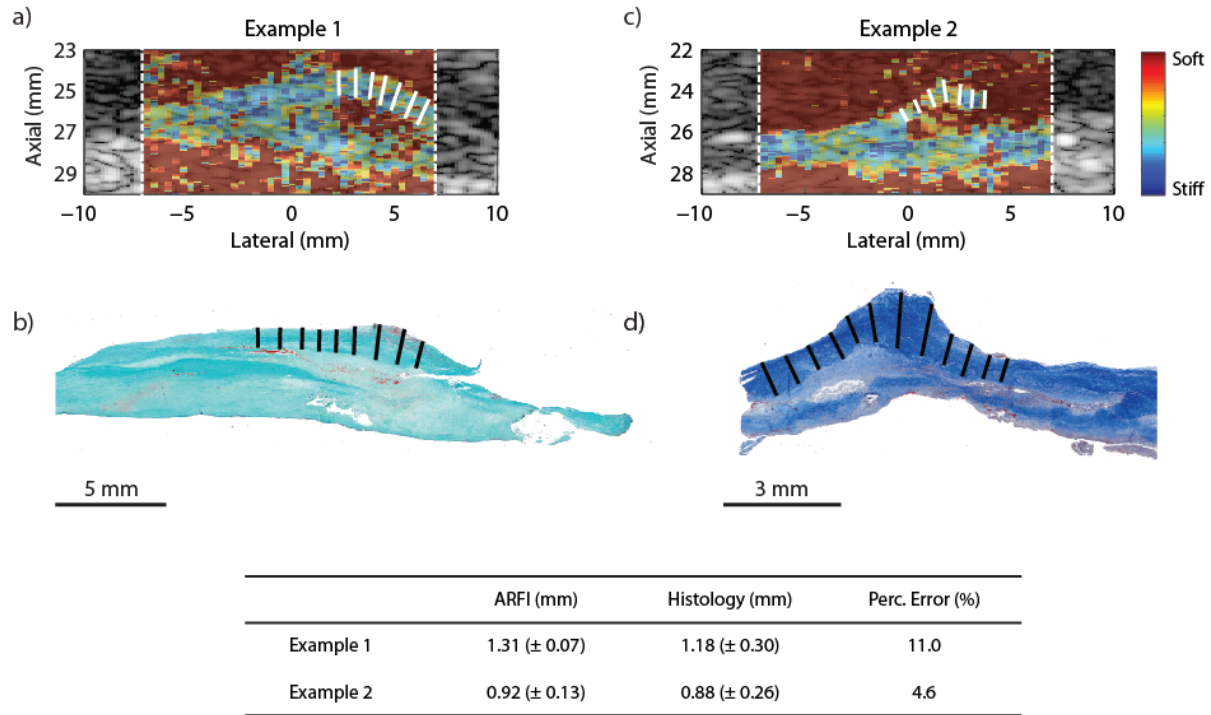


Figure 7.16: FC thicknesses measured from ARFI images taken in vivo and compared against histology. (a) ARFI PD image of a Type Va carotid plaque showing the FC measurement lines in white. (b) Combined Masson's elastin stain showing the FC thickness measurement for plaque example 1. (c) ARFI PD image of another Type Va carotid plaque. (d) Lillie's-modified Masson's trichrome stain for plaque in example 2. The table reports mean (\pm standard deviation) FC thicknesses measured from ARFI and histology as well as ARFI percent error. The tracking pulse frequency in these examples was 6.15 MHz, and a motion tracking kernel size of 1λ was utilized. Data to create this figure were adapted from Chapter 6.

(± 0.26) mm, representing a 4.6% overestimation by ARFI. Both images were captured with a tracking frequency of 6.15 MHz and processed with a 0.25 mm (1λ) kernel.

Figure 7.17 depicts the impact of kernel size and dynamic range on the two *in vivo* examples. ARFI images from example 1 are shown with four different kernel sizes (0.5λ , 1.5λ , 2.5λ , and 3.5λ) and two different dynamic ranges (maximum PD values set to $2.7 \mu\text{m}$ corresponding to median + $2*\text{MAD}$ and $4.2 \mu\text{m}$ corresponding to median + $4*\text{MAD}$). FC measurements are illustrated on the ARFI images as white lines, and average FC thickness for all eight kernel sizes and two dynamic range settings are quantified in the plot on the right. As predicted from the simulation results, higher kernel sizes

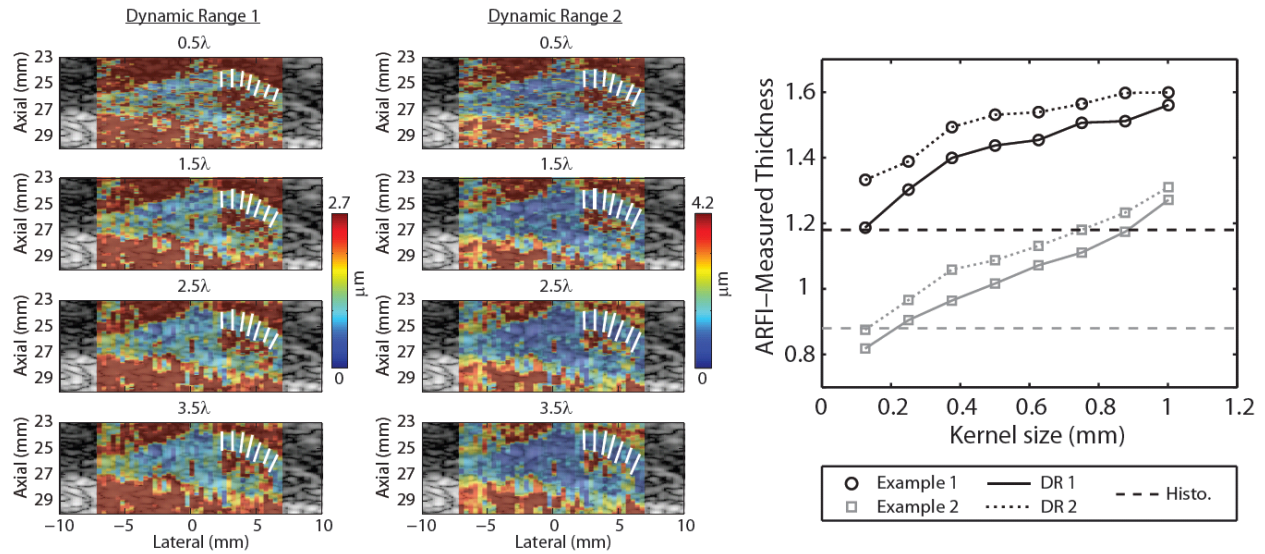


Figure 7.17: The impact of kernel size and dynamic range (DR) color scaling on mean ARFI-measured fibrous cap thickness for two *in vivo* examples. ARFI images, motion tracked with various kernel sizes from Figure 7.16 (example 1), are shown in two columns. The first column shows images scaled using the median + 2*MAD color scaling (for a dynamic range of 2.7 μm), while the second column shows images scaled using median + 4*MAD color scaling (for a dynamic range of 4.2 μm). Four motion tracking kernels for each color scaling are shown (0.5λ , 1.5λ , 2.5λ , and 3.5λ) and fibrous cap measurement lines are displayed as white lines. Mean fibrous cap thickness for all kernel sizes and both *in vivo* examples is shown in the plot on the right. Note that both larger kernel size and higher dynamic range increases measurement bias. ARFI, acoustic radiation force impulse; MAD, median absolute deviation.

introduced higher positive bias into the FC measurements. The magnitude of bias from kernel size in the *in vivo* examples (~ 0.4 mm with a 4λ kernel) was moderately larger than predicted by simulation (~ 0.25 mm). Additionally, larger dynamic range (akin to lower β values) also resulted in higher positive bias, again mirroring the simulations results.

Finally, *in vivo* results for contrast and CNR are shown in Figure 7.18. In this figure, data from the dynamic range with the lowest positive bias (i.e. median + 2*MAD) is graphed alongside data from an “unsaturated” dynamic range (i.e. the maximum PD in the necrotic core). As predicted from the simulations (Figure 7.13(c) and (f) and Figure 7.15(c) and (f)), saturation decreased contrast but increased CNR. The magnitude of decrease and increase varied between examples, with example 1 demonstrating the largest decrease in contrast (~ 6 dB) and increase in CNR (~ 0.5) with saturation. Interestingly, the

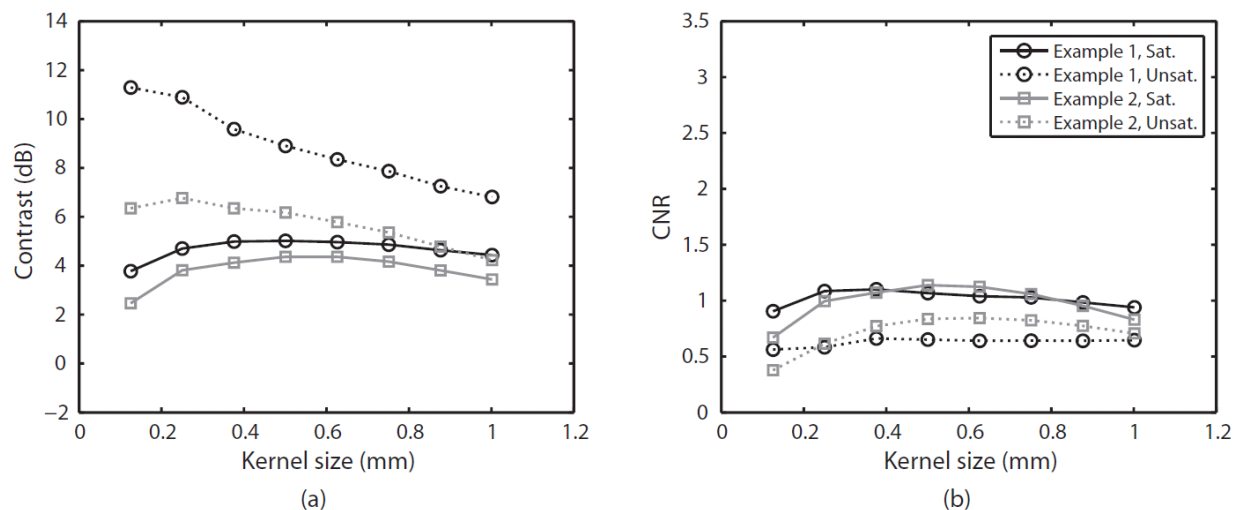


Figure 7.18: ARFI-measured contrast and CNR between the necrotic core and fibrous cap for two *in vivo* examples from Figure 7.16. In each plot, two dynamic ranges are shown; one scaled using the median + 2*MAD (solid lines), and the other scaled to the maximum displacement within the necrotic core, i.e. an unsaturated image (dashed lines). Note that the saturated and unsaturated cases loosely reflect the simulated $\beta = 0.75$ and $\beta = 0$ saturation levels, respectively, as depicted in Figure 7.13 and Figure 7.15.

overall magnitude of CNR in the *in vivo* examples was moderately lower than in simulation. For example, in simulations with 1.0 mm FCs and utilizing color saturation, the CNR values exceeded 1.5, however *in vivo* the color-saturated CNRs were closer to 1.0.

7.4 Discussion

In this study, a simulation framework for testing the capability of ARFI imaging to quantify the thickness of thin, mechanically stiff layers, representing atherosclerotic fibrous caps, was presented. As mentioned previously, to be clinically relevant for vulnerable carotid plaque characterization, an ARFI system should be capable of accurately detecting plaques with an average FC thickness of <0.5 mm and/or a minimum thickness of <0.2 mm. The results of this study suggest that 0.2 mm is actually the lower limit of ARFI's detection potential even with optimal imaging parameters, so while measuring caps less than 0.2 mm may be challenging, measuring caps around 0.5 mm should be feasible.

Three specific imaging parameters were explored in this study in detail – center frequency, kernel size, and image saturation level. It is well known that increasing center frequency improves the resolution of ultrasonic imaging, and, specifically in the context of ARFI imaging, has the added benefits of reducing motion tracking jitter [223] and increasing contrast by mitigating displacement underestimation from shearing [230]. Although the results shown in Figure 7.9 suggest that both the 9 MHz and 12 MHz tracking pulses performed similarly in terms of the smallest detectable FC (0.2 mm), the 12 MHz tracking pulses attained the lowest amount of positive bias (Figure 7.11), the highest contrast values (Figure 7.12), and the highest CNR values (Figure 7.14). This was mostly likely due to the shortened pulse length at higher frequencies (fractional bandwidth for each simulated transducer was held constant at 60%).

To date, ARFI plaque characterization in clinical studies has been implemented with 6 MHz [268] and 9 MHz [213] tracking pulses, but 12 MHz sequences have yet to be tested *in vivo*. At such high frequencies, depth of penetration may be an issue, however 12 MHz B-mode is currently the upper limit that is utilized in the clinic for carotid imaging [273], suggesting this frequency may be relevant in an ARFI setting as well. Another practical challenge for implementing ARFI with a 12 MHz tracking pulse is the requirement of increased transducer bandwidth in order to maintain a low center frequency for the ARFI pushing pulses. In this simulation study, the pushing pulse was kept constant at 4 MHz, which has typically been used in carotid ARFI studies done *in vivo*. Therefore, a transducer that can push at 4 MHz and track at 12 MHz would require a center frequency of 8 MHz and a minimum fractional bandwidth of 100% (or alternatively, a transducer centered at 12 MHz with fractional bandwidth of 67%). While this bandwidth requirement is high, advancements in transducer materials and design have demonstrated the capability of operating at greater than 100% bandwidth [274] suggesting this hurdle may be overcome as well.

In regards to kernel size, smaller kernel sizes were necessary to achieve more accurate measurement of the FC. For each center frequency that was tested, the smallest kernel size (0.5λ) resulted in the lowest positive bias (Figure 7.11). However, these kernel sizes also yielded lower CNR values (Figure 7.15) when compared to larger kernel sizes (e.g. 1λ or 1.5λ), indicating higher variance (i.e. jitter)

in motion tracking. These results are consistent with previous studies [206] that reported a tradeoff between bias and jitter when utilizing small, sub-wavelength kernel sizes. When kernel sizes become too small, corruptive jitter dominates the measurements and obviates the marginal improvement in bias. Notably, using large kernel sizes (e.g. 3λ or 4λ) also resulted in poor FC thickness measurement performance, as seen by the increased positive bias (Figure 7.11 and Figure 7.17), reduced contrast (Figure 7.13 and Figure 7.18), and even a reduction of CNR in some cases (Figure 7.15 and Figure 7.18). The benefits of using a large kernel are mainly related to the reduction in jitter; however, due to the thin size of the feature being measured, large kernel sizes quickly exceed the size of the FC and cause undesirable averaging and smoothing to occur, making their implementation impractical in this application of ARFI. Therefore, based on the simulations and preliminary *in vivo* results, a kernel size of 1λ or 1.5λ is recommended for clinical implementation of FC thickness measurement.

Lastly, image color saturation was determined to be highly important for accurate measurement of the FC, largely due to the mechanical coupling between the FC and NC. As seen in Figure 7.5 and Figure 7.6, the ideal saturation level occurs when the maximum PD in the image is capped to a certain percentage above the PD in the FC. By saturating the image, the inherent contrast in PD between the FC and NC is reduced (Figure 7.12) in order to improve the bias. Interestingly, high levels of saturation can obviate the impact of displacement underestimation, which substantially reduces the PD measured in the soft NC and ultimately reduces contrast from the FC. This effect can be observed in Figure 7.12(c) where the ARFI-measured contrast nearly matches the FEM-measured contrast after saturation. Further, saturation improves the CNR metric, as seen in Figure 7.14(c), due to the reduction in PD variance in the NC.

In the simulations, the image saturation level was chosen adaptively based on the known FEM displacements in the regions of FC and NC. In practice, these PD values are not known *a priori*, making adaptive color saturation one of the most significant challenges for ARFI in this application. In order for ARFI to be able to consistently quantify FC thickness, a standardized color-scaling algorithm will need to be developed. It was previously proposed to set the color scaling based on the median PD measured

across the entire plaque (Chapter 5), and this same scheme was utilized for the two clinical examples presented in Figure 7.16. In both cases, the chosen color scaling demonstrated good contrast between the NC and the FC, and the positive bias in the ARFI-derived thickness measurements (0.13 mm and 0.04 mm) agreed with the predicted bias of 0.13 (± 0.05) for the corresponding frequency and kernel size (Figure 7.11) suggesting appropriate color scaling was used. However, due to the limited number of *in vivo* cases, further studies are necessary to determine if this color-scaling algorithm is relevant for wide-scale application to carotid ARFI images.

There were a number of potential limitations in this study. First, all simulated FCs were highly idealized, oriented perfectly orthogonal to the axial direction of the transducer, and were of homogeneous thickness across the lateral dimension. In reality, as seen in Figure 7.16, plaques may have curvature, may be imaged at non-90° angles relative to the transducer due to patient anatomy, and may have variable thickness across the lateral field of view. The lateral resolution of an ARFI system is expected to be worse than the axial resolution, and displacements may experience more averaging bias due to side lobes of the tracking point spread function, which may explain the increased kernel bias observed in the *in vivo* data set as compared to the simulation (Figure 7.17). Therefore, it is predicted that utilizing the highest tracking frequency may be even more beneficial to making FC thickness measurements *in vivo* than shown in this manuscript. A second limitation to this study was in the modeling of the layer interfaces, specifically the lumen/FC interface and the FC/NC interface. The lumen/FC interface was not simulated with FEM, meaning that the mechanical interaction between lumen and the FC was not evaluated in this study. It is possible that the forces exerted on the FC by flowing blood may impact displacements measured with ARFI, however the similarity observed between simulation and *in vivo* data sets suggests that this impact should be minimal (note that *in vivo* data sets were gated to diastole, where blood flow is expected to be at its slowest). Regarding the FC/NC interface, as shown in Figure 7.5, mechanical coupling between the FC and NC layers significantly impacted bias in layer thickness measurement. It is unclear whether this coupling accurately modelled the mechanical interaction between the two features *in vivo*. Indeed, NCs have sometimes been described as “semi-solid” [275], and previous studies have shown

that atheroma lipids can exist in any of three states; liquid, liquid crystalline, or crystalline [251], suggesting the mechanical coupling between the FC and NC may be more complicated, e.g. as a fluid-solid interaction. Anecdotal evidence from our two *in vivo* examples suggests sharper transitions between the FC and NC, which could indicate a weaker mechanical coupling than was modelled in this study; however, more data need to be collected before this observation can be confirmed.

7.5 Conclusion

Overall, these simulation studies have demonstrated the feasibility of quantifying the thickness of thin, stiff layers with transcutaneous ARFI imaging and provide insight into the factors impacting ARFI's ability to quantify fibrous cap thickness in carotid plaques. The FEM results revealed that mechanical coupling between the stiff and soft layer may introduce substantial positive bias into the ARFI measurements. To counteract this positive bias, image contrast saturation can be utilized to reduce the dynamic range of the ARFI image and improve the thickness measurement. Regarding ultrasonic tracking parameters, the results suggest that utilizing high center frequency tracking pulses (12 MHz) achieve the best thickness measurements as seen by the lower bias, higher contrast, and higher CNR. The results also demonstrated that motion-tracking kernel size can have a large impact in thickness measurements performance; setting the kernel too small will cause large amount of jitter and decrease CNR, while setting the kernel too high will introduce large amounts of positive bias. In each case, using a kernel size of approximately one wavelength gave the optimal balance between bias, contrast, and CNR. In two *in vivo* clinical examples, one with a 0.88 mm cap and the other with a 1.18 mm cap, ARFI was able to measure average FC thickness to within 11% error of the histologically verified thickness. Given appropriate imaging parameters, these simulations suggest that transcutaneous ARFI may be capable of measuring average carotid fibrous cap thickness of 0.2 – 0.3 mm, which could aid in the stratification of plaque vulnerability for rupture and future ischemic event.

CHAPTER 8

ARFI-Derived Carotid Plaque Stiffness Measurements Compared with Histology II: In Vivo Assessment of Fibrous Cap Thickness and Rupture

8.1 Introduction

In this chapter, we continue our analysis of ARFI images taken in patients undergoing CEA and present a comprehensive case-by-case analysis of all plaques that were imaged during the course of our clinical study. In our preliminary analysis of data collected early in the study (Chapter 6 and Chapter 7), we gained a considerable appreciation for the challenges involved with comparing ultrasound images to histological CEA samples. In particular, two of the greatest difficulties that we encountered were maintaining plaque alignment between ultrasound and histology and processing heavily calcified samples.

In the literature, the most common approach to processing heavily calcified samples is to simply decalcify them prior to embedding. This approach can pose problems for an imaging validation study such as this one where quantifying performance for detecting calcium is a main goal [276]. Indeed, in Chapter 6 we avoided decalcification of our samples in order to prevent missing important features. This decision turned out to be moderately beneficial in the two Type Va plaques (small calcifications could easily be identified on VK staining and even used to aid in specimen alignment) but was detrimental in the two Type Vb plaques, causing histological slices to be torn during sectioning. A solution to this was found in the CT literature [76], in which the authors utilized *ex vivo* μ CT of CEA samples prior to

© 2015 IEEE. Portions reprinted, with permission, from T. J. Czernuszewicz, J. W. Homeister, M. C. Caughey, M. A. Farber, J. J. Fulton, P. F. Ford, W. A. Marston, R. Vallabhaneni, T. C. Nichols, and C. M. Gallippi, "In vivo carotid plaque stiffness measurements with ARFI ultrasound in endarterectomy patients," in Proc. IEEE Ultrason. Symp., Taipei, Taiwan, 2015.

decalcification to serve as the gold standard for calcium deposition. This study showed that CT had perfect sensitivity and specificity for calcifications and that μ CT could yield isotropic resolution down to 30 μ m. Therefore, we decided that the optimal processing approach for our CEA specimens going forward would be to scan samples *ex vivo* with μ CT followed by decalcified histology.

As will be described in this chapter, this approach not only made processing and spatial alignment of calcified samples possible, but also improved our selection of the histological cutting plane.

8.2 Methods

The *in vivo* imaging methods implemented in this chapter utilize many of those described in Chapters 6. They are reiterated here briefly, but the reader is referred to the previous chapters for more detail.

8.2.1 Patients

Data sets were obtained from an additional seventeen patients undergoing clinically indicated CEA at UNC Hospitals (bringing the total enrollment to N = 25). Inclusion criteria remained the same; individuals with either symptomatic carotid artery disease with a stenosis in the carotid artery thought to be the source of emboli or asymptomatic carotid artery disease with >60% stenosis that were unresponsive to medical management were enrolled. Institutional review board (IRB) approval was obtained and informed consent was given from each study participant.

8.2.2 Ultrasonic Imaging

ARFI imaging was performed using the same ultrasound system and imaging parameters described in Chapter 6. The imaging protocol was modified slightly to include the capture of additional transverse B-modes of the carotid bifurcation (by rotating the transducer 90° from the longitudinal imaging plane). Both static B-modes and CINE loops of the sonographer sweeping the transducer up from the common carotid were captured to aid in specimen alignment.

Signal processing of raw RF data was done as described in Chapter 6 using normalized cross correlation and linear motion filtering to measure ARFI displacements. PD images were rendered and the dynamic range was set using the adaptive color saturation approach described in Chapter 7. This process involved outlining the plaque manually, and then setting the maximum of the dynamic range to the median PD plus two median absolute deviations (MAD).

8.2.3 *Ex Vivo* Specimen Imaging

Extracted CEA specimens were immediately photographed and transferred to 10% neutral-buffered formalin for a minimum of 48 hours. After fixation, *ex vivo* μ CT imaging was performed on the samples with a Scanco μ CT 40 (Scanco Medical AG, Bassersdorf, Switzerland) at 20- μ m isotropic voxel resolution. To mount the specimen for μ CT imaging, a Styrofoam packing peanut was placed at the bottom of the μ CT cassette to serve as a radiolucent spacer. To prevent sample dehydration, a small amount of formalin was poured into the μ CT cassette, and the cassette was sealed by stretching Parafilm across the top opening. Scan times varied depending on the length of the specimens, but on average, were approximately 30 minutes long.

Post-processing of the μ CT data involved a number of steps. First, the raw DICOM files were imported into Fiji (<http://fiji.sc>), an open source image processing toolkit based on NIH ImageJ, in order to downsample the μ CT volume and crop the outline of the μ CT cassette. Downsampling was done to reduce computational overhead when volume rendering and was achieved using the Import -> Image Sequence option in Fiji to isotropically reduce the data by a factor of 2 (increasing voxel size to 40 μ m). Next, a single image frame in the sequence that only displayed the outline of the μ CT tube was identified, and the inner ring of the tube was segmented using the Magic Wand tool and Thresholding. All pixels outside of the inner ring were cleared using the Edit -> “Clear Outside” option, and the setting was applied to all image frames in the volume. The edited volume was then exported to a Stacked TIFF file.

Stacked TIFF volumes were imported into 3D Slicer 4.3.1 (<http://www.slicer.org>), a freely available medical image processing and volume-rendering software. First, the volume was segmented

into two tissue types – calcifications and soft tissue – by defining two label maps in Slicer. Segmentation was achieved by using empirically determined thresholds on pixel intensity values (which were 16-bit integers ranging in value from 0 to 2^{16}). Calcification was identified as any pixel exceeding a value of 38,000, while soft tissue was identified as pixels ranging between 33,500 and 37,000. Spurious pixels were removed using the Remove Island Effect (with Morphology Method) option in Slicer. After segmenting the volume, the axial (red) slice was adjusted to match the vessel morphology, such that it yielded a true axial view of the specimen (i.e. a transverse slice of the carotid). With the axial panel aligned, the carotid bifurcation was identified, and the slice was rotated to match the ICA/ECA orientation from *in vivo* transverse B-modes captured at the time of ARFI imaging. Finally, the sagittal (yellow) slice was displayed and adjusted to represent the orthogonal view that would be achieved by rotating the transducer 90° and compared to the longitudinal B-mode images. In this way, the approximate location of the ultrasound-imaging plane could be located, and used to guide histological sectioning.

8.2.4 Histology

After *ex vivo* imaging, samples were decalcified for at least 24 hours with Immunocal decalcifier (StatLab Medical, McKinney, TX). Next, specimens were cut longitudinally into two halves following the ultrasound plane predicted from μ CT and B-mode, and marked with tissue marking dye (Polysciences Inc., Warrington, PA) to indicate sample orientation. Once the tissue was marked, gross microscopic images of the luminal surface ($6.3\times$ magnification) were taken with a dissecting microscope (MZ9.5, Leica Microsystems GmbH, Wetzlar, Germany) for reference, and the tissue was embedded in paraffin. In most cases, the cutting plane was oriented with the surgeon's anterior/longitudinal incision, however, when it did not, samples were embedded whole to prevent fragmentation (in which case, no dissecting-microscope images were captured). Samples were then sectioned with a microtome at 5- μ m slice thickness and stained with hematoxylin and eosin (H&E) and a combined Masson's elastin (CME) stain for collagen and elastin.

Table 8.1: Patient characteristics.

	Total (N = 25)
Male (number)	16 (64%)
Age (years)	62.4 ± 10.52
Doppler-indicated systolic velocity (cm/s)	404.68 ± 131.18
Doppler-indicated diastolic velocity (cm/s)	150.91 ± 63.89
Symptomatic	18 (72%)
Amaurosis fugax	5
TIA	8
Completed stroke	6
ARFI focal depth (cm)	2.2 ± 0.42
Peripheral vascular disease	9 (36%)
Diabetes mellitus	6 (24%)
Hyperlipidemia	22 (88%)
Hypertension	22 (88%)
Smoking history	21 (84%)

Histological slides were digitized with a Scanscope slide scanner (Aperio Technologies Inc., Vista, CA) at 20× magnification. A pathologist examined and manually segmented the digitized slides using ImageScope (Aperio Technologies Inc., Vista, CA), a freely-available slide viewing/annotation software package, and indicated areas of necrotic core, fibrous cap, calcification (with help from the μ CT images), fibrosis, and hemorrhage. Fibrous cap thickness was manually measured from pathologist annotations by drawing lines with the *imdistline* tool in MATLAB. After annotation, plaques were assigned grades based on the American Heart Association (AHA) plaque classification system [16].

8.3 Results

Carotid plaques were successfully imaged without adverse event from an additional 11 males and 6 females. Of these samples, 3 were noted to be badly damaged/fractured after surgery and were difficult

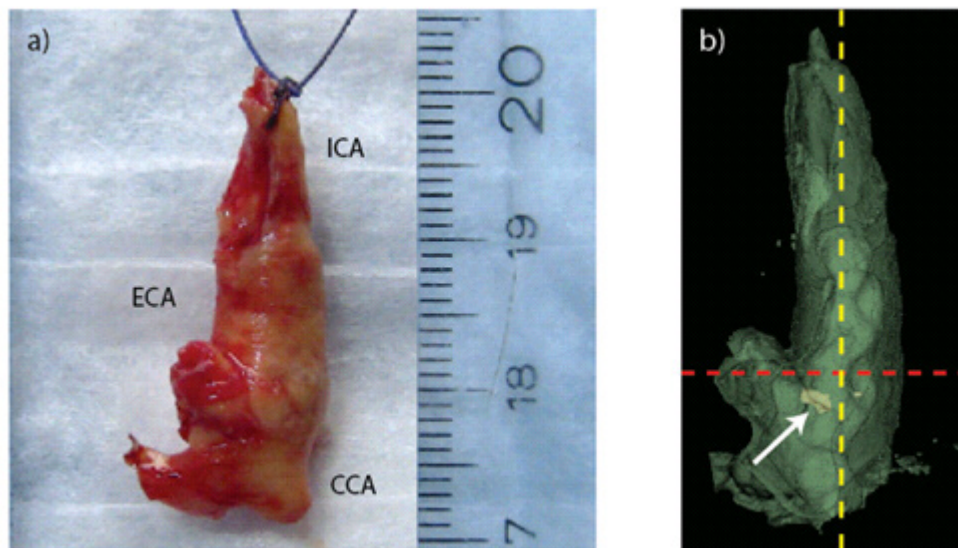


Figure 8.1: Comparison of gross CEA specimen and μ CT 3D rendering. (a) Gross photograph of CEA specimen. (b) 3D rendering of μ CT volume. Green pixels represent soft tissue while yellow pixels represent calcium. Only one small calcification was seen in this plaque, located directly at the bifurcation (white arrow). The dashed lines represent positions of the axial (red) and sagittal (yellow) slices that correspond with the transverse and longitudinal ultrasound images.

to align, and 14 underwent μ CT imaging. Patient characteristics for the full data set including patients from Chapter 6 are given in Table 8.1 (N = 25 patients).

Figure 8.1 and Figure 8.2 show an example of how specimens were aligned using μ CT. This particular sample was extracted from a symptomatic (TIA) 71 year-old male with a past medical history of coronary artery disease, myocardial infarction, and previous contralateral CEA. Figure 8.1 shows the gross specimen photograph next to a 3D μ CT rendering in a coronal perspective. The bifurcation is clearly identified at the bottom of the specimen in both photograph and 3D rendering, and is confirmed by the surgeon's suture which marks the cephalad portion of the ICA. The axial and sagittal slices (oriented dynamically with Slicer) are depicted with red and yellow dashed lines. From the μ CT data, a small calcification is identified almost precisely at the location of the bifurcation (white arrow). *In vivo* B-mode imaging of the bifurcation shows that the ICA and ECA in this patient were oriented next to each other

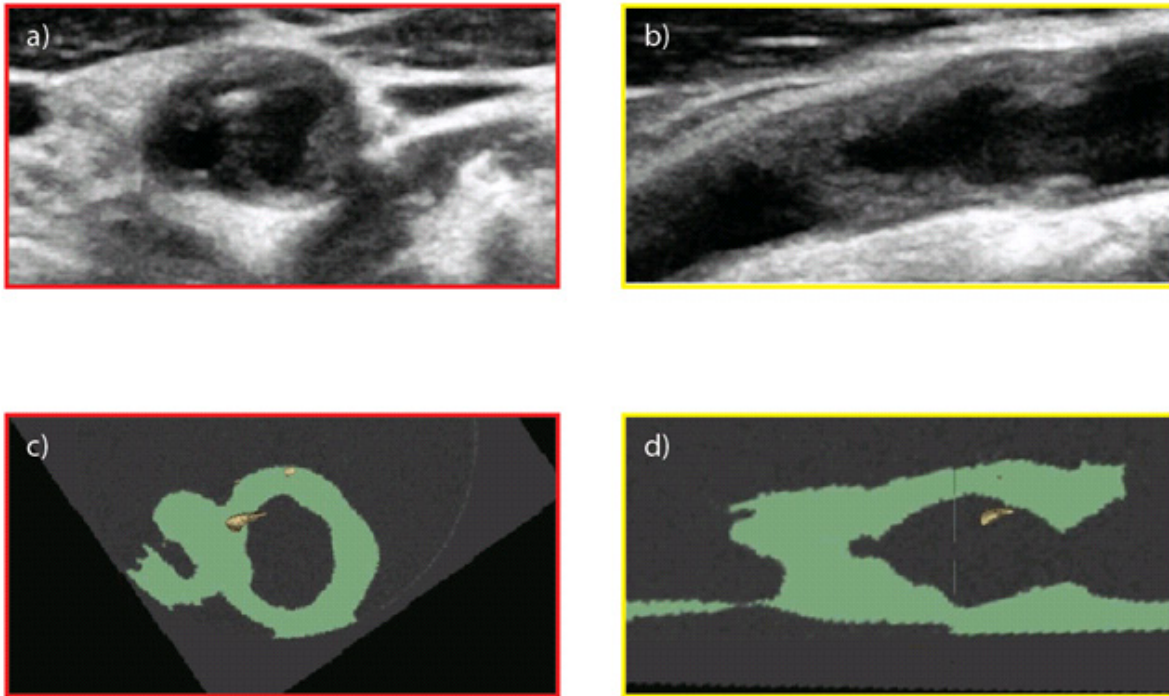


Figure 8.2: Example of plaque alignment using ex vivo μ CT imaging. (a) Transverse B-mode image showing the carotid bifurcation. The small calcification appears as a bright spot in the B-mode. (b) Longitudinal B-mode of the ICA showing a focal stenosis just past the bifurcation. (c) Axial slice through μ CT volume positioned such that the ICA and ECA orientation match the *in vivo* B-mode. (d) Sagittal slice through μ CT volume showing nice agreement with longitudinal B-mode. The orientation determined in panels (c) and (d) guided how the sample was embedded for sectioning. The 3D rendering of the μ CT volume is shown in Figure 3.2.

(Figure 8.2a), and that there was substantial stenosis in the proximal ICA (Figure 8.2b). Aligning the μ CT volume to the transverse B-mode (Figure 8.2c), and taking the corresponding sagittal slice yielded a μ CT image that matched nearly perfectly with the longitudinal B-mode (Figure 8.2d). Note that B-modes shown in Figure 8.2 were taken from the patient's medical record and not captured simultaneously with ARFI imaging. Finally, the matching histological plane and corresponding ARFI image are shown in Figure 8.3. Histology demonstrated that this was a complicated Type VI plaque with a large necrotic core and ruptured fibrous cap at the point of maximal stenosis identified previously by B-mode. ARFI-

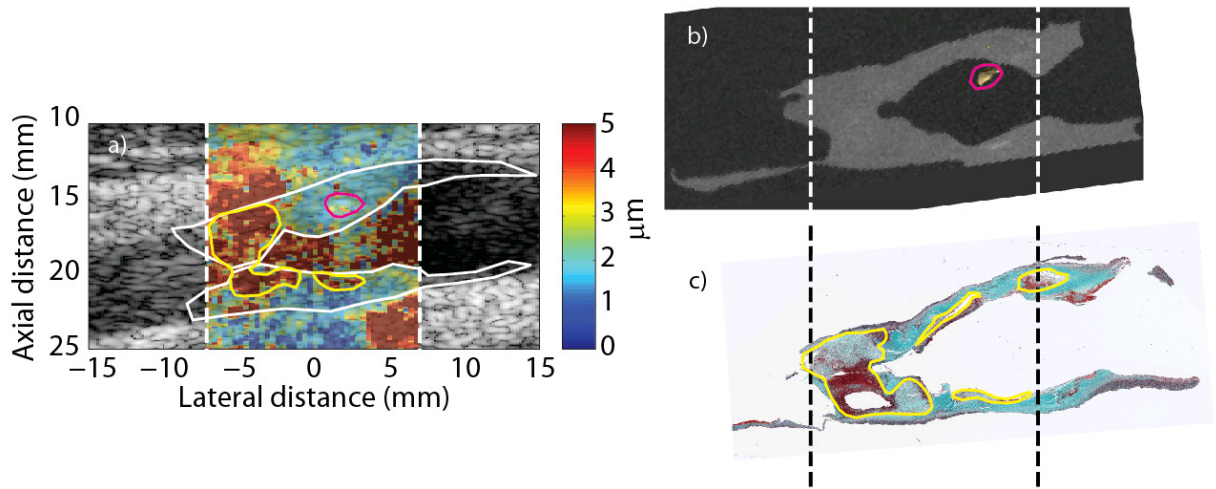


Figure 8.3: Carotid ARFI image with matched histology and ex vivo μ CT imaging from a symptomatic 71-year-old male. (a) Hybrid ARFI/B-mode peak displacement image showing a focal stenosis with high peak displacement (yellow outline) and a bright echogenic region embedded in a region of low displacement (magenta outline). (b) μ CT image showing minor calcification (magenta outline) proximal to the focal stenosis. (c) CME stain shows a complicated Type VI plaque with large necrotic core and hemorrhage at the main stenosis, co-aligned with the region of high displacement on ARFI imaging. Smaller necrotic cores present in the proximal wall do not appear in the ARFI image. A very thin fibrous cap is measured in the distal wall (0.24 ± 0.09 mm)

measured displacements in the region of the hemorrhagic necrotic core were high, 6.6 ± 6.7 μ m compared to the rest of the plaque (2.15 ± 0.79 μ m). Average fibrous cap thickness measured from histology was 0.24 ± 0.09 mm, the thinnest cap observed in this study. Although difficult to see in ARFI imaging, a small band of lower displacing pixels was observed at the location of the fibrous cap. This band of lower-displacing pixels was measured to be 0.51 ± 0.15 mm thick, substantially overestimating the FC thickness measured from histology. However, the band appeared to be discontinuous from the rest of the low-displacing pixels suggesting that plaque rupture may be inferred by the lack of low-displacing pixels separating the high-displacing plaque region from the lumen.

Figure 8.4 shows the imaging results from the right internal carotid artery (ICA) of a symptomatic 45-year-old female. B-mode imaging shows a generally echolucent plaque, with an area of bright echogenicity toward the right side of the distal wall plaque. ARFI imaging, focused at a depth of 16 mm,

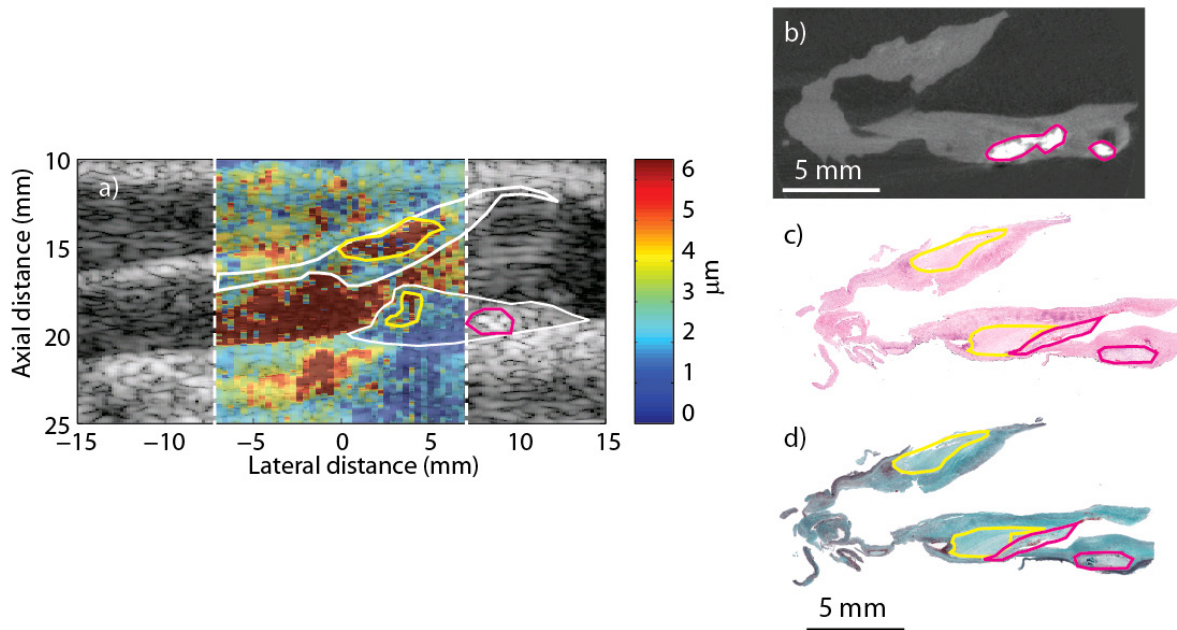


Figure 8.4: Carotid ARFI image with matched histology and ex vivo μ CT imaging from a 45-year-old symptomatic female. (a) ARFI peak displacement image. Significant stenosis is visible due to plaque in both the proximal and distal wall. In the proximal wall, an area of large displacement (yellow outline) is observed, covered by a lower displacing cap. Relatively larger displacements are also seen in the distal wall, but with smaller absolute magnitude. (b) μ CT image showing minor calcification in the distal wall (magenta outline), that matches with a bright spot on B-mode (magenta). (c) H&E stain and (d) CME stain show a Type Va plaque with necrotic core in both the proximal and distal walls (yellow outline).

shows a focal stenosis with plaque in both proximal and distal walls. Plaque in the proximal wall appears to displace far ($10.8 \pm 11.7 \mu\text{m}$) and is covered by a low-displacing region ($2.8 \pm 0.9 \mu\text{m}$ disp., 0.93 ± 0.4 mm thick) suggesting necrotic core and fibrous cap. Plaque in the bottom wall appears to have a focal region of relatively higher displacement ($3.0 \pm 1.6 \mu\text{m}$) also covered by a stiffer region ($1.5 \pm 0.5 \mu\text{m}$ disp., 0.56 ± 0.1 mm thick). Histology confirms the presence of AHA Type Va plaques in both proximal and distal walls, with necrotic core and fibrous caps with thicknesses of 0.91 ± 0.1 mm, and 0.60 ± 0.1 mm, respectively). Although not depicted in the ARFI field of view, the echogenic region in the right part of the distal wall plaque spatially aligned with a region of calcification as seen on μ CT.

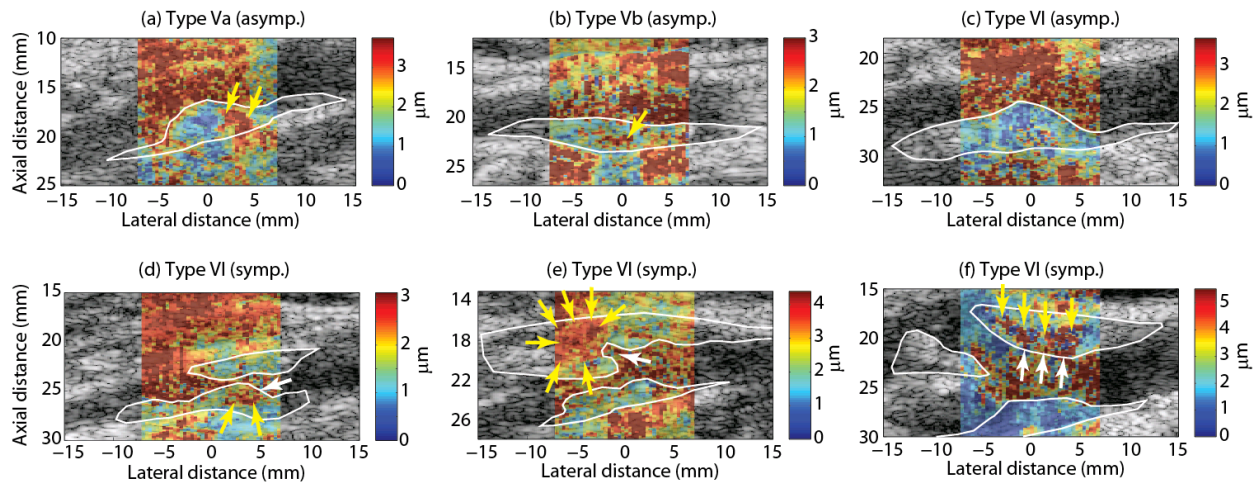


Figure 8.5: Series of ARFI peak displacement images taken from six endarterectomy patients. (a) Type Va plaque from asymptomatic 65 y/o male. Histology showed substantial collagen deposition next to a necrotic core covered by a thin fibrous cap (0.34 ± 0.11 mm). (b) Type Vb plaque from asymptomatic 64 y/o male. Histology showed substantial calcification of the fibrous cap. (c) Type VI plaque from asymptomatic 65 y/o female. Histology showed hemorrhage interspersed with significant calcification. (d) Type VI plaque from symptomatic 46 y/o female. Histology revealed hemorrhaged necrotic core at the focal stenosis point. (e) Type VI plaque from symptomatic 75 y/o male. Histology revealed ulcerated plaque with mild calcification and hemorrhage. (f) Type VI plaque from symptomatic 71 y/o male. Histology showed plaque with large hemorrhaged necrotic core and mild calcification. Yellow arrows depict regions of increased ARFI displacement that correlate to underlying necrotic/hemorrhagic regions on histology. White arrows depict regions where lumen communicates with region of high-displacement suggesting plaque rupture/hemorrhage.

Figure 8.5 shows a series of ARFI PD images from three asymptomatic patients and three symptomatic patients. Regions of high displacement are indicated with yellow arrows, and areas where the lumen appears to communicate with a region of high displacement (which may indicate rupture) are shown with white arrows. Figure 8.5a shows a Type Va plaque (large necrotic core covered by a fibrous cap) from an asymptomatic patient. The corresponding ARFI image shows a plaque with a large low-displacing region (1.34 ± 0.5 μm disp.) coincident to an area of dense collagen on histology to the left of a region of high displacement (3.39 ± 0.9 μm disp.). The low-displacing region separating the high-displacing region from the lumen was measured to be 0.65 ± 0.13 mm thick, which overestimates the fibrous cap thickness measured from histology (0.34 ± 0.11 mm thick).

Figure 8.5b shows a Type Vb plaque (plaque with substantial calcification) from an asymptomatic patient. In the ARFI image, the plaque appears to be generally low-displacing ($1.49 \pm 0.6 \mu\text{m}$) with exception of a small, slightly higher-displacing region ($2.12 \pm 0.7 \mu\text{m}$) located in the center (yellow arrow). Histology demonstrates a plaque with calcified fibrous cap overlaying a region of necrosis. The low-displacing region separating the high-displacing region from the lumen in the ARFI image was measured to be $1.05 \pm 0.28 \text{ mm}$ thick, which does not agree well with the fibrous cap measured from histology ($0.38 \pm 0.12 \text{ mm}$). However, if calcification (which is expected to give a stiff response) is included in the cap thickness measurement, the thickness measured from histology increases to $1.16 \pm 0.44 \text{ mm}$. This example demonstrates that ARFI-based plaque characterization may be influenced by concomitant features with similar material stiffnesses.

Figure 8.5c shows a Type VI plaque (complicated plaque with hemorrhage) with substantial calcification from an asymptomatic patient. Despite the presence of hemorrhage, the ARFI image shows a homogeneously low-displacing plaque ($1.39 \pm 0.6 \mu\text{m disp.}$). Like the previous example, this plaque demonstrates that ARFI plaque characterization may be hampered by concomitant calcium, which in this case causes a complicated Type VI plaque to appear stiff. Interestingly though, in both Figure 8.5b and Figure 8.5c, the patients were asymptomatic. Further prospective studies must be performed to determine whether ARFI can predict which of these plaques would be likely to develop symptoms or cause future stroke.

Figure 8.5d-f show three examples of Type VI plaques from symptomatic patients. In each of these examples, plaque rupture/ulceration appears to be evident as a communication between the lumen and a region of high displacement (white arrows). The ARFI images all show areas of very large peak displacements (yellow arrows), suggesting very soft plaques, that spatially align with areas of hemorrhage/necrotic core. Peak displacements in these regions were measured to be $2.52 \pm 0.7 \mu\text{m}$, $3.63 \pm 0.8 \mu\text{m}$, and $6.66 \pm 9.7 \mu\text{m}$, for panels d, e, and f, respectively. Interestingly, average fibrous cap thicknesses from each of these examples were measured to be quite thick at $0.83 \pm 0.28 \text{ mm}$, 0.82 ± 0.4

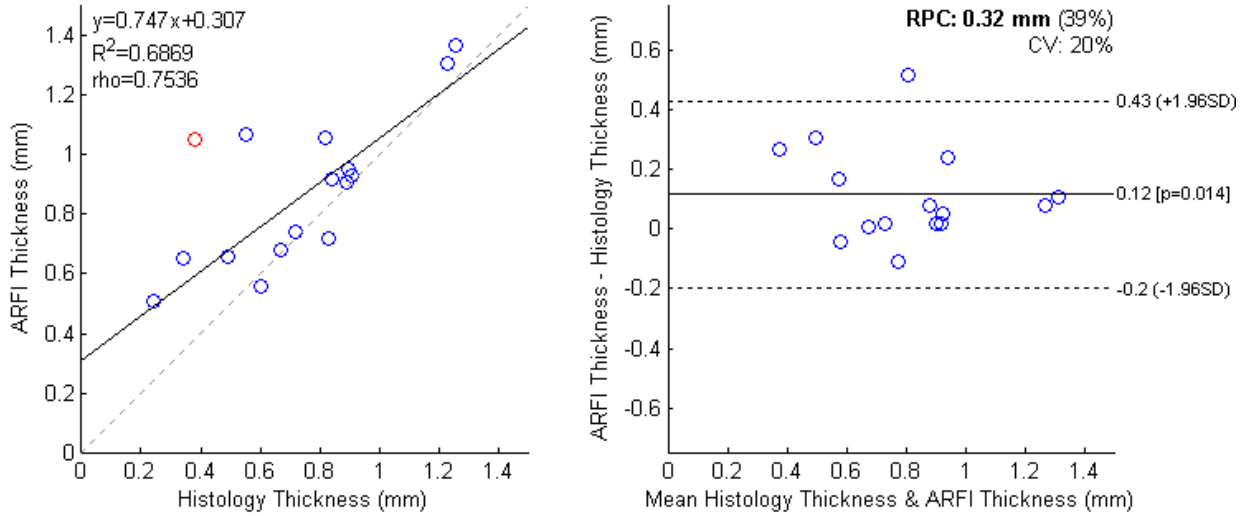


Figure 8.6: Linear regression and Bland-Altman analysis on ARFI-measured fibrous cap thickness versus histology-measured fibrous cap thickness for an unblinded reader. One sample (shown in red) was excluded from analysis due to the coinciding calcification in the fibrous cap that made it appear much thicker on ARFI imaging.

mm, and 0.895 ± 0.16 mm from histology, and 0.72 ± 0.19 mm, 1.06 ± 0.3 mm, and 0.95 ± 0.29 mm from ARFI.

Finally, Figure 8.6 shows a quantitative comparison of ARFI-derived fibrous cap thickness compared against histology utilizing Bland-Altman (BA) analysis. Note that one example was excluded (shown as a red circle) due to excessive calcification of the fibrous cap, which made it appear thicker than indicated on histology (the plaque shown in Figure 8.5b). BA analysis showed that ARFI had a small but statistically significant positive bias (0.12 ± 0.16 mm, $p = 0.014$) for estimating fibrous cap thickness. This bias matched very closely to that predicted by FEM for the corresponding imaging parameters (0.13 ± 0.05 mm), although with slightly higher standard deviation. When fibrous caps below the expected ARFI imaging resolution of 0.4 mm were excluded from analysis, the positive bias fell slightly to 0.08 ± 0.16 mm and was not statistically significant ($p = 0.1$).

8.4 Discussion

The results presented in this chapter further demonstrate the applicability of ARFI imaging for atherosclerotic plaque characterization. ARFI peak displacements were shown to compare favorably with underlying histology, with areas of lipid/necrotic core tending to displace farther than areas of collagen or calcium. Additionally, ARFI images of ruptured/hemorrhaged plaques were captured for the first time. As hypothesized, these regions had higher displacements than areas of collagen; however, the upper limit of displacements was similar to that of necrotic core making it difficult to discriminate hemorrhage uniquely. Nevertheless, as shown in Figure 8.5, it may be possible to infer hemorrhage by identifying regions where high-displacing plaque communicates with the lumen. One aspect of hemorrhage that could not be tested thoroughly in this study was the impact of old versus new hemorrhage. It may be expected that old hemorrhage that has sufficiently clotted may actually increase the plaque stiffness as compared to a non-ruptured necrotic core. However, larger clinical studies must be performed to determine if this is the case.

In addition to confirming expected stiffness responses of various plaque features, this study also demonstrated the capability of ARFI to measure fibrous cap thickness in an *in vivo* setting. BA and regression analysis showed that ARFI-measured thickness was correlated to histological thickness and tended to have a positive bias compared to the true fibrous cap thickness. Encouragingly, the magnitude of the experimentally measured bias matched very closely with that predicted from FEM in Chapter 7. Unfortunately, due to the lack of fibrous cap examples with average thickness below 0.5 mm and the resolution limitation of 0.4 mm of the imaging system, it was not possible to rigorously test the performance of ARFI for detecting “critical” fibrous caps. Nonetheless, the agreement of *in vivo* results with FEM suggests that improvements in frequency and bandwidth of ARFI systems may allow for detection of these thin caps in future studies.

One limitation of ARFI observed in this study was the dependence on focal depth. In a number of examples, the diameter of the carotid artery exceeded the depth of field of the ARFI pushing pulse, and the plaque in the wall outside of the focus would incorrectly represent the underlying histology. Even

when plaques in both proximal and distal wall fell within the ARFI focus, choosing only one dynamic range setting tended to affect interpretation of the deeper wall. For example, in the plaque shown in Figure 8.4, the chosen dynamic range favored detection of the necrotic core in the proximal wall because displacements in this wall drove the dynamic range up. PDs in the necrotic core of the proximal wall were over 3 times higher than PDs in the necrotic core of the distal wall, despite the fact that the distal wall had a thinner cap (which should increase the PD of the necrotic core as seen in Chapter 7). In the future, utilizing advanced imaging techniques, such as rapid multi-focal-zone ARFI [240], may help mitigate some of the focusing and uneven force distribution problems observed in this study.

Calcification posed another challenge in a number of ARFI images in this study, particularly calcification in the proximal wall. Calcification is well known to be a strong ultrasound absorber/reflector, and thus very difficult to image around. In ARFI imaging, calcification can make features behind it appear stiffer than they should by reducing the overall ARF delivered to that tissue. Additionally, calcification was observed to introduce reverberation clutter, which also created low-displacement streaking artifacts behind the calcification and obscuring displacements in the distal wall. This type of artifact can be seen in Figure 8.3, where the otherwise red-colored lumen appears blue/yellow in the region directly below the small calcification. Although the penetration problem through calcium can only be mitigated by either increasing the acoustic intensity of the ARFI pulse or using more sensitive displacement estimators (to measure displacements smaller than the CRLB), the problems of the reverberation artifact may be improved by utilizing clutter suppression techniques such as harmonic imaging [237].

8.5 Conclusion

Overall, this study supports the hypothesis that ARFI stiffness measurements reflect underlying plaque composition. As demonstrated previously on smaller scales, it was confirmed that relatively higher ARFI displacements tend to correspond to areas of lipid/necrotic core, while lower displacements corresponded to areas of collagen or calcium. Furthermore, it was shown for the first time that

ruptured/hemorrhaged plaques also exhibit a “soft” response to ARFI, although the displacement ranges were similar to those measured in intact necrotic core suggesting that it may be difficult to identify hemorrhage uniquely via PD measurements alone. However, based on a number of examples of ruptured plaques seen in this chapter, it is hypothesized that hemorrhage may be inferred by identifying regions of high-displacement in the plaque that communicate with the lumen and are not separated by a band of low-displacing pixels that indicate fibrous cap. Finally, the capability of ARFI to measure fibrous cap thickness directly was demonstrated for a greater number of plaques than done previously. In the following chapter, these data sets will be presented to blinded image readers to confirm whether plaque features are identifiable when the underlying histology is unknown.

CHAPTER 9

Blinded-Reader Performance of ARFI Plaque Characterization

9.1 Introduction

Previous chapters have shown the feasibility of ARFI for delineating carotid plaque features such as soft lipid/necrotic core (NC) and fibrous cap (FC). However, up to this point, all analysis was performed by a single image reader who was not blinded to the histology. To truly demonstrate ARFI's clinical potential, these results must be reproducible by unbiased image readers who are blinded to the true answers.

In this chapter, we continue our analysis of the ARFI images taken in CEA patients by rigorously testing performance in a blinded reader study involving trained medical professionals. Similar to Chapter 5, ARFI images are scored for various plaque compositional elements, and the detectability is determined by receiver operating characteristic (ROC) curve analysis. Additionally, a qualitative plaque stiffness scale (similar to the Gray-Weale echogenicity scale [110]) is developed for ARFI ultrasound and correlated to underlying plaque features. Finally, the blinded reader's capability of measuring FC thickness is assessed, as was done with an unblinded reader in Chapter 8.

9.2 Methods

The methods implemented in this chapter utilize the same ARFI images taken from patients undergoing CEA that were presented in Chapters 6 through 8. The reader is referred to these chapters for details on imaging methods and patient clinical characteristics (Table 8.1).

9.2.1 Reader Evaluation Study

Six readers were recruited to evaluate ARFI images. The readers included three attending radiologists from UNC Hospital (two from neuroradiology and one from abdominal radiology), one sonographer, one interventional cardiologist, and one pathologist who served as a reader in the *ex vivo* study presented in Chapter 5. Most readers had no previous experience with ARFI imaging and were trained for approximately 2 hours prior to commencing ARFI image evaluation. The training regimen involved introducing the readers to the fundamentals of ARFI imaging, reviewing examples from preclinical and outside clinical studies [210], [267], and instructing readers on the annotation software (which is described in greater detail below). The six readers were kept blinded to the histological results of the CEA specimens and patient clinical presentation during the course of ARFI image assessment.

To facilitate reader evaluation, a custom graphical user interface (GUI) was developed in MATLAB to show image sets in a random order and save responses to the reader's hard drive (Figure 9.1). As was done in Chapter 5, the GUI consisted of two parts, an "overall" rating and segmentation portion, and a "subsection" rating portion. However, in contrast to the previous study that only utilized ARFI images, in this study, the B-mode and ARFI/B-mode overlay were shown side-by-side to better represent how ARFI would be used clinically. The reader was also given additional options to aid their interpretation of the image. A button was added that allowed the reader to look at the B-mode from the patient's medical record leading up to surgery.

Typically, this B-mode was higher quality (i.e. captured with harmonic imaging for reduced clutter, and frequencies around 9 MHz) than the B-modes captured in conjunction with ARFI sequences and more similar to the images that are seen in routine clinical practice. The high quality B-mode was stripped of any identifying information as well as any sonographer notes. Readers were also given an option to turn on image smoothing to reduce noise in the ARFI peak displacement image. The smoothing algorithm consisted of an interpolation step in the lateral dimension ($3\times$ spline interpolation) followed by 2D wiener filtering (1×1 mm kernel size) using the *wiener2* function in MATLAB. The smoothed

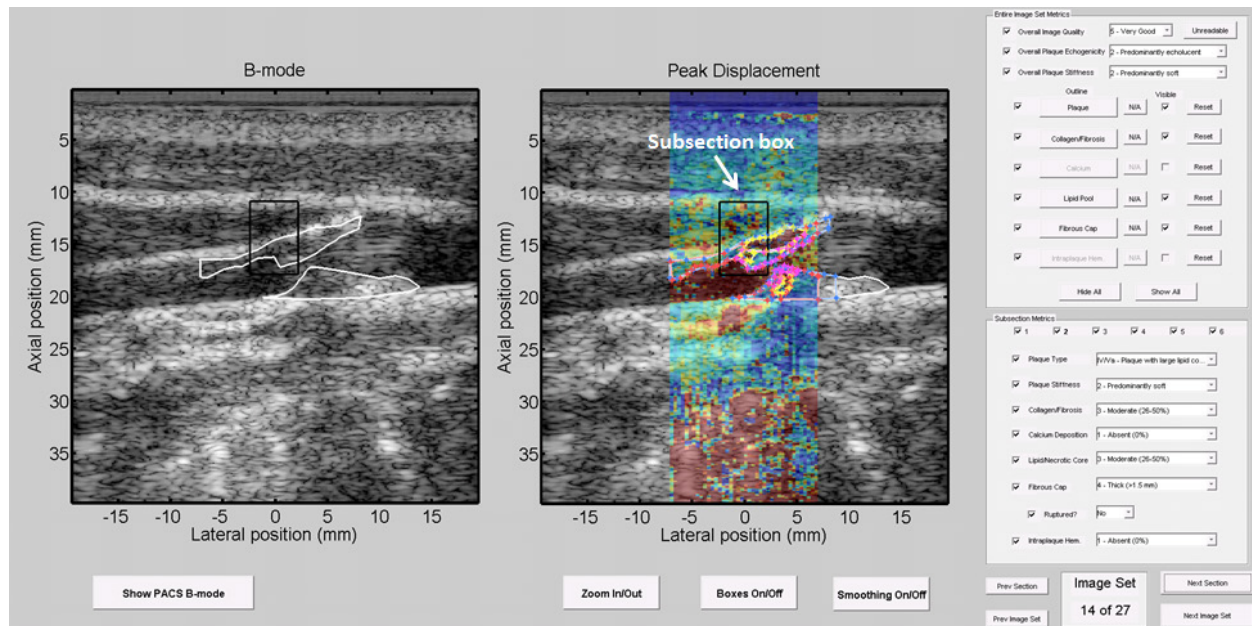


Figure 9.1: GUI used by readers to grade and segment ARFI images. Note that in this screenshot the plaque is outlined in white (i.e. “guided” analysis). Readers also evaluated images when no outline was shown (i.e. “unguided” analysis). Segmentation colors are as follows (collagen – red, necrotic core – yellow, fibrous cap – magenta).

images appeared similarly to elastograms produced by commercial ARF-elastography products such as Siemens’ Virtual Touch™ Imaging (Siemens Medical Solutions USA Inc., Ultrasound Division).

For the overall rating portion, the reader was first asked to give the image set a quality rating using a five-point scale: 1-Very bad; 2-Bad; 3-OK; 4-Good; 5-Very good. Next the reader scored the plaque echogenicity using the modified Gray-Weale scale [110]: 1-Uniformly echolucent; 2-Predominantly echolucent; 3-Predominantly echogenic; 4-Uniformly echogenic; 5-Cannot be classified due to shadowing. A coronary plaque stiffness scale was developed for ARFI imaging and rated next: 1-Uniformly soft; 2-Predominantly soft; 3-Predominantly stiff; 4-Uniformly stiff; 5-Cannot be classified due to shadowing. Finally, the reader was asked to segment various features including: plaque outline; collagen/fibrosis; calcium; lipid/necrotic core; fibrous cap; and intraplaque hemorrhage (IPH). Segmentation was performed interactively using the *impoly* tool in MATLAB.

After segmenting the plaque and rating the overall plaque appearance, the readers moved on to

the subsection analysis, which was implemented similarly to Chapter 5. The GUI drew a black box on top of the ARFI and B-mode images, and the reader was instructed to independently rate the plaque features that were present inside the box. Four of the five plaque features that were segmented above (collagen, calcium, NC, and IPH) were rated on ordinal scales based on percent area of the feature. The rating scale was as follows: 1-Absent (0%); 2-Slight (1-25%); 3-Moderate (26-50%); 4-Extensive (51-75%); 5-Severe (76-100%). Fibrous cap was rated on a slightly different scale: 1-Absent; 2-Thin (~0.5 mm); 3-Moderate (~1 mm); 4-Thick (~1.5 mm). And finally, the reader was asked to judge if the plaque was ruptured (1-No, 2-Yes) and also to grade the plaque type based on the modified-AHA plaque rating scale [76]. The readers were instructed to judge plaque rupture and IPH if they saw an area of lumen communicating with a soft region in the plaque. Ratings were performed for six subsections for every ARFI image (three on the proximal wall and three on the distal wall).

After rating all ARFI images, the readers were asked to repeat their analyses, but now with ARFI images indicating the true plaque outline as determined by an unblinded reader (i.e. the author of this dissertation). Using this knowledge of the plaque outline, the readers were allowed to change their answers for feature segmentations and subsection ratings if desired. Both the unguided and guided readings of the data set were saved for analysis.

9.2.2 Histology

As was done in previous chapters, histology was rated by an expert pathologist who was blinded to the ARFI results. The pathologist's rating was facilitated with another custom GUI developed in MATLAB (Figure 9.2). The histology GUI was similar to the ARFI GUI but only displayed histology slides instead of ARFI images, and had a few different options. First, the ultrasound-specific ratings were removed (e.g. image quality, echogenicity, plaque stiffness). Second, an additional ordinal rating option was added to the AHA pull-down and was labelled "N/A" that was used by the pathologist to indicate that a given subsection did not have enough tissue to be rated. Lastly, an additional plaque component category, termed "Loose Matrix", was introduced to indicate areas of plaque that did not fall within the

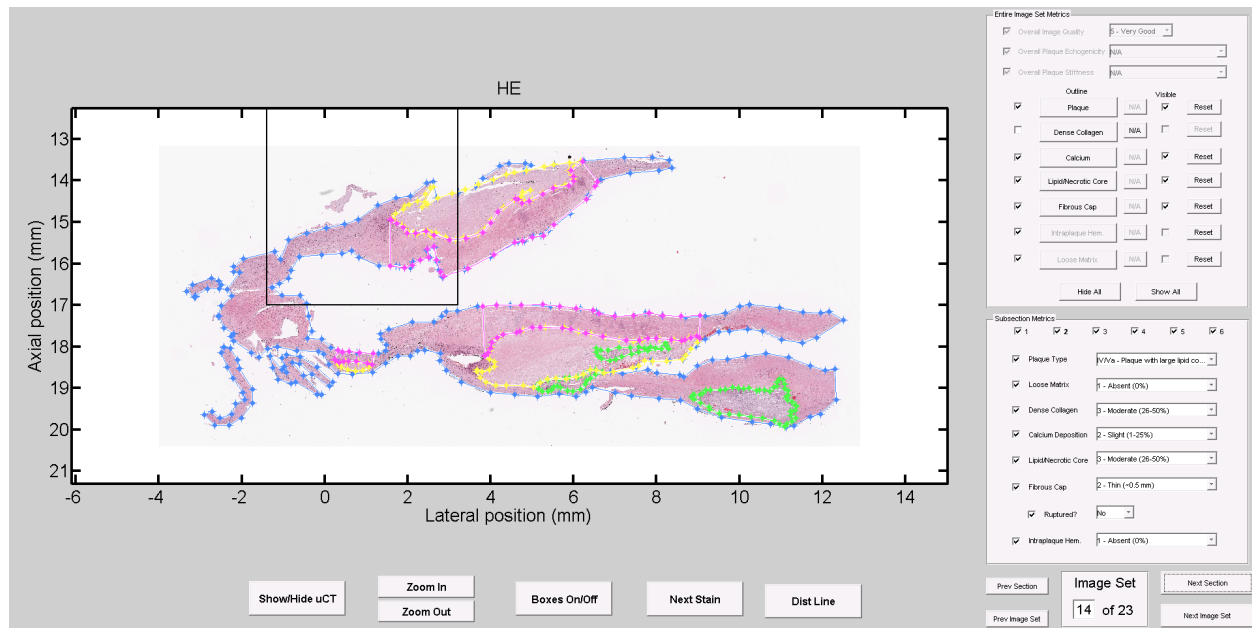


Figure 9.2: GUI used by pathologist to grade and segment histology. Segmentation colors are as follows (plaque outline – blue, necrotic core – yellow, fibrous cap – magenta, calcium – green).

classification of dense fibrosis (dark collagen stain, highly organized structure) or NC (light collagen stain, cholesterol clefts, cellular debris, amorphous structure). The loose matrix category followed the same ordinal scale as other the plaque features: 1-Absent (0%); 2-Slight (1-25%); 3-Moderate (26-50%); 4-Extensive (51-75%); 5-Severe (76-100%).

9.2.3 Statistical Analysis

ARFI performance for identifying plaque features was quantified using a number of statistical approaches. To test performance for plaque components, parametric ROC curve analysis (bi-gamma) was performed on a subsection basis, similar to Chapter 5. Histological dichotomization was applied to create “true negative” and “true positive” distributions, and every dichotomization threshold was tested (results are only shown for the best threshold). Performance for a given plaque feature was determined by evaluating the area under the ROC curve (AUC), and by choosing an operating point that maximized sensitivity and specificity (with the constraint that sensitivity be greater than specificity) [277].

In addition to testing each plaque component separately, combined plaque component categories were created that merged plaque features with similar expected ARFI responses, i.e. collagen and calcium (which are expected to both be stiff) and NC and IPH (which are expected to both be soft). Merging categories was done by taking the highest ordinal response from the two categories, and comparing it to the equivalently combined histological response.

To test the accuracy of AHA ratings, unweighted Cohen's kappa (κ), a coefficient that describes level of agreement (on a scale of 0 to 1, where 0 – no agreement, 1 – perfect agreement), was computed. The κ values were computed for the strictest case where no categories were combined (i.e. a 6×6 contingency table for AHA ratings), and also for less-strict, collapsed cases (i.e. 2×2 tables), as done in Wintermark et al. [76]. Additionally, Spearman correlation coefficients (ρ) were calculated between plaque stiffness ordinal responses and histological plaque feature grades.

Finally, contrast between the FC and NC in readers' segmentations was calculated for ARFI and B-mode images following equation (7.3). To normalize contrast measurements between the two imaging modes, contrast was computed directly from pixel values of the displayed images (scaled between 0-255), and the ARFI color map was changed to an inverted grayscale (high displacement = low pixel value, low displacement = high pixel value) to match with the expected B-mode response (echolucent = low pixel value, echogenic = high pixel value).

9.2.4 Image Inclusion Criteria

Due to the challenges of spatially aligning CEA samples with six subsections in the ARFI image, detailed inclusion criteria were developed to only include well-matched data. First, subsections from any plaque specimen that were not whole after CEA were automatically rejected from statistical analysis. While histological processing was usually possible on fractured samples, these samples lacked notable landmarks, such as the carotid bifurcation, that were needed to spatially align them to the corresponding ARFI images. Next, any subsections that were rated as N/A by the pathologist (indicating that no tissue was present in histology) were excluded because there was no gold standard for these subsections. After

these histological exclusions, two ARFI exclusions were also implemented. First, any plaque with a mean image quality rating of less than 2 (“Bad”) was automatically excluded. Second, if either the proximal or the distal wall was outside of the ARFI focus, then all three subsections from that wall were excluded. The ARFI focus was expected to span approximately 5 mm; therefore, if the distance from the medial edges of the plaques in proximal and distal wall exceeded this, then only the wall that was within the focus was chosen for analysis.

9.3 Results

During the course of this clinical study, 26 plaques were harvested from 25 CEA patients (Table 8.1) representing a total of 156 possible subsections (26 plaques \times 6 subsection per plaque) and 52 walls (26 plaques \times 2 walls per plaque). Six plaques were badly damaged, lost, or fractured during CEA, preventing spatial alignment, and one plaque was excluded due to image quality being less than two. Finally, an additional 14 subsections were removed due to pathologist rating of N/A, and 42 subsections (14 walls) were removed due to being outside the focus. The final data set included 58 subsections spanning 22 walls from 17 plaques extracted from 16 patients. Figure 9.3 shows a flowchart detailing the exclusion procedure. Figure 9.4 shows histograms of the final counts of plaque types that were included for analysis as well as the plaque types that were excluded after discounting those outside the ARFI focus. From the included plaque samples, the pathologist was able to measure 16 with fibrous caps (from 15 plaques), which reduced to 14 after ARFI image quality exclusion.

Boxplots of AUC values achieved by the readers (with plaque outline guides) are shown in Figure 9.5 for each of the four plaque components evaluated in this study (collagen, calcium, NC, IPH), as well as the combined categories (collagen/calcium and NC/IPH). For these results, the histological category “collagen” was merged with the “loose matrix” category by taking the maximum ordinal response between the two for a given subsection, and a histological dichotomization threshold of >2 was used (i.e. ratings of “Absent” and “Slight” were counted as true negatives while ratings of “Moderate”, “Extensive”, and “Severe” were counted as true positives).

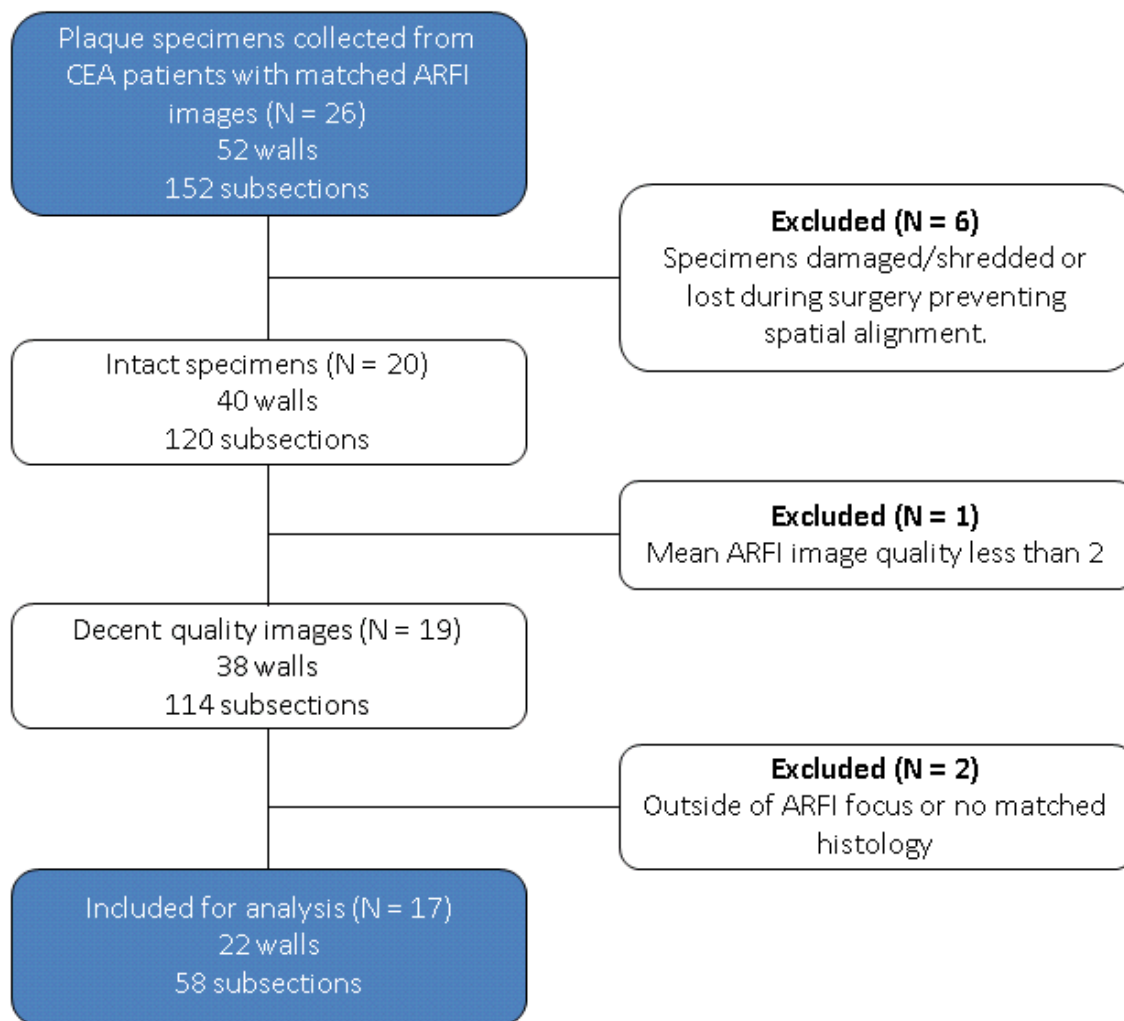


Figure 9.3: Flowchart for specimen inclusion in blinded reader study.

Figure 9.5a depicts the results for all six readers, and Figure 9.5b shows the results for the radiologists alone. When all readers were considered (Figure 9.5a), the median AUCs for each feature (ordered from highest to lowest) were as follows: NC, 0.762; dense collagen, 0.647; IPH, 0.636; calcium, 0.566. The median AUC for the combined categories were higher than both taken separately, with the collagen/calcium category reaching a median AUC of 0.755 and the NC/IPH category reaching a median AUC of 0.877. Not surprisingly, the radiologists (readers 1, 2, and 3) outperformed the non-radiologists,

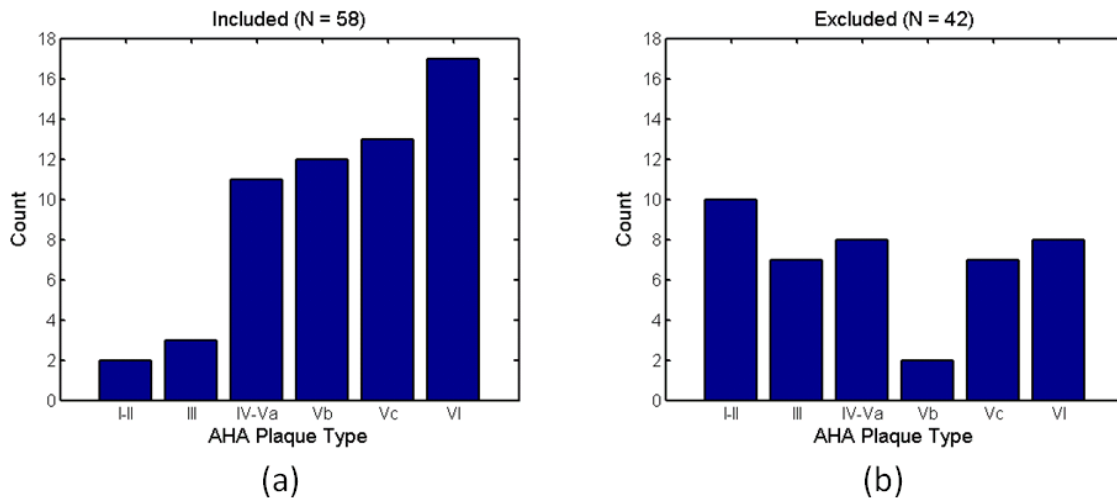


Figure 9.4: Histograms showing counts of excluded and included subsections broken down by AHA plaque types.

having the three highest AUCs in the collagen/calcium category and three out of the top four in the NC/IPH category.

When only the AUCs from the radiologists were considered (Figure 9.5b), the median AUCs for each feature were as follows: NC, 0.809; dense collagen, 0.696; IPH, 0.639; calcium, 0.612. The median AUC for the combined metrics when only considering radiologists were 0.859 for collagen/calcium and 0.887 for NC/IPH. The radiologists' ROC curves for the combined categories are shown in Figure 9.6, and the corresponding sensitivities and specificities for an operating point that maximizes their sum is given in Table 9.1.

Figure 9.7 shows the change in median AUC when readers utilized the plaque outlines and were given the chance to change their answer. A positive change indicates that AUC increased with the outlines, while a negative change indicates the AUC decreased with the outlines. In nearly all cases the AUC increased as a result of giving the readers the plaque outlines. When considering all readers, the AUCs for the combined metrics improved by almost 8 percentage points equally between the stiff and soft groups. When only including the radiologists, the collagen/calcium combined metric improved

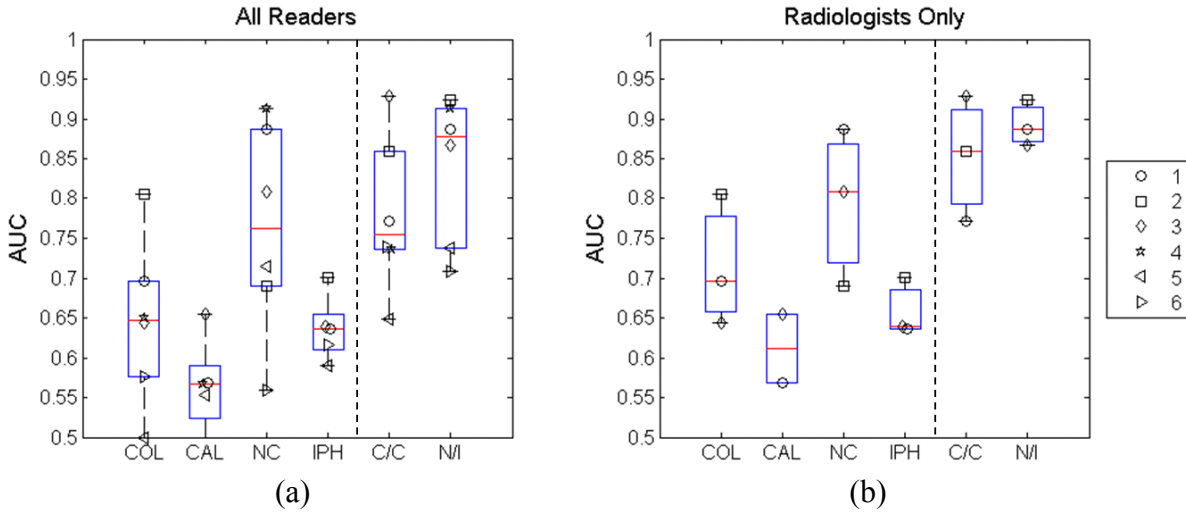
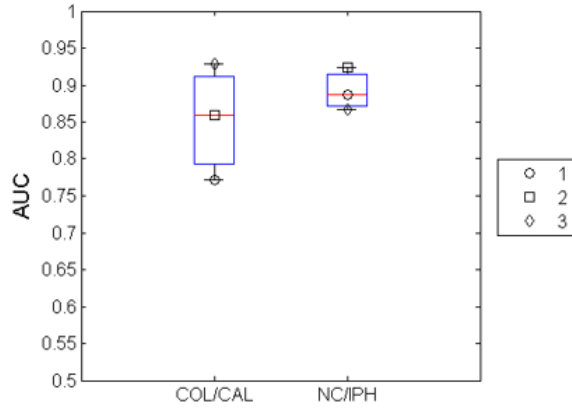


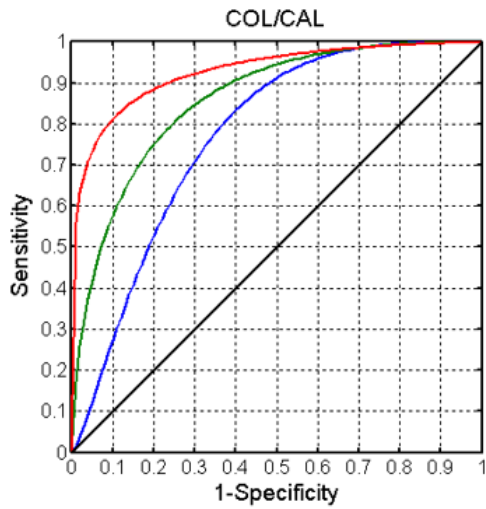
Figure 9.5: Boxplots of reader AUC for various plaque composition elements. Results for all readers are shown in (a), while results for just the radiologists are shown in (b). Dashed vertical line separates the individual plaque categories from the combined categories. COL, collagen; CAL, calcium; NC, lipid/necrotic core; IPH, wide intraplaque hemorrhage; C/C, combined collagen/calcium; N/I, combined necrotic core and intraplaque hemorrhage.

substantially more than the NC/IPH category (16 percentage points compared to 5 percentage points, respectively) after the inclusion of the plaque outlines.

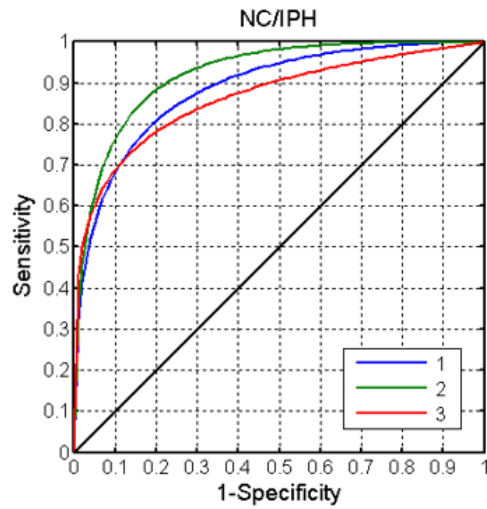
Figure 9.8 shows the Spearman correlation coefficient between the qualitative ARFI stiffness score (from the three radiologists) and the pathologist's rating for a given plaque compositional element. The nature of the stiffness scale is such that high values on the scale indicate stiff plaque and should be positively correlated with stiff features, while low values indicate soft plaque and should be inversely correlated to soft histological features. As expected, the results demonstrate that qualitative ARFI stiffness ratings were positively correlated with collagen (median: 0.329, $p = 0.012$) and inversely correlated with NC (median: -0.515, $p < 0.001$) and IPH (median: -0.274, $p = 0.037$). Surprisingly, calcium only showed a weak positive correlation (median: 0.165, $p = 0.217$); however, it was not statistically significant. The combined categories yielded slightly higher median correlation coefficients than their individual members; the collagen/calcium category was positively correlated (median: 0.379, $p = 0.003$) while the NC/IPH category was negatively correlated (-0.531, $p < 0.001$).



(a)



(b)



(c)

Figure 9.6: ROC curves for radiologists for detecting combined stiff features (collagen and calcium) and combined soft features (necrotic core and intraplaque hemorrhage). Boxplots showing AUC for the two categories are reprinted from Figure 9.5 for comparison.

Table 9.1: Sensitivity and specificity for combined plaque categories.

Reader	<u>Collagen/Calcium</u>		<u>Necrotic Core/Hemorrhage</u>	
	Sensitivity	Specificity	Sensitivity	Specificity
1	0.832	0.602	0.805	0.804
2	0.795	0.76	0.853	0.835
3	0.854	0.853	0.789	0.788

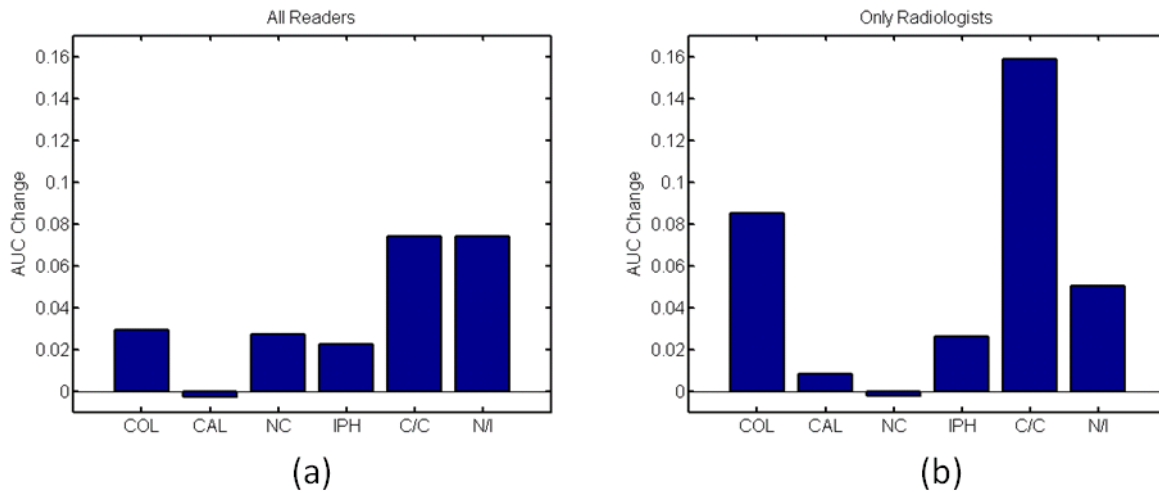


Figure 9.7: Barplots showing the difference in median AUC when readers were given the plaque outline versus when they were not. Positive change indicates that median AUC increased after showing plaque outlines, negative change indicates that median AUC decreased after showing plaque outlines. COL, collagen; CAL, calcium; LPL, lipid/necrotic core; IPH, wide intraplaque hemorrhage; C/C, combined collagen/calcium; L/I, combined lipid and intraplaque hemorrhage.

Cohen’s kappa analysis for AHA plaque rating (Figure 9.9) reflected the performances observed in the ROC analysis. When evaluating each plaque type individually (i.e. a 6×6 frequency table), the ARFI-determined AHA plaque ratings did not agree strongly with the gold standard (median $\kappa = 0.215$, $p = 0.02$), although it was statistically significant. However, when the frequency table was collapsed and merged (i.e. 2×2 tables) to evaluate agreement between combined categories (Type Va or Type VI) and (Type Vb or Vc), concordance between ARFI and histology ratings increased substantially. When plaques with large NC (Type Va) and plaques with IPH (Type VI) were combined, the median kappa coefficient was 0.515 ($p < 0.001$), and when plaques with large calcifications (Type Vb) and plaques with dense collagen (Type Vc) were combined, the median kappa coefficient was 0.468 ($p = 0.003$).

Performance for measuring FC thickness is demonstrated in Figure 9.10 and Figure 9.11. Figure 9.10 shows a comparison of ARFI-measured FC thickness to histologically measured FC thickness for all readers as well as just the radiologists. The dashed line represents the line of equivalency. Average FC thickness as measured by histology ranged from 0.24 mm up to 1.26 mm. When considering all readers

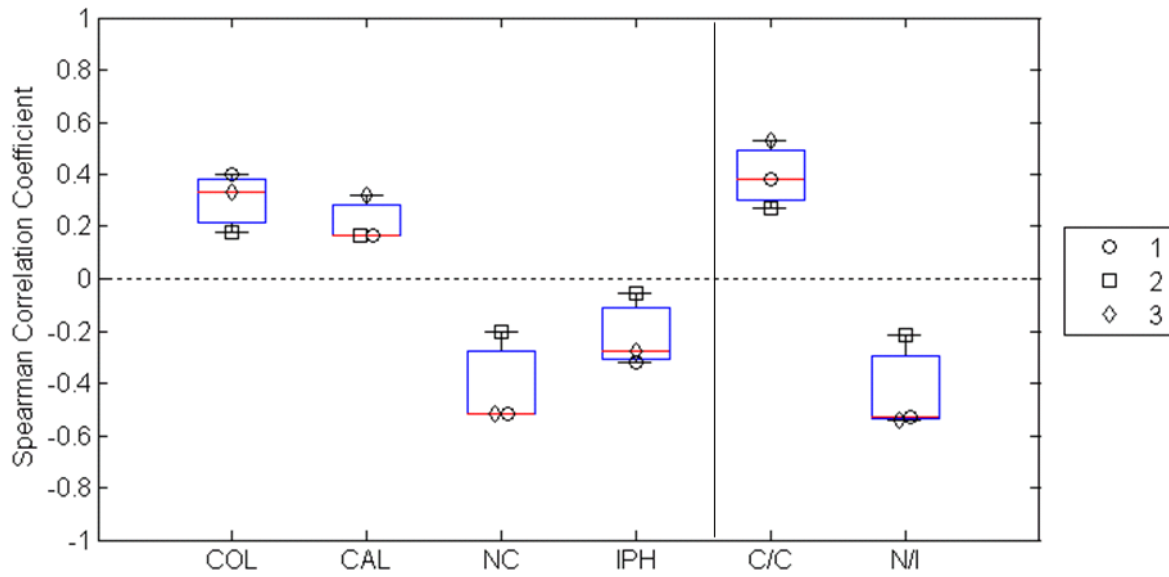


Figure 9.8: Spearman correlation coefficient between reader-assigned qualitative stiffness score and plaque components. Data shown for radiologists only. Vertical line indicates separation between individual categories and combined categories. COL, collagen; CAL, calcium; LPL, lipid/necrotic core; IPH, wide intraplaque hemorrhage; C/C, combined collagen/calcium; N/I, combined necrotic core and intraplaque hemorrhage.

(Figure 9.10a), performance for accurately measuring FC thickness was poor; reader 5 in particular struggled to identify any of the FCs and had substantial error in their measurements. Agreement between ARFI-measured thicknesses improved dramatically when only considering results from the three radiologists (Figure 9.10b). Regression and Bland-Altman (BA) analysis on each individual radiologist (Figure 9.11) demonstrated that readers 1 and 2 (i.e. the neuroradiologists) had the highest agreement for measuring FC thickness with coefficients of determination (R^2) values of 0.64 and 0.89, respectively. BA analysis showed that reader 1 had a slightly wider spread of measurement error, however, with a non-significant negative bias (-0.048 ± 0.18 mm, $p = 0.41$), while reader 2 had a tighter spread but with a significant positive bias (0.13 ± 0.09 mm, $p = 0.007$). When results from all three radiologists were combined, a statistically significant positive bias was also measured (0.12 ± 0.30 mm, $p = 0.037$). Of note, the mean positive bias across all three radiologists matched nearly identically to the mean positive

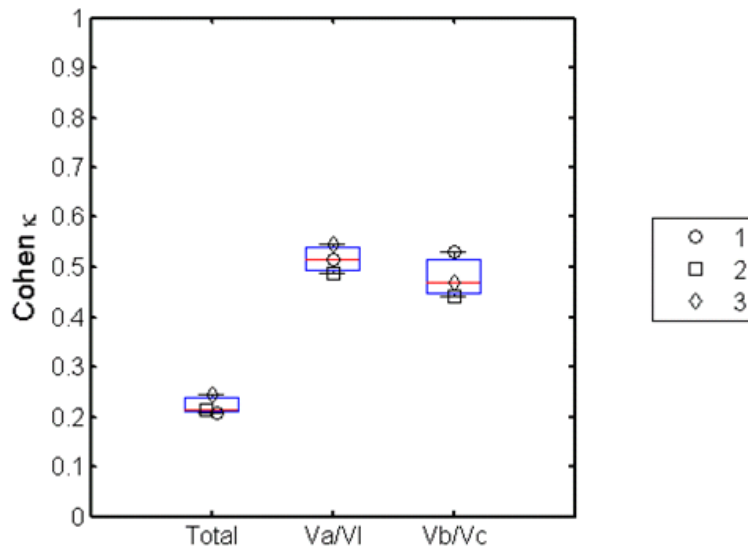


Figure 9.9: Cohen's kappa for AHA plaque type ratings. Data shown for the full contingency table (6×6), and two collapsed tables (2×2) where type Va and VI plaques (i.e. soft plaques) were combined and type Vb and Vc (i.e. stiff plaques) were combined.

bias predicted by FEM in Chapter 7 (0.13 ± 0.05 mm) for the equivalent imaging parameters (6 MHz and 1.5λ tracking kernel). Given the considerably larger standard deviation on the radiologist's measurements as compared to FEM (± 0.3 mm vs. ± 0.05 mm), it is possible that this result was coincidental, nevertheless, the level of agreement between FEM and *in vivo* measurements was highly encouraging.

Lastly, Figure 9.12 shows a comparison of the contrast between the FC and the NC in both B-mode and ARFI PD images, as segmented by the radiologists. In each case, contrast from ARFI statistically significantly exceeded that of B-mode. Median ARFI contrast for each reader ranged from 4.4 dB to 8.9 dB, while median B-mode contrast ranged from -0.29 dB to 0.35 dB. These results suggest that without ARFI, the radiologists would not be able to contrast the FC from NC/IPH using the provided B-modes alone.

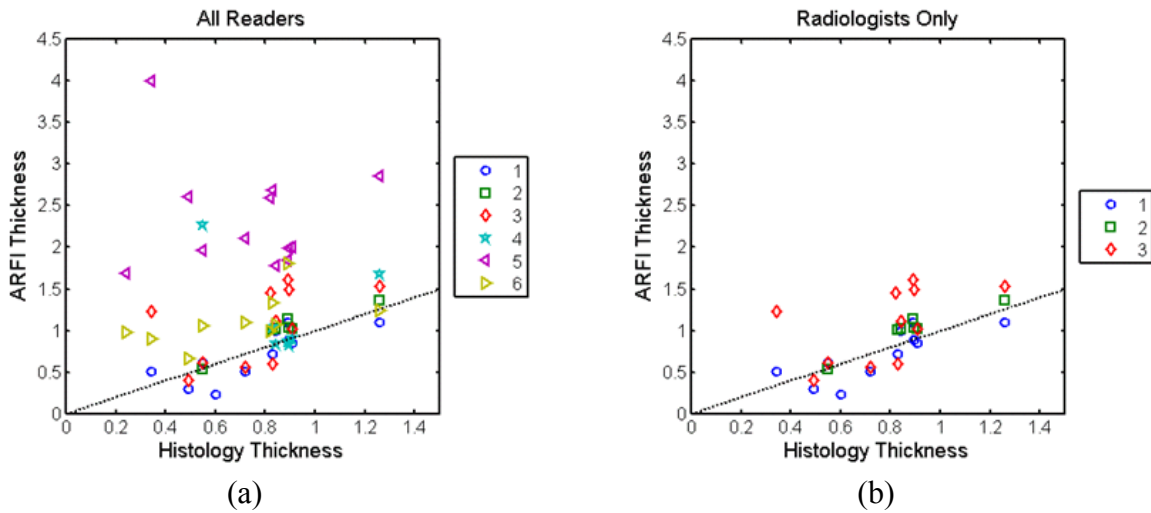


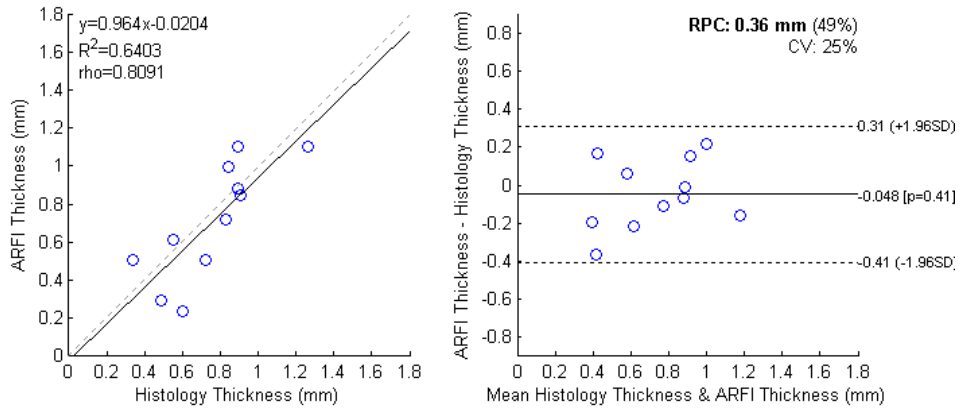
Figure 9.10: ARFI-measured fibrous cap thickness measurements by blinded readers compared against histological thickness. (a) Results for all readers. (b) Results for radiologists only. Reader ID number is given in the legend.

9.4 Discussion

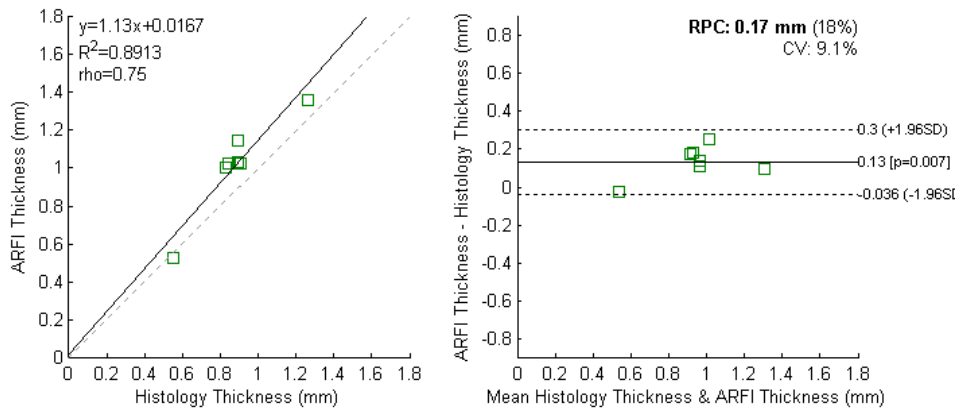
This study represents the first quantitative *in vivo* validation of ARFI carotid plaque characterization done in humans. Six blinded readers spanning a wide range of medical professionals evaluated ARFI images and were able to distinguish soft lipid-rich or hemorrhagic plaques from stiff fibrotic or calcified plaques with varying levels of success. In general, readers were able to better characterize features when the borders of the plaque were identified for them, and readers with greater levels of experience evaluating medical images, i.e. the radiologists, tended to outperform their non-radiologist counterparts. Neuroradiologists, specifically, achieved the highest agreement for measuring FC thickness, suggesting that reader familiarity with carotid ultrasound improved reader performance.

Examining the AUC values presented in Figure 9.5, it is clear that ARFI struggled to distinguish regions of collagen, calcium, and hemorrhage when each category was taken separately. In each case, median AUCs never exceeded a value of 0.7, even when only considering the performance of radiologists. Of the individual categories, NC had the highest detection rate with a median AUC of 0.809,

Reader 1



Reader 2



Reader 3

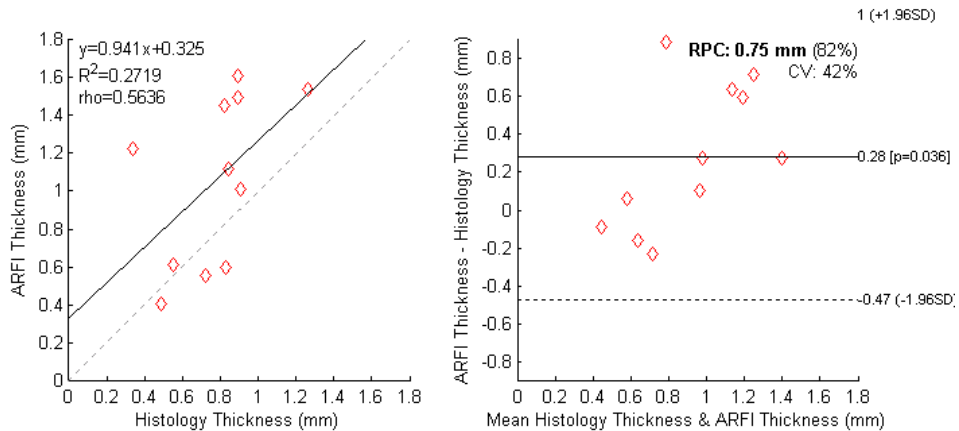


Figure 9.11: Regression and Bland-Altman analysis of ARFI-measured fibrous cap thickness versus histology from three blinded radiologists. R^2 , coefficient of determination; ρ , Spearman correlation; RPC, reproducibility coefficient; CV, coefficient of variation; SD, standard deviation.

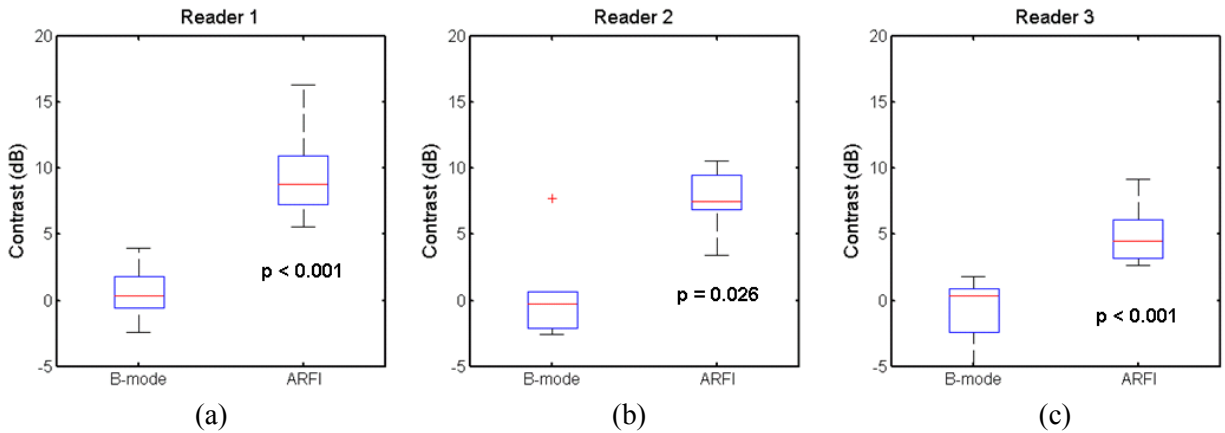


Figure 9.12: Comparison of B-mode and ARFI contrast between fibrous cap and necrotic core. For all readers, ARFI gave statistically significantly higher contrast than B-mode.

albeit with a wide range (0.690 – 0.888). As predicted in prior chapters, ARFI performance was substantially improved when features with like stiffness were grouped into combined categories, namely collagen and calcium, and NC and IPH. AUCs for the combined metrics had median values of 0.859 and 0.887, respectively, with upper ranges reaching as high as 0.92. These results are reinforced by the analysis of Spearman correlation for the plaque stiffness scale (Figure 9.8) and Cohen’s κ (Figure 9.9) which show similar trends. Clinically, these data are encouraging because plaques with either NC or hemorrhage have both been shown to be relevant to predicting future ischemic events, with mean hazard ratios of 3.00 and 4.59, respectively [102].

Although discrimination of IPH from NC and calcium from collagen was not realized in this study, it is expected that these features may be differentiable with improved reader training and enhancements to the ARFI imaging system. As mentioned previously, readers were largely untrained prior to enrolling in the study due to the limited number of training examples available to them. Because of this, no training was done on samples harvested from enrolled CEA patients in order to have the highest sample size possible for statistical analysis. Therefore, readers were limited to training mainly on porcine plaque examples taken from our prior studies and a small number of previously published *in vivo* human examples. This likely impacted IPH detection the most because none of these prior studies

included examples of complicated Type VI plaques. With further training, it is possible that readers may be able to better identify disruptions in FCs as shown in Chapter 8.

In terms of calcium and collagen discrimination, it is likely that simply incorporating modern B-mode imaging techniques (such as harmonic imaging and spatial compounding) will greatly improve detection of these features independent of each other. B-mode sensitivity to calcium has been shown to be quite high in other studies (88.2%) [278], whereas in this study it was low, suggesting either that our B-modes were inferior or that ARFI data confounded the reader interpretation of calcium causing them to alter their answers. The former is more likely to be the case considering that B-mode images captured with the Siemens URI tool only included fundamental-frequency images with no additional processing and, anecdotally, readers expressed concerns that B-modes were difficult to interpret during training sessions. However, the second hypothesis may also be valid because ARFI displacements in regions of calcification tended to be noisier than in collagen alone (most likely due to poor displacement tracking). Although beyond the scope of this study, a thorough evaluation comparing ARFI/B-mode to B-mode alone for plaque characterization should be conducted and will be a topic of future experiments.

In addition to improving the B-mode images, it is expected that utilizing higher-energy ARFI excitations (or improved motion tracking techniques [279]) may aid in discrimination of these features as well. As seen in Chapters 6 and 8, displacements in fibrotic/calcified plaques were relatively low (~1-2 μm) and approached the fundamental noise floor of the cross-correlation tracking algorithm. If displacements in these features could be increased (via higher energy ARFI pulses), or the noise floor itself could be reduced (via improved tracking algorithms), it may be possible for ARFI to discriminate the two features.

This study also demonstrated the capability for utilizing ARFI to make FC thickness measurements (Figure 9.11). Two of the three radiologists, specifically the two neuroradiologists, were able to achieve high R^2 values (0.64 and 0.89), and good agreement on Bland-Altman analysis. However, due to the small number of FCs with a true average thickness of <0.5 mm, the capability of ARFI for detecting “critical” caps could not be assessed rigorously. There were only three examples in the data set

of FCs that were less than 0.5 mm thick. The thinnest cap (0.24 mm) was completely missed by all three radiologists, the second thinnest cap (0.34 mm) was caught by two radiologists but incorrectly classified by both as having a thickness of >0.5 mm, and the third cap (0.49 mm) was caught by two radiologists and correctly classified by both as having a thickness of <0.5 mm. Not surprisingly, this third cap in the series was the only one that was thicker than the expected axial resolution limit of the system ($0.4 \mu\text{m}$ at 6.15 MHz and 1.5λ tracking kernel). Although more data should be collected to determine whether ARFI is sensitive to <0.5 mm caps, the results depicted in Figure 9.11 suggest that ARFI should be able to determine whether a cap is “non-critical” (i.e. >0.5 mm) with relatively high accuracy. This performance is also expected to increase by utilizing higher frequency ARFI configurations as seen in Chapter 7.

There were a number of limitations to this study. First, a large number of plaque subsections ($N = 42$, out of 100) had to be excluded because a given wall fell outside of the ARFI focus. This represents one of the main drawbacks of ARFI; namely, that if the focus is not set precisely, complete plaque characterization may be hindered. This problem may be alleviated in the future using rapid multi-focal-zone ARFI techniques to extend the depth of field of an ARFI image [240]. Second, as described previously, perfect alignment between ultrasound and histology was challenging. Histological samples were occasionally warped or poorly adhered to the slide (particularly NC tissue), which sometimes made rating samples difficult. Great care was taken to ensure that each histological slice was aligned to the corresponding ARFI image prior to being given to the pathologist for rating; however, it is expected that there remained some amount of disagreement between histology and ARFI imaging planes (particularly for images that were acquired prior to the development of the μCT alignment techniques described in Chapter 8). Finally, as was done in Chapter 5, each subsection was considered to be an independent sample for statistical analysis. This assumption is valid for most cases, but not valid for adjacent subsections from the same plaque wall. Due to the challenges with describing a correlation function for a given reader between adjacent subsections, this assumption was accepted, as was done in Chapter 5, under the justification that our parametric estimations of reader response distributions should still be statistically consistent even without knowing the correlation structure.

9.5 Conclusion

This study has demonstrated the potential for blinded readers to use ARFI for discriminating soft from stiff plaque components under guided conditions (i.e. when the plaque border is outlined). Although the readers achieved relatively low AUC for distinguishing individual plaque components, performance improved for combined stiff collagen and calcium (median AUC: 0.859) and soft lipid-rich necrotic core and hemorrhage (median AUC: 0.887) categories. Additionally, ARFI was capable of measuring fibrous cap thickness as thin as approximately 0.49 mm and showed good agreement with histologically measured thickness. Lastly, the performance of ARFI for plaque characterization was shown to be highly dependent on reader specialization (with radiologists performing better than non-radiologists). Given these encouraging preliminary results, the next step to translating ARFI to the clinic will be to perform prospective clinical trials to determine whether ARFI features can be used to predict plaque vulnerability and future ischemic events.

CHAPTER 10

Towards Intravascular ARFI (IV-ARFI) Imaging

The following chapter describes a novel, dual-frequency ultrasound transducer designed for catheter-based ARFI imaging with application in coronary plaque characterization. Two designs are presented; an initial prototype transducer with a 5 MHz pushing element and a 40 MHz tracking element, and a second-generation design with 6.5 MHz pushing element and 26 MHz tracking element. Feasibility of ARF generation is shown first using optical tracking techniques, followed by full ARFI ensemble acquisition in a tissue-mimicking phantom. Additionally, acoustic characterization is performed for both transducers. The results of this study show that ARFI imaging is feasible on a small-aperture transducer fit for IVUS implementation.

10.1 Introduction

The methods presented thus far for ARFI-based plaque characterization have focused on imaging plaque specifically in the peripheral arteries, such as the carotid arteries. Peripheral arteries are typically superficial and have relatively large diameter making them ideal imaging targets for ARFI. Coronary arteries, on the other hand, are small, deep, and obstructed by ribs. Transthoracic ultrasound can be used to image all three of the major coronary arteries (left anterior descending, circumflex, and right coronary

© 2014 IEEE. Portions reprinted, with permission, from T. J. Czernuszewicz, C. M. Gallippi, Z. Wang, J. Ma, and X. Jiang, "Acoustic radiation force (ARF) generation with a novel dual-frequency intravascular transducer," in Proc. IEEE Ultrason. Symp., Chicago, IL, USA, 2014.

© 2015 IEEE. Portions reprinted, with permission, from Z. Wang, T. J. Czernuszewicz, C. M. Gallippi, X. Jiang, "Dual frequency IVUS transducer for acoustic radiation force impulse (ARFI) imaging," in Proc. IEEE Ultrason. Symp., Taipei, Taiwan, 2015.

artery) [280]; however, the frequencies (3-5 MHz) and small aperture sizes (≤ 1 cm) required for this type of imaging are far too low to image vulnerable plaque features such as thin fibrous caps (< 0.65 mm). Therefore, ultrasonic coronary plaque imaging is typically performed with minimally-invasive intravascular ultrasound (IVUS) [281]. In IVUS, an ultrasound transducer (single element or an array) is placed at the end of a catheter and guided to the coronary vasculature through a femoral access site.

A significant challenge with implementing ARFI on an IVUS system is that IVUS transducers and arrays typically operate at very high frequencies (20-45 MHz) and are not designed to sustain the high-voltage, long-duration pulses required for ARFI imaging. Additionally, when high frequencies are used for the ARF pulse, the magnitude of the displacements may be reduced due to the significant attenuation of acoustic intensity at higher frequencies. Indeed, in a preliminary study that implemented ARFI on two modified Volcano IVUS arrays [282], higher peak displacements were observed using 9 MHz ARF pulses compared to 20 MHz, suggesting a tradeoff between spatial resolution and ARFI signal-to-noise ratio (SNR) when using single-frequency transducers. Therefore, an optimal IV-ARFI implementation for high-resolution coronary plaque characterization will most likely require a dual-frequency approach similar to that proposed for corneal imaging [283].

In this chapter, ARFI is first implemented on a small-aperture, dual-frequency IVUS transducer previously designed for microbubble contrast imaging [284]. The transducer's capability to generate displacement with ARF is evaluated using previously described optical tracking methods [272]. Then, a second-generation transducer is designed to improve the performance of the IV-ARFI transducer and full acoustic tracking along with ARF-generation is demonstrated in a graphite phantom.

10.2 Methods

10.2.1 Transducer Design (1st Generation)

The first generation transducer used in this study is described in detail in Ma et al. [284]. Briefly, the transducer was designed as a dual-element layered structure. The low-frequency “pushing” element ($0.6 \times 3.0 \times 0.3$ mm) comprised the lower layer of the transducer with the high-frequency “tracking”

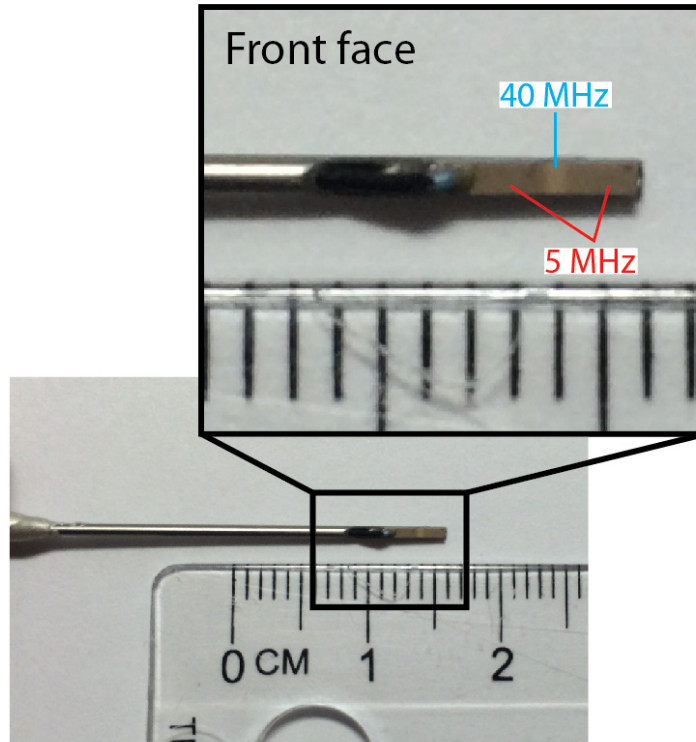


Figure 10.1: Photograph of the front face of the first-generation dual-frequency IVUS probe mounted on the end of a 20-gauge needle tip.

element ($0.6 \times 0.5 \times 0.065$ mm) resting on top. Matching layers of $\text{Al}_2\text{O}_3/\text{epoxy}$ and Parylene were casted and coated on top of the low-frequency and high-frequency elements, respectively, to improve acoustic output and sensitivity. A frequency-selective isolation layer was placed between the two elements to serve as a backing for the high-frequency element, and the entire structure was mounted on the tip of a 20-gauge hypodermic needle. The active piezoelectric material used for both low and high frequency elements was lead magnesium niobate-lead titanate (PMN-PT). A photograph of the transducer is shown in Figure 10.1.

10.2.2 Optical Phantom Construction

A translucent, gelatin-based, tissue-mimicking phantom was constructed based on the formulation described in Appendix A. The phantom recipe consisted of the following ingredients (with percent

composition by mass in parentheses): 300 bloom type-A gelatin (4%; Sigma-Aldrich Corp., St. Louis, MO), agar (0.5%; Fisher Scientific, Fair Lawn, NJ), <15- μ m graphite (0.36%), n-propanol (1%), corn syrup (15.5%) and de-ionized water (78.64%). The agar powder was left unmelted and served as the main acoustic scatterer, while the graphite particles served as markers for optical tracking. Corn syrup was added to increase the acoustic attenuation while maintaining translucency. Attenuation in the phantom was measured to be 0.3 dB/cm/MHz.

Phantom stiffness was measured using ultrasonically-based shear wave speed measurement implemented on a Siemens Acuson Antares (Siemens Medical Solutions USA Inc., Ultrasound Division) scanner. Shear wave group velocity was measured using lateral time to peak methods described previously [189].

10.2.3 Optical Tracking of ARF Displacement

ARF-induced displacements were measured in the translucent phantom with a custom high-speed camera setup described in Appendix A. The setup consisted of an acrylic water tank mounted on an Olympus IX71 inverted microscope (Olympus America Inc., Melville, NY) fitted with a 10 \times objective and opposing, coaxial, 100-W halogen illumination source. Optical data from the microscope were digitized with a Fastcam SA1 high-speed camera (Photron USA Inc., San Diego, California, USA) configured to acquire frames at 150 kHz across a 128 x 128 pixel field of view (FOV). Prior to data collection, the optical and acoustic foci were aligned using a needle hydrophone (HNC-0400, Onda Corp. Sunnyvale, CA) mounted on a manual micro-positioning stage. Figure 10.2 shows an illustration of the optical setup.

With the acoustic and optical foci aligned, the needle hydrophone was replaced with an optical phantom held in an acrylic holder. Using the manual positioning stage, the phantom was translated until a graphite particle was visualized in the microscopes FOV. Once positioned, the manual and digital motion stages were locked for a stable data collection.

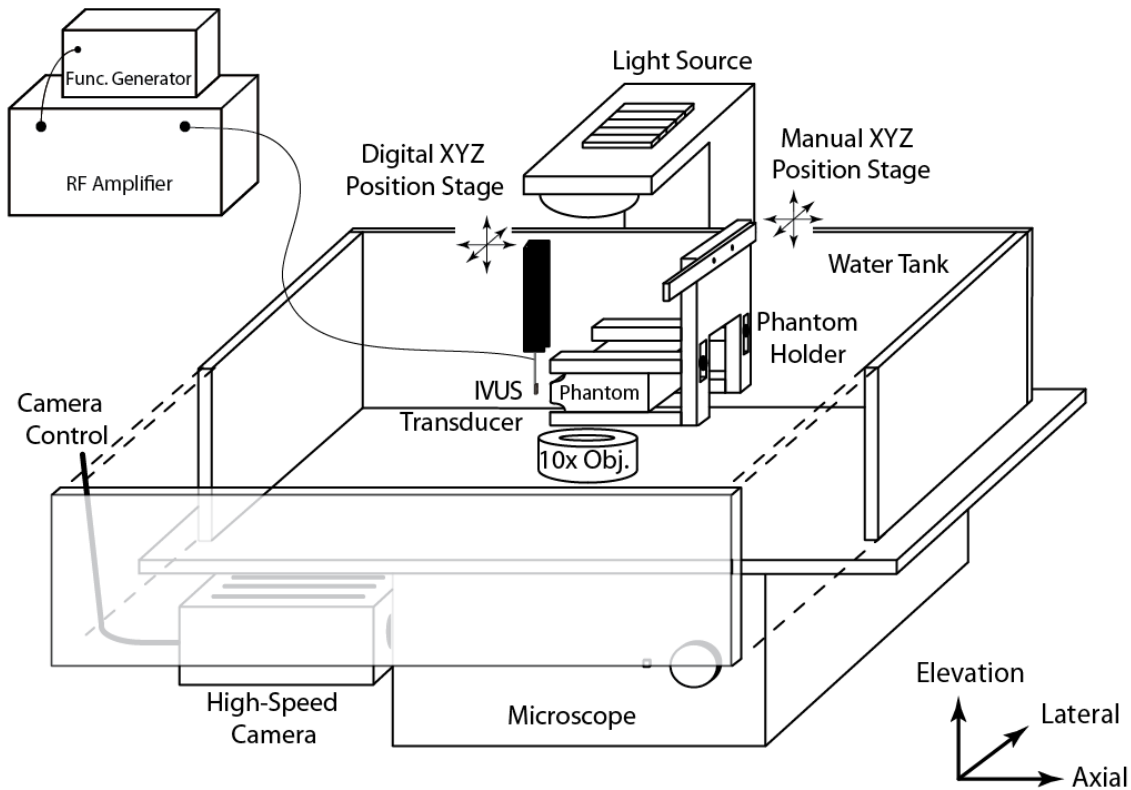


Figure 10.2: Illustration of IV-ARFI optical tracking setup.

To generate ARF, sinusoidal bursts with varying pulse length (300, 600, 900, and 1200 cycles) at 5 MHz were generated with an arbitrary function generator (AFG3102, Tektronix Inc., Portland, OR) and amplified by 50 dB with a radiofrequency amplifier (3200L, Electronic Navigation Industries Inc. Rochester, NY). The amplitude of the pre-amplified burst was set to 600 mV_{pp} (190V after amplification). To synchronize data capture, the function generator was set to manual trigger mode, and the trigger output was connected to the TTL trigger of the high-speed camera. Five repeated acquisitions were captured at each of the pulse durations, and saved to disk for processing.

Optical motion tracking was performed using 2D normalized cross correlation (NCC). Two-stage interpolation was utilized to measure subsample displacements; first, optical movie frames were upsampled by a factor of 4 using spline interpolation prior to running NCC, and then correlation curves

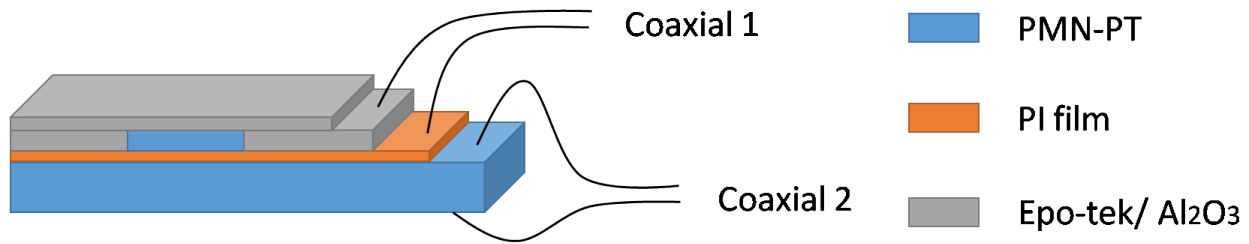


Figure 10.3: Structure of the second-generation IV-ARFI transducer. Single-crystal PMN-PT served as the active material for both the high (coaxial 1) and low (coaxial 2) frequency elements. PI film was used as a frequency-selective isolation layer. Epo-tek epoxy and Al_2O_3 was used for the matching layers.

were further upsampled by a factor of 4 prior to selecting the maximum. Finally, displacement profiles were filtered with a fourth-order 10 kHz lowpass Butterworth filter to reduce high-frequency noise.

10.2.4 Acoustic Backscatter Test

Individual A-lines were captured from the phantom using a custom program developed in Labview (National Instruments, Austin, TX). To test the motion-tracking capabilities of the transducer, one A-line was captured for reference and the transducer was moved with a manual motion stage ~ 0.1 mm away from the phantom face. A-lines were imported into MATLAB, filtered with a fourth-order Butterworth bandpass (30-55 MHz), and motion tracked using one-dimensional normalized cross-correlation. Specific parameters of the cross-correlation algorithm included upsampling the RF data with $4\times$ spline interpolation, and motion-tracking kernel sizes of 5λ , 6λ and 7λ .

The pulse/echo capability of the high frequency element was tested using a standard non-translucent graphite gelatin phantom. The phantom recipe consisted of the following ingredients: 300 bloom type-A gelatin (5%), graphite (5%), n-propanol (1%), and de-ionized water (89%). The phantom was congealed in a plastic container and a cylindrical hole (~ 5 mm diameter) was cut into the phantom from the top so the IVUS probe could be inserted. To generate acoustic pulses, the high-frequency element was driven with a pulser/receiver (5900PR, Panametrics Inc., Waltham, MA) using $1 \mu\text{J}$ output energy. The receive settings on the pulser included a 10-50 MHz analog bandpass filter and 48 dB gain.

Table 10.1: Parameters of 2nd-generation IV-ARFI design.

Parameter	Pushing layer	Tracking layer
Center Frequency	6.5 MHz	26 MHz
Active material	PMN-PT	PMN-PT
Active material impedance (MRayl)	32	32
Active material width (mm)	0.6	0.6
Active material length (mm)	5	0.6
Active material thickness (μm)	300	70
Matching	$\text{Al}_2\text{O}_3/\text{epoxy}$	$\text{Al}_2\text{O}_3/\text{epoxy}$ and Parylene C
Matching impedance (MRayl)	5.5	5.5 and 2.6
Matching thickness (μm)	110	20 and 12
Isolation material	-	Polyimide
Isolation impedance (MRayl)	-	3.5
Isolation layer thickness (μm)	-	12.5

The received voltage signal from the pulser was sampled with an A/D card (PDA16; Signatec Inc., Newport Beach, CA) at 160 MHz.

10.2.5 Transducer Design (2nd Generation)

The second-generation dual-frequency IVUS transducer similarly consisted of a PMN-PT single crystal low-frequency pushing element (6.5 MHz) and a PMN-PT single crystal high-frequency tracking element (26 MHz). The dimensions of the low-frequency pushing and high-frequency tracking elements were $5.0 \text{ mm} \times 0.6 \text{ mm} \times 0.3 \text{ mm}$ and $0.5 \text{ mm} \times 0.6 \text{ mm} \times 0.07 \text{ mm}$, respectively (Figure 10.3). Similar to the first generation transducer, an acoustic isolation layer was placed between the two piezoelectric layers. However, a substantial change in this transducer was the addition of a second ground wire to help isolate the low and high frequency elements.

A polyimide (PI) film was chosen to be used as the isolation layer of the high-frequency element and the thermal barrier because of its low acoustic impedance and low thermal conductivity. This thermal

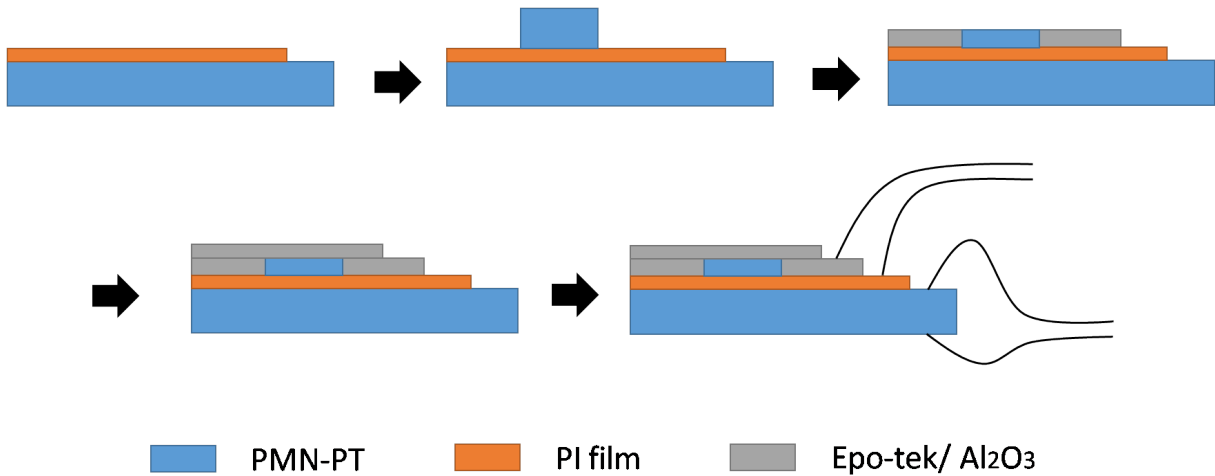


Figure 10.4: Fabrication process of a dual-frequency IVUS transducer.

barrier layer protects the high-frequency tracking element when a high voltage, long-duration pulse is applied to the low-frequency pushing element.

The isolation layer thickness and the pulse-echo responses of high-frequency element were designed using the KLM model [285]. For the high-frequency element, a dual-matching-layer structure was designed to increase the bandwidth and the sensitivity. Primary design parameters are listed in Table 10.1.

A flow diagram of the fabrication strategy is shown in Figure 10.4. A PMN-PT single-crystal plate ($5\text{ mm} \times 5\text{ mm} \times 0.3\text{ mm}$) with Cr/Au as electrodes on both $5\text{ mm} \times 5\text{ mm}$ surfaces was prepared first. A $12\text{-}\mu\text{m}$ PI film (Kapton HN, DuPont, Wilmington, DE) was metalized with Ti/Au on the top surface by using e-beam deposition as a connection with the bottom electrode of the high-frequency element. The PI film was bonded on top of the low-frequency element by using Epo-tek 301 (Epoxy Technology Inc., Billerica, MA). A small PMN-PT chip ($5.0\text{ mm} \times 0.6\text{ mm} \times 0.3\text{ mm}$) was then bonded on top of the PI film. An Al_2O_3 /epoxy layer was poured to surround the high-frequency element and lapped to the designed thickness (0.07 mm). The top electrode (100\AA Ti, 1000\AA Au) of the high-frequency element was deposited by e-beam deposition. Afterwards, the matching layer of the high-frequency element (Al_2O_3 /epoxy) was poured on the high-frequency element and lapped to $20\text{ }\mu\text{m}$. Then

the whole package was bonded to a 20-gauge needle by using silver epoxy (8331-14G, M.G. Chemicals, Surrey, B.C., Canada). Two coaxial cables (MCX 40232, Hitachi Cable America Inc., Purchase, NY) were bonded to the high-frequency element and low-frequency element of the transducer, separately, using silver epoxy. Finally, a passivation layer and the second matching layer of the high-frequency element, Parylene C, with a thickness of 12 μm was coated by using the SCS Labcoter® 2 vacuum deposition system (PDS 2010, Specialty Coating Systems, Inc., Indianapolis, IN). Transducer design and fabrication was performed by collaborators at North Carolina State University (Zhuochen Wang, and Dr. Xiaoning Jiang).

10.2.6 Transducer Characterization

The second-generation dual-frequency IVUS transducer was characterized by measuring the complex electrical impedance, pulse-echo responses of the high-frequency element, and acoustic pressure transmission generated by the low-frequency element. Electrical impedance and phase were measured with an impedance analyzer (Agilent 4294A, Agilent Technologies Inc., Santa Clara, CA).

The center frequency and fractional bandwidth of the high-frequency element were obtained from the pulse-echo measurement in a water tank using a pulser/receiver (5900 PR, Olympus Corp, Waltham, MA) and an oscilloscope (Agilent DSO7014B, Agilent Technologies Inc., Santa Clara, CA). The energy of the applied pulse was set to 1 μJ during pulse-echo test. A point target was placed in front of the high frequency element as the reflection target at a distance of 3 mm away from the aperture.

The acoustic pressure measurement of the low frequency element was conducted by using a hydrophone (HNA-0400, ONDA Co, Sunnyvale, CA) positioned at 5 mm axially away from the transducer surface. A 5 V, 10-cycle sinusoidal burst at 6.5 MHz was generated by an arbitrary function generator (AFG3101, Tektronix Inc., Beaverton, OR). Pressure output was recorded using an oscilloscope (Agilent DSO7014B, Agilent Technologies Inc., Santa Clara, CA).

10.2.7 ARFI Testing

A standard non-translucent graphite gelatin phantom with 10 kPa elastic moduli was prepared. The phantom recipe consisted of the following ingredients: 300 bloom type-A gelatin (5%), graphite (5%), n-propanol (1%), and de-ionized water (89%). The phantom was congealed in a plastic container and a cylindrical hole (~5 mm diameter) was cut into the phantom from the top so the IVUS probe could be inserted (Figure 10.5a). Phantom stiffness was measured using ultrasonically-based shear wave speed measurement implemented on a Siemens Acuson Antares (Siemens Medical Solutions USA Inc., Ultrasound Division) scanner.

A custom program developed in Labview (National Instruments, Austin, TX) was used to control the low frequency pushing and high frequency tracking during the ARFI test (Figure 10.5b). The ARFI test was performed by pushing the phantom with 600, 900, and 1200-cycle sinusoidal bursts (92.3, 138.5, and 184.6 μ s, respectively) using the low-frequency pushing element. The excitation bursts were generated with an arbitrary function generator (AFG3102, Tektronix Inc., Beaverton, OR) and amplified to 160 Vpp with a radiofrequency amplifier (3200L, Electronic Navigation Industries Inc., Rochester, NY). In order to track the displacement of the phantom, the high frequency element was driven with a pulser/receiver (5900PR, Olympus Corp, Waltham, MA) using 2 μ J output energy. The pulse/echo settings on the pulser included a 10-50 MHz analog bandpass filter and 48 dB gain. The received voltage signal from the pulser was sampled with an A/D card (PDA16; Signatec Inc., Newport Beach, CA) at 160 MHz. The ARFI transmission and pulse/echo tracking were synchronized by the arbitrary function generator – channel 1 was programmed to output the ARF burst after a time delay of 0.2 ms, while channel 2 was programmed to output a trigger signal to drive the pulser/receiver at the tracking PRF.

The ARFI pulse sequence was designed as 1) two reference A-lines followed by 2) a pushing pulse at the same location, and 3) 58 tracking pulses to monitor phantom displacement. A pulse repetition frequency (PRF) of 10 kHz was used for the pulse sequence. All raw RF data were saved to disk for offline processing. Prior to motion tracking the data were filtered with a 5-tap Butterworth bandpass (10-40 MHz) and up-sampled by a factor of 4 using spline interpolation. Displacement was calculated using

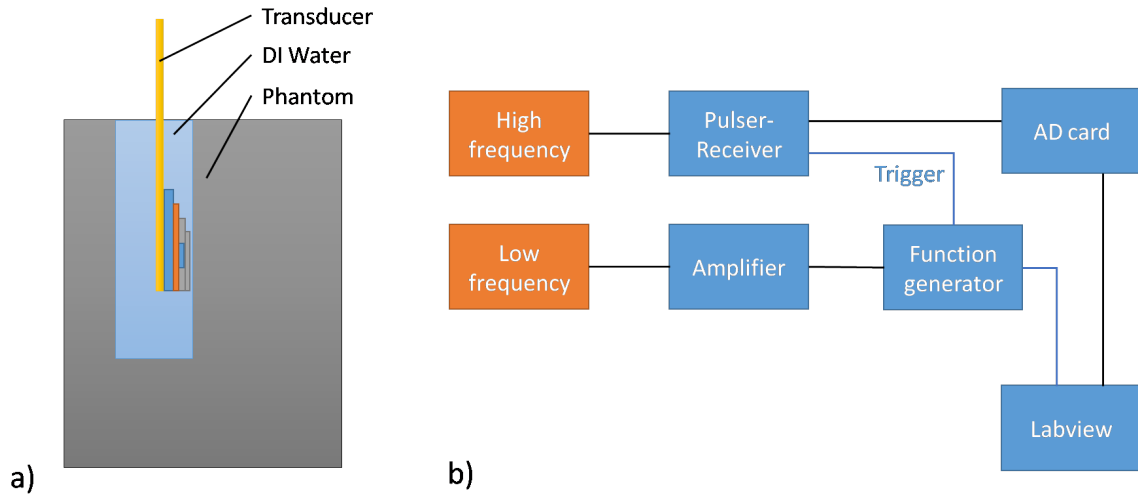


Figure 10.5: Experimental setup for ARFI test in the phantom. a) The IVUS-ARFI transducer was put in the cylindrical hole and merged in the deionized water. b) The block diagram of ARFI test.

normalized cross-correlation between the up-sampled reference and tracking lines [206]. Peak-hops, due to subtle inconsistencies with the pulser PRF, were observed and removed using a custom approach. This was implemented by motion tracking a known stationary echo (i.e. the transmit ring-down present in the nearfield), and subtracting the motion of the stationary echo from the displacement profile at the depth of interest (located $\sim 2\text{-}5$ mm away from the transducer).

10.3 Results/Discussion

10.3.1 First-Generation Transducer

Figure 10.6a shows the results of the optical tracking experiments for the first generation transducer in an $8.1 (\pm 0.8)$ kPa phantom using ARF bursts of 300 ($60 \mu\text{s}$), 600 ($120 \mu\text{s}$), 900 ($180 \mu\text{s}$), and 1200 cycles ($240 \mu\text{s}$) at 5 MHz. Each graph represents the median of 5 repeated acquisitions. As expected, longer pulse durations increased the magnitude of ARF displacement up to $\sim 1.5 \mu\text{m}$ for the longest pulse. At approximately 4 ms, a shear wave reflection is seen from the front face of the phantom (arrow) altering the exponential recovery of the displacement curve. Figure 10.6b shows boxplots of peak displacement versus ARF pulse duration for the repeated acquisitions (whiskers represent 1.5 times the

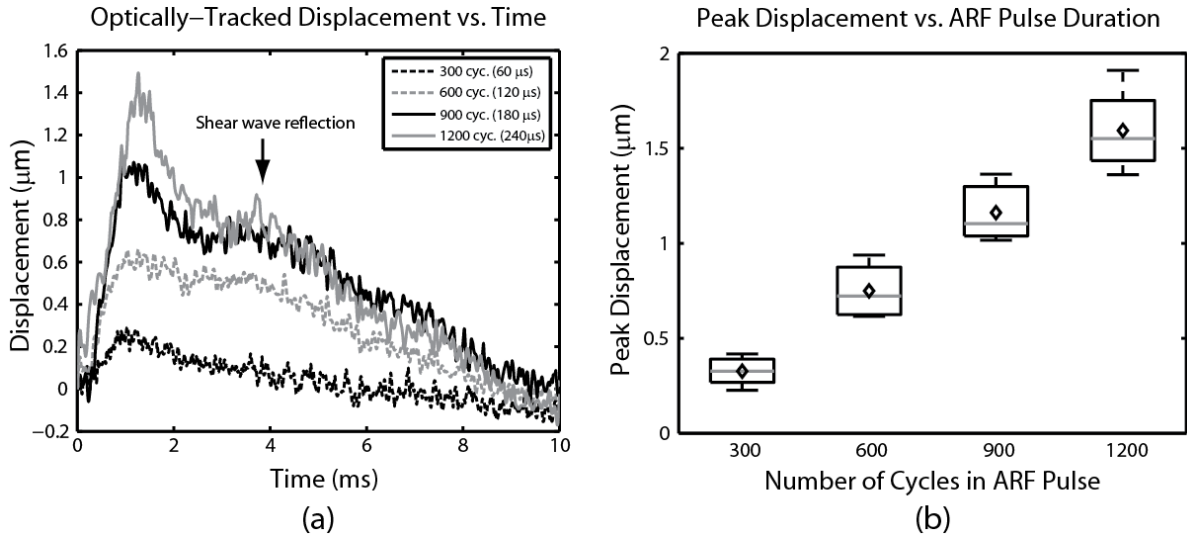


Figure 10.6: Displacements measured optically from first generation IV-ARFI transducer. (a) Median displacement vs. time curves tracked optically (legend indicated the duration of the ARF-burst in number of cycles). As the number of cycles in the ARF burst is increased, peak displacement increases. A shear wave reflection from the front face of the phantom is seen at ~ 4 ms (arrow). (b) Boxplots showing peak displacement versus ARF pulse duration measured from the 5 repeated acquisitions. Whiskers represent 1.5 times the IQR. Mean plotted as a diamond on top of each box.

inter-quartile range). Median (IQR) peak displacement for 300, 600, 900, and 1200 cycles were 0.33 (0.27 – 0.39) μm , 0.72 (0.62 – 0.87) μm , 1.1 (1.0 – 1.3) μm , and 1.6 (1.43 – 1.75) μm , respectively.

Figure 10.7 shows an A-line captured with the 40 MHz element of the first generation IV-ARFI transducer in an opaque graphite phantom. The edge of the phantom is clearly seen at ~ 3 mm axial depth, and identifiable backscatter extends ~ 2 mm into the phantom (indicated by the gray fill in the image) before attenuating to the noise floor. Maximum signal amplitude (measured in the region between 3-5 mm) was 16.7 dB higher than the maximum amplitude of the electronic noise (measured in the region between 5 and 7 mm). Figure 10.8 shows two A-lines taken with the 40 MHz element, one prior to movement (shown previously in Figure 10.7) and the other after ~ 100 μm of bulk motion from a manual motion stage. Median (median absolute deviation) displacements measured with NCC from the range of 3-5 mm were 111.6 (± 39.9) μm , 111.7 (± 8.0) μm , and 111.7 (± 1.9) μm using kernel lengths of 5λ , 6λ and 7λ , respectively. As expected, larger kernel sizes decreased error on the displacement measurements.

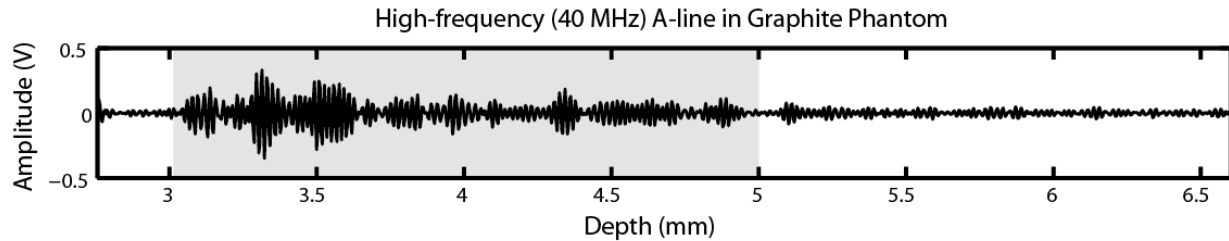


Figure 10.8: A-line acquired by the high-frequency element of first generation IV-ARFI transducer in a graphite phantom to illustrate the capability for pulse/echo imaging. The phantom edge occurs at ~ 3 mm from the transducer face, and measurable backscatter extends ~ 2 mm into the phantom (indicated by the gray fill) before attenuating below the noise floor. Maximum signal amplitude is 16.7 dB higher than the noise floor.

While the preliminary results from the first generation IV-ARFI transducer were promising, a number of challenges arose. First, a full ARFI acquisition with acoustic tracking was not realizable due to electrical cross-talk between the low and high-frequency elements. Second, the signal-to-noise ratio (16.7 dB maximum) of the high-frequency element was low compared to conventional ARFI implementations

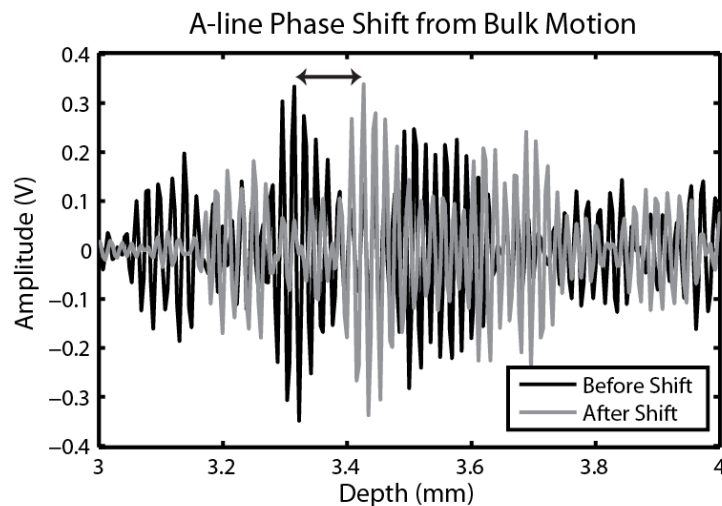


Figure 10.7: Two A-lines taken with the high-frequency element, one prior to movement, and the other after ~ 0.1 mm of bulk motion with a manual motion stage. The two A-lines are out of phase (double-sided arrow) suggesting that motion can be tracked with the high-frequency element.

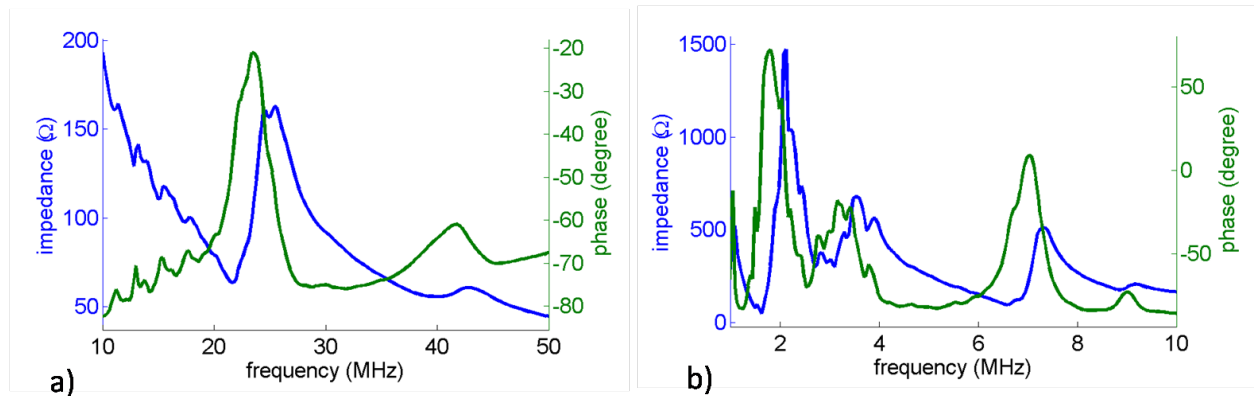


Figure 10.9: Electrical impedance and phase spectrum of 2nd-generation transducer. a) High frequency element and b) low frequency element.

(~40 dB), requiring much larger tracking kernel sizes in order to reduce the effects of jitter. Lower SNR may be expected in IVUS applications because acoustic pulses are unfocused, however the higher frequencies utilized in IVUS would be expected to reduce jitter. Lastly, ARFI displacements measured optically only reached ~1.5 μm in an 8.1 kPa phantom. While this level of ARF generation may be enough to differentiate a soft necrotic core from the rest of the plaque, stiffer plaque components may not be differentiable without increasing the magnitude of the applied ARF. A number of these challenges were addressed with the second-generation transducer, which is detailed in the following section.

10.3.2 Second-Generation Transducer

The transducer characterization results are shown in Figure 10.9 and Figure 10.10, which depict the electrical-impedance/phase spectra and fractional bandwidth, respectively. The electrical impedance for both active layers was approximately 50 Ohms, with resonances at 26 MHz and 6.5 MHz for the high- and low-frequency elements, respectively. The -6 dB fractional bandwidth of the high frequency pulse/echo element was measured to be 47%, covering a frequency span of 20 to 32.7 MHz (Figure 10.10a). The peak-to-peak pressure generated by the low-frequency pushing element with the 5 V, 10-cycle burst excitation was measured to be 233 kPa at 5 mm axially from the transducer surface (Figure 10.10b).

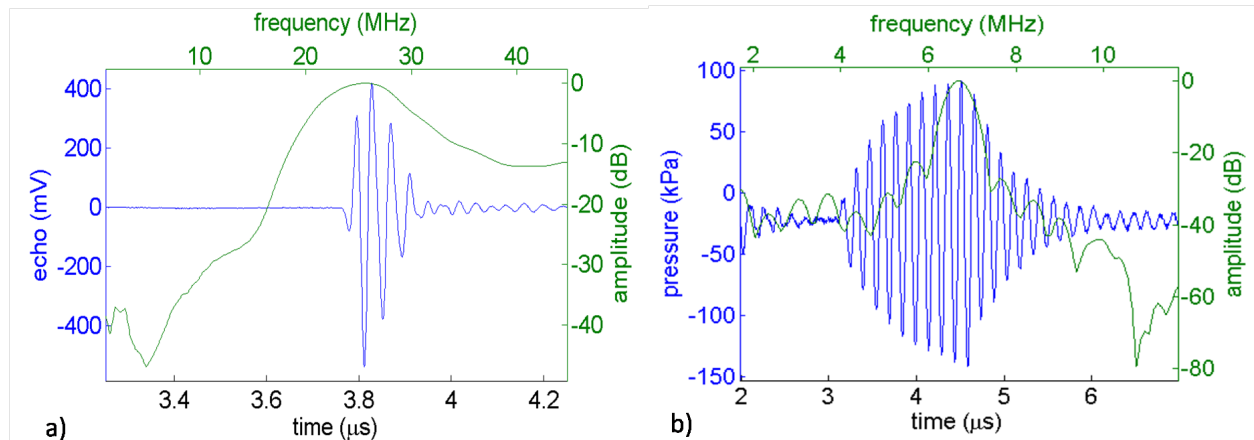


Figure 10.10: Pulse/echo and hydrophone characterization of 2nd-generation transducer. a) Pulse-echo response of high frequency element. b) Hydrophone measurement of low frequency element using a 5 V 10-cycle burst excitation.

Figure 10.11 shows the results of ARFI testing utilizing a 1200 cycle burst and acoustic tracking. Interestingly, the PD vs. axial position graph (Figure 10.11a) shows a soft region located approximately 3 mm away from the phantom surface that displaced more than two times further than the phantom closer to the transducer ($\sim 12 \mu\text{m}$ vs. $\sim 5 \mu\text{m}$, respectively). Displacement vs. time curves for the stiff and soft regions are shown in Figure 10.11b and c.

Figure 10.12 shows PD vs. axial position for a number of ARF burst lengths taken at a different location in the phantom. As expected, the average displacement in the phantom increases as a function of burst duration, and the phantom appears to be much more homogenous throughout the ARFI depth of field (2-5 mm) as compared to the imaging location depicted in Figure 10.11. In both cases, acoustic tracking becomes unpredictable and highly variable at depths greater than 5 mm. This is due to the poor depth penetration and SNR of the tracking pulses, which leads to a substantial increase in jitter. Additionally, the phantom material near to the transducer (less than 2 mm) appears to not displace much. This portion resides in the near field of the low-frequency element, so the low displacement observed in these regions could be due to poor ARF-generation at such shallow depths. Alternatively, it was noted that these transducers suffer from substantial ringdown from the transmitted pulses due to the lack of a

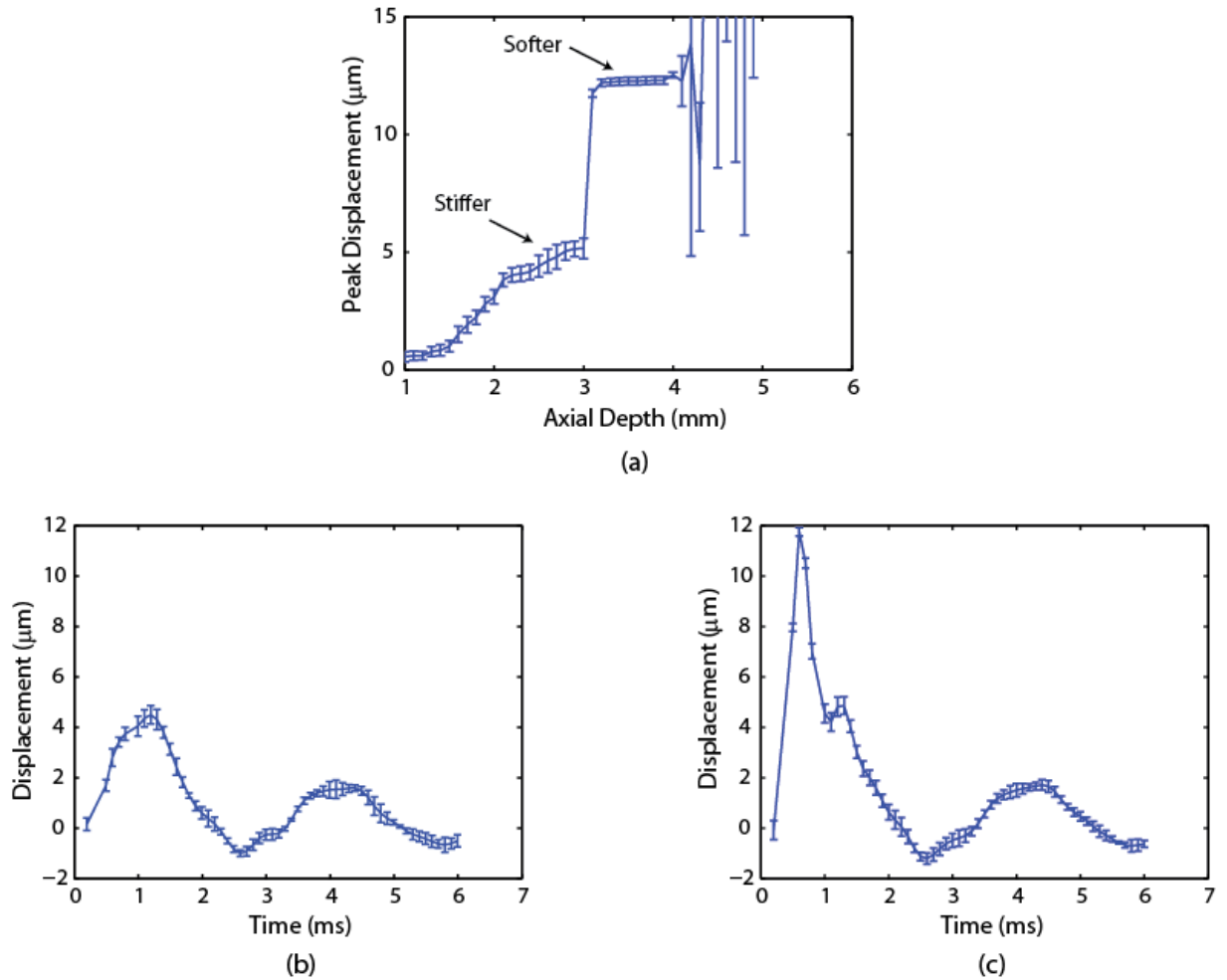


Figure 10.11: Acoustically tracked displacements with 2nd-generation transducer. (a) Peak displacement vs. axial depth showing a soft region in the phantom. (b) Displacement vs. time curve in the stiffer phantom region (2.5 mm axial depth). (c) Displacement vs. time curve in the softer phantom region (3.1 mm axial depth).

true backing layer, which could write stationary clutter into the near-field regions and be measured as little to no motion.

Indeed, the ringdown was utilized as a stationary source to mitigate the effect of peak-hopping that resulted from the instability of the pulser PRF. Although it is expected that the arterial wall will be located around 1-2 mm from the IVUS probe face, future designs will probably require improved backing and ringdown suppression to ensure that measurements of displacement are not biased by stationary echoes.

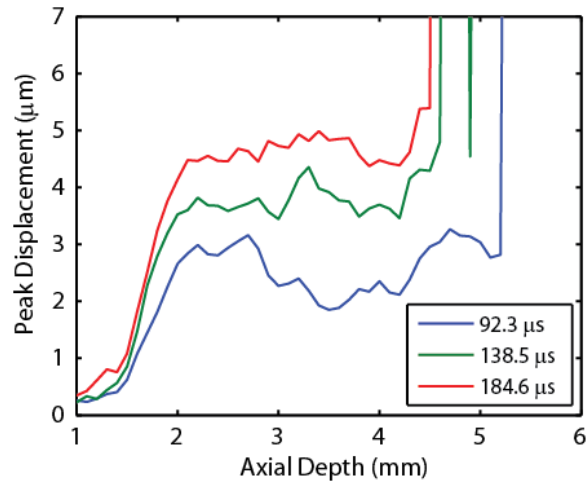


Figure 10.12: Acoustically measured peak displacement vs. time for three different ARF-burst durations. Note this data was acquired at a different phantom location than data in previous figure.

10.4 Conclusion

In this chapter, a novel prototype IVUS transducer capable of performing intravascular ARFI imaging was developed and tested. Using a 2nd-generation design, ARFI displacements of up to 12 μm were measured in a tissue-mimicking phantom with average stiffness of 10 kPa. As expected, ARF displacement was proportional to the pulse duration of the ARF burst, with the longest bursts (~200 μs) resulting in the most displacement. In the future, this transducer will need to be mounted on a rotational motor to generate 2D IV-ARFI images, and tested on actual atherosclerotic plaques to determine whether it can differentiate vulnerable plaque features.

This chapter represents the final piece of research that was completed as part of this dissertation. In the following chapter, a summary of important conclusions derived from this work is given, and some future directions for improving ARFI plaque characterization are presented.

CHAPTER 11

Conclusions and Future Directions

11.1 Conclusions

The results presented in this dissertation support the hypothesis that ARFI ultrasound is capable of noninvasively characterizing atherosclerotic plaque composition in humans by interrogating mechanical stiffness. In general, it was demonstrated that areas of elevated peak displacement correlate with the presence of necrotic core or intraplaque hemorrhage, while areas of decreased peak displacement correlate with the presence of fibrosis or calcification. Not only was it shown that ARFI stiffness can reveal underlying plaque composition, but that largely untrained readers can identify these regions while blinded to the histological result, so long as the readers are guided to the location of the plaque border. In the best cases, some radiologists were able to achieve AUCs exceeding 0.9 for the combined lipid/hemorrhage and collagen/calcium rating categories. This result is a key accomplishment of this dissertation and suggests that ARFI is not only an effective technique, but also a facile one that can be learned quickly. It is expected that as ARFI-based elastography methods continue to penetrate into clinics and hospitals, radiologists will become more familiar with them and performance should improve beyond that demonstrated in these preliminary studies.

In addition to measuring performance, ARFI was shown to be relevant to quantifying fibrous cap thickness with both FEM simulation and *in vivo* validation. In the FEM studies, it was shown that ARFI has the potential to visualize fibrous caps down to 0.2 mm when using the highest possible tracking frequency (12 MHz) and best signal processing parameters (1λ tracking kernel, and optimal dynamic range scaling). An important result from FEM analysis was that coupling between the stiff fibrous cap and the necrotic core introduces a positive bias into ARFI measurements that is largely independent of

imaging parameters. The bias was shown to be consistent across a wide range of fibrous cap thicknesses (0.1 – 1 mm) with an average magnitude of approximately 0.13 mm. Due to the consistency of the bias, it is possible that a simple correction factor could be developed to remove it if fibrous cap measurement is implemented clinically. However, the simulations also revealed that the bias is highly sensitive to image dynamic range. Improved methods of automatically scaling ARFI images will be critical for the success of fibrous cap thickness measurement with ARFI.

Finally, this work was the first to demonstrate ARFI in ruptured plaques with hemorrhage, a feature that has otherwise never been imaged before with ARFI. As predicted, ARFI displacements were elevated in regions of hemorrhage, with similar magnitude to that seen in necrotic core. Although blinded readers were not able to uniquely identify hemorrhage from necrotic core, careful unblinded analysis of ARFI images showed that rupture may be directly visualized by identifying locations where high-displacing plaque regions communicate with the lumen.

11.2 Future Directions

There were a number of challenges encountered during the course of this work that serve as starting points for future directions of ARFI plaque characterization. First was the inability of ARFI to uniquely describe intraplaque hemorrhage from necrotic core. Prospective MRI studies have shown that the presence of intraplaque hemorrhage and thinning/ruptured fibrous cap carry slightly higher hazard ratios for future ischemic events compared to intact necrotic core (4.59 and 5.93 compared to 3.00) [102]. Therefore, improving ARFI's sensitivity to rupture and hemorrhage should be a priority going forward. This could be achieved by utilizing higher resolution ARFI systems, and potentially implementing advanced clutter suppression techniques such as harmonic ARFI imaging to enhance image quality. A lower priority, but no less important, would be the improvement of ARFI for distinguishing between collagen and calcium. The literature on the dangers of calcification is mixed, with some studies showing that it helps stabilize plaque and others that show it destabilizes [286]. For ARFI to reach its full potential as a plaque characterization technique, it will need to uniquely discriminate calcium in order to determine

the cases where it increases vulnerability. Some of these features may be better discriminated by considering more than peak displacement alone and, instead, evaluating the full motion dynamics in response to an ARFI excitation. Methods that utilize robust principal component analysis (PCA) to reduce and cluster ARFI data sets [287] or fit biomechanical models to the measured tissue displacements to evaluate viscoelastic parameters [207] may be relevant in this regard.

Second, readers, in general, had lower AUC performance when the plaque border was not identified for them. This could have been attributed to the unsophisticated B-mode imaging that was used in these studies, or to the lack of definition of the lumen in some ARFI images, or both. These conclusions are based on the experience of the unblinded reader, who ultimately determined the true plaque outlines. Even with knowledge of the histology, the unblinded reader sometimes had difficulty perceiving the plaque outline in some hybrid B-mode/ARFI images. The plaque borders were truly made clear when the higher-resolution B-mode images from the patient's medical record and power Doppler representations of the lumen were also seen. Therefore, it is expected that the "unguided" blinded readers' AUCs would have matched more closely with the "guided" AUCs because the plaque outlines would have been detected more accurately. Implementing high resolution B-mode and Doppler methods should be possible in second generation ARFI plaque characterization systems because combined ARFI/Doppler pulse sequences have since been developed [256].

Third, due to the small number of patients enrolled in this study, it was difficult to assess the differences between plaques from symptomatic and asymptomatic patients. In general, it appeared that the asymptomatic patients had more heavily calcified plaques and had less distinct "soft features" on ARFI images. More patients need to be imaged to determine whether these trends hold true. Improving the sensitivity of noninvasive imaging to dangerous asymptomatic atherosclerosis is regarded as one of the top priorities in the medical community due to new evidence suggesting CEA may no longer be the best intervention strategy for asymptomatic disease [63]. Therefore, future ARFI studies should specifically target asymptomatic patients to determine what additional information can be provided by this modality.

Finally, the next step to bringing ARFI closer to the clinic will likely be the conduction of larger prospective clinical trials that correlate ARFI plaque signatures to future ischemic events. While it was necessary to utilize CEA patients in this dissertation to validate ARFI's capability of detecting plaque features, these patients represent a sort of "best case" scenario for imaging because plaques in these patients are usually highly advanced and features are large. It is expected that lower grade plaques may be more challenging to image as features get smaller. For ARFI to make a significant impact on standard of care, it has to exceed the performance of Duplex ultrasound for predicting which plaques are likely to cause a stroke. This means that it must be effective in asymptomatic patients and patients with much lower stenosis levels than were imaged in this CEA study. Prospective studies will be critical to getting ARFI accepted as a relevant carotid imaging technique.

While there is still much work to be done, the research presented in this dissertation suggests that ARFI is very capable of detecting vulnerable plaque features and has the potential of greatly improving diagnosis of atherosclerosis in peripheral arteries. Future studies should build on the work presented herein and utilize the data sets provided to improve the next generation of ARFI plaque imaging systems.

APPENDIX A

Experimental Validation of Displacement Underestimation in ARFI Ultrasound

In this appendix, optical tracking was utilized to experimentally measure the displacement underestimation achieved by acoustic tracking using a clinical ultrasound system. Three optically translucent phantoms of varying stiffness were created, embedded with sub-wavelength diameter microspheres, and ARFI excitation pulses with F/1.5 or F/3 lateral focal configurations were transmitted from a standard linear array to induce phantom motion. Displacements were tracked using confocal optical and acoustic methods. As predicted by earlier FEM studies, significant acoustic displacement underestimation was observed for both excitation focal configurations; the maximum underestimation error was 35% of the optically measured displacement for the F/1.5 excitation pulse in the softest phantom. Using higher F/#, less tightly focused beams in the lateral dimension improved accuracy of displacements by approximately 10 percentage points. This work experimentally demonstrates limitations of ARFI implemented on a clinical scanner using a standard linear array and sets up a framework for future displacement tracking validation studies.

A.1 Introduction

Acoustic radiation force impulse (ARFI) ultrasound is a non-invasive imaging technique that is used to investigate the mechanical properties of internal tissues [205]. Fundamentally, ARFI works by employing a long duration ultrasonic pulse that, through transfer of momentum, generates a force in the

© 2013 SAGE Publications. Portions reprinted, with permission, from T. J. Czernuszewicz, J. E. Streeter, P. A. Dayton, and C. M. Gallippi, "Experimental validation of displacement underestimation in ARFI ultrasound", *Ultrason. Imaging*, vol. 35, no. 3, pp. 196–213, Jul. 2013.

propagating medium. This force displaces the underlying tissue in a highly localized manner serving as a precise, virtualized form of palpation.

The physics behind acoustic radiation force (ARF) have been extensively studied, and in an absorbing media, under simplified plane wave assumptions, the force has been shown to be proportional to the intensity of the acoustic pulse (see Section 4.2). When applied impulsively, this force creates a μm -order, uniaxial deformation in the direction of wave propagation that can be tracked using various ultrasound-based time delay estimators (TDEs). In practice, the same transducer can be used to generate both the ARF pulse and the tracking pulses. This ensures that the tracking pulses are co-located with the induced motion, thereby increasing the accuracy of displacement estimation by largely eliminating decorrelation from off-axis motion. Decorrelation has been shown to be a key source of variance in ultrasound-based motion tracking as predicted by the Cramér-Rao lower bound [223].

Using the same transducer for both pushing and tracking is elegant in design, but not without side effect. Namely, the displacement estimates are susceptible to another form of decorrelation called shearing artifact. Shearing artifact is the result of non-uniform, on-axis scatterer displacement within the tracking point spread function (PSF) that is caused by the gradient of force induced by the pushing pulse. Because some scatterers are not moving as far as others under the tracking PSF, averaging occurs and the final displacement estimates do not depict the full extent of tissue motion (see Section 4.4.4). An analytic expression for the magnitude of this type of decorrelation was derived by McAleavey et al. [228], which mitigated this effect by modifying the focal configuration, or $F/\#$ (defined as the ratio of aperture width, z , to focal depth, d), of the pushing and tracking pulses appropriately. It was concluded that a broad defocused pushing pulse combined with a narrow focused tracking pulse will yield both the highest correlations and the highest ARFI displacement estimates. Furthermore, it was predicted that in a common imaging scenario (1D linear array) where control over $F/\#$ can only be exerted in the lateral dimension, ARFI-measured displacement could, at most, be only $1/\sqrt{2}$ of the true peak displacement.

A number of studies have since been published that have investigated the impact of shearing decorrelation using finite element method (FEM) modeling [229], [230]. In Palmeri et al. [230], ultrasonic

tracking of an ARFI induced deformation with a 1D linear array was simulated in homogenous media with various elastic constants. It was shown that underestimation due to shearing was not constant over time (i.e. underestimation was worst in the early time points, as low as ~50% of the true induced motion) and the accuracy of estimation improved more rapidly with stiffer material. The reason ARFI displacement estimation improves over time is that shear waves radiate out from the region of excitation (ROE) and the distortive shear wave front is no longer within the tracking PSF. The stiffer the material, the faster the shear waves are able to traverse the resolution cell, and the accuracy of the estimation is improved at a correspondingly higher rate. In Dhanaliwala et al. [229], an expression for signal-to-noise ratio (SNR) in an ARFI image was derived by extending the original McAleavey derivation for shearing decorrelation, and FEM experiments were performed with a 1.5D linear array. The authors show that using a smaller elevational aperture for the pushing pulse results in ARFI images with higher SNR due to the improvements in the shearing decorrelation.

While shearing artifact has been comprehensively studied in the literature with FEM, there is a notable lack of experimental measurements of the phenomenon. The only published data in this regard is from [228] in which the TDE correlation values taken in a single phantom were shown to change as a function of the ratio of pushing to tracking elements. The fact that experimental measurements are sparse is not entirely surprising due to the inherent complexity of developing an apparatus that can truly measure ARF-induced dynamics; displacements are usually very small (μm -order), the motion fast (msec-order recovery times), and ROEs located deep (cm-order) within tissue. A number of groups have approached this problem using optically-based techniques [288]–[291], the most recent of which includes tracking ARF-induced motion with a high-speed camera [292], [293]. Initially, Bouchard et al. [292] used two opposing piston transducers (one to push and one to track) that were confocally aligned on a metal wire embedded near the surface of a phantom, and tracked the motion induced by the pushing piston with a high-speed camera. These methods were further refined by Bouchard et al. [293], where instead of a metallic marker, small sub-wavelength size (10- μm diameter) polystyrene beads were embedded in a translucent phantom to provide a more realistic ARFI imaging scenario. ARFI displacements, again

induced by a single element piston transducer, were motion tracked optically to investigate the dynamics of an ARFI excitation at depth within a phantom but were not simultaneously tracked acoustically as done previously.

In the following appendix, the high-speed camera framework proposed by Bouchard et al. is extended and utilized to experimentally validate ARFI displacement estimates taken with a clinical imaging system. A conventional linear array transducer is confocally aligned with a high-speed camera to simultaneously capture ARFI displacements measured acoustically and optically in translucent phantoms. The acoustically tracked displacements are then validated using the optical gold standard to experimentally measure the displacement underestimation previously demonstrated with FEM simulations. In addition, experiments are performed on phantoms with varying material stiffness using different excitation focal configurations to investigate the impact of these parameters on acoustic displacement tracking.

A.2 Methods

A.2.1 Optical Phantom Construction

Three custom, translucent, gelatin-based, tissue-mimicking phantoms were constructed adapting the formulation of Bouchard et al [293]. The phantom recipes consisted of the following ingredients: type-A gelatin (Acros Organics, Geel, Belgium), agar (Fisher Scientific, Fair Lawn, NJ, USA), black polystyrene microspheres (10- μm , Polysciences Inc., Warrington, PA, USA), *n*-propanol, and de-ionized water (concentrations are given in Table A.1). The agar powder was added to each phantom for acoustic scattering while the polystyrene beads served as markers for optical tracking. The diameter of the agar particles was not published by the manufacturer and was measured experimentally with an Accusizer 780A (Particle Sizing Systems, Santa Barbara, CA, USA) system to be $28.4 \pm 33.5 \mu\text{m}$. The estimated concentration for the polystyrene bead suspension given by the manufacturer was 4.55×10^7 particles/mL.

To evaluate the scattering of the two different particles (agar versus polystyrene), the estimated differential scattering cross-section (σ_d) was computed for each using the following formula [294]:

Table A.1: Phantom Recipes and Material Parameters

Ingredient	Phantom 1	Phantom 2	Phantom 3
Type-A gelatin (g)	12.9	22	34
n-propanol (mL)	10	10	10
Water (mL)	190	190	190
Agar (g)	1	1	1
Polystyrene microspheres (drops)	10	10	10
Parameter	Phantom 1	Phantom 2	Phantom 3
Speed of sound (m/s)	1521.9 ± 0.26	1533.7 ± 0.44	1555.9 ± 0.32
Attenuation (dB/cm @ 3.5 MHz)	0.25 ± 0.05	0.51 ± 0.05	0.44 ± 0.04
Young's Modulus (kPa)	6.6 ± 0.49	19.8 ± 0.93	30.2 ± 1.48
Speckle SNR	1.89 ± 0.11	1.82 ± 0.08	1.84 ± 0.07

*Young's modulus values were measured using shear wave velocimetry. Values for speed of sound, attenuation, and Young's modulus are reported as mean ± one standard deviation.

$$\sigma_d(\theta) = \left(\frac{\left(\frac{\omega}{c_o}\right)^4 a^6}{9} \right) \left(\left(\frac{1}{\rho_v c_v^2} - \frac{1}{\rho_o c_o^2} \right) + \frac{3(\rho_v - \rho_o)}{2\rho_v + \rho_o} \cos \theta \right)^2 \quad (\text{A.1})$$

where ω is the angular acoustic center frequency, a is the radius of the scatterer, c_o and c_v are the speeds of sound in the background and scatterer respectively, ρ_o and ρ_v are the densities of the background and scatterer respectively, and θ is the angle of the scatterer with respect to the center of the transducer (assumed to be 180°). The density (ρ_v) and speed of sound (c_v) values for agar and polystyrene were assumed to be 1.04 g/cm³ and 1500 m/s, and 1.05 g/cm³ and 2350 m/s, respectively. The values for ρ_o and c_o were assumed to be 0.98 g/cm³ and 1540 m/s respectively for the gelatin background. Using these parameters, the differential scattering cross-section was estimated to be higher for the agar (2.98×10^{-9} cm² sr⁻¹) compared to the polystyrene (8.39×10^{-13} cm² sr⁻¹). The backscatter coefficient (η_{BS}) was also calculated with the following equation:

$$\eta_{BS} = n\sigma_d \quad (\text{A.2})$$

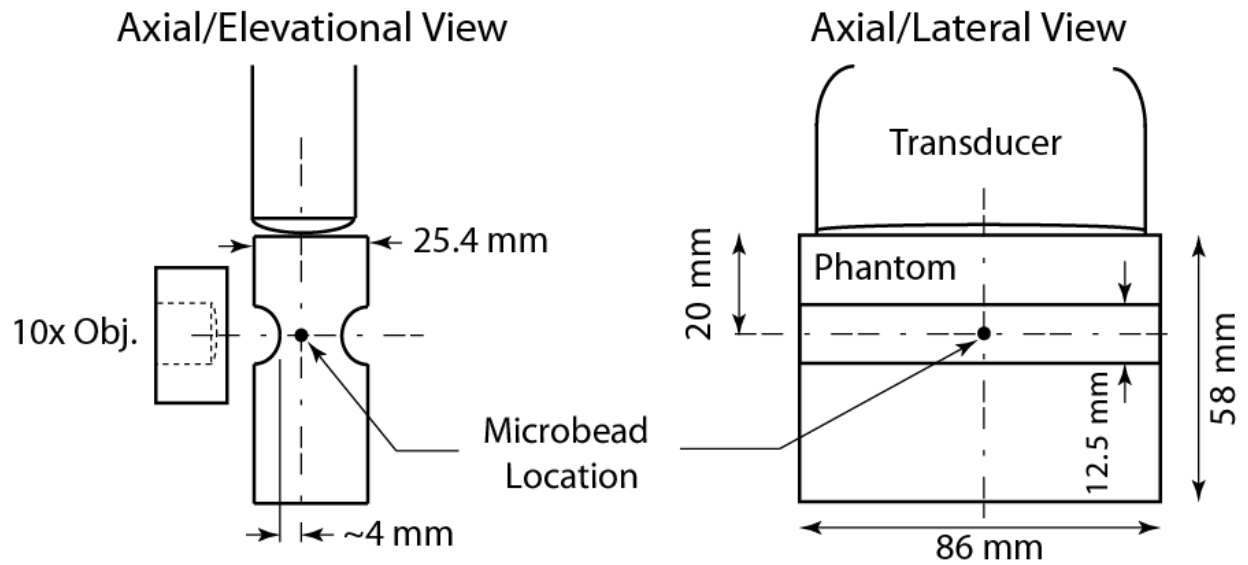


Figure A.1: Schematics of phantom design and confocal alignment of optical and acoustic foci showing the axial/elevational view and the axial/lateral view. Although only one microbead is shown in these schematics, many microbeads ($\sim 2.28 \times 10^7$ beads) were dispersed throughout the whole volume of the phantom.

where n is the number density of the scatterers. The number density of agar was measured by the Accusizer to be 3.50×10^5 particles/mL, while the number density of polystyrene beads was estimated to be 1.14×10^5 particles/mL based on the manufacturer's reported concentration. Therefore, the backscatter coefficient was calculated as $1.04 \times 10^{-3} \text{ cm}^{-1} \text{ sr}^{-1}$ for agar, and $9.54 \times 10^{-8} \text{ cm}^{-1} \text{ sr}^{-1}$ for polystyrene.

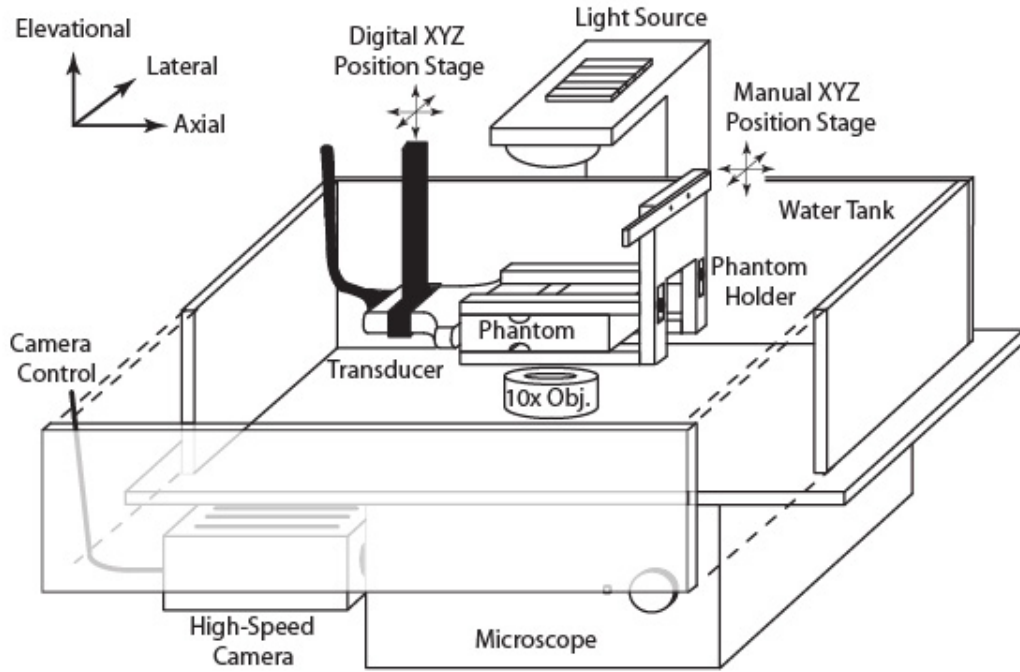
Three phantoms were heated to 40°C and congealed in a rectangular acrylic cast (inner dimensions: $86 \times 86 \times 25.4 \text{ mm}$); their elasticity was varied by adjusting the amount of gelatin powder. A cylindrical acrylic piece with a diameter of 12.5 mm was cut in half and glued to the top and bottom of the acrylic cast to create a groove in each phantom that improved light transmission and ensured uniform sound transmission elevationally. Approximately 28 mm of phantom was cut with a wire in order to situate the groove $\sim 20 \text{ mm}$ (the desired axial focal depth) from one edge of the phantom. Figure A.1 depicts the phantom design, showing close-up schematics of the phantom, transducer, and microscope objective.

A.2.2 Experimental Setup

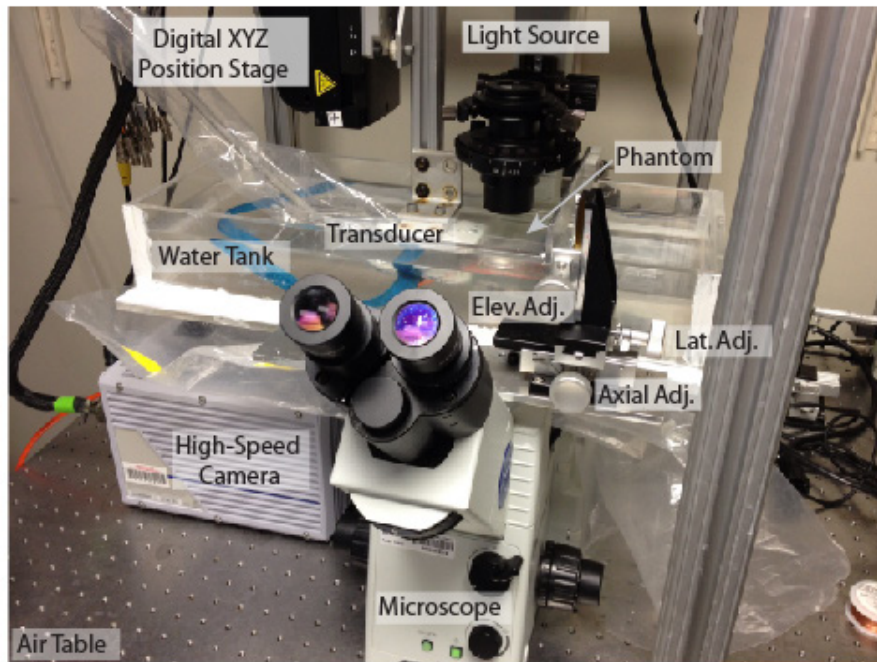
The general experimental setup is shown in Figure A.2(a) and (b). Ultrasonic imaging was performed with a Siemens Acuson Antares™ imaging system (Siemens Medical Solutions USA, Ultrasound Division), equipped with the Axius Direct Ultrasound Research Interface (URI) that allowed customizable beam sequencing and access to the raw radiofrequency (RF) data, and a VF7-3 linear array transducer. The transducer was secured in a holder connected to a digital three-axis motion controller mounted on an optical air table (Newport Corp., Irvine, CA, USA). A custom acrylic water tank was constructed and mounted on an Olympus IX71 microscope (Olympus America Inc., Melville, NY, USA) fitted with a 10× objective and opposing, coaxial, 100-W halogen illumination source (U-LH100L-3, Olympus America Inc., Melville, NY, USA). A Fastcam SA1 high-speed camera (Photron USA Inc., San Diego, CA, USA) was coupled to the microscope for digital frame capture.

Alignment of the optical and acoustic foci was achieved following methods similar to Bouchard et al. [293]. First, an Onda HNC-0400 needle hydrophone (Onda Corp., Sunnyvale, CA, USA) was mounted on a manual micro-positioning stage, and the tip was aligned to the optical focus of the microscope. Next, the needle hydrophone was connected to a Signatec PDA14A analog-to-digital (A/D) convertor (Signatec Inc., Newport Beach, CA, USA), and, using a custom program developed in LabVIEW (National Instruments, Austin, TX, USA), the transducer was swept across the hydrophone in the lateral/elevational dimensions while transmitting a single A-line to generate a 2D map of the acoustic point spread function (PSF). Using the 2D PSF map as a guide, the transducer was then positioned such that the peak amplitude was centered on the hydrophone. This process of mapping the PSF and positioning the transducer was repeated iteratively with smaller ranges and finer step resolutions to achieve precise lateral/elevational alignment of the transducer.

Due to the difference in the speed of sound (SOS) in water and the phantoms, axial alignment was not performed by measuring acoustic intensity with the hydrophone, but rather by positioning the transducer a known distance away from the optical focus (in this case, 20 mm). This positioning was achieved ultrasonically, using the pulse-echo RF data of a single A-line captured by the ultrasound



(a)



(b)

Figure A.2: Schematic and photograph of optical experimental setup.

scanner; the tip of the needle hydrophone (i.e. the optical focus) served as a strong reflector, and the transducer was positioned accordingly after measuring the SOS in water.

With the acoustic and optical foci aligned, the needle hydrophone was removed and replaced with a phantom held in an acrylic holder. At the back of the holder, a piece of strong attenuating rubber was placed to minimize sound reflections. Finally, the phantom was translated laterally and elevationally, using the manual positioning stage, until a polystyrene bead was centered in the microscope's FOV, after which data collection began.

A.2.3 Data Collection

ARFI ensembles consisted of two reference pulses, one acoustic radiation force (ARF) excitation pulse, and 500 tracking lines with an 11 kHz pulse repetition frequency (PRF). ARFI excitations were 300 cycles at 4.21 MHz, and both tracking and reference lines were two cycles at 6.15 MHz. Two different focal configurations (F/#) were used for the excitation pulse (F/1.5 or F/3), while the reference/tracking pulses always used an F/1.5 configuration on transmit and dynamic focusing and aperture growth (F/0.75) on receive. The focus in elevation, set by a cylindrical lens, was 3.8 cm. For each acquisition, a single ensemble was captured, spatially corresponding to the line that was used when mapping the PSF. Prior to each ARFI ensemble, a matched B-mode was also acquired (220 RF lines spaced 0.18 mm apart).

The high-speed camera was configured to acquire frames at a 150 kHz frame rate, across a 128 x 128 pixel FOV. To synchronize the ultrasound system and the camera, the electrocardiogram (ECG) triggering features on the Antares were utilized. An ECG simulator was connected via a standard three wire ECG cable to the Antares ECG input port, and the camera's "trigger in" port was connected to the Antares' auxiliary ECG output port. When the ECG simulator was switched on, the Antares simultaneously triggered ARFI acquisition and output a trigger pulse that synchronized the camera. In this manner, optical and acoustic data was captured for 10 different beads in each phantom, with 3 matched

Table A.2: Empirically determined power settings for the Antares for each phantom and pushing pulse focal configuration (F/#) to yield equivalent displacement.

F/#	Output Power Setting		
	Phantom 1 (%)	Phantom 2 (%)	Phantom 3 (%)
F/1.5	28.3	38.0	47.0
F/3	43.6	70.0	90.0

acquisitions per bead for a total of 180 data sets (3 phantoms \times 2 F/#'s \times 10 beads \times 3 repeated acquisitions).

In order to control for displacement magnitude decorrelation, the output power of the Antares was empirically calibrated such that the maximum displacement magnitude was normalized across all phantom stiffnesses and focal configurations. Starting with the stiffest phantom and F/3 pushing pulse, the scanner was arbitrarily set to a high output power (90%), and the displacement of the bead was tracked optically, yielding a peak displacement of $\sim 18 \mu\text{m}$ (see “Data Processing” for description of optical tracking methods). The output power for all other phantoms and focal configurations was then scaled down appropriately by iteratively searching for a setting that resulted in an optically tracked peak displacement matching $\sim 18 \mu\text{m}$. Table A.2 shows the empirically determined power settings used for every phantom and focal configuration combination.

Elasticity of each phantom was measured using ultrasonically based shear wave velocimetry [186], [189]. The beam sequence used to perform these measurements consisted of 40 ARFI ensembles (300 cycle, F/1.5 pushing pulse) spaced 0.53 mm apart laterally with a stationary region of excitation (ROE) positioned at the center of the lateral FOV. Shear wave group velocity was computed from this data using lateral time to peak (TTP) methods, and subsequently related to Young’s modulus following previously derived equations [189].

A.2.4 Data Processing

Acoustic motion tracking was performed by one-dimensional normalized cross correlation (kernel length = $4.5\lambda \approx 1.1$ mm, where λ is the wavelength of the tracking pulses) applied to the raw RF data. As demonstrated by Palmeri et al. [230], a kernel size of up to 5λ reduces noise from jitter without significantly changing mean displacement estimates, which was desirable for this study due to the relatively small sample size of beads per phantom. Optical motion tracking was performed by two-dimensional normalized cross correlation. Two-stage interpolation was used in both the acoustic and optical data to track sub-sample displacements; the first stage included upsampling the raw RF data (or raw grayscale pixel data) by a factor of 4 with spline interpolation, while the second included fitting a parabola to the maximum of the correlation function in the case of the acoustic data, and upsampling the correlation curve by a factor of 4 in the optical case [206], [293]. Finally, acoustically tracked displacements were scaled by the measured SOSs in the phantoms (see “Speed of Sound and Attenuation Measurements” for SOS measurement methods) to convert time delays to distance measurements.

To validate acoustic displacement measurements and compute displacement underestimation a number of steps were performed to align the acoustic and optical data. First, to reduce experimental noise, the median displacement curve was computed from the three matched acquisitions taken from each bead (this was done for the three acoustic acquisitions as well as the three optical acquisitions). Next, a time correction factor was computed for the optical data to correct for a small delay that occurred between the trigger and the start of the ARFI acquisition (the delay was caused by dummy frames that had to be added to the beam sequence to allow proper ECG synchronization). This was done by identifying the frame in which the camera first saw motion (axial displacement ≥ 1 μm), and setting the time of this frame equal to the time of ARF pulse plus the time-of-flight (TOF) to the bead. The time correction (Δt) was calculated using the following equation:

$$\Delta t = \frac{i_0}{FPS} - (t_{ARF} + t_{TOF}) \quad (\text{A.3})$$

$$t_{TOF} = \frac{z}{c_p} \quad (\text{A.4})$$

where i_0 is the index of the camera frame where motion is first observed, FPS is the frame rate of the camera acquisition, t_{ARF} is the time the ARF pulse is fired and t_{TOF} is the time of flight of the ARF pulse to the microbead (defined as the distance to the bead from the transducer, z , divided by the measured SOS in the phantom, c_p). With the optical and acoustic data aligned in time, linear interpolation was used on the optical displacement curves to get the true displacement at each acoustic time point. This interpolation was necessary because the PRF of the ultrasonic scanner was not an integer multiple of the camera framerate, and therefore the clocks were not synchronized perfectly sample for sample. Finally, with the optical and acoustic data aligned, two-sample Wilcoxon rank sum tests ($\alpha = 0.01$) were performed at each time step to test for statistical difference between the optical and acoustic displacement measurement. A flow chart of the data collection and data processing steps is given in Figure A.3.

To ensure the phantoms exhibited fully developed speckle, speckle signal-to-noise ratio (SNR) was computed over a 4×4 mm region of interest (ROI) centered at the location of each bead on the envelope detected B-mode data (calculated as the absolute value of the Hilbert transformed RF data). The measured speckle SNR values are reported in Table A.1.

A.2.5 Speed of Sound and Attenuation Measurements

The SOS for each phantom was measured with a 0.5" (1.27 cm) diameter element, 2" (5.08 cm) spherically focused Panametrics-NDT 3.5 MHz piston transducer (Olympus, Waltham, MA, USA) in a custom-built water tank. First, an aluminum plate reflector was positioned approximately 5 cm from the transducer face. Using a Panametrics-NDT Pulsar/Receiver (Olympus, Waltham, MA, USA) in pulse-echo mode (negative impulse), two different A-lines were obtained at precisely 10 mm apart using a Newport motion-stage with micron resolution (Newport Corp., Irvine, CA, USA). The SOS in water, c_w , was calculated using the following equation:

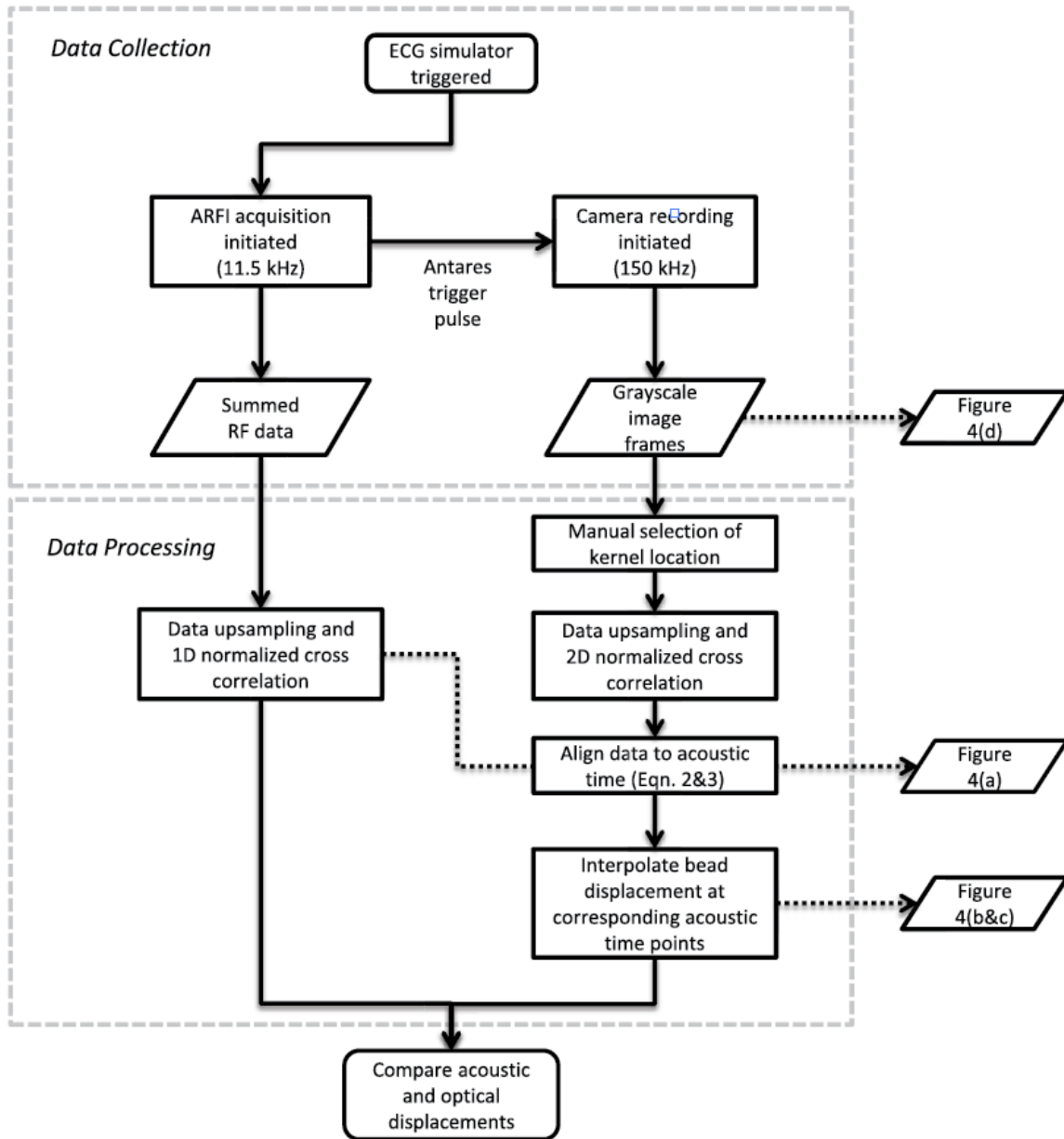


Figure A.3: Flow chart describing data collection and data processing steps of optical experiments. ECG = electrocardiogram; ARFI = acoustic radiation force impulse; RF = radiofrequency; 1D = one dimension; 2D = two dimension.

$$c_w = \frac{2(\Delta d)}{|t_1 - t_2|} \quad (\text{A.5})$$

where Δd is the distance the transducer was moved between A-lines, t_1 is the time of peak negative pressure of the first A-line and t_2 is the time of peak negative pressure of the second A-line. The measured SOS (1496.8 m/s) was subsequently verified using a Fluke 51 II Thermometer (Fluke Corp., Everett, Washington, USA) to determine the water bath temperature (24.6°C) and compared to published data [295].

Using the empirically determined SOS in water, the piston transducer was positioned precisely 5.08 cm from the plate reflector by aligning the peak negative pressure to the time (67.9 μsec) associated with a distance of 5.08 cm. Ten different A-lines were acquired with each phantom positioned between the transducer and the plate reflector. Since the phantom width was constructed to be 2.54 cm, each A-line would travel through 5.08 cm of phantom and 5.08 cm of water in one round-trip path. Thus, the SOS measurements in each phantom, c_p , were calculated using the following equations:

$$c_p = \frac{2(d_p)}{(t_{p+w} - t_w)} \quad (\text{A.6})$$

$$t_w = \frac{2(d_w)}{c_w} \quad (\text{A.7})$$

Where d_p is distance the sound traveled in the phantom, t_{p+w} is the time associated with the peak negative pressure of each acquired A-line, t_w is the calculated round-trip time that it takes the sound wave to travel through water, d_w is distance the sound traveled in water.

Attenuation, α , was measured directly after measuring SOS using the same pulse-echo experimental set up and was calculated using the following formula:

$$\alpha = \frac{20 \log_{10} \left(\frac{V_w}{V_{p+w}} \right)}{2(d_p)} \quad (\text{A.8})$$

where V_w and V_{p+w} are the peak negative echo voltage amplitudes from water only and phantom and water, respectively.

A.3 Results

Figure A.4 shows an example of the raw data taken from the 30.2 kPa phantom with an F/1.5 pushing pulse focal configuration. Panel (a) shows the optically and acoustically tracked data, in their native sample rates, plotted on top of each other. Two artifacts can be seen in this plot: first, a broad, low displacement peak appears in both the optical and acoustic traces at ~ 1.5 msec, and second, a sharp, negative displacement peak (suggesting significant motion *towards* the transducer) appears in the optical trace at 0.19 msec. The broad, low-displacement artifact was observed previously by Bouchard et al. [293] and is the result of a shear wave reflection off of the proximal (*w.r.t.* the camera) edge of the phantom. The sharp negative displacement, on the other hand, is due to the high frequency compressional motion that the microbead experiences as the ARF pulse passes through it. The reason this motion is misregistered as a bulk negative motion is that the high frequency (4.21 MHz) compressional displacement is severely undersampled by the camera (150 kHz) and aliasing occurs. This phenomenon is shown more clearly in panels (b), (c), and (d), which show zoomed in versions of displacement, correlation coefficient (ρ), and filmstrip of the raw camera data, respectively. Looking at panel (d) first, the bead appears blurry for 11 frames (73.3 μ sec) at the beginning of displacement, which corresponds to the duration of a 300 cycle ARF pulse oscillating at 4.21 MHz (71.3 μ sec). During this time, the edges of the bead appear smeared over the axial extent of compressional vibration, and the correlation coefficient (panel (c)) drops significantly ($\rho \approx 0.8$). Callé et al. [290] reported similar findings using an optical interferometric technique, which was not limited by frame rate and could fully sample the compressional motion of an ARF pulse as it passed through a Mylar sheet embedded in a phantom. In the context of this study, the negative tracking artifact was disregarded because no acoustic tracking data was taken at time points coinciding with the compressional motion.

Figure A.5 shows how the displacement estimate varies as a function of time using both optical and acoustic tracking methods, which are matched sample for sample for all experiments. The top row corresponds to displacements tracked in the 6.6 kPa phantom, while the center and bottom rows

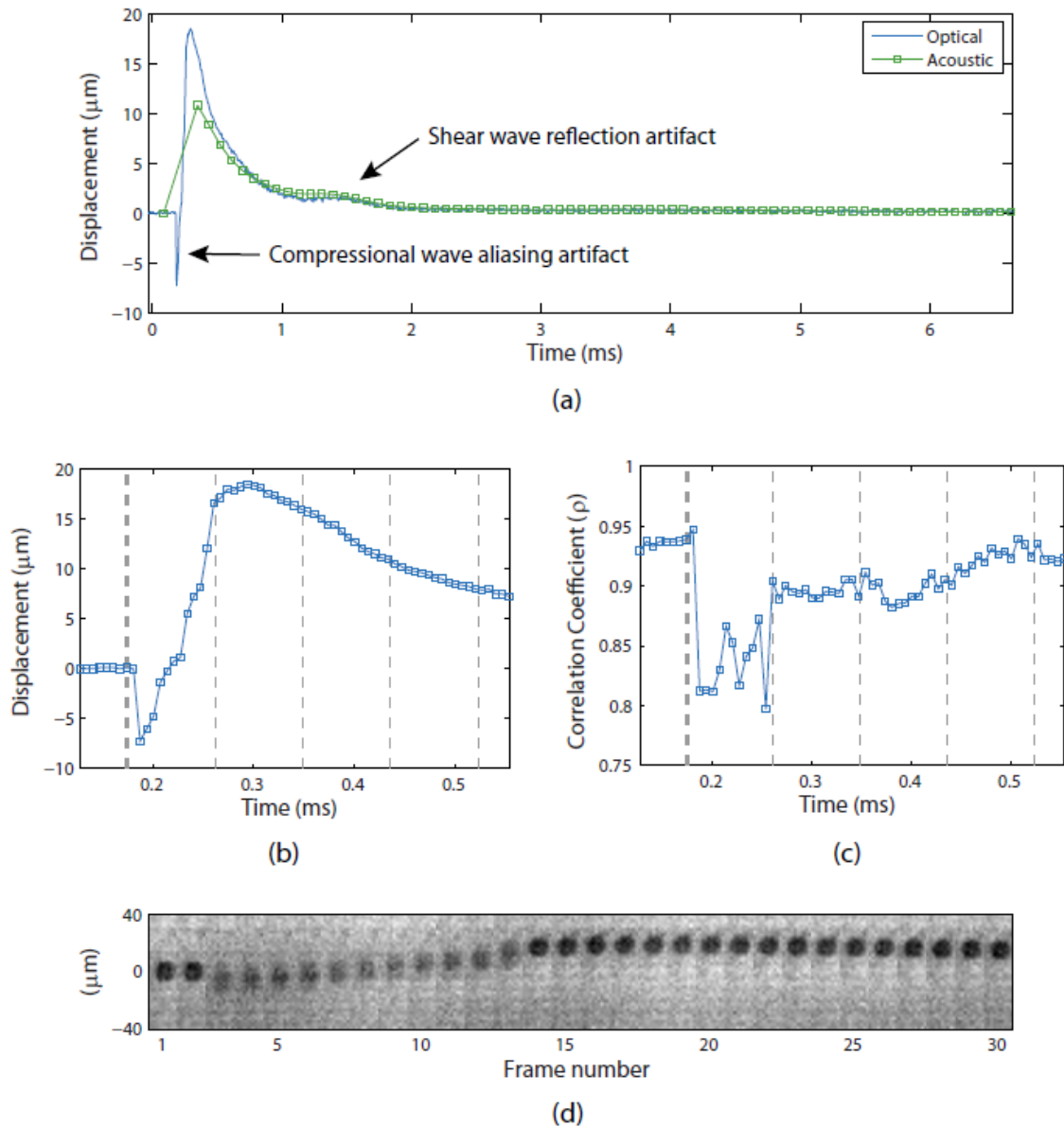


Figure A.4: Example of displacement profiles tracked optically and acoustically. (a) Displacement profiles in the 30.2 kPa phantom with an F/1.5 ARF pulse focal configuration. Note two anomalous displacements: a broad, low displacement occurring at ~ 1.5 msec corresponding to a shear wave reflection off the proximal phantom boundary, and a sharp, negative displacement occurring before the first acoustically tracked point at ~ 0.19 msec corresponding to aliased compressional motion from the high frequency 300-cycle ARF pulse. (b) Zoomed in version of the optical displacement vs. time trace. (c) Zoomed in time scale showing the maximum correlation coefficients calculated for each optical time point. Vertical lines in both (b) and (c) depict timing of acoustic pulses: thicker black line indicates the ARF pulse, while thinner black lines indicate tracking pulses. (d) Filmstrip showing the camera frames over time. Note that the bead appears blurry while the ARF pulse oscillates the bead at the carrier frequency (4.21 MHz) in frames 3-13. During this time, the correlation coefficient of optical tracking drops significantly (c), and a negative displacement artifact appears in the optical trace (b).

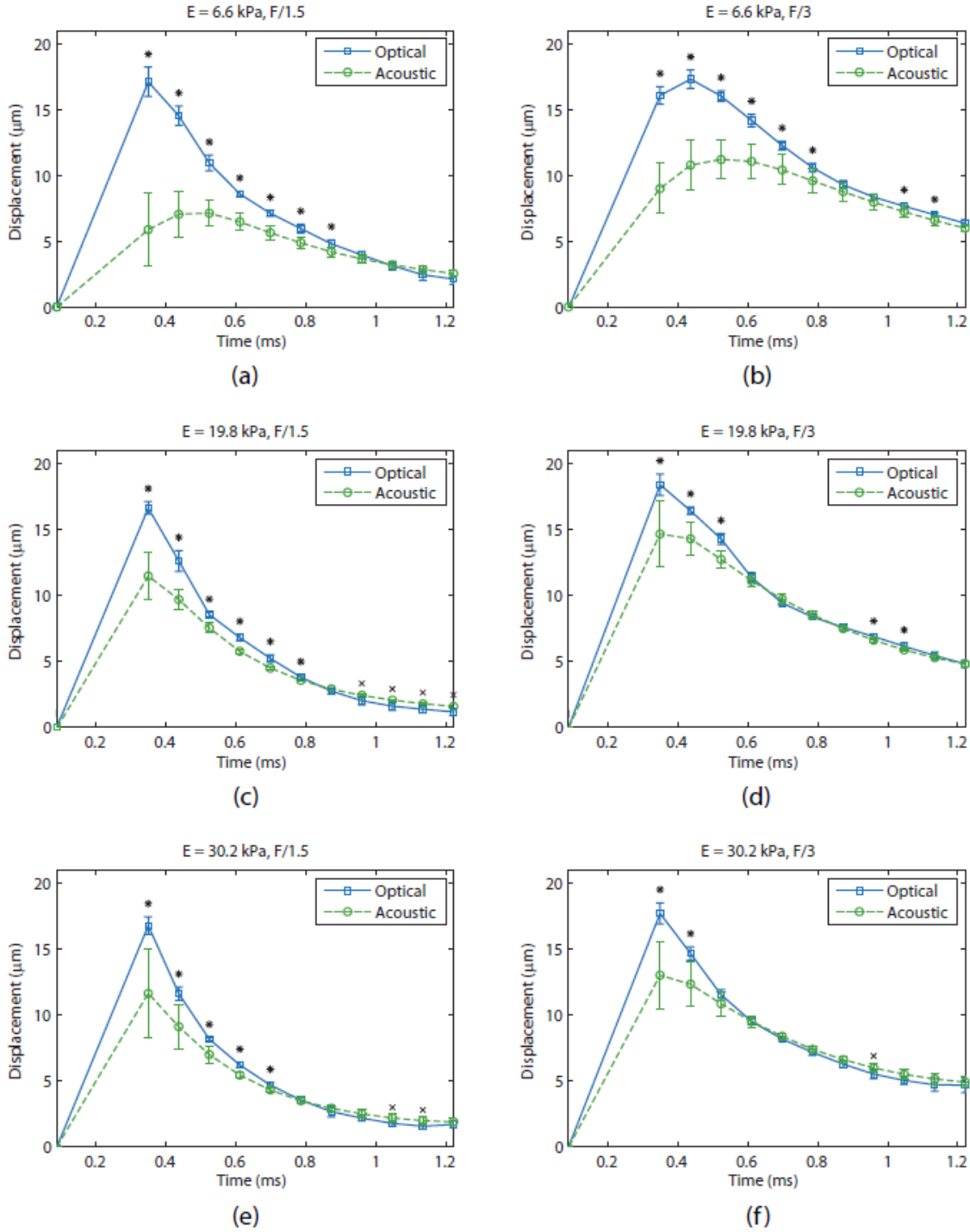


Figure A.5: Displacement through time measured both acoustically and optically for the 6.6, 19.8, and 30.2 kPa phantoms with F/1.5 and F/3 excitation pulse focal configurations. The tracking transmit pulse focal configuration was F/1.5 for all cases. Error bars indicate one standard deviation. Statistical significance ($p < 0.01$) is indicated by a black asterisk or cross for higher optical or acoustic values, respectively. Note that as the phantom gets stiffer or F/# increases, the time over which the acoustic and optical measurements are statistically different decreases.

Table A.3: Time points at which mean acoustic and optical displacements become non-significantly different in Figure A.5.

Stiffness (kPa)	Excitation F/#	
	F/1.5 (ms)	F/3 (ms)
6.6	0.96	0.87
19.8	0.87	0.61
30.2	0.78	0.52

correspond to the 19.8 kPa and 30.2 kPa phantoms, respectively. The left column shows the results using an F/1.5 focal configuration for the ARF pulse, with the right showing F/3. Each data point represents the mean displacement measured across 10 beads with error bars showing one standard deviation. Statistical differences ($p < 0.01$) between mean optical and acoustic displacements are indicated with an asterisk when the optical mean is higher and a cross when the acoustic mean is higher. Note that as the stiffness of the phantom or F/# increases, the mean displacements measured acoustically match the optical displacements at earlier time points (listed in Table A.3).

Figure A.6 shows the mean acoustic displacement as a percentage of the mean optical gold standard over time for the 6.6 kPa (a), 19.8 kPa (b), and 30.2 kPa (c) phantoms. Note that the underestimation is worst in the first time step, and the accuracy improves with time until ultimately reaching 100% of the optical measurement.

Finally, Figure A.7 shows the mean optical displacement traces for each phantom, with different F/# excitations plotted on top of each other. This data is re-plotted in order to illustrate the effect of F/# on the recovery profile of the phantom; namely, as the F/# is increased, the recovery time (RT) and time-to-peak (TTP) is observed to elongate. Table A.4 lists the measured values of peak displacement, recovery time, and TTP across F/# and phantom stiffness for comparison.

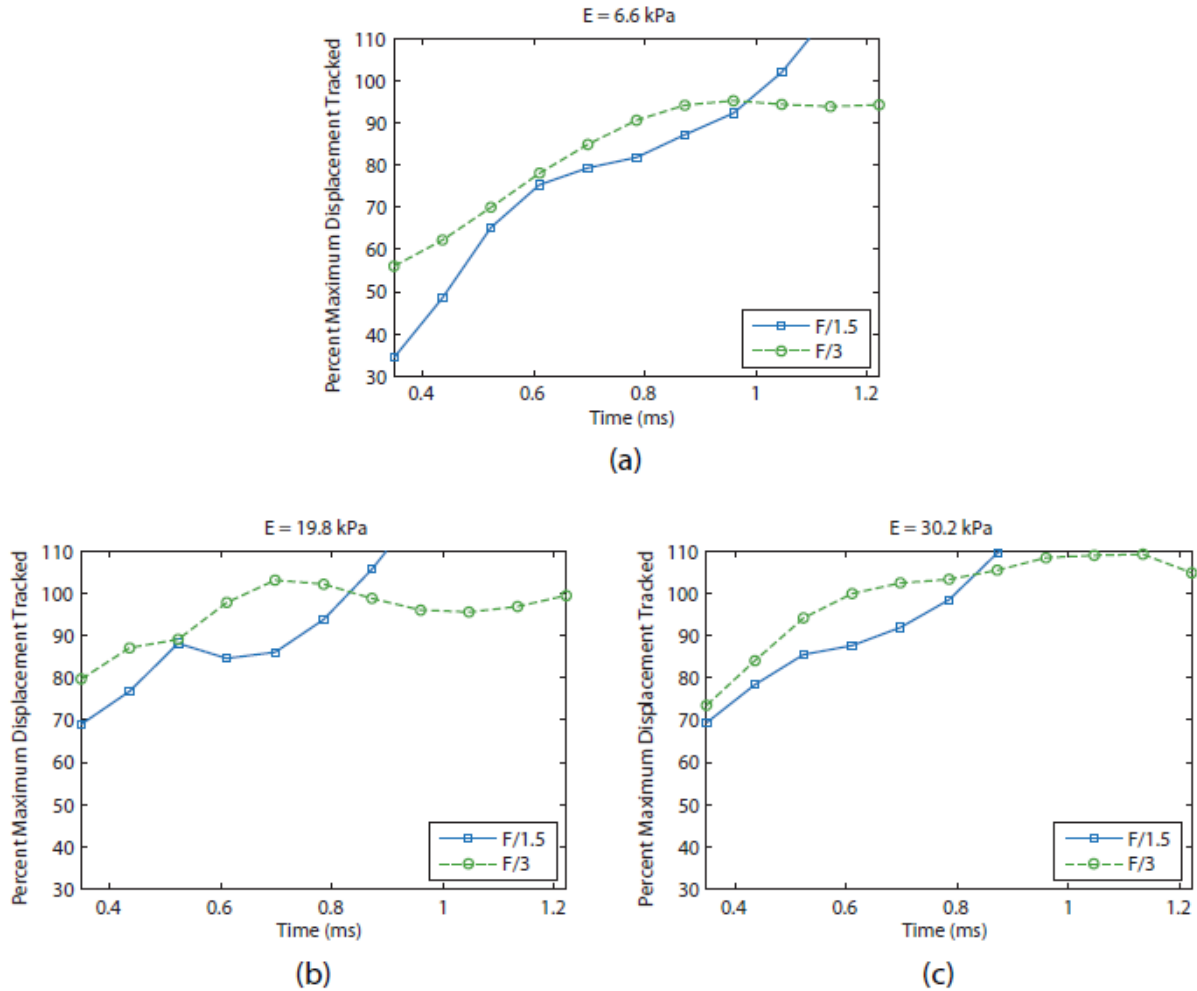


Figure A.6: Percentage of optical displacement tracked acoustically in phantoms of 6.6 kPa, 19.8 kPa, and 30.2 kPa with two different excitation pulse focal configurations (F/1.5 and F/3). The tracking transmit pulse focal configuration was F/1.5 for all cases. Note that the F/1.5 excitation results in a larger displacement underestimation at the early time points. Percentage values were calculated from the mean displacement values at each time point in Figure A.5.

A.4 Discussion

Previous analytical and FEM studies have shown that ultrasonic motion tracking of ARF-induced displacements is subject to underestimation due to scatterer shearing in the lateral and elevational dimension [228], [230]. This underestimation is dependent on the underlying material stiffness and can be mitigated by beamforming the excitation PSF to encompass the tracking PSF

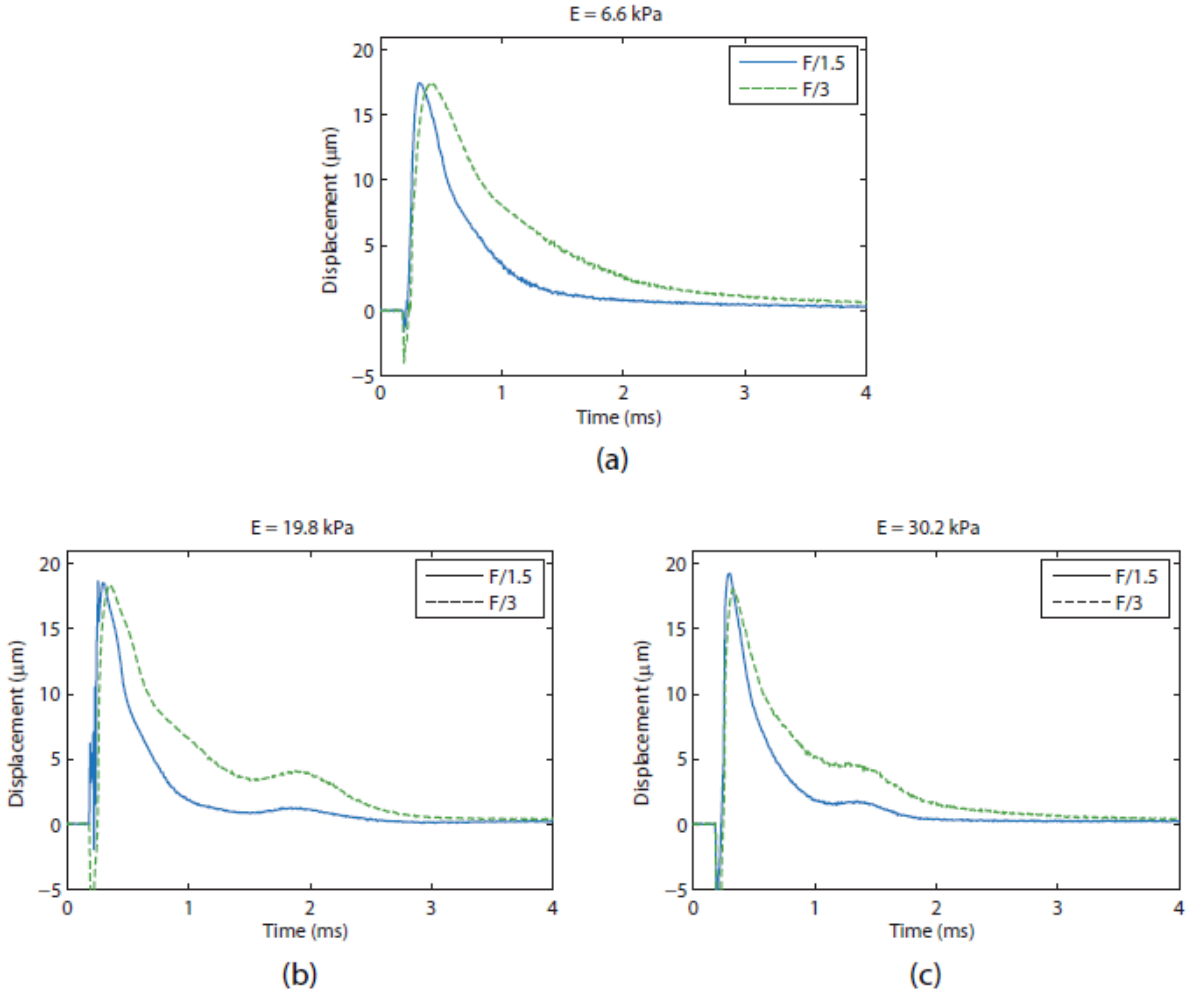


Figure A.7: Mean optically traced displacements with F/1.5 and F/3 ARF pulse focal configurations plotted on top of each other to show the effect of pushing F/# on phantom recovery time. In each phantom, time to 67% recovery of maximum displacement and time to peak is elongated when a less focused pushing pulse is utilized.

(i.e. defocus the pushing beam laterally/elevationally and/or lower its center frequency). Material stiffness impacts underestimation because it affects the speed at which shear waves propagate away from the ROE. The faster the shear wave, the more quickly the displacement field broadens over time in the lateral and elevational dimensions, making the scatterer motion under the tracking PSF more uniform and reducing the underestimation error. In the same respect, defocusing the excitation beam also reduces displacement

Table A.4: Mean peak displacement, time to 67% recovery, and time to peak measured optically across 10 beads (± 1 standard deviation).

Parameter	F/#	Phantom		
		6.6 kPa	19.8 kPa	30.2 kPa
Peak (μm)	F1.5	17.7 ± 1.6	18.5 ± 1.3	19.8 ± 1.7
	F3	17.6 ± 0.8	18.5 ± 0.8	18.2 ± 0.9
Recovery (ms)	F1.5	0.46 ± 0.04	0.35 ± 0.03	0.3 ± 0.03
	F3	0.87 ± 0.05	0.69 ± 0.05	0.56 ± 0.04
TTP (ms)	F1.5	0.14 ± 0.012	0.11 ± 0.014	0.10 ± 0.007
	F3	0.22 ± 0.013	0.16 ± 0.005	0.14 ± 0.005

underestimation by increasing the cross-sectional area over which force is initially deposited and broadening the extent of the displacement field relative to the tracking PSF.

Figure A.5 and Figure A.6 confirm the FEM predicted phenomena, showing improvement in the accuracy of acoustically derived displacements as either the stiffness of the phantom or the excitation F/# is increased. Figure A.6 shows that the first acoustic time point, which coincides with the highest optical displacement in almost all cases, has the greatest underestimation. This underestimation then resolves with time at a rate governed by the stiffness of the phantom, which is depicted numerically in Table A.3. As expected, the stiffest phantom matches the optical displacement at the earliest time point. Figure A.6 and Table A.3 also show that doubling the F/# of the excitation pulse in the lateral dimension results in improved displacement estimation accuracy and shorter times to non-significant difference from optically measured displacements. The acoustic estimates with F/3 excitations were on average 7.7, 10.4, and 7.7% closer to the optical measurements for the 6.6, 19.8, and 30.2 kPa phantoms, respectively (over the time period that it takes F/1.5 to reach non-significant difference). Finally, the variance (i.e. jitter) of the acoustic displacement estimates was observed to be worst in the earliest time points, consistent with previously simulated data.

Figure A.6 also shows that the F/1.5 excitation resulted in a small amount (~ 10 to 20%) of acoustic overestimation of the measured displacement in all three phantoms (at ~ 0.9 msec and later),

which was generally not observed with the $F/3$ excitation. This overestimation, like the underestimation at the earlier time points, could occur if the scatterers at the edge of the PSF are displacing more than the scatterers in the center of the PSF. Due to the large -6 dB elevational beamwidth (~ 2.4 mm) at an axial focus of 20 mm, this could conceivably occur if either the shear wave front has not entirely left the PSF at the time the center scatterers begin to recover, or if the shear wave reflection artifact has returned into the PSF. Figure A.7 suggests that the shear wave reflection does not coincide with the time of overestimation in the 6.6 and 19.8 kPa phantoms, but could coincide in the 30.2 kPa phantom. A more in-depth investigation that is not confounded by shear wave reflections is needed to conclusively determine the mechanisms underlying displacement overestimation.

Figure A.7 and Table A.4 show an interesting phenomenon associated with increasing the $F/\#$ of the excitation pulse; the RT and TTP of the phantoms are both elongated. In all three stiffnesses, the optically measured RT was increased by a factor of 2, while the TTP was increased by a factor of 1.5 when the excitation $F/\#$ was increased from $F/1.5$ to $F/3$. Elongated TTP by $F/\#$ was previously reported by Palmeri et al. [231] in FEM studies and was attributed to the broader cross-sectional area of the pushing beam, but the effect on RT was either not observed or not reported. It would be expected that the same inertial (mass) effects described by Palmeri et al. [231] that explain the increase in TTP would increase RT as well, but it was outside of the scope of this study to investigate these dynamics in further detail.

There were a number of potential sources of error in this study that could have contributed to erroneous measurement of displacement underestimation: focal alignment mismatch between optical and acoustic data sets, jitter in optical displacement estimation, and sample-for-sample timing uncertainty. As described previously, focal alignment was carried out in water, which had a slightly different SOS than the gelatin phantoms. Because of this, the axial focus of the transducer was not precisely positioned on the microbead when the experiments were carried out. For the purpose of this study, though, it was not critical that the microbead be precisely at the acoustic focus axially, only that the position of the bead relative to the transducer be known so that it could be located within the range of the acoustic A-line.

Therefore, to discern the axial position of the microbead two empirical SOS measurements had to be made, both subject to experimental error; the first was a measurement in water to precisely position the transducer 20 mm from the needle hydrophone, and the second was a measurement in each phantom in order to calibrate the fast-time dimension of the acoustic RF data. If either of these measurements was incorrect, the acoustic data would be slightly misaligned axially and the measured underestimation erroneous. The standard deviation on both SOS measurements was generally small though (< 1 m/s) and would result in a one or two sample axial shift (~ 20 to 40 μm) that was not expected to have a significant impact on the results of this study.

Jitter in the optical measurements was another possible source of error. Like acoustic displacement estimation, optical displacement estimation was subject to jitter errors arising from limited camera pixel resolution and electronic noise from camera components. To quantify the impact of optical jitter error, the standard deviation was calculated on the last 100 samples of every optical data set and averaged together resulting in an empirical jitter error of 0.11 μm on optical measurements, which is low compared to the displacements induced in this study. Finally, timing uncertainty could have impacted the sample-per-sample alignment of the optical and acoustic data. One of the consequences of this experimental design is that the camera and the ultrasound system run on different clocks, and the Antares scanner did not output a trigger with every ultrasonic pulse. Therefore, optical data had to be interpolated when the time step of the acoustic pulse did not align precisely with the optical sample. Any error arising from this interpolation step, though, was deemed to be insignificant due to the high frame rate of the camera acquisition (150 kHz).

Understanding displacement underestimation is important in the context of imaging mechanically heterogeneous tissues because of its potential to impact contrast. The most common 2D parametric images created from an ARFI acquisition show peak displacement values measured at each pixel. In this type of image, areas of low peak displacement represent stiffer tissues while areas of high displacement represent softer tissues. The underestimation phenomenon, though, works in the opposite direction; the stiffer structures have higher shear wave speeds and are less underestimated (i.e. have higher

displacement) while the softer structures have slower shear wave speeds and are more underestimated (i.e. have lower displacement). Therefore, correcting displacement underestimation, either through excitation pulse geometry and transducer design [229] or filtering and motion tracking techniques [232], [233], could have major impact on the field of ARFI imaging. This work presents an experimental framework for testing and validating these novel approaches to reducing displacement underestimation.

A.5 Conclusion

Acoustic displacement underestimation in ARFI, previously predicted by theory and FEM modeling, was validated experimentally. A high $F/\#$ excitation pulse was seen to reduce the amount of displacement underestimation due to lateral shearing. Likewise, a dependence on material stiffness was observed, where stiffer phantoms showed less underestimation and faster times to matching the true displacements. These experiments set up a framework for future displacement tracking validation studies using relevant diagnostic ultrasound hardware.

APPENDIX B

Optimal ARFI Frequency Derivation

In this appendix, a simple equation is derived to determine the optimal ARFI pushing frequency for a given focal depth and tissue attenuation coefficient. The derivation is based on the simple formulation that relates acoustic intensity to acoustic radiation force. The results demonstrate an inverse exponential relationship between the desired depth of penetration and optimal pushing frequency.

B.1 Theory

Under simplified plane wave assumptions, in an absorbing media the force has been shown to be proportional to the intensity of the acoustic pulse as follows:

$$F = \frac{2\alpha I}{c} \quad (\text{B.1})$$

where α is the absorption coefficient of the medium, I is the temporal-average beam intensity, and c is the speed of the sound through the medium [178], [296]. From equation (B.1), two terms can be described as functions of both frequency and propagation depth; the absorption coefficient (α), and the temporal-average intensity (I). The following will develop an expression for frequency as a function of propagation distance, assuming an exponential derating scheme for in-situ pulse intensity.

Start with the equation (B.1) and add in extra variables for frequency (f) and position (x). Units for the equations are as follows: α [$\frac{\text{neper}}{\text{cm MHz}}$], f [MHz], c [$\frac{\text{cm}}{\text{s}}$], x [cm], and I [$\frac{\text{g cm}^2}{\text{s}^3}$].

$$F(x, f) = \frac{2\alpha f}{c} I(x, f) \quad (\text{B.2})$$

Define derated intensity equation:

$$I(x, f) = I_0 e^{-2\alpha f x} \quad (\text{B.3})$$

Substitute (B.3) into (B.2):

$$F(x, f) = \frac{2\alpha f}{c} I_0 e^{-2\alpha f x} \quad (\text{B.4})$$

Take partial derivative of (B.4) with respect to frequency, and set to zero to find maxima (i.e. the maximum ARF magnitude):

$$\frac{\partial}{\partial f} F(x, f) = \frac{-2\alpha I_0}{c} e^{-2\alpha f x} (2\alpha f x - 1) = 0 \quad (\text{B.5})$$

Simplify, and solve for f in terms of x :

$$\frac{-4\alpha^2 x f I_0}{c} e^{-2\alpha f x} + \frac{2\alpha I_0}{c} e^{-2\alpha f x} = 0 \quad (\text{B.6})$$

$$\frac{-4\alpha^2 x f I_0}{c} e^{-2\alpha f x} = \frac{-2\alpha I_0}{c} e^{-2\alpha f x} \quad (\text{B.7})$$

$$4\alpha f x = 2 \quad (\text{B.8})$$

Finally, the optimal ARFI frequency (MHz) can be written as a function of attenuation coefficient ($\frac{\text{neper}}{\text{cm MHz}}$) and depth (cm).

$$f = \frac{1}{2\alpha x} \quad (\text{B.9})$$

B.2 Methods

To verify equation (B.9), radiation force magnitude was computed numerically using equation (B.1) for a range of attenuation coefficients (0.3, 0.5, and 1.0 dB/cm/MHz), depths (0.1 to 15 cm), and frequencies (0.5 to 100 MHz). Using this data, the frequency that maximizes ARF magnitude could be determined by taking the maximum at each simulated focal zone. These results are then compared against the predicted maxima given by equation (B.9).

B.3 Results/Discussion

Figure B.1 shows the results of the numerical analysis of equation (B.1). ARF magnitude is plotted as a function of focal depth and frequency, derived numerically by simply inputting values into

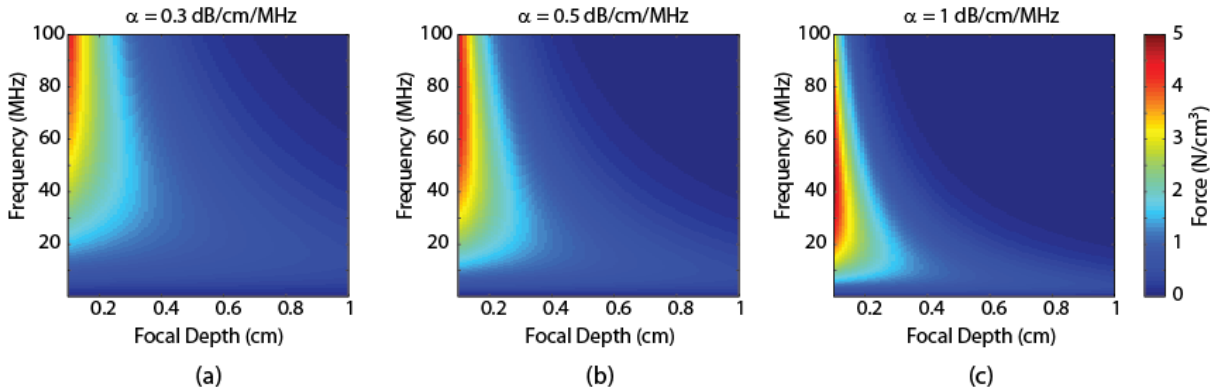


Figure B.1: ARF magnitude as a function of frequency and focal depth for three attenuation coefficients.

(B.1). The results show that ARF should be maximized by very high frequencies when the desired focal depth is very shallow, and decreases as the focal depth is moved deeper in the tissue.

Figure B.2 shows the results predicted by equation (B.9), with the frequency of maximum ARF magnitude plotted as a function of focal depth. Figure B.2a shows the results for near-field targets (i.e. targets less than 1 cm from the transducer face), while Figure B.2b shows the results for farther targets (1 – 5 cm). As expected, the frequency that maximizes ARF decreases exponentially as the desired focal depth is moved farther from the transducer. Finally, Table B.1 shows a range of ideal ARF pushing frequencies for a number of imaging targets based on attenuation and depth values reported in literature assuming that the attenuation coefficient to reach these depths is a constant 0.5 dB/cm/MHz.

While these simulations are useful to quickly assess the optimal frequency needed for an ARF excitation for a given focal depth, there are a number of limitations. First, the model assumes that attenuation increases linearly with frequency, which is an incorrect assumption in some tissue types. Second, the model does not take into account the fractional bandwidth of a given transducer, which will dictate the amount of intensity that a given transducer can output at a given frequency. In practice, a given transducer will output the highest intensity at its resonance frequency, while off-resonance will have slightly less intensity. Finally, attenuation varies greatly with tissue types. The current model does not support a piece-wise sound attenuation path as would be expected when imaging some of the deeper

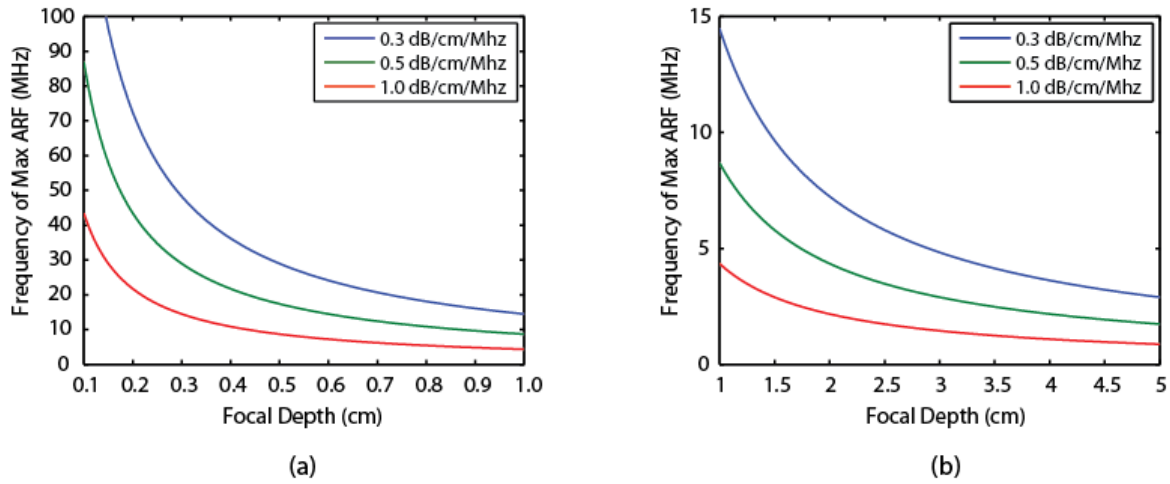


Figure B.2: Frequency of maximum ARF as a function of focal depth, determined by equation (B.9). (a) Shallow focal depths. (b) Mid-range focal depths. Blue, green, and red lines depict different absorption coefficients (0.3, 0.5, and 1.0 dB/cm/MHz, respectively).

organs. For example, to reach the deepest parts of the liver, the sound must first travel through layers of skin, muscle, and fat, and then propagate a significant distance through liver itself, which has distinct attenuation characteristics. To improve the model in the future it would be useful to incorporate various attenuation paths as well as transducer fractional bandwidth in order to select the ideal pushing frequency for a given imaging scenario.

Table B.1: Predicted optimal pushing frequency for various targets.

Organ	Depth (cm)	Optimal Pushing Frequency (MHz)
Carotid Artery	2 – 3	4.3 – 2.9
Kidney	4 – 10	2.2 – 0.87
Liver	5 – 13	1.7 – 0.67
Muscle	1 – 4	8.7 – 2.2
Thyroid	<2 cm	>4.3

REFERENCES

- [1] D. Mozaffarian, E. J. Benjamin, A. S. Go, D. K. Arnett, M. J. Blaha, M. Cushman, S. de Ferranti, J.-P. Després, H. J. Fullerton, V. J. Howard, M. D. Huffman, S. E. Judd, B. M. Kissela, D. T. Lackland, J. H. Lichtman, L. D. Lisabeth, S. Liu, R. H. Mackey, D. B. Matchar, D. K. McGuire, E. R. Mohler, C. S. Moy, P. Muntner, M. E. Mussolino, K. Nasir, R. W. Neumar, G. Nichol, L. Palaniappan, D. K. Pandey, M. J. Reeves, C. J. Rodriguez, P. D. Sorlie, J. Stein, A. Towfighi, T. N. Turan, S. S. Virani, J. Z. Willey, D. Woo, R. W. Yeh, M. B. Turner, and American Heart Association Statistics Committee and Stroke Statistics Subcommittee, “Heart disease and stroke statistics--2015 update: a report from the American Heart Association.,” *Circulation*, vol. 131, no. 4, pp. e29–322, Jan. 2015.
- [2] A. V Finn, M. Nakano, J. Narula, F. D. Kolodgie, and R. Virmani, “Concept of vulnerable/unstable plaque.,” *Arterioscler. Thromb. Vasc. Biol.*, vol. 30, no. 7, pp. 1282–92, Jul. 2010.
- [3] G. L. ten Kate, E. J. Sijbrands, D. Staub, B. Coll, F. J. ten Cate, S. B. Feinstein, and A. F. L. Schinkel, “Noninvasive imaging of the vulnerable atherosclerotic plaque.,” *Curr. Probl. Cardiol.*, vol. 35, no. 11, pp. 556–91, Nov. 2010.
- [4] I. Tabas, G. García-Cardena, and G. K. Owens, “Recent insights into the cellular biology of atherosclerosis.,” *J. Cell Biol.*, vol. 209, no. 1, pp. 13–22, Apr. 2015.
- [5] R. Ross, “Atherosclerosis--an inflammatory disease.,” *N. Engl. J. Med.*, vol. 340, no. 2, pp. 115–26, Jan. 1999.
- [6] P. Libby, P. M. Ridker, and G. K. Hansson, “Progress and challenges in translating the biology of atherosclerosis.,” *Nature*, vol. 473, no. 7347, pp. 317–25, May 2011.
- [7] F. Otsuka, K. Sakakura, K. Yahagi, M. Joner, and R. Virmani, “Has our understanding of calcification in human coronary atherosclerosis progressed?,” *Arterioscler. Thromb. Vasc. Biol.*, vol. 34, no. 4, pp. 724–36, Apr. 2014.
- [8] T. M. Doherty, K. Asotra, L. A. Fitzpatrick, J.-H. Qiao, D. J. Wilkin, R. C. Detrano, C. R. Dunstan, P. K. Shah, and T. B. Rajavashisth, “Calcification in atherosclerosis: bone biology and chronic inflammation at the arterial crossroads.,” *Proc. Natl. Acad. Sci. U. S. A.*, vol. 100, no. 20, pp. 11201–6, Sep. 2003.
- [9] P. K. Shah, “Mechanisms of plaque vulnerability and rupture.,” *J. Am. Coll. Cardiol.*, vol. 41, no. 4 Suppl S, p. 15S–22S, Feb. 2003.
- [10] A. Farb, A. P. Burke, A. L. Tang, T. Y. Liang, P. Mannan, J. Smialek, and R. Virmani, “Coronary plaque erosion without rupture into a lipid core. A frequent cause of coronary thrombosis in sudden coronary death.,” *Circulation*, vol. 93, no. 7, pp. 1354–1363, Apr. 1996.
- [11] S. P. Jackson, “Arterial thrombosis--insidious, unpredictable and deadly.,” *Nat. Med.*, vol. 17, no. 11, pp. 1423–36, Jan. 2011.
- [12] A. P. Burke, F. D. Kolodgie, A. Farb, D. K. Weber, G. T. Malcom, J. Smialek, and R. Virmani, “Healed plaque ruptures and sudden coronary death: evidence that subclinical rupture has a role in plaque progression.,” *Circulation*, vol. 103, no. 7, pp. 934–40, Mar. 2001.

- [13] A. Arbab-Zadeh, M. Nakano, R. Virmani, and V. Fuster, "Acute coronary events.," *Circulation*, vol. 125, no. 9, pp. 1147–56, Mar. 2012.
- [14] H. C. Stary, D. H. Blankenhorn, A. B. Chandler, S. Glagov, W. Insull, M. Richardson, M. E. Rosenfeld, S. A. Schaffer, C. J. Schwartz, and W. D. Wagner, "A definition of the intima of human arteries and of its atherosclerosis-prone regions. A report from the Committee on Vascular Lesions of the Council on Arteriosclerosis, American Heart Association.," *Arterioscler. Thromb.*, vol. 12, no. 1, pp. 120–34, Jan. 1992.
- [15] H. C. Stary, A. B. Chandler, S. Glagov, J. R. Guyton, W. Insull, M. E. Rosenfeld, S. A. Schaffer, C. J. Schwartz, W. D. Wagner, and R. W. Wissler, "A definition of initial, fatty streak, and intermediate lesions of atherosclerosis. A report from the Committee on Vascular Lesions of the Council on Arteriosclerosis, American Heart Association.," *Circulation*, vol. 89, no. 5, pp. 2462–78, May 1994.
- [16] H. C. Stary, A. B. Chandler, R. E. Dinsmore, V. Fuster, S. Glagov, W. Insull, M. E. Rosenfeld, C. J. Schwartz, W. D. Wagner, and R. W. Wissler, "A definition of advanced types of atherosclerotic lesions and a histological classification of atherosclerosis. A report from the Committee on Vascular Lesions of the Council on Arteriosclerosis, American Heart Association.," *Circulation*, vol. 92, no. 5, pp. 1355–74, Sep. 1995.
- [17] H. C. Stary, "Natural history and histological classification of atherosclerotic lesions: an update.," *Arterioscler. Thromb. Vasc. Biol.*, vol. 20, no. 5, pp. 1177–8, May 2000.
- [18] R. Virmani, F. D. Kolodgie, A. P. Burke, A. Farb, and S. M. Schwartz, "Lessons from sudden coronary death: a comprehensive morphological classification scheme for atherosclerotic lesions.," *Arterioscler. Thromb. Vasc. Biol.*, vol. 20, no. 5, pp. 1262–1275, May 2000.
- [19] P. R. Moreno, "Vulnerable plaque: definition, diagnosis, and treatment.," *Cardiol. Clin.*, vol. 28, no. 1, pp. 1–30, Feb. 2010.
- [20] A. P. Burke, A. Farb, G. T. Malcom, Y. H. Liang, J. Smialek, and R. Virmani, "Coronary risk factors and plaque morphology in men with coronary disease who died suddenly.," *N. Engl. J. Med.*, vol. 336, no. 18, pp. 1276–82, May 1997.
- [21] J. N. Redgrave, P. Gallagher, J. K. Lovett, and P. M. Rothwell, "Critical cap thickness and rupture in symptomatic carotid plaques: the oxford plaque study.," *Stroke.*, vol. 39, no. 6, pp. 1722–9, Jun. 2008.
- [22] H. M. Loree, R. D. Kamm, R. G. Stringfellow, and R. T. Lee, "Effects of fibrous cap thickness on peak circumferential stress in model atherosclerotic vessels.," *Circ. Res.*, vol. 71, no. 4, pp. 850–8, Oct. 1992.
- [23] Z.-Y. Li, S. P. S. Howarth, T. Tang, and J. H. Gillard, "How critical is fibrous cap thickness to carotid plaque stability? A flow-plaque interaction model.," *Stroke.*, vol. 37, no. 5, pp. 1195–9, May 2006.
- [24] P. K. Shah, E. Falk, J. J. Badimon, A. Fernandez-Ortiz, A. Mailhac, G. Villareal-Levy, J. T. Fallon, J. Regnstrom, and V. Fuster, "Human monocyte-derived macrophages induce collagen breakdown in fibrous caps of atherosclerotic plaques. Potential role of matrix-degrading metalloproteinases and implications for plaque rupture.," *Circulation*, vol. 92, no. 6, pp. 1565–9, Sep. 1995.

- [25] Z. S. Galis and J. J. Khatri, "Matrix metalloproteinases in vascular remodeling and atherogenesis: the good, the bad, and the ugly.," *Circ. Res.*, vol. 90, no. 3, pp. 251–62, Feb. 2002.
- [26] L. Cardoso and S. Weinbaum, "Changing Views of the Biomechanics of Vulnerable Plaque Rupture: A Review.," *Ann. Biomed. Eng.*, Jul. 2013.
- [27] A. Fernández-Ortiz, J. J. Badimon, E. Falk, V. Fuster, B. Meyer, A. Mailhac, D. Weng, P. K. Shah, and L. Badimon, "Characterization of the relative thrombogenicity of atherosclerotic plaque components: implications for consequences of plaque rupture.," *J. Am. Coll. Cardiol.*, vol. 23, no. 7, pp. 1562–9, Jun. 1994.
- [28] R. Virmani, A. P. Burke, A. Farb, and F. D. Kolodgie, "Pathology of the vulnerable plaque.," *J. Am. Coll. Cardiol.*, vol. 47, no. 8 Suppl, pp. C13–8, Apr. 2006.
- [29] J. Ohayon, G. Finet, A. M. Gharib, D. A. Herzka, P. Tracqui, J. Heroux, G. Rioufol, M. S. Kotys, A. Elagha, and R. I. Pettigrew, "Necrotic core thickness and positive arterial remodeling index: emergent biomechanical factors for evaluating the risk of plaque rupture.," *Am. J. Physiol. Heart Circ. Physiol.*, vol. 295, no. 2, pp. H717–27, Aug. 2008.
- [30] A. P. Burke, F. D. Kolodgie, A. Farb, D. Weber, and R. Virmani, "Morphological predictors of arterial remodeling in coronary atherosclerosis.," *Circulation*, vol. 105, no. 3, pp. 297–303, Jan. 2002.
- [31] S. Glagov, E. Weisenberg, C. K. Zarins, R. Stankunavicius, and G. J. Kolettis, "Compensatory enlargement of human atherosclerotic coronary arteries.," *N. Engl. J. Med.*, vol. 316, no. 22, pp. 1371–5, May 1987.
- [32] P. Schoenhagen, K. M. Ziada, S. R. Kapadia, T. D. Crowe, S. E. Nissen, and E. M. Tuzcu, "Extent and direction of arterial remodeling in stable versus unstable coronary syndromes : an intravascular ultrasound study.," *Circulation*, vol. 101, no. 6, pp. 598–603, Feb. 2000.
- [33] P. R. Moreno, K. R. Purushothaman, E. Zias, J. Sanz, and V. Fuster, "Neovascularization in human atherosclerosis.," *Curr. Mol. Med.*, vol. 6, no. 5, pp. 457–77, Aug. 2006.
- [34] S. Frantz, K. A. Vincent, O. Feron, and R. A. Kelly, "Innate immunity and angiogenesis.," *Circ. Res.*, vol. 96, no. 1, pp. 15–26, Jan. 2005.
- [35] A. P. Levy and P. R. Moreno, "Intraplaque hemorrhage.," *Curr. Mol. Med.*, vol. 6, no. 5, pp. 479–88, Aug. 2006.
- [36] B. Chu, A. Kampschulte, M. S. Ferguson, W. S. Kerwin, V. L. Yarnykh, K. D. O'Brien, N. L. Polissar, T. S. Hatsukami, and C. Yuan, "Hemorrhage in the atherosclerotic carotid plaque: a high-resolution MRI study.," *Stroke.*, vol. 35, no. 5, pp. 1079–84, May 2004.
- [37] R. J. Lusby, L. D. Ferrell, W. K. Ehrenfeld, R. J. Stoney, and E. J. Wylie, "Carotid plaque hemorrhage. Its role in production of cerebral ischemia.," *Arch. Surg.*, vol. 117, no. 11, pp. 1479–88, Nov. 1982.
- [38] J. N. E. Redgrave, J. K. Lovett, P. J. Gallagher, and P. M. Rothwell, "Histological assessment of 526 symptomatic carotid plaques in relation to the nature and timing of ischemic symptoms: the Oxford plaque study.," *Circulation*, vol. 113, no. 19, pp. 2320–8, May 2006.
- [39] R. Virmani, E. R. Ladich, A. P. Burke, and F. D. Kolodgie, "Histopathology of carotid atherosclerotic disease.," *Neurosurgery*, vol. 59, no. 5 Suppl 3, pp. S219–27; discussion S3–13,

Nov. 2006.

- [40] J. A. Ambrose, M. A. Tannenbaum, D. Alexopoulos, C. E. Hjeldahl-Monsen, J. Leavy, M. Weiss, S. Borrico, R. Gorlin, and V. Fuster, "Angiographic progression of coronary artery disease and the development of myocardial infarction.," *J. Am. Coll. Cardiol.*, vol. 12, no. 1, pp. 56–62, Jul. 1988.
- [41] S. Dalager-Pedersen, E. Falk, S. Ringgaard, I. B. Kristensen, and E. M. Pedersen, "Effects of temperature and histopathologic preparation on the size and morphology of atherosclerotic carotid arteries as imaged by MRI.," *J. Magn. Reson. Imaging*, vol. 10, no. 5, pp. 876–85, Nov. 1999.
- [42] R. Ross, T. N. Wight, E. Strandness, and B. Thiele, "Human atherosclerosis. I. Cell constitution and characteristics of advanced lesions of the superficial femoral artery.," *Am. J. Pathol.*, vol. 114, no. 1, pp. 79–93, Jan. 1984.
- [43] J. Orbe, L. Fernandez, J. A. Rodríguez, G. Rábago, M. Belzunce, A. Monasterio, C. Roncal, and J. A. Páramo, "Different expression of MMPs/TIMP-1 in human atherosclerotic lesions. Relation to plaque features and vascular bed.," *Atherosclerosis*, vol. 170, no. 2, pp. 269–76, Oct. 2003.
- [44] G. Pasterkamp, A. H. Schoneveld, W. van Wolferen, B. Hillen, R. J. Clarijs, C. C. Haudenschild, and C. Borst, "The impact of atherosclerotic arterial remodeling on percentage of luminal stenosis varies widely within the arterial system. A postmortem study.," *Arterioscler. Thromb. Vasc. Biol.*, vol. 17, no. 11, pp. 3057–63, Nov. 1997.
- [45] C. Stancu and A. Sima, "Statins: mechanism of action and effects.," *J. Cell. Mol. Med.*, vol. 5, no. 4, pp. 378–87, 2001.
- [46] S. E. Nissen, "Effect of intensive lipid lowering on progression of coronary atherosclerosis: evidence for an early benefit from the Reversal of Atherosclerosis with Aggressive Lipid Lowering (REVERSAL) trial.," *Am. J. Cardiol.*, vol. 96, no. 5A, p. 61F–68F, Sep. 2005.
- [47] P. M. Ridker, E. Danielson, F. A. Fonseca, J. Genest, A. M. Gotto, J. J. Kastelein, W. Koenig, P. Libby, A. J. Lorenzatti, J. G. Macfadyen, B. G. Nordestgaard, J. Shepherd, J. T. Willerson, R. J. Glynn, and JUPITER Trial Study Group, "Reduction in C-reactive protein and LDL cholesterol and cardiovascular event rates after initiation of rosuvastatin: a prospective study of the JUPITER trial.," *Lancet (London, England)*, vol. 373, no. 9670, pp. 1175–82, Apr. 2009.
- [48] C. M. Ballantyne, N. Abate, Z. Yuan, T. R. King, and J. Palmisano, "Dose-comparison study of the combination of ezetimibe and simvastatin (Vytorin) versus atorvastatin in patients with hypercholesterolemia: the Vytorin Versus Atorvastatin (VYVA) study.," *Am. Heart J.*, vol. 149, no. 3, pp. 464–73, Mar. 2005.
- [49] C. P. Cannon, M. A. Blazing, R. P. Giugliano, A. McCagg, J. A. White, P. Theroux, H. Darius, B. S. Lewis, T. O. Ophuis, J. W. Jukema, G. M. De Ferrari, W. Ruzyllo, P. De Lucca, K. Im, E. A. Bohula, C. Reist, S. D. Wiviott, A. M. Tershakovec, T. A. Musliner, E. Braunwald, R. M. Califf, and IMPROVE-IT Investigators, "Ezetimibe Added to Statin Therapy after Acute Coronary Syndromes.," *N. Engl. J. Med.*, vol. 372, no. 25, pp. 2387–97, Jun. 2015.
- [50] I. Goldenberg, U. Goldbourt, V. Boyko, S. Behar, H. Reicher-Reiss, and BIP Study Group, "Relation between on-treatment increments in serum high-density lipoprotein cholesterol levels and cardiac mortality in patients with coronary heart disease (from the Bezafibrate Infarction Prevention trial).," *Am. J. Cardiol.*, vol. 97, no. 4, pp. 466–71, Feb. 2006.

- [51] R. Corti, J. Osende, R. Hutter, J. F. Viles-Gonzalez, U. Zafar, C. Valdivieso, G. Mizsei, J. T. Fallon, V. Fuster, and J. J. Badimon, “Fenofibrate induces plaque regression in hypercholesterolemic atherosclerotic rabbits: in vivo demonstration by high-resolution MRI,” *Atherosclerosis*, vol. 190, no. 1, pp. 106–13, Jan. 2007.
- [52] C. Weber and H. Noels, “Atherosclerosis: current pathogenesis and therapeutic options.,” *Nat. Med.*, vol. 17, no. 11, pp. 1410–22, 2011.
- [53] I. Sipahi, E. M. Tuzcu, K. E. Wolski, S. J. Nicholls, P. Schoenhagen, B. Hu, C. Balog, M. Shishehbor, W. A. Magyar, T. D. Crowe, S. Kapadia, and S. E. Nissen, “Beta-blockers and progression of coronary atherosclerosis: pooled analysis of 4 intravascular ultrasonography trials.,” *Ann. Intern. Med.*, vol. 147, no. 1, pp. 10–8, Jul. 2007.
- [54] ONTARGET Investigators, S. Yusuf, K. K. Teo, J. Pogue, L. Dyal, I. Copland, H. Schumacher, G. Dagenais, P. Sleight, and C. Anderson, “Telmisartan, ramipril, or both in patients at high risk for vascular events.,” *N. Engl. J. Med.*, vol. 358, no. 15, pp. 1547–59, Apr. 2008.
- [55] P. von Hundelshausen and C. Weber, “Platelets as immune cells: bridging inflammation and cardiovascular disease.,” *Circ. Res.*, vol. 100, no. 1, pp. 27–40, Jan. 2007.
- [56] L. Wallentin, R. C. Becker, A. Budaj, C. P. Cannon, H. Emanuelsson, C. Held, J. Horrow, S. Husted, S. James, H. Katus, K. W. Mahaffey, B. M. Scirica, A. Skene, P. G. Steg, R. F. Storey, R. A. Harrington, PLATO Investigators, A. Freij, and M. Thorsén, “Ticagrelor versus clopidogrel in patients with acute coronary syndromes.,” *N. Engl. J. Med.*, vol. 361, no. 11, pp. 1045–57, Sep. 2009.
- [57] C. P. Cannon, E. Braunwald, C. H. McCabe, D. J. Rader, J. L. Rouleau, R. Belder, S. V Joyal, K. A. Hill, M. A. Pfeffer, A. M. Skene, and Pravastatin or Atorvastatin Evaluation and Infection Therapy-Thrombolysis in Myocardial Infarction 22 Investigators, “Intensive versus moderate lipid lowering with statins after acute coronary syndromes.,” *N. Engl. J. Med.*, vol. 350, no. 15, pp. 1495–504, Apr. 2004.
- [58] G. De Luca, M. T. Dirksen, C. Spaulding, H. Kelbaek, M. Schalij, L. Thuesen, B. van der Hoeven, M. A. Vink, C. Kaiser, C. Musto, T. Chechi, G. Spaziani, L. S. Díaz de la Llera, V. Pasceri, E. Di Lorenzo, R. Violini, G. Cortese, H. Suryapranata, G. W. Stone, and Drug-Eluting Stent in Primary Angioplasty (DESERT) Cooperation, “Drug-eluting vs bare-metal stents in primary angioplasty: a pooled patient-level meta-analysis of randomized trials.,” *Arch. Intern. Med.*, vol. 172, no. 8, pp. 611–21; discussion 621–2, Apr. 2012.
- [59] L. D. Hillis, P. K. Smith, J. L. Anderson, J. A. Bittl, C. R. Bridges, J. G. Byrne, J. E. Cigarroa, V. J. DiSesa, L. F. Hiratzka, A. M. Hutter, M. E. Jessen, E. C. Keeley, S. J. Lahey, R. A. Lange, M. J. London, M. J. Mack, M. R. Patel, J. D. Puskas, J. F. Sabik, O. Selnes, D. M. Shahian, J. C. Trost, M. D. Winniford, A. K. Jacobs, J. L. Anderson, N. Albert, M. A. Creager, S. M. Ettinger, R. A. Guyton, J. L. Halperin, J. S. Hochman, F. G. Kushner, E. M. Ohman, W. Stevenson, C. W. Yancy, and American College of Cardiology Foundation/American Heart Association Task Force on Practice Guidelines, “2011 ACCF/AHA guideline for coronary artery bypass graft surgery: executive summary: a report of the American College of Cardiology Foundation/American Heart Association Task Force on Practice Guidelines.,” *J. Thorac. Cardiovasc. Surg.*, vol. 143, no. 1, pp. 4–34, Jan. 2012.
- [60] P. M. Rothwell, M. Eliasziw, S. a Gutnikov, a J. Fox, D. W. Taylor, M. R. Mayberg, C. P. Warlow, and H. J. M. Barnett, “Analysis of pooled data from the randomised controlled trials of endarterectomy for symptomatic carotid stenosis.,” *Lancet*, vol. 361, no. 9352, pp. 107–16, Jan.

2003.

- [61] A. Halliday, M. Harrison, E. Hayter, X. Kong, A. Mansfield, J. Marro, H. Pan, R. Peto, J. Potter, K. Rahimi, A. Rau, S. Robertson, J. Streifler, and D. Thomas, "10-year stroke prevention after successful carotid endarterectomy for asymptomatic stenosis (ACST-1): a multicentre randomised trial.," *Lancet*, vol. 376, no. 9746, pp. 1074–84, Sep. 2010.
- [62] M. H. Selim and C. a Molina, "Medical versus surgical treatment of asymptomatic carotid stenosis: the ever-changing nature of evidence-based medicine.," *Stroke.*, vol. 42, no. 4, pp. 1156–7, Apr. 2011.
- [63] A. L. Abbott, "Medical (nonsurgical) intervention alone is now best for prevention of stroke associated with asymptomatic severe carotid stenosis: results of a systematic review and analysis.," *Stroke.*, vol. 40, no. 10, pp. e573–83, Oct. 2009.
- [64] G. S. Getz and C. A. Reardon, "Animal models of atherosclerosis.," *Arterioscler. Thromb. Vasc. Biol.*, vol. 32, no. 5, pp. 1104–15, May 2012.
- [65] R. Reiser, M. F. Sorrels, and M. C. Williams, "Influence of high levels of dietary fats and cholesterol on atherosclerosis and lipid distribution in swine.," *Circ. Res.*, vol. 7, pp. 833–46, Nov. 1959.
- [66] B. H. Skold, R. Getty, and F. K. Ramsey, "Spontaneous atherosclerosis in the arterial system of aging swine.," *Am. J. Vet. Res.*, vol. 27, no. 116, pp. 257–73, Jan. 1966.
- [67] J. O. Hasler-Rapacz, T. C. Nichols, T. R. Griggs, D. A. Bellinger, and J. Rapacz, "Familial and diet-induced hypercholesterolemia in swine. Lipid, ApoB, and ApoA-I concentrations and distributions in plasma and lipoprotein subfractions.," *Arterioscler. Thromb.*, vol. 14, no. 6, pp. 923–30, Jun. 1994.
- [68] N. Brodala, E. P. Merricks, D. A. Bellinger, D. Damrongsri, S. Offenbacher, J. Beck, P. Madianos, D. Sotres, Y.-L. Chang, G. Koch, and T. C. Nichols, "Porphyromonas gingivalis bacteremia induces coronary and aortic atherosclerosis in normocholesterolemic and hypercholesterolemic pigs.," *Arterioscler. Thromb. Vasc. Biol.*, vol. 25, no. 7, pp. 1446–51, Jul. 2005.
- [69] J. Alvarez-Linera, J. Benito-León, J. Escribano, J. Campollo, and R. Gesto, "Prospective evaluation of carotid artery stenosis: elliptic centric contrast-enhanced MR angiography and spiral CT angiography compared with digital subtraction angiography.," *AJNR. Am. J. Neuroradiol.*, vol. 24, no. 5, pp. 1012–9, May 2003.
- [70] J. E. Van Velzen, J. D. Schuijff, F. R. De Graaf, J. W. Jukema, A. De Roos, L. J. Kroft, M. J. Schalij, J. H. Reiber, E. E. Van Der Wall, and J. J. Bax, "Imaging of atherosclerosis: invasive and noninvasive techniques.," *Hell. J. Cardiol. HJC = Hellēnikē Kardiol. Ep.*, vol. 50, no. 4, pp. 245–63, 2009.
- [71] M. Eliasziw, J. Y. Streifler, A. J. Fox, V. C. Hachinski, G. G. Ferguson, and H. J. Barnett, "Significance of plaque ulceration in symptomatic patients with high- grade carotid stenosis. North American Symptomatic Carotid Endarterectomy Trial," *Stroke*, vol. 25, no. 2, pp. 304–308, Feb. 1994.
- [72] M. M. Sadeghi, D. K. Glover, G. M. Lanza, Z. a Fayad, and L. L. Johnson, "Imaging atherosclerosis and vulnerable plaque.," *J. Nucl. Med.*, vol. 51 Suppl 1, p. 51S–65S, May 2010.

- [73] S. Voros, S. Rinehart, Z. Qian, P. Joshi, G. Vazquez, C. Fischer, P. Belur, E. Hulten, and T. C. Villines, "Coronary atherosclerosis imaging by coronary CT angiography: current status, correlation with intravascular interrogation and meta-analysis.," *JACC. Cardiovasc. Imaging*, vol. 4, no. 5, pp. 537–48, May 2011.
- [74] G. B. Anderson, R. Ashforth, D. E. Steinke, R. Ferdinandy, and J. M. Findlay, "CT Angiography for the Detection and Characterization of Carotid Artery Bifurcation Disease," *Stroke*, vol. 31, no. 9, pp. 2168–2174, Sep. 2000.
- [75] M. J. Gough, "Preprocedural imaging strategies in symptomatic carotid artery stenosis.," *J. Vasc. Surg.*, vol. 54, no. 4, pp. 1215–8, Oct. 2011.
- [76] M. Wintermark, S. S. Jawadi, J. H. Rapp, T. Tihan, E. Tong, D. V Glidden, S. Abedin, S. Schaeffer, G. Acevedo-Bolton, B. Boudignon, B. Orwoll, X. Pan, and D. Saloner, "High-resolution CT imaging of carotid artery atherosclerotic plaques.," *AJNR. Am. J. Neuroradiol.*, vol. 29, no. 5, pp. 875–82, May 2008.
- [77] C. Caussin, A. Ohanessian, S. Ghostine, L. Jacq, B. Lancelin, G. Dambrin, A. Sigal-Cinqualbre, C.-Y. Angel, and J.-F. Paul, "Characterization of vulnerable nonstenotic plaque with 16-slice computed tomography compared with intravascular ultrasound.," *Am. J. Cardiol.*, vol. 94, no. 1, pp. 99–104, Jul. 2004.
- [78] A. S. Agatston, W. R. Janowitz, F. J. Hildner, N. R. Zusmer, M. Viamonte, and R. Detrano, "Quantification of coronary artery calcium using ultrafast computed tomography.," *J. Am. Coll. Cardiol.*, vol. 15, no. 4, pp. 827–32, Mar. 1990.
- [79] N. Sunkara, N. D. Wong, and S. Malik, "Role of coronary artery calcium in cardiovascular risk assessment," *Expert Rev. Cardiovasc. Ther.*, vol. 12, no. 1, pp. 87–94, 2014.
- [80] R. S. Elkeles, I. F. Godsland, M. D. Feher, M. B. Rubens, M. Roughton, F. Nugara, S. E. Humphries, W. Richmond, and M. D. Flather, "Coronary calcium measurement improves prediction of cardiovascular events in asymptomatic patients with type 2 diabetes: The PREDICT study," *Eur. Heart J.*, vol. 29, no. 18, pp. 2244–2251, 2008.
- [81] L. J. Shaw, J. Narula, and Y. Chandrasekhar, "The Never-Ending Story on Coronary Calcium," *J. Am. Coll. Cardiol.*, vol. 65, no. 13, pp. 1283–1285, Apr. 2015.
- [82] J. Chen, A. J. Einstein, R. Fazel, H. M. Krumholz, Y. Wang, J. S. Ross, H. H. Ting, N. D. Shah, K. Nasir, and B. K. Nallamothu, "Cumulative exposure to ionizing radiation from diagnostic and therapeutic cardiac imaging procedures: A population-based analysis," *J. Am. Coll. Cardiol.*, vol. 56, no. 9, pp. 702–711, 2010.
- [83] K. S. Wildy, C. Yuan, J. S. Tsuruda, M. S. Ferguson, N. Wen, D. S. Subramaniam, and D. E. Strandness, "Atherosclerosis of the carotid artery: evaluation by magnetic resonance angiography.," *J. Magn. Reson. Imaging*, vol. 6, no. 5, pp. 726–32, 1996.
- [84] C. Yuan, K. W. Beach, L. H. Smith, and T. S. Hatsukami, "Measurement of atherosclerotic carotid plaque size in vivo using high resolution magnetic resonance imaging.," *Circulation*, vol. 98, no. 24, pp. 2666–71, Dec. 1998.
- [85] M. Shinnar, J. T. Fallon, S. Wehrli, M. Levin, D. Dalmacy, Z. a. Fayad, J. J. Badimon, M. Harrington, E. Harrington, and V. Fuster, "The diagnostic accuracy of ex vivo MRI for human atherosclerotic plaque characterization.," *Arterioscler. Thromb. Vasc. Biol.*, vol. 19, no. 11, pp.

2756–61, Nov. 1999.

- [86] T. S. Hatsukami, R. Ross, N. L. Polissar, and C. Yuan, “Visualization of fibrous cap thickness and rupture in human atherosclerotic carotid plaque in vivo with high-resolution magnetic resonance imaging,” *Circulation*, vol. 102, no. 9, pp. 959–64, Aug. 2000.
- [87] J. M. Serfaty, L. Chaabane, A. Tabib, J. M. Chevallier, A. Briguet, and P. C. Douek, “Atherosclerotic plaques: classification and characterization with T2-weighted high-spatial-resolution MR imaging-- an in vitro study,” *Radiology*, vol. 219, no. 2, pp. 403–10, May 2001.
- [88] C. Yuan, L. M. Mitsumori, M. S. Ferguson, N. L. Polissar, D. Echelard, G. Ortiz, R. Small, J. W. Davies, W. S. Kerwin, and T. S. Hatsukami, “In vivo accuracy of multispectral magnetic resonance imaging for identifying lipid-rich necrotic cores and intraplaque hemorrhage in advanced human carotid plaques,” *Circulation*, vol. 104, no. 17, pp. 2051–6, Oct. 2001.
- [89] J. M. Cai, T. S. Hatsukami, M. S. Ferguson, R. Small, N. L. Polissar, and C. Yuan, “Classification of human carotid atherosclerotic lesions with in vivo multicontrast magnetic resonance imaging,” *Circulation*, vol. 106, no. 11, pp. 1368–1373, 2002.
- [90] L. M. Mitsumori, T. S. Hatsukami, M. S. Ferguson, W. S. Kerwin, J. Cai, and C. Yuan, “In vivo accuracy of multisequence MR imaging for identifying unstable fibrous caps in advanced human carotid plaques,” *J. Magn. Reson. Imaging*, vol. 17, no. 4, pp. 410–20, Apr. 2003.
- [91] A. R. Moody, R. E. Murphy, P. S. Morgan, A. L. Martel, G. S. Delay, S. Allder, S. T. MacSweeney, W. G. Tennant, J. Gladman, J. Lowe, and B. J. Hunt, “Characterization of complicated carotid plaque with magnetic resonance direct thrombus imaging in patients with cerebral ischemia,” *Circulation*, vol. 107, no. 24, pp. 3047–52, Jun. 2003.
- [92] J. Morrisett, W. Vick, R. Sharma, G. Lawrie, M. Reardon, E. Ezell, J. Schwartz, G. Hunter, and D. Gorenstein, “Discrimination of components in atherosclerotic plaques from human carotid endarterectomy specimens by magnetic resonance imaging ex vivo,” *Magn. Reson. Imaging*, vol. 21, no. 5, pp. 465–74, Jun. 2003.
- [93] R. A. Trivedi, J.-M. U-King-Im, M. J. Graves, J. Horsley, M. Goddard, P. J. Kirkpatrick, and J. H. Gillard, “MRI-derived measurements of fibrous-cap and lipid-core thickness: the potential for identifying vulnerable carotid plaques in vivo,” *Neuroradiology*, vol. 46, no. 9, pp. 738–43, Sep. 2004.
- [94] T. Saam, M. S. Ferguson, V. L. Yarnykh, N. Takaya, D. Xu, N. L. Polissar, T. S. Hatsukami, and C. Yuan, “Quantitative evaluation of carotid plaque composition by in vivo MRI,” *Arterioscler. Thromb. Vasc. Biol.*, vol. 25, no. 1, pp. 234–9, Jan. 2005.
- [95] B. A. Wasserman, R. J. Wityk, H. H. Trout, and R. Virmani, “Low-grade carotid stenosis: looking beyond the lumen with MRI,” *Stroke*, vol. 36, no. 11, pp. 2504–13, Nov. 2005.
- [96] Y. Watanabe, M. Nagayama, T. Suga, K. Yoshida, S. Yamagata, A. Okumura, Y. Amoh, S. Nakashita, M. Van Cauteren, and Y. Dodo, “Characterization of atherosclerotic plaque of carotid arteries with histopathological correlation: vascular wall MR imaging vs. color Doppler ultrasonography (US),” *J. Magn. Reson. Imaging*, vol. 28, no. 2, pp. 478–85, Aug. 2008.
- [97] K. Yoshida, O. Narumi, M. Chin, K. Inoue, T. Tabuchi, K. Oda, M. Nagayama, N. Egawa, M. Hojo, Y. Goto, Y. Watanabe, and S. Yamagata, “Characterization of carotid atherosclerosis and detection of soft plaque with use of black-blood MR imaging,” *AJNR. Am. J. Neuroradiol.*, vol.

- 29, no. 5, pp. 868–74, May 2008.
- [98] L. Dong, W. S. Kerwin, M. S. Ferguson, R. Li, J. Wang, H. Chen, G. Canton, T. S. Hatsukami, and C. Yuan, “Cardiovascular magnetic resonance in carotid atherosclerotic disease.,” *J. Cardiovasc. Magn. Reson.*, vol. 11, no. 53, Dec. 2009.
- [99] N. Takaya, C. Yuan, B. Chu, T. Saam, H. Underhill, J. Cai, N. Tran, N. L. Polissar, C. Isaac, M. S. Ferguson, G. a Garden, S. C. Cramer, K. R. Maravilla, B. Hashimoto, and T. S. Hatsukami, “Association between carotid plaque characteristics and subsequent ischemic cerebrovascular events: a prospective assessment with MRI--initial results.,” *Stroke*, vol. 37, no. 3, pp. 818–23, Mar. 2006.
- [100] A. E. H. Zavodni, B. A. Wasserman, R. L. McClelland, A. S. Gomes, A. R. Folsom, J. F. Polak, J. A. C. Lima, and D. A. Bluemke, “Carotid Artery Plaque Morphology and Composition in Relation to Incident Cardiovascular Events: The Multi-Ethnic Study of Atherosclerosis (MESA).,” *Radiology*, vol. 271, no. 2, pp. 381–9, May 2014.
- [101] V. Hartwig, G. Giovannetti, N. Vanello, M. Lombardi, L. Landini, and S. Simi, “Biological effects and safety in magnetic resonance imaging: a review.,” *Int. J. Environ. Res. Public Health*, vol. 6, no. 6, pp. 1778–98, Jun. 2009.
- [102] A. Gupta, H. Baradaran, A. D. Schweitzer, H. Kamel, A. Pandya, D. Delgado, A. Dunning, A. I. Mushlin, and P. C. Sanelli, “Carotid plaque MRI and stroke risk: a systematic review and meta-analysis.,” *Stroke.*, vol. 44, no. 11, pp. 3071–7, Nov. 2013.
- [103] L. Saba, M. Anzidei, R. Sanfilippo, R. Montisci, P. Lucatelli, C. Catalano, R. Passariello, and G. Mallarini, “Imaging of the carotid artery.,” *Atherosclerosis*, vol. 220, no. 2, pp. 294–309, Feb. 2012.
- [104] E. G. Grant, a J. Duerinckx, S. M. El Saden, M. L. Melany, G. M. Hathout, P. T. Zimmerman, a K. Marumoto, S. N. Cohen, and J. D. Baker, “Ability to use duplex US to quantify internal carotid arterial stenoses: fact or fiction?,” *Radiology*, vol. 214, no. 1, pp. 247–52, Jan. 2000.
- [105] P. Pignoli, E. Tremoli, A. Poli, P. Oreste, and R. Paoletti, “Intimal plus medial thickness of the arterial wall: a direct measurement with ultrasound imaging.,” *Circulation*, vol. 74, no. 6, pp. 1399–406, Dec. 1986.
- [106] M. L. Bots, D. E. Grobbee, A. Hofman, and J. C. M. Witteman, “Common carotid intima-media thickness and risk of acute myocardial infarction: the role of lumen diameter.,” *Stroke.*, vol. 36, no. 4, pp. 762–7, Apr. 2005.
- [107] M. L. Bots, A. W. Hoes, P. J. Koudstaal, A. Hofman, and D. E. Grobbee, “Common carotid intima-media thickness and risk of stroke and myocardial infarction: the Rotterdam Study.,” *Circulation*, vol. 96, no. 5, pp. 1432–7, Sep. 1997.
- [108] J. Roquer, T. Segura, J. Serena, E. Cuadrado-Godia, M. Blanco, J. García-García, and J. Castillo, “Value of carotid intima-media thickness and significant carotid stenosis as markers of stroke recurrence.,” *Stroke.*, vol. 42, no. 11, pp. 3099–104, Nov. 2011.
- [109] A. C. Gray-Weale, J. C. Graham, J. R. Burnett, K. Byrne, and R. J. Lusby, “Carotid artery atheroma: comparison of preoperative B-mode ultrasound appearance with carotid endarterectomy specimen pathology.,” *J. Cardiovasc. Surg. (Torino).*, vol. 29, no. 6, pp. 676–81, 1988.

- [110] G. Geroulakos, G. Ramaswami, A. Nicolaides, K. James, N. Labropoulos, G. Belcaro, and M. Holloway, "Characterization of symptomatic and asymptomatic carotid plaques using high-resolution real-time ultrasonography.," *Br. J. Surg.*, vol. 80, no. 10, pp. 1274–7, Oct. 1993.
- [111] D. G. Kardoulas, A. N. Katsamouris, P. T. Gallis, T. P. Philippides, N. K. Anagnostakos, D. S. Gorgoyannis, and N. C. Gourtsoyannis, "Ultrasonographic and histologic characteristics of symptom-free and symptomatic carotid plaque.," *Cardiovasc. Surg.*, vol. 4, no. 5, pp. 580–90, Oct. 1996.
- [112] M.-L. M. Grønholdt, B. G. Nordestgaard, J. Bentzon, B. M. Wiebe, J. Zhou, E. Falk, and H. Sillesen, "Macrophages are associated with lipid-rich carotid artery plaques, echolucency on B-mode imaging, and elevated plasma lipid levels.," *J. Vasc. Surg.*, vol. 35, no. 1, pp. 137–45, Jan. 2002.
- [113] M. L. Grønholdt, B. M. Wiebe, H. Laursen, T. G. Nielsen, T. V Schroeder, and H. Sillesen, "Lipid-rich carotid artery plaques appear echolucent on ultrasound B-mode images and may be associated with intraplaque haemorrhage.," *Eur. J. Vasc. Endovasc. Surg.*, vol. 14, no. 6, pp. 439–45, Dec. 1997.
- [114] G. Devuyst, T. Karapanayiotides, P. Ruchat, M. Pusztaszeri, J.-A. Lobrinus, L. Jonasson, O. Cuisinaire, A. Kalangos, P.-A. Despland, J.-P. Thiran, and J. Bogousslavsky, "Ultrasound measurement of the fibrous cap in symptomatic and asymptomatic atheromatous carotid plaques.," *Circulation*, vol. 111, no. 21, pp. 2776–82, May 2005.
- [115] K. Ariyoshi, S. Okuya, I. Kunitsugu, K. Matsunaga, Y. Nagao, R. Nomiyama, K. Takeda, and Y. Tanizawa, "Ultrasound analysis of gray-scale median value of carotid plaques is a useful reference index for cerebro-cardiovascular events in patients with type 2 diabetes.," *J. Diabetes Investig.*, vol. 6, no. 1, pp. 91–7, Jan. 2015.
- [116] G. M. Biasi, P. M. Mingazzini, L. Baronio, M. R. Piglionica, S. A. Ferrari, T. S. Elatrozy, and A. N. Nicolaides, "Carotid plaque characterization using digital image processing and its potential in future studies of carotid endarterectomy and angioplasty.," *J. Endovasc. Surg.*, vol. 5, no. 3, pp. 240–6, Aug. 1998.
- [117] M. I. Matsagas, S. N. Vasdekis, A. G. Gugulakis, A. Lazaris, M. Foteinou, and M. N. Sechas, "Computer-assisted ultrasonographic analysis of carotid plaques in relation to cerebrovascular symptoms, cerebral infarction, and histology.," *Ann. Vasc. Surg.*, vol. 14, no. 2, pp. 130–7, Mar. 2000.
- [118] I. Gonçalves, M. W. Lindholm, L. M. Pedro, N. Dias, J. Fernandes e Fernandes, G. N. Fredrikson, J. Nilsson, J. Moses, and M. P. S. Ares, "Elastin and calcium rather than collagen or lipid content are associated with echogenicity of human carotid plaques.," *Stroke.*, vol. 35, no. 12, pp. 2795–800, Dec. 2004.
- [119] A. Nair, B. D. Kuban, E. M. Tuzcu, P. Schoenhagen, S. E. Nissen, and D. G. Vince, "Coronary plaque classification with intravascular ultrasound radiofrequency data analysis.," *Circulation*, vol. 106, no. 17, pp. 2200–6, Oct. 2002.
- [120] W.-S. Lee, S.-W. Kim, S.-A. Hong, T.-J. Lee, E.-S. Park, H.-J. Kim, K. J. Lee, T. H. Kim, C. J. Kim, and W. S. Ryu, "Atherosclerotic progression attenuates the expression of Nogo-B in autopsied coronary artery: pathology and virtual histology intravascular ultrasound analysis.," *J. Korean Med. Sci.*, vol. 24, no. 4, pp. 596–604, Aug. 2009.

- [121] S. Inaba, G. S. Mintz, N. Z. Farhat, J. Fajadet, D. Dudek, A. Marzocchi, B. Templin, G. Weisz, K. Xu, B. de Bruyne, P. W. Serruys, G. W. Stone, and A. Maehara, "Impact of positive and negative lesion site remodeling on clinical outcomes: insights from PROSPECT.," *JACC. Cardiovasc. Imaging*, vol. 7, no. 1, pp. 70–8, Jan. 2014.
- [122] C. V. Bourantas, H. M. Garcia-Garcia, V. Farooq, A. Maehara, K. Xu, P. Généreux, R. Diletti, T. Muramatsu, M. Fahy, G. Weisz, G. W. Stone, and P. W. Serruys, "Clinical and angiographic characteristics of patients likely to have vulnerable plaques: analysis from the PROSPECT study.," *JACC. Cardiovasc. Imaging*, vol. 6, no. 12, pp. 1263–72, Dec. 2013.
- [123] X. Wu, A. Maehara, G. S. Mintz, T. Kubo, K. Xu, S.-Y. Choi, Y. He, N. Guo, J. W. Moses, M. B. Leon, B. De Bruyne, P. W. Serruys, and G. W. Stone, "Virtual histology intravascular ultrasound analysis of non-culprit attenuated plaques detected by grayscale intravascular ultrasound in patients with acute coronary syndromes.," *Am. J. Cardiol.*, vol. 105, no. 1, pp. 48–53, Jan. 2010.
- [124] G. Zheng, Y. Li, H. Huang, J. Wang, A. Hirayama, and J. Lin, "The Effect of Statin Therapy on Coronary Plaque Composition Using Virtual Histology Intravascular Ultrasound: A Meta-Analysis.," *PLoS One*, vol. 10, no. 7, p. e0133433, 2015.
- [125] T. Lefèvre, A. Erglis, R. Gil, J. Legutko, M. Thomas, P. Brunel, M. Gilard, O. Darremont, H. Bøtker, C. von Birgelen, S. Marso, A. Khashaba, and P. Guyon, "Initial results of BLAST: bifurcation lesion analysis and stenting of thin cap fibroatheroma (TCFA/FA) as measured by VH-intravascular ultrasound - a global multicentre, prospective, randomised study," *EuroIntervention*, vol. 7, no. Supplement M, 2011.
- [126] A. Arbab-Zadeh and V. Fuster, "The myth of the 'vulnerable plaque': transitioning from a focus on individual lesions to atherosclerotic disease burden for coronary artery disease risk assessment.," *J. Am. Coll. Cardiol.*, vol. 65, no. 8, pp. 846–55, Mar. 2015.
- [127] A. S. Jahromi, C. S. Cinà, Y. Liu, and C. M. Clase, "Sensitivity and specificity of color duplex ultrasound measurement in the estimation of internal carotid artery stenosis: a systematic review and meta-analysis.," *J. Vasc. Surg.*, vol. 41, no. 6, pp. 962–72, Jun. 2005.
- [128] T. Wolff, J. Guirguis-Blake, T. Miller, M. Gillespie, and R. Harris, "Screening for carotid artery stenosis: an update of the evidence for the U.S. Preventive Services Task Force.," *Ann. Intern. Med.*, vol. 147, no. 12, pp. 860–70, Dec. 2007.
- [129] G. E. Trahey, S. W. Smith, and O. T. von Ramm, "Speckle pattern correlation with lateral aperture translation: experimental results and implications for spatial compounding.," *IEEE Trans. Ultrason. Ferroelectr. Freq. Control*, vol. 33, no. 3, pp. 257–64, Jan. 1986.
- [130] F. Tranquart, N. Grenier, V. Eder, and L. Pourcelot, "Clinical use of ultrasound tissue harmonic imaging.," *Ultrasound Med. Biol.*, vol. 25, no. 6, pp. 889–94, Jul. 1999.
- [131] J. J. Dahl, D. Hyun, M. Lediju, and G. E. Trahey, "Lesion detectability in diagnostic ultrasound with short-lag spatial coherence imaging.," *Ultrason. Imaging*, vol. 33, no. 2, pp. 119–33, Apr. 2011.
- [132] D. Huang, E. A. Swanson, C. P. Lin, J. S. Schuman, W. G. Stinson, W. Chang, M. R. Hee, T. Flotte, K. Gregory, and C. A. Puliafito, "Optical coherence tomography.," *Science*, vol. 254, no. 5035, pp. 1178–81, Nov. 1991.
- [133] T. Roleder, J. Jąkała, G. L. Kaluża, Ł. Partyka, K. Proniewska, E. Pociask, W. Zasada, W.

- Wojakowski, Z. Gašior, and D. Dudek, “The basics of intravascular optical coherence tomography.,” *Postępy w Kardiol. interwencyjnej = Adv. Interv. Cardiol.*, vol. 11, no. 2, pp. 74–83, 2015.
- [134] J. D. Caplan, S. Waxman, R. W. Nesto, and J. E. Muller, “Near-infrared spectroscopy for the detection of vulnerable coronary artery plaques.,” *J. Am. Coll. Cardiol.*, vol. 47, no. 8 Suppl, pp. C92–6, Apr. 2006.
- [135] M. Jaguszewski, R. Klingenberg, and U. Landmesser, “Intracoronary Near-Infrared Spectroscopy (NIRS) Imaging for Detection of Lipid Content of Coronary Plaques: Current Experience and Future Perspectives.,” *Curr. Cardiovasc. Imaging Rep.*, vol. 6, pp. 426–430, Jan. 2013.
- [136] S. W. E. van de Poll, T. J. Römer, G. J. Puppels, and A. van der Laarse, “Imaging of atherosclerosis. Raman spectroscopy of atherosclerosis.,” *J. Cardiovasc. Risk*, vol. 9, no. 5, pp. 255–61, Oct. 2002.
- [137] L. Marcu, Q. Fang, J. A. Jo, T. Papaioannou, A. Dorafshar, T. Reil, J.-H. Qiao, J. D. Baker, J. A. Freischlag, and M. C. Fishbein, “In vivo detection of macrophages in a rabbit atherosclerotic model by time-resolved laser-induced fluorescence spectroscopy.,” *Atherosclerosis*, vol. 181, no. 2, pp. 295–303, Aug. 2005.
- [138] L. Marcu, J. A. Jo, Q. Fang, T. Papaioannou, T. Reil, J.-H. Qiao, J. D. Baker, J. A. Freischlag, and M. C. Fishbein, “Detection of rupture-prone atherosclerotic plaques by time-resolved laser-induced fluorescence spectroscopy.,” *Atherosclerosis*, vol. 204, no. 1, pp. 156–64, May 2009.
- [139] K. Jansen, G. van Soest, and A. F. W. van der Steen, “Intravascular photoacoustic imaging: a new tool for vulnerable plaque identification.,” *Ultrasound Med. Biol.*, vol. 40, no. 6, pp. 1037–48, Jun. 2014.
- [140] R. T. Lee, S. G. Richardson, H. M. Loree, A. J. Grodzinsky, S. A. Gharib, F. J. Schoen, and N. Pandian, “Prediction of mechanical properties of human atherosclerotic tissue by high-frequency intravascular ultrasound imaging. An in vitro study.,” *Arterioscler. Thromb.*, vol. 12, no. 1, pp. 1–5, Jan. 1992.
- [141] S. D. Williamson, Y. Lam, H. F. Younis, H. Huang, S. Patel, M. R. Kaazempur-Mofrad, and R. D. Kamm, “On the sensitivity of wall stresses in diseased arteries to variable material properties.,” *J. Biomech. Eng.*, vol. 125, no. 1, pp. 147–55, Feb. 2003.
- [142] S. Golemati, A. Sassano, M. J. Lever, A. A. Bharath, S. Dhanjil, and A. N. Nicolaides, “Carotid artery wall motion estimated from B-mode ultrasound using region tracking and block matching.,” *Ultrasound Med. Biol.*, vol. 29, no. 3, pp. 387–99, Mar. 2003.
- [143] H. Kanai, H. Hasegawa, M. Ichiki, F. Tezuka, and Y. Koiwa, “Elasticity imaging of atheroma with transcutaneous ultrasound: preliminary study.,” *Circulation*, vol. 107, no. 24, pp. 3018–21, Jun. 2003.
- [144] H. Ribbers, R. G. P. Lopata, S. Holewijn, G. Pasterkamp, J. D. Blankensteijn, and C. L. de Korte, “Noninvasive two-dimensional strain imaging of arteries: validation in phantoms and preliminary experience in carotid arteries in vivo.,” *Ultrasound Med. Biol.*, vol. 33, no. 4, pp. 530–40, Apr. 2007.
- [145] H. Shi, C. C. Mitchell, M. McCormick, M. A. Kliwer, R. J. Dempsey, and T. Varghese, “Preliminary in vivo atherosclerotic carotid plaque characterization using the accumulated axial

- strain and relative lateral shift strain indices.,” *Phys. Med. Biol.*, vol. 53, no. 22, pp. 6377–94, Nov. 2008.
- [146] R. L. Maurice, J. Ohayon, Y. Frétigny, M. Bertrand, G. Soulez, and G. Cloutier, “Noninvasive vascular elastography: theoretical framework.,” *IEEE Trans. Med. Imaging*, vol. 23, no. 2, pp. 164–80, Feb. 2004.
- [147] C. Schmitt, G. Soulez, R. L. Maurice, M.-F. Giroux, and G. Cloutier, “Noninvasive vascular elastography: toward a complementary characterization tool of atherosclerosis in carotid arteries.,” *Ultrasound Med. Biol.*, vol. 33, no. 12, pp. 1841–58, Dec. 2007.
- [148] R. L. Maurice, G. Soulez, M.-F. Giroux, and G. Cloutier, “Noninvasive vascular elastography for carotid artery characterization on subjects without previous history of atherosclerosis.,” *Med. Phys.*, vol. 35, no. 8, pp. 3436–43, Aug. 2008.
- [149] C. Naim, G. Cloutier, E. Mercure, F. Destrempes, Z. Qin, W. El-Abyad, S. Lanthier, M.-F. Giroux, and G. Soulez, “Characterisation of carotid plaques with ultrasound elastography: feasibility and correlation with high-resolution magnetic resonance imaging.,” *Eur. Radiol.*, vol. 23, no. 7, pp. 2030–41, Jul. 2013.
- [150] K. Fujikura, J. Luo, V. Gamarnik, M. Pernot, R. Fukumoto, M. D. Tilson, and E. E. Konofagou, “A novel noninvasive technique for pulse-wave imaging and characterization of clinically-significant vascular mechanical properties in vivo.,” *Ultrason. Imaging*, vol. 29, no. 3, pp. 137–54, Jul. 2007.
- [151] W. Nichols and M. O’Rourke, *McDonald’s Blood Flow in Arteries: Theoretical, Experimental and Clinical Principles*, 5th ed. London: Hodder Arnold Publication, 2005.
- [152] J. Luo, K. Fujikura, L. S. Tyrie, M. D. Tilson, and E. E. Konofagou, “Pulse wave imaging of normal and aneurysmal abdominal aortas in vivo.,” *IEEE Trans. Med. Imaging*, vol. 28, no. 4, pp. 477–86, Apr. 2009.
- [153] J. Vappou, J. Luo, and E. E. Konofagou, “Pulse wave imaging for noninvasive and quantitative measurement of arterial stiffness in vivo.,” *Am. J. Hypertens.*, vol. 23, no. 4, pp. 393–8, May 2010.
- [154] R. X. Li, J. Luo, S. K. Balaram, F. A. Chaudhry, D. Shahmirzadi, and E. E. Konofagou, “Pulse wave imaging in normal, hypertensive and aneurysmal human aortas in vivo: a feasibility study.,” *Phys. Med. Biol.*, vol. 58, no. 13, pp. 4549–62, Jul. 2013.
- [155] S. D. Nandlall, M. P. Goldklang, A. Kalashian, N. A. Dangra, J. M. D’Armiento, and E. E. Konofagou, “Monitoring and staging abdominal aortic aneurysm disease with pulse wave imaging.,” *Ultrasound Med. Biol.*, vol. 40, no. 10, pp. 2404–14, Oct. 2014.
- [156] J. Luo, R. X. Li, and E. E. Konofagou, “Pulse wave imaging of the human carotid artery: an in vivo feasibility study.,” *IEEE Trans. Ultrason. Ferroelectr. Freq. Control*, vol. 59, no. 1, pp. 174–81, Jan. 2012.
- [157] I. Apostolakis, S. Nandlall, and E. Konofagou, “Piecewise Pulse Wave Imaging (pPWI) for detection and monitoring of focal vascular disease in murine aortas and carotids in vivo.,” *IEEE Trans. Med. Imaging*, Jul. 2015.
- [158] C. L. de Korte, A. F. van der Steen, E. I. Cépedes, G. Pasterkamp, S. G. Carlier, F. Mastik, A. H. Schoneveld, P. W. Serruys, and N. Bom, “Characterization of plaque components and

- vulnerability with intravascular ultrasound elastography.,” *Phys. Med. Biol.*, vol. 45, no. 6, pp. 1465–75, Jun. 2000.
- [159] C. L. De Korte, M. J. Sierevogel, F. Mastik, C. Strijder, J. A. Schaar, E. Velema, G. Pasterkamp, P. W. Serruys, and A. F. W. Van der Steen, “Identification of atherosclerotic plaque components with intravascular ultrasound elastography in vivo: A Yucatan pig study,” *Circulation*, vol. 105, no. 14, pp. 1627–1630, 2002.
- [160] J. a Schaar, C. L. de Korte, F. Mastik, R. Baldewsing, E. Regar, P. de Feyter, C. J. Slager, A. F. W. van der Steen, and P. W. Serruys, “Intravascular palpography for high-risk vulnerable plaque assessment.,” *Herz*, vol. 28, no. 6, pp. 488–95, Sep. 2003.
- [161] J. A. Schaar, C. L. De Korte, F. Mastik, C. Strijder, G. Pasterkamp, E. Boersma, P. W. Serruys, and A. F. W. Van Der Steen, “Characterizing vulnerable plaque features with intravascular elastography.,” *Circulation*, vol. 108, no. 21, pp. 2636–41, Nov. 2003.
- [162] E. Mercure, F. Destrempes, M.-H. Roy Cardinal, J. Porée, G. Soulez, J. Ohayon, and G. Cloutier, “A local angle compensation method based on kinematics constraints for non-invasive vascular axial strain computations on human carotid arteries.,” *Comput. Med. Imaging Graph.*, vol. 38, no. 2, pp. 123–36, Mar. 2014.
- [163] F. Deleaval, A. Bouvier, G. Finet, G. Cloutier, S. K. Yazdani, S. Le Floc’h, P. Clarysse, R. I. Pettigrew, and J. Ohayon, “The intravascular ultrasound elasticity-palpography technique revisited: a reliable tool for the in vivo detection of vulnerable coronary atherosclerotic plaques.,” *Ultrasound Med. Biol.*, vol. 39, no. 8, pp. 1469–81, Aug. 2013.
- [164] J. Ophir, I. Céspedes, H. Ponnekanti, Y. Yazdi, and X. Li, “Elastography: a quantitative method for imaging the elasticity of biological tissues.,” *Ultrason. Imaging*, vol. 13, no. 2, pp. 111–34, Apr. 1991.
- [165] K. J. Parker, M. M. Doyley, and D. J. Rubens, “Imaging the elastic properties of tissue: the 20 year perspective.,” *Phys. Med. Biol.*, vol. 56, no. 1, pp. R1–R29, Jan. 2011.
- [166] R. Muthupillai, D. J. Lomas, P. J. Rossman, J. F. Greenleaf, A. Manduca, and R. L. Ehman, “Magnetic resonance elastography by direct visualization of propagating acoustic strain waves.,” *Science*, vol. 269, no. 5232, pp. 1854–7, Sep. 1995.
- [167] L. Huwart, F. Peeters, R. Sinkus, L. Annet, N. Salameh, L. C. ter Beek, Y. Horsmans, and B. E. Van Beers, “Liver fibrosis: non-invasive assessment with MR elastography.,” *NMR Biomed.*, vol. 19, no. 2, pp. 173–9, Apr. 2006.
- [168] L. Xu, J. Chen, K. J. Glaser, M. Yin, P. J. Rossman, and R. L. Ehman, “MR elastography of the human abdominal aorta: a preliminary study.,” *J. Magn. Reson. Imaging*, vol. 38, no. 6, pp. 1549–53, Dec. 2013.
- [169] L. Xu, J. Chen, M. Yin, K. J. Glaser, Q. Chen, D. A. Woodrum, and R. L. Ehman, “Assessment of stiffness changes in the ex vivo porcine aortic wall using magnetic resonance elastography.,” *Magn. Reson. Imaging*, vol. 30, no. 1, pp. 122–7, Jan. 2012.
- [170] W. E. Kenyhercz, B. Raterman, V. S. P. Illapani, J. Dowell, X. Mo, R. D. White, and A. Kolipaka, “Quantification of aortic stiffness using magnetic resonance elastography: Measurement reproducibility, pulse wave velocity comparison, changes over cardiac cycle, and relationship with age.,” *Magn. Reson. Med.*, Jun. 2015.

- [171] A. R. Damughatla, B. Raterman, T. Sharkey-Toppen, N. Jin, O. P. Simonetti, R. D. White, and A. Kolipaka, "Quantification of aortic stiffness using MR elastography and its comparison to MRI-based pulse wave velocity.," *J. Magn. Reson. Imaging*, vol. 41, no. 1, pp. 44–51, Jan. 2015.
- [172] A. Kolipaka, D. Woodrum, P. A. Araoz, and R. L. Ehman, "MR elastography of the in vivo abdominal aorta: a feasibility study for comparing aortic stiffness between hypertensives and normotensives.," *J. Magn. Reson. Imaging*, vol. 35, no. 3, pp. 582–6, Mar. 2012.
- [173] A. P. Sarvazyan, O. V Rudenko, and W. L. Nyborg, "Biomedical applications of radiation force of ultrasound: historical roots and physical basis.," *Ultrasound Med. Biol.*, vol. 36, no. 9, pp. 1379–94, Sep. 2010.
- [174] Lord Rayleigh, "On the pressure of vibrations," *Philos. Mag. Ser. 6*, vol. 3, no. 15, pp. 338–346, Mar. 1902.
- [175] T. Sugimoto, S. Ueha, and K. Itoh, "Tissue hardness measurement using the radiation force of focused ultrasound," in *Proc. IEEE Ultrason. Symp.*, 1990, pp. 1377–1380.
- [176] M. L. Palmeri, A. C. Sharma, R. R. Bouchard, R. W. Nightingale, and K. R. Nightingale, "A finite-element method model of soft tissue response to impulsive acoustic radiation force.," *IEEE Trans. Ultrason. Ferroelectr. Freq. Control*, vol. 52, no. 10, pp. 1699–712, Oct. 2005.
- [177] J. R. Doherty, G. E. Trahey, K. R. Nightingale, and M. L. Palmeri, "Acoustic radiation force elasticity imaging in diagnostic ultrasound.," *IEEE Trans. Ultrason. Ferroelectr. Freq. Control*, vol. 60, no. 4, pp. 685–701, Apr. 2013.
- [178] W. L. M. Nyborg, "Acoustic Streaming," in *Physical Acoustics*, vol. IIB, W. P. Mason, Ed. New York: Academic Press, 1965, pp. 265–331.
- [179] H. C. Starritt, F. A. Duck, and V. F. Humphrey, "Forces acting in the direction of propagation in pulsed ultrasound fields.," *Phys. Med. Biol.*, vol. 36, no. 11, pp. 1465–74, Nov. 1991.
- [180] E. V. Dontsov and B. B. Guzina, "Acoustic radiation force in tissue-like solids due to modulated sound field," *J. Mech. Phys. Solids*, vol. 60, no. 10, pp. 1791–1813, 2012.
- [181] S. Catheline, J. L. Gennisson, and M. Fink, "Measurement of elastic nonlinearity of soft solid with transient elastography.," *J. Acoust. Soc. Am.*, vol. 114, no. 6 Pt 1, pp. 3087–91, Dec. 2003.
- [182] M. Fatemi and J. F. Greenleaf, "Vibro-acoustography: an imaging modality based on ultrasound-stimulated acoustic emission.," *Proc. Natl. Acad. Sci. U. S. A.*, vol. 96, no. 12, pp. 6603–8, Jun. 1999.
- [183] M. W. Urban, A. Alizad, W. Aquino, J. F. Greenleaf, and M. Fatemi, "A Review of Vibro-acoustography and its Applications in Medicine.," *Curr. Med. Imaging Rev.*, vol. 7, no. 4, pp. 350–359, Nov. 2011.
- [184] A. Alizad, M. Fatemi, D. H. Whaley, and J. F. Greenleaf, "Application of vibro-acoustography for detection of calcified arteries in breast tissue.," *J. Ultrasound Med.*, vol. 23, no. 2, pp. 267–73, Feb. 2004.
- [185] C. Pislaru, B. Kantor, R. R. Kinnick, J. L. Anderson, M.-C. Aubry, M. W. Urban, M. Fatemi, and J. F. Greenleaf, "In vivo vibroacoustography of large peripheral arteries.," *Invest. Radiol.*, vol. 43, no. 4, pp. 243–52, Apr. 2008.

- [186] A. P. Sarvazyan, O. V Rudenko, S. D. Swanson, J. B. Fowlkes, and S. Y. Emelianov, "Shear wave elasticity imaging: a new ultrasonic technology of medical diagnostics.," *Ultrasound Med. Biol.*, vol. 24, no. 9, pp. 1419–35, Nov. 1998.
- [187] J. Bercoff, M. Tanter, and M. Fink, "Supersonic shear imaging: a new technique for soft tissue elasticity mapping.," *IEEE Trans. Ultrason. Ferroelectr. Freq. Control*, vol. 51, no. 4, pp. 396–409, Apr. 2004.
- [188] K. Nightingale, S. McAleavey, and G. Trahey, "Shear-wave generation using acoustic radiation force: in vivo and ex vivo results.," *Ultrasound Med. Biol.*, vol. 29, no. 12, pp. 1715–23, Dec. 2003.
- [189] M. L. Palmeri, M. H. Wang, J. J. Dahl, K. D. Frinkley, and K. R. Nightingale, "Quantifying hepatic shear modulus in vivo using acoustic radiation force.," *Ultrasound Med. Biol.*, vol. 34, no. 4, pp. 546–58, Apr. 2008.
- [190] J. McLaughlin and D. Renzi, "Shear wave speed recovery in transient elastography and supersonic imaging using propagating fronts," *Inverse Probl.*, vol. 22, no. 2, pp. 681–706, 2006.
- [191] N. C. Rouze, M. H. Wang, M. L. Palmeri, and K. R. Nightingale, "Robust estimation of time-of-flight shear wave speed using a radon sum transformation.," *IEEE Trans. Ultrason. Ferroelectr. Freq. Control*, vol. 57, no. 12, pp. 2662–70, Dec. 2010.
- [192] M. H. Wang, M. L. Palmeri, V. M. Rotemberg, N. C. Rouze, and K. R. Nightingale, "Improving the robustness of time-of-flight based shear wave speed reconstruction methods using RANSAC in human liver in vivo.," *Ultrasound Med. Biol.*, vol. 36, no. 5, pp. 802–13, May 2010.
- [193] R. W. Ogden, "Anisotropy and Nonlinear Elasticity in Arterial Wall Mechanics," in *Biomechanical Modelling at the Molecular, Cellular and Tissue Levels*, Springer Vienna, 2009, pp. 179–258.
- [194] X. Zhang, R. R. Kinnick, M. Fatemi, and J. F. Greenleaf, "Noninvasive method for estimation of complex elastic modulus of arterial vessels.," *IEEE Trans. Ultrason. Ferroelectr. Freq. Control*, vol. 52, no. 4, pp. 642–52, Apr. 2005.
- [195] M. Couade, M. Pernot, C. Prada, E. Messas, J. Emmerich, P. Bruneval, A. Criton, M. Fink, and M. Tanter, "Quantitative assessment of arterial wall biomechanical properties using shear wave imaging.," *Ultrasound Med. Biol.*, vol. 36, no. 10, pp. 1662–76, Oct. 2010.
- [196] A. P. Tierney, D. M. Dumont, A. Callanan, G. E. Trahey, and T. M. McGloughlin, "Acoustic radiation force impulse imaging on ex vivo abdominal aortic aneurysm model.," *Ultrasound Med. Biol.*, vol. 36, no. 5, pp. 821–32, May 2010.
- [197] E. Widman, E. Maksuti, D. Larsson, M. W. Urban, A. Bjällmark, and M. Larsson, "Shear wave elastography plaque characterization with mechanical testing validation: a phantom study.," *Phys. Med. Biol.*, vol. 60, no. 8, pp. 3151–74, Apr. 2015.
- [198] K. V Ramnarine, J. W. Garrard, B. Kanber, S. Nduwayo, T. C. Hartshorne, and T. G. Robinson, "Shear wave elastography imaging of carotid plaques: feasible, reproducible and of clinical potential.," *Cardiovasc. Ultrasound*, vol. 12, no. 1, p. 49, 2014.
- [199] J. W. Garrard, P. Ummur, S. Nduwayo, B. Kanber, T. C. Hartshorne, K. P. West, D. Moore, T. G. Robinson, and K. V Ramnarine, "Shear Wave Elastography May Be Superior to Greyscale

- Median for the Identification of Carotid Plaque Vulnerability: A Comparison with Histology.,” *Ultraschall Med.*, vol. 36, no. 4, pp. 386–90, Aug. 2015.
- [200] S. Chen, M. Fatemi, and J. F. Greenleaf, “Quantifying elasticity and viscosity from measurement of shear wave speed dispersion.,” *J. Acoust. Soc. Am.*, vol. 115, no. 6, pp. 2781–5, Jun. 2004.
- [201] I. Z. Nenadic, M. W. Urban, S. A. Mitchell, and J. F. Greenleaf, “Lamb wave dispersion ultrasound vibrometry (LDUV) method for quantifying mechanical properties of viscoelastic solids.,” *Phys. Med. Biol.*, vol. 56, no. 7, pp. 2245–64, Apr. 2011.
- [202] S. Chen, M. W. Urban, C. Pislaru, R. Kinnick, Y. Zheng, A. Yao, and J. F. Greenleaf, “Shearwave dispersion ultrasound vibrometry (SDUV) for measuring tissue elasticity and viscosity.,” *IEEE Trans. Ultrason. Ferroelectr. Freq. Control*, vol. 56, no. 1, pp. 55–62, Jan. 2009.
- [203] T. Deffieux, G. Montaldo, M. Tanter, and M. Fink, “Shear wave spectroscopy for in vivo quantification of human soft tissues visco-elasticity.,” *IEEE Trans. Med. Imaging*, vol. 28, no. 3, pp. 313–22, Mar. 2009.
- [204] M. Bernal, I. Nenadic, M. W. Urban, and J. F. Greenleaf, “Material property estimation for tubes and arteries using ultrasound radiation force and analysis of propagating modes.,” *J. Acoust. Soc. Am.*, vol. 129, no. 3, pp. 1344–54, Mar. 2011.
- [205] K. Nightingale, M. S. Soo, R. Nightingale, and G. Trahey, “Acoustic radiation force impulse imaging: in vivo demonstration of clinical feasibility.,” *Ultrasound Med. Biol.*, vol. 28, no. 2, pp. 227–35, Feb. 2002.
- [206] G. F. Pinton, J. J. Dahl, and G. E. Trahey, “Rapid tracking of small displacements with ultrasound.,” *IEEE Trans. Ultrason. Ferroelectr. Freq. Control*, vol. 53, no. 6, pp. 1103–17, Jun. 2006.
- [207] M. R. Selzo and C. M. Gallippi, “Viscoelastic response (VisR) imaging for assessment of viscoelasticity in Voigt materials.,” *IEEE Trans. Ultrason. Ferroelectr. Freq. Control*, vol. 60, no. 12, pp. 2488–500, Dec. 2013.
- [208] G. E. Trahey, M. L. Palmeri, R. C. Bentley, and K. R. Nightingale, “Acoustic radiation force impulse imaging of the mechanical properties of arteries: in vivo and ex vivo results.,” *Ultrasound Med. Biol.*, vol. 30, no. 9, pp. 1163–71, Sep. 2004.
- [209] D. Dumont, R. H. Behler, T. C. Nichols, E. P. Merricks, and C. M. Gallippi, “ARFI imaging for noninvasive material characterization of atherosclerosis.,” *Ultrasound Med. Biol.*, vol. 32, no. 11, pp. 1703–11, Nov. 2006.
- [210] R. H. Behler, T. C. Nichols, H. Zhu, E. P. Merricks, and C. M. Gallippi, “ARFI imaging for noninvasive material characterization of atherosclerosis. Part II: toward in vivo characterization.,” *Ultrasound Med. Biol.*, vol. 35, no. 2, pp. 278–95, Feb. 2009.
- [211] D. Dumont, J. Dahl, E. Miller, J. Allen, B. Fahey, and G. Trahey, “Lower-limb vascular imaging with acoustic radiation force elastography: demonstration of in vivo feasibility.,” *IEEE Trans. Ultrason. Ferroelectr. Freq. Control*, vol. 56, no. 5, pp. 931–44, May 2009.
- [212] J. J. Dahl, D. M. Dumont, J. D. Allen, E. M. Miller, and G. E. Trahey, “Acoustic radiation force impulse imaging for noninvasive characterization of carotid artery atherosclerotic plaques: a feasibility study.,” *Ultrasound Med. Biol.*, vol. 35, no. 5, pp. 707–16, May 2009.

- [213] J. R. Doherty, J. J. Dahl, P. G. Kranz, N. El Husseini, H.-C. Chang, N. Chen, J. D. Allen, K. L. Ham, and G. E. Trahey, "Comparison of Acoustic Radiation Force Impulse Imaging Derived Carotid Plaque Stiffness With Spatially Registered MRI Determined Composition.," *IEEE Trans. Med. Imaging*, vol. 34, no. 11, pp. 2354–65, Nov. 2015.
- [214] T. a Bigelow, C. C. Church, K. Sandstrom, J. G. Abbott, M. C. Ziskin, P. D. Edmonds, B. Herman, K. E. Thomenius, and T. J. Teo, "The thermal index: its strengths, weaknesses, and proposed improvements.," *J. Ultrasound Med.*, vol. 30, no. 5, pp. 714–34, May 2011.
- [215] W. D. O'Brien, C. X. Deng, G. R. Harris, B. A. Herman, C. R. Merritt, N. Sanghvi, and J. F. Zachary, "The risk of exposure to diagnostic ultrasound in postnatal subjects: thermal effects.," *J. Ultrasound Med.*, vol. 27, no. 4, pp. 517–35, Apr. 2008.
- [216] M. L. Palmeri and K. R. Nightingale, "On the thermal effects associated with radiation force imaging of soft tissue.," *IEEE Trans. Ultrason. Ferroelectr. Freq. Control*, vol. 51, no. 5, pp. 551–65, May 2004.
- [217] M. L. Palmeri, K. D. Frinkley, and K. R. Nightingale, "Experimental studies of the thermal effects associated with radiation force imaging of soft tissue.," *Ultrason. Imaging*, vol. 26, no. 2, pp. 100–14, Apr. 2004.
- [218] C. C. Church, E. L. Carstensen, W. L. Nyborg, P. L. Carson, L. a Frizzell, and M. R. Bailey, "The risk of exposure to diagnostic ultrasound in postnatal subjects: nonthermal mechanisms.," *J. Ultrasound Med.*, vol. 27, no. 4, pp. 565–92, Apr. 2008.
- [219] C. C. Church, C. Labuda, and K. Nightingale, "Should the mechanical index be revised for ARFI imaging?," *IEEE Int. Ultrason. Symp. IUS*, pp. 17–20, 2012.
- [220] J. R. Doherty, D. M. Dumont, G. E. Trahey, and M. L. Palmeri, "Acoustic radiation force impulse imaging of vulnerable plaques: a finite element method parametric analysis.," *J. Biomech.*, vol. 46, no. 1, pp. 83–90, Jan. 2013.
- [221] B. J. Fahey, M. L. Palmeri, and G. E. Trahey, "The impact of physiological motion on tissue tracking during radiation force imaging.," *Ultrasound Med. Biol.*, vol. 33, no. 7, pp. 1149–66, Jul. 2007.
- [222] D. M. Giannantonio, D. M. Dumont, G. E. Trahey, and B. C. Byram, "Comparison of physiological motion filters for in vivo cardiac ARFI.," *Ultrason. Imaging*, vol. 33, no. 2, pp. 89–108, Apr. 2011.
- [223] W. F. Walker and G. E. Trahey, "A Fundamental Limit on Delay Estimation Using Partially Correlated Speckle Signals," *IEEE Trans. Ultrason. Ferroelectr. Freq. Control*, vol. 42, no. 2, pp. 301–308, 1995.
- [224] T. Loupas, R. B. Peterson, and R. W. Gill, "Experimental evaluation of velocity and power estimation for ultrasound blood flow imaging, by means of a two-dimensional autocorrelation approach," *IEEE Trans. Ultrason. Ferroelectr. Freq. Control*, vol. 42, no. 4, pp. 689–699, Jul. 1995.
- [225] C. Kasai, K. Namekawa, A. Koyano, and R. Omoto, "Real-Time Two-Dimensional Blood-Flow Imaging Using an Auto-Correlation Technique," *Ieee Trans. Sonics Ultrason.*, vol. 32, no. 3, pp. 458–464, 1985.

- [226] B. Byram, G. E. Trahey, and M. Palmeri, "Bayesian speckle tracking. Part I: an implementable perturbation to the likelihood function for ultrasound displacement estimation.," *IEEE Trans. Ultrason. Ferroelectr. Freq. Control*, vol. 60, no. 1, pp. 132–43, Jan. 2013.
- [227] B. Byram, G. E. Trahey, and M. Palmeri, "Bayesian speckle tracking. Part II: biased ultrasound displacement estimation.," *IEEE Trans. Ultrason. Ferroelectr. Freq. Control*, vol. 60, no. 1, pp. 144–57, Jan. 2013.
- [228] S. A. McAleavey, K. R. Nightingale, and G. E. Trahey, "Estimates of echo correlation and measurement bias in acoustic radiation force impulse imaging.," *IEEE Trans. Ultrason. Ferroelectr. Freq. Control*, vol. 50, no. 6, pp. 631–41, Jun. 2003.
- [229] A. H. Dhanaliwala, J. A. Hossack, and F. W. Mauldin, "Assessing and improving acoustic radiation force image quality using a 1.5-D transducer design.," *IEEE Trans. Ultrason. Ferroelectr. Freq. Control*, vol. 59, no. 7, pp. 1602–8, Jul. 2012.
- [230] M. L. Palmeri, S. A. McAleavey, G. E. Trahey, and K. R. Nightingale, "Ultrasonic tracking of acoustic radiation force-induced displacements in homogeneous media," *IEEE Trans. Ultrason. Ferroelectr. Freq. Control*, vol. 53, no. 7, pp. 1300–1313, Jul. 2006.
- [231] M. L. Palmeri, S. A. McAleavey, K. L. Fong, G. E. Trahey, and K. R. Nightingale, "Dynamic mechanical response of elastic spherical inclusions to impulsive acoustic radiation force excitation.," *IEEE Trans. Ultrason. Ferroelectr. Freq. Control*, vol. 53, no. 11, pp. 2065–79, Nov. 2006.
- [232] F. W. Mauldin, F. Viola, and W. F. Walker, "Reduction of echo decorrelation via complex principal component filtering.," *Ultrasound Med. Biol.*, vol. 35, no. 8, pp. 1325–43, Aug. 2009.
- [233] F. W. Mauldin, F. Viola, and W. F. Walker, "Complex principal components for robust motion estimation.," *IEEE Trans. Ultrason. Ferroelectr. Freq. Control*, vol. 57, no. 11, pp. 2437–49, Nov. 2010.
- [234] M. a Lediju, M. J. Pihl, J. J. Dahl, and G. E. Trahey, "Quantitative assessment of the magnitude, impact and spatial extent of ultrasonic clutter.," *Ultrason. Imaging*, vol. 30, no. 3, pp. 151–68, Jul. 2008.
- [235] E. J. Boote, "AAPM/RSNA physics tutorial for residents: topics in US: Doppler US techniques: concepts of blood flow detection and flow dynamics.," *Radiographics*, vol. 23, no. 5, pp. 1315–1327, 2003.
- [236] G. F. Pinton, G. E. Trahey, and J. J. Dahl, "Sources of image degradation in fundamental and harmonic ultrasound imaging: a nonlinear, full-wave, simulation study.," *IEEE Trans. Ultrason. Ferroelectr. Freq. Control*, vol. 58, no. 6, pp. 1272–83, Jun. 2011.
- [237] J. R. Doherty, J. J. Dahl, and G. E. Trahey, "Harmonic tracking of acoustic radiation force-induced displacements.," *IEEE Trans. Ultrason. Ferroelectr. Freq. Control*, vol. 60, no. 11, pp. 2347–58, Nov. 2013.
- [238] P. Song, H. Zhao, M. Urban, A. Manduca, S. Pislaru, R. Kinnick, C. Pislaru, J. Greenleaf, and S. Chen, "Improved Shear Wave Motion Detection Using Pulse-Inversion Harmonic Imaging with a Phased Array Transducer.," *IEEE Trans. Med. Imaging*, vol. 32, no. 12, pp. 2299–2310, Sep. 2013.

- [239] M. L. Palmeri, J. J. Dahl, D. B. MacLeod, S. a Grant, and K. R. Nightingale, "On the feasibility of imaging peripheral nerves using acoustic radiation force impulse imaging.," *Ultrasound Med. Biol.*, vol. 31, no. 3, pp. 172–182, 2009.
- [240] S. Rosenzweig, M. Palmeri, and K. Nightingale, "Analysis of rapid multi-focal-zone ARFI imaging.," *IEEE Trans. Ultrason. Ferroelectr. Freq. Control*, vol. 62, no. 2, pp. 280–9, Feb. 2015.
- [241] K. Nightingale, M. Palmeri, and G. Trahey, "Analysis of contrast in images generated with transient acoustic radiation force.," *Ultrasound Med. Biol.*, vol. 32, no. 1, pp. 61–72, Jan. 2006.
- [242] J. J. Dahl, G. F. Pinton, M. L. Palmeri, V. Agrawal, K. R. Nightingale, and G. E. Trahey, "A parallel tracking method for acoustic radiation force impulse imaging.," *IEEE Trans. Ultrason. Ferroelectr. Freq. Control*, vol. 54, no. 2, pp. 301–12, Feb. 2007.
- [243] R. R. Bouchard, J. J. Dahl, S. J. Hsu, M. L. Palmeri, and G. E. Trahey, "Image quality, tissue heating, and frame rate trade-offs in acoustic radiation force impulse imaging.," *IEEE Trans. Ultrason. Ferroelectr. Freq. Control*, vol. 56, no. 1, pp. 63–76, Jan. 2009.
- [244] S. Rosenzweig, M. Palmeri, and K. Nightingale, "GPU-based real-time small displacement estimation with ultrasound.," *IEEE Trans. Ultrason. Ferroelectr. Freq. Control*, vol. 58, no. 2, pp. 399–405, Feb. 2011.
- [245] H. C. Han and D. N. Ku, "Contractile responses in arteries subjected to hypertensive pressure in seven-day organ culture.," *Ann. Biomed. Eng.*, vol. 29, no. 6, pp. 467–75, Jun. 2001.
- [246] P. N. T. Wells and H.-D. Liang, "Medical ultrasound: imaging of soft tissue strain and elasticity.," *J. R. Soc. Interface*, vol. 8, no. 64, pp. 1521–49, Nov. 2011.
- [247] R. H. Behler, M. R. Scola, and C. M. Gallippi, "Reverberation artifact rejection and masking in arterial ARFI imaging," in *Proc. IEEE Ultrason. Symp.*, 2009, pp. 2367–2370.
- [248] D. Gao, N. Ning, Y. Guo, W. Ning, X. Niu, and J. Yang, "Computed tomography for detecting coronary artery plaques: a meta-analysis.," *Atherosclerosis*, vol. 219, no. 2, pp. 603–9, Dec. 2011.
- [249] D. P. Shattuck, M. D. Weinschenker, S. W. Smith, and O. T. von Ramm, "Explososcan: a parallel processing technique for high speed ultrasound imaging with linear phased arrays.," *J. Acoust. Soc. Am.*, vol. 75, no. 4, pp. 1273–82, Apr. 1984.
- [250] H. M. Loree, B. J. Tobias, L. J. Gibson, R. D. Kamm, D. M. Small, and R. T. Lee, "Mechanical properties of model atherosclerotic lesion lipid pools.," *Arterioscler. Thromb.*, vol. 14, no. 2, pp. 230–4, Feb. 1994.
- [251] B. Lundberg, "Chemical composition and physical state of lipid deposits in atherosclerosis.," *Atherosclerosis*, vol. 56, no. 1, pp. 93–110, Jul. 1985.
- [252] N. C. Rouze, M. H. Wang, M. L. Palmeri, and K. R. Nightingale, "Parameters affecting the resolution and accuracy of 2-D quantitative shear wave images.," *IEEE Trans. Ultrason. Ferroelectr. Freq. Control*, vol. 59, no. 8, pp. 1729–40, Aug. 2012.
- [253] T. Deffieux, J.-L. Gennisson, J. Bercoff, and M. Tanter, "On the effects of reflected waves in transient shear wave elastography.," *IEEE Trans. Ultrason. Ferroelectr. Freq. Control*, vol. 58, no. 10, pp. 2032–5, Oct. 2011.
- [254] Q. Chen, S. I. Ringleb, A. Manduca, R. L. Ehman, and K.-N. An, "Differential effects of pre-

- tension on shear wave propagation in elastic media with different boundary conditions as measured by magnetic resonance elastography and finite element modeling.," *J. Biomech.*, vol. 39, no. 8, pp. 1428–34, Jan. 2006.
- [255] J. L. Prince and J. M. Links, *Medical imaging signals and systems*. Upper Saddle River, NJ: Pearson Prentice Hall, 2006.
- [256] D. M. Dumont, J. R. Doherty, and G. E. Trahey, "Noninvasive assessment of wall-shear rate and vascular elasticity using combined ARFI/SWEI/spectral Doppler imaging system.," *Ultrason. Imaging*, vol. 33, no. 3, pp. 165–88, Jul. 2011.
- [257] M. G. Menon and S. McAleavey, "Resolution Estimation and Bias Reduction in Acoustic Radiation Force Impulse Imaging," University of Rochester, Rochester, NY, 2010.
- [258] X. H. Zhou, N. A. Obuchowski, and D. K. McClish, *Statistical Methods in Diagnostic Medicine*. New York: Wiley-Interscience, 2002.
- [259] K.-Y. Liang and S. L. Zeger, "Longitudinal data analysis using generalized linear models," *Biometrika*, vol. 73, no. 1, pp. 13–22, 1986.
- [260] M. M. Mughal, M. K. Khan, J. K. DeMarco, A. Majid, F. Shamoun, and G. S. Abela, "Symptomatic and asymptomatic carotid artery plaque.," *Expert Rev. Cardiovasc. Ther.*, vol. 9, no. 10, pp. 1315–30, Oct. 2011.
- [261] T. G. Brott, J. L. Halperin, S. Abbara, J. M. Bacharach, J. D. Barr, R. L. Bush, C. U. Cates, M. a Creager, S. B. Fowler, G. Friday, V. S. Hertzberg, E. B. McIff, W. S. Moore, P. D. Panagos, T. S. Riles, R. H. Rosenwasser, and A. J. Taylor, "2011 ASA/ACCF/AHA/AANN/AANS/ACR/ASNR/CNS/SAIP/SCAI/SIR/SNIS/SVM/SVS guideline on the management of patients with extracranial carotid and vertebral artery disease: executive summary: a report of the American College of Cardiology Foundation/American Heart," *J. Am. Coll. Cardiol.*, vol. 57, no. 8, pp. 1002–44, Feb. 2011.
- [262] A. C. Newby, S. J. George, Y. Ismail, J. L. Johnson, G. B. Sala-Newby, and A. C. Thomas, "Vulnerable atherosclerotic plaque metalloproteinases and foam cell phenotypes.," *Thromb. Haemost.*, vol. 101, no. 6, pp. 1006–11, Jun. 2009.
- [263] H.-C. Chan, L.-Y. Ke, C.-S. Chu, A.-S. Lee, M.-Y. Shen, M. a Cruz, J.-F. Hsu, K.-H. Cheng, H.-C. B. Chan, J. Lu, W.-T. Lai, T. Sawamura, S.-H. Sheu, J.-H. Yen, and C.-H. Chen, "Highly electronegative LDL from patients with ST-elevation myocardial infarction triggers platelet activation and aggregation.," *Blood*, vol. 122, no. 22, pp. 3632–41, Nov. 2013.
- [264] H. Shi, T. Varghese, C. C. Mitchell, M. McCormick, R. J. Dempsey, and M. A. Kliewer, "In vivo attenuation and equivalent scatterer size parameters for atherosclerotic carotid plaque: preliminary results.," *Ultrasonics*, vol. 49, no. 8, pp. 779–85, Dec. 2009.
- [265] K. Nightingale, "Acoustic Radiation Force Impulse (ARFI) Imaging: a Review.," *Curr. Med. Imaging Rev.*, vol. 7, no. 4, pp. 328–339, Nov. 2011.
- [266] R. Righetti, J. Ophir, and P. Ktonas, "Axial resolution in elastography.," *Ultrasound Med. Biol.*, vol. 28, no. 1, pp. 101–13, Jan. 2002.
- [267] J. D. Allen, K. L. Ham, D. M. Dumont, B. Sileshi, G. E. Trahey, and J. J. Dahl, "The development and potential of acoustic radiation force impulse (ARFI) imaging for carotid artery plaque

- characterization.," *Vasc. Med.*, vol. 16, no. 4, pp. 302–11, Aug. 2011.
- [268] T. J. Czernuszewicz, J. W. Homeister, M. C. Caughey, M. A. Farber, J. J. Fulton, P. F. Ford, W. A. Marston, R. Vallabhaneni, T. C. Nichols, and C. M. Gallippi, "Non-invasive in vivo characterization of human carotid plaques with acoustic radiation force impulse ultrasound: comparison with histology after endarterectomy.," *Ultrasound Med. Biol.*, vol. 41, no. 3, pp. 685–97, Mar. 2015.
- [269] J. A. Jensen and N. B. Svendsen, "Calculation of pressure fields from arbitrarily shaped, apodized, and excited ultrasound transducers.," *IEEE Trans. Ultrason. Ferroelectr. Freq. Control*, vol. 39, no. 2, pp. 262–7, Jan. 1992.
- [270] J. A. Jensen, "Field: A Program for Simulating Ultrasound Systems," in *10th Nordic-Baltic Conference on Biomedical Imaging*, 1996, vol. 34, pp. 351–353.
- [271] C. Leys, C. Ley, O. Klein, P. Bernard, and L. Licata, "Detecting outliers: Do not use standard deviation around the mean, use absolute deviation around the median," *J. Exp. Soc. Psychol.*, vol. 49, no. 4, pp. 764–766, 2013.
- [272] T. J. Czernuszewicz, J. E. Streeter, P. A. Dayton, and C. M. Gallippi, "Experimental validation of displacement underestimation in ARFI ultrasound.," *Ultrason. Imaging*, vol. 35, no. 3, pp. 196–213, Jul. 2013.
- [273] R. E. Zierler and D. L. Dawson, *Strandness's Duplex Scanning in Vascular Disorders*, Fifth Ed. Lippincott Williams & Wilkins, 2015.
- [274] P. R. Hoskins, K. Martin, and A. Thrush, *Diagnostic Ultrasound: Physics and Equipment*. Cambridge University Press, 2010.
- [275] R. J. Frink, "Atheromas Are Caseous Abscesses," in *Inflammatory Atherosclerosis: Characteristics of the Injurious Agent*, Sacramento, CA: Heart Research Foundation, 2002.
- [276] J. K. Lovett, J. N. E. Redgrave, and P. M. Rothwell, "A critical appraisal of the performance, reporting, and interpretation of studies comparing carotid plaque imaging with histology.," *Stroke.*, vol. 36, no. 5, pp. 1091–7, May 2005.
- [277] K. Kaivanto, "Maximization of the sum of sensitivity and specificity as a diagnostic cutpoint criterion.," *J. Clin. Epidemiol.*, vol. 61, no. 5, pp. 517–8, May 2008.
- [278] F. Jashari, P. Ibrahimi, E. Johansson, J. Ahlqvist, C. Arnerlöv, M. Garoff, E. L. Jäghagen, P. Wester, and M. Y. Henein, "Atherosclerotic Calcification Detection: A Comparative Study of Carotid Ultrasound and Cone Beam CT.," *Int. J. Mol. Sci.*, vol. 16, no. 8, pp. 19978–88, 2015.
- [279] D. Dumont and B. Byram, "Robust Tracking of Small Displacements with a Bayesian Estimator.," *IEEE Trans. Ultrason. Ferroelectr. Freq. Control*, Oct. 2015.
- [280] M. Krzanowski, W. Bodzoń, and P. P. Dimitrow, "Imaging of all three coronary arteries by transthoracic echocardiography. An illustrated guide.," *Cardiovasc. Ultrasound*, vol. 1, no. 1, p. 16, 2003.
- [281] H. M. Garcia-Garcia, M. a Costa, and P. W. Serruys, "Imaging of coronary atherosclerosis: intravascular ultrasound.," *Eur. Heart J.*, vol. 31, no. 20, pp. 2456–69, Oct. 2010.
- [282] V. Patel, J. J. Dahl, D. P. Bradway, J. R. Doherty, S. Y. Lee, and S. W. Smith, "Acoustic

- Radiation Force Impulse Imaging (ARFI) on an IVUS Circular Array.,” *Ultrason. Imaging*, vol. 36, no. 2, pp. 98–111, Apr. 2014.
- [283] C.-C. Shih, C.-C. Huang, Q. Zhou, and K. K. Shung, “High-resolution acoustic-radiation-force-impulse imaging for assessing corneal sclerosis.,” *IEEE Trans. Med. Imaging*, vol. 32, no. 7, pp. 1316–24, Jul. 2013.
- [284] J. Ma, K. Martin, P. A. Dayton, and X. Jiang, “A preliminary engineering design of intravascular dual-frequency transducers for contrast-enhanced acoustic angiography and molecular imaging.,” *IEEE Trans. Ultrason. Ferroelectr. Freq. Control*, vol. 61, no. 5, pp. 870–80, May 2014.
- [285] R. Krimholtz, D. A. Leedom, and G. L. Matthaei, “New equivalent circuits for elementary piezoelectric transducers,” *Electron. Lett.*, vol. 6, no. 13, p. 398, 1970.
- [286] B. Wu, X. Pei, Z. Li, and M. Engineering, “How Does Calcification Influence Plaque Vulnerability? Insights from Fatigue Analysis,” *Sci. World J.*, vol. 2014, no. 417324, p. 8, 2014.
- [287] F. W. Mauldin, H. T. Zhu, R. H. Behler, T. C. Nichols, and C. M. Gallippi, “Robust principal component analysis and clustering methods for automated classification of tissue response to ARFI excitation.,” *Ultrasound Med. Biol.*, vol. 34, no. 2, pp. 309–25, Feb. 2008.
- [288] V. G. Andreev, V. N. Dmitriev, Y. A. Pischalnikov, O. V Rudenko, O. A. Sapozhnikov, and A. P. Sarvazyan, “Observation of shear waves excited by focused ultrasound in a rubber-like media,” *Acoust. Phys.*, vol. 43, pp. 123–128, 1997.
- [289] E. Bossy, A. R. Funke, K. Daoudi, A. C. Boccara, M. Tanter, and M. Fink, “Transient optoelastography in optically diffusive media,” *Appl. Phys. Lett.*, vol. 90, no. 17, 2007.
- [290] S. Callé, J.-P. Remenieras, O. B. Matar, M. E. Hachemi, and F. Patat, “Temporal analysis of tissue displacement induced by a transient ultrasound radiation force.,” *J. Acoust. Soc. Am.*, vol. 118, no. 5, pp. 2829–40, Nov. 2005.
- [291] S. G. Chen, M. Fatemi, and J. F. Greenleaf, “Remote measurement of material properties from radiation force induced vibration of an embedded sphere,” *J. Acoust. Soc. Am.*, vol. 112, no. 3, pp. 884–889, 2002.
- [292] R. R. Bouchard, G. Van Soest, G. E. Trahey, and A. F. Van Der Steen, “Optical tracking of superficial dynamics from an acoustic radiation force-induced excitation,” *Ultrason. Imaging*, vol. 31, no. 1, pp. 17–30, 2009.
- [293] R. R. Bouchard, M. L. Palmeri, G. F. Pinton, G. E. Trahey, J. E. Streeter, and P. A. Dayton, “Optical tracking of acoustic radiation force impulse-induced dynamics in a tissue-mimicking phantom.,” *J. Acoust. Soc. Am.*, vol. 126, no. 5, pp. 2733–45, Nov. 2009.
- [294] R. S. C. Cobbold, “Scattering of Ultrasound,” in *Foundations of Biomedical Ultrasound*, NY: Oxford University Press, 2007.
- [295] M. Greenspan and C. E. Tschiegg, “Speed of Sound in Water by a Direct Method,” *J. Res. Natl. Bur. Stand. (1934)*, vol. 59, no. 4, pp. 249–254, 1957.
- [296] G. R. Torr, “The Acoustic Radiation Force,” *Am. J. Phys.*, vol. 52, no. 5, pp. 402–408, 1984.